UNIVERSITY *of* TASMANIA

School of Physical Sciences

MALT-45: A 7 mm survey of the southern Galaxy

Christopher Harry Jordan
Bachelor of Engineering with Honours - Bachelor of Science
(Electrical and Electronic / Mathematics)

September 2015

Supervisors:
Dr. Andrew Walsh
Prof. Simon Ellingsen
Dr. Maxim Voronkov

Submitted in fulfilment of the requirements for the Degree of
Doctor of Philosophy

Declaration of Originality

This thesis contains no material which has been accepted for a degree or diploma by the University or any other institution, except by way of background information and duly acknowledged in the thesis, and to the best of my knowledge and belief no material previously published or written by another person except where due acknowledgement is made in the text of the thesis, nor does the thesis contain any material that infringes copyright.

Signed: _____

Date: 17 / 09 / 15

Authority of Access

Signed: _____

Date: 17 / 09 / 15

Statement of Co-Authorship

The following people contributed to the publication of work undertaken as part of this thesis:

Candidate	Jordan, C. H.	University of Tasmania, CSIRO Astronomy & Space Science
Co-Author 1	Walsh, A. J.	International Centre for Radio Astronomy Research, University of Tasmania
Co-Author 2	Ellingsen, S. P.	University of Tasmania
Co-Author 3	Voronkov, M. A.	CSIRO Astronomy & Space Science
Co-Author 4	Breen, S. L.	CSIRO Astronomy & Space Science

Chapter 2: *Pilot observations for MALT-45: a Galactic plane survey at 7 mm*
Candidate (80%), Co-Author 1 (20%)
Candidate was the primary author and Co-Author 1 contributed to the idea, its formalisation, development and refinement. Writing was done primarily by the Candidate, with some paragraphs and feedback provided by Co-Author 1. Feedback and editing for the purposes of publication was provided by the remaining authors.

Chapter 3: *MALT-45: A 7 mm survey of the southern Galaxy - I. Techniques and spectral line data*
Candidate (80%), Co-Author 1 (10%), Co-Author 2 (5%), remaining Co-Authors (5%)
Candidate was the primary author and Co-Author 1 contributed to the idea, its formalisation, development and refinement. Writing was done primarily by the Candidate. Feedback and editing for the purposes of publication was provided by the remaining authors.

Chapter 4: *MALT-45: A 7 mm survey of the southern Galaxy - II. Follow-up observations of 44 GHz class I methanol masers*
Candidate (90%), Co-Authors 1, 2, 3 and 4 (10%)
Candidate was the primary author and Co-Authors 1, 2, 3 and 4 contributed to the idea, its formalisation, development and refinement. Writing was done primarily by the Candidate. Feedback and editing for the purposes of publication was provided by the Co-Authors 1, 2, 3 and 4.

Signed: _____

Date: 17 / 09 / 15

Dr. Andrew Walsh, Primary Supervisor
International Centre for Radio Astronomy Research, Curtin University

Abstract

The last decade has seen vast improvement in the knowledge of star formation within our Galaxy, largely owing to improvements in instrumentation, allowing astronomers to compile more data. However, despite the advances of technology, the quest for understanding high-mass star formation (HMSF) continues. As we go on, breakthroughs have occurred; a prime example is the discovery of the class II methanol maser, which exclusively signposts on-going sites of HMSF, but still lacks the detail necessary to identify HMSF in all forms. Once we have understood where, why and how HMSF can occur, we will be able to diagnose Galactic structure and evolution.

Untargeted, large area surveys of molecular gas are ideal for identifying HMSF regions across a broad range of evolutionary phases. For example, searches for molecular species with a high critical density can highlight dense gases, which can then be used to probe Galactic structure and star formation. Because HMSF occurs in regions of dense molecular gas, mapping high-density tracers serves well to identify regions for study. The (1,1), (2,2) and (3,3) inversion transitions of ammonia (NH_3) have been successfully mapped by the H_2O Southern Galactic Plane Survey (HOPS), identifying previously unknown sites of star formation, as well as probing the structure of the Milky Way's spiral arms. Fortunately, HMSF can be identified by bright spectral lines in maser emission; HOPS also mapped the Galactic plane for water (H_2O) masers and, perhaps more importantly, the Methanol MultiBeam survey identifies class II methanol (CH_3OH) masers, which are exclusively associated with HMSF. While class II CH_3OH masers always signpost HMSF, they appear only in a specific evolutionary stage, and therefore other species (such as H_2O masers) are required to identify other stages.

Another, even higher density gas tracer useful for detecting HMSF and mapping the structure of our Galaxy is carbon monosulfide (CS). The ground state transition $J = 1 \rightarrow 0$ for CS lies within the 7 mm waveband, which also contains the poorly understood class I CH_3OH maser. Unlike the class II variant, class I masers are not exclusively associated with HMSF, but do appear in star-forming regions across a wide range of evolutionary stages. A large problem for class I CH_3OH maser studies is the bias in the targeted searches which have been used to find them; they have only been identified towards other masing regions (such as class II CH_3OH), and therefore the properties of these masers are somewhat unclear.

In this thesis, results focus on the MALT-45 survey using the Australia Telescope Compact Array (ATCA) in auto-correlation ('single-dish' mode). To date, MALT-45 has mapped the Galactic plane within $330^\circ < l < 335^\circ$, $|b| < 0.5^\circ$, which contains several known star-forming regions, including the G333 giant molecular cloud. MALT-45 surveys 12 spectral lines, but primarily CS (1–0), class I CH_3OH masers and SiO (1–0) $v = 0, 1, 2, 3$. Bright, extended CS emission is detected across the survey region, and highlight two distinct velocities, due to different spiral arms of the Galaxy. In addition to the previously known 19 class I CH_3OH masers, 58 new masers were detected. SiO masers were detected towards 47 regions, in various combinations of vibrational mode $v = 1, 2, 3$, all towards evolved infrared stars. Thermal SiO $v = 0$ emission is also detected across the survey region.

Major science results from MALT-45 include:

(i) A CS to NH_3 comparison, which highlights cold, dense clumps as well as hot, evolved clumps. The cold and dense clumps appear to have self-absorption of CS emission in their centres and a relative over-abundance of NH_3, while evolved clumps appear to have very little NH_3 emission, despite being a dense gas tracer;

(ii) Almost all (94 per cent) of ATLASGAL 870 μm dust emission point sources are associated with at least a 3σ peak of CS emission;

(iii) By comparing with peak CS velocities, class I CH_3OH masers are good indicators of the systemic velocities of clouds;

(iv) More than half (55 per cent) of the detected class I CH_3OH masers are not associated with any other kind of maser;

(v) Class II CH_3OH, H_2O and hydroxyl (OH) masers associate well with class I CH_3OH masers, confirming that class I CH_3OH masers occur towards a wide range of evolutionary stages in HMSF;

(vi) Class I CH_3OH masers appear to have no correlation in intensity or luminosity with other maser species;

(vii) Class I CH_3OH masers have typical projected linear distances from other masers associated with star formation, peaks of CS and 870 μm point sources within 0.5 pc;

(viii) Class I CH_3OH masers are spread over a larger area when also associated with class II CH_3OH or OH masers, perhaps due to their more evolved state;

(ix) Almost all (95 per cent) of class I CH_3OH masers are associated with an ATLASGAL source;

(x) Using ATLASGAL source parameters, a clump mass is calculated. The population of class I CH_3OH masers has a broad range of associated masses ($10^{1.5}$ to $10^{4.5}\,M_\odot$), but peaks between $10^{3.0}$ and $10^{3.5}\,M_\odot$. Higher masses tend to be associated with evolved regions of star formation, while lower masses tend to be non-evolved regions;

(xi) SiO masers typically decrease in intensity with vibrational mode ($v = 1, 2, 3$), but eleven cases of stronger $v = 2$ than $v = 1$ emission were found, and two regions of only $v = 2$ emission were found;

(xii) The relatively rare $v = 3$ vibrational mode of SiO (1–0) was detected towards three evolved infrared stars.

Acknowledgements

This PhD project and thesis has really pushed me to the limit. As difficult as it has been, without the support offered by many people over the years, I would have crumbled under the pressure.

The work leading up to this thesis began at James Cook University, and due to unfortunate circumstances, could not continue there. Townsville was home for a long time, with many friends and family members helping my work to become a reality. I have been a university dweller for nearly 10 years, and it has taken me most of this time to realise how good my family has been to me. Without their unquestioning support, this thesis was surely doomed from the start. I also want to thank the 'uni crew', in no particular order: Bronson, Patty, Nick, Rhys, Clair, Liam, Nathan and Tim. Without your laughter and encouragement, nothing would have been possible.

I was incredibly fortunate to find a new home at the University of Tasmania. My new school, despite the cold climate (especially relative to Townsville!), was warm and friendly right from the start. That welcome was something I'll never forget, and helped me through a very stressful time. I am indebted to all of the staff, but I particularly want to thank a few people. John Dickey had a knack for offering key advice at the right time. Jim Lovell was kind and considerate, supporting me during my UTAS years with many, many hours of paid observational work. Shari Breen, while not formally part of UTAS, always felt close by and has helped me at many points of my candidature. Simon Ellingsen deserves my biggest praise, for being a fantastic supervisor (especially in the circumstances). I don't think I ever once heard him complain, even as I've received many comments on my poor attempt at writing. I am proud and grateful to have conducted my work through UTAS.

Thanks must also go to CSIRO Astronomy and Space Science. The opportunities granted to me through many duty astronomer shifts, schools and discussions with staff proved invaluable, and I hope future students are as lucky as I was. Maxim Voronkov co-supervised me with methanol maser expertise; always friendly and helpful, it was great to have someone so passionate on board.

My time in Tasmania was supported by many other wonderful people, possibly too many to name. Jay and Anita were always nearby, and helped me fit right in. Vasaant was always up for an interesting chat, especially concerning emacs. Courtney shared many laughs with me, especially towards the end, sharing an office where we were both finishing our theses. A few friendly Europeans - Lucia, Liza, Alvaro, Sara (and Jamie, the native Tasmanian) - were great company with garlic prawn pizzas at the nearby pub. Finally, I had amazing housemates in Dave and Tim; between many curry nights, there are way too many laughs to remember. One final mention to Christian (Kevin), who could always crack me up. Thank you all so much.

Special mention goes to my Rebecca, who has participated in many fantastic holidays, shares my dreams and has particularly given a lot of support at the end of this thesis. I hope that this thesis acts as a foundation to build our successes upon.

Finally, last but certainly not least, I give my biggest thanks to Andrew Walsh. He has been with me from the start, and I could not have asked for a better supervisor. But more

than a supervisor, he was a mentor and a great friend. Always generously facilitating his love of beer, many good times have passed over the years. I can never repay the effort lent to me, but I hope that I can at least pass on the kindness to others in the future. Cheers!

Contents

List of Figures

List of Tables

List of Equations

Chapter 0

Motivation for MALT-45

High-mass star formation (HMSF) is a difficult problem in astrophysics. In the infancy of HMSF study, astronomers would target known regions of star formation, such as Orion, to attempt to understand the underlying physics. More recently, technological advancements have allowed for more sophisticated observations, even allowing large-scale surveys of the Galaxy. While targeted observations of HMSF regions have been productive in identifying many underlying properties, untargeted surveys are necessary to remove the bias from these studies, and determine the global properties of HMSF. To this end, several untargeted surveys have been conducted, each focusing on different aspects of HMSF, such as cold dust, warm dust, H II regions, dense gas and maser emission. These surveys are especially useful when compared with one another; for example, the class II methanol maser is associated only with HMSF, but is destroyed as a star-forming region evolves into a H II region.

This thesis details the MALT-45 survey, which aims to further our understanding of HMSF through providing additional spectral line data which complements and builds upon information from other surveys of star formation. MALT-45 primarily surveys for three families of spectral lines:

i) The ground-state transition of carbon monosulfide is a bright, very-dense gas tracer, which has previously only been observed in targeted regions. By comparing the large-scale distribution of this spectral line with another dense gas tracer, such as ammonia, we can observe the differences between carbon-bearing and nitrogen-bearing species in cold, dense regions. A survey of carbon monosulfide may also reveal dense gas structure across the Galaxy not seen before.

ii) Interstellar masers are excellent signposts for regions of HMSF. Of these, class I methanol masers are least well understood, and are known in relatively few locations. By identifying a statistically-complete of these masers, we can understand what conditions they trace, and how they relate to other masers as well as HMSF.

iii) Thermal silicon monoxide emission is well established as a shocked-gas tracer in HMSF, but a large-scale search for this spectral line has not been conducted before. The distribution of this gas, as well as its association with outflows in HMSF, can be tested. Simultaneously, silicon monoxide masers can be identified. These masers are usually found toward evolved stars, but some rare instances are found toward HMSF.

Chapter 1

Introduction

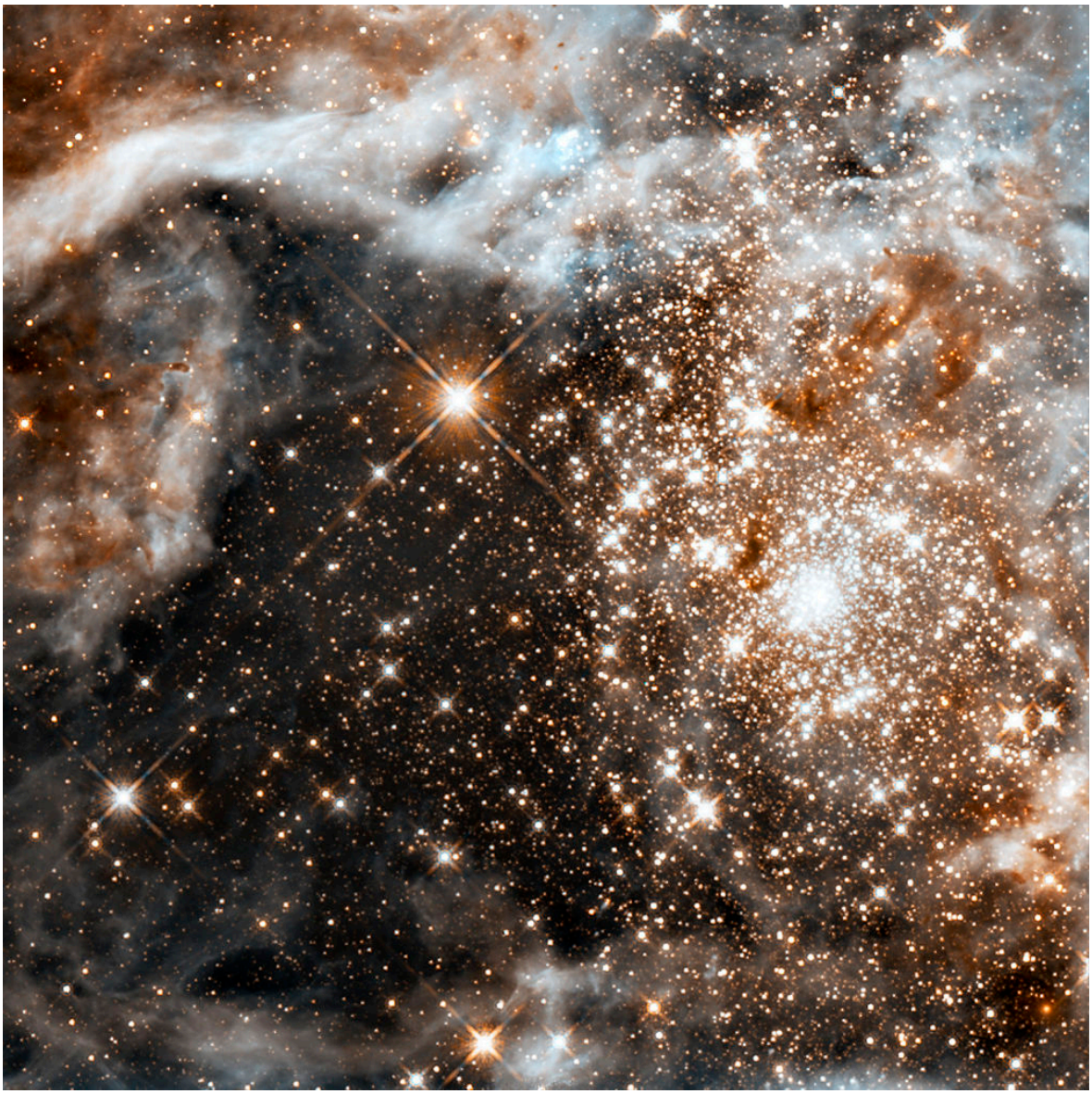

Figure 1.1: R136, a star cluster within the Tarantula nebula, contains hundreds of high-mass stars. This image was taken in infrared from the Hubble space telescope.

1.1 Motivation

How are stars created? Until the realisation of gravity, this was perhaps too difficult a question to broach throughout human history. Newton was indeed a talented individual: along with his theory of Gravity, he was the first to speculate on gravitational collapse being a chief component. This provided the catalyst for research, and after many centuries, we have a good understanding for the overall process of star formation.

However, nature is not without complication. Star formation is not a readily explained simple procedure, applicable everywhere; it can be divided into sub-categories of low- and high-mass star formation (LMSF, HMSF). LMSF is better understood and characterised, and often occurs in isolation with minimal requirements. HMSF, however, is vastly more complicated. Perhaps the most striking difference is that low-mass stars are simultaneously created alongside the high-mass stars, yielding an entire star cluster, such as that seen in Fig. 1.1. Formally, high-mass stars are categorised by possessing eight or more solar masses ($>8\,M_{\odot}$, also known as O- or B-type stars), as such stars die via supernovae. HMSF is defined as the formation of such stars. High-mass stars are important, as only they provide the means for producing heavy elements (such as iron), and scatter these throughout the interstellar medium (ISM). High-mass stars are also incredibly energetic; the amount of energy they produce over their lifetime rivals that of their supernova deaths. By understanding how high-mass stars are created, we are able to determine galaxy evolution and structure, through the evolution of molecular clouds and spiral arms. A simplified, generalised timeline of LMSF is outlined in Fig. 1.2.

HMSF is more complicated than the LMSF scenario: it is not a simply 'scaled-up' version of LMSF. Unlike LMSF, accretion continues once a high-mass YSO has joined the main sequence (Kahn 1974), and the turbulence of HMSF greatly slows the in-falling rate of the gas (Caselli & Myers 1995). Additionally, bigger and hotter stars may restrict further accretion with significant blackbody radiation, yielding an outward pressure. Once complete, HMSF does not yield one or a few high-mass objects; rather, a whole cluster of stars with a distribution of mass is created. Despite decades of research, the exact physical process of HMSF is still poorly understood. Observationally, there are a few factors which slow progress:

i) HMSF requires a minimum mass of the parent molecular clouds (Kauffmann et al. 2010), and the nearest to Earth is Orion at $\sim$450 pc, while LMSF has been observed even closer (e.g. Taurus-Auriga, 150 pc). High resolution instruments are needed to discern the finer details at great distances;

ii) HMSF occurs in the most dense regions of molecular clouds, effectively requiring the use of radio and infrared astronomy. Shorter-wavelength emission from YSOs is re-processed into long-wavelengths by the natal environment. Ground-based observations are susceptible to radio frequency interference as well as atmospheric effects, increasing the difficulty of observations;

iii) Rather than forming isolated stars, HMSF tends to form clusters of stars (which, depending on the mass of the stars, may also be called OB associations). Isolating the conditions feeding a high-mass YSO are difficult when the whole region is star-forming;

iv) High-mass stars are created and evolve over much shorter timescales than low-mass

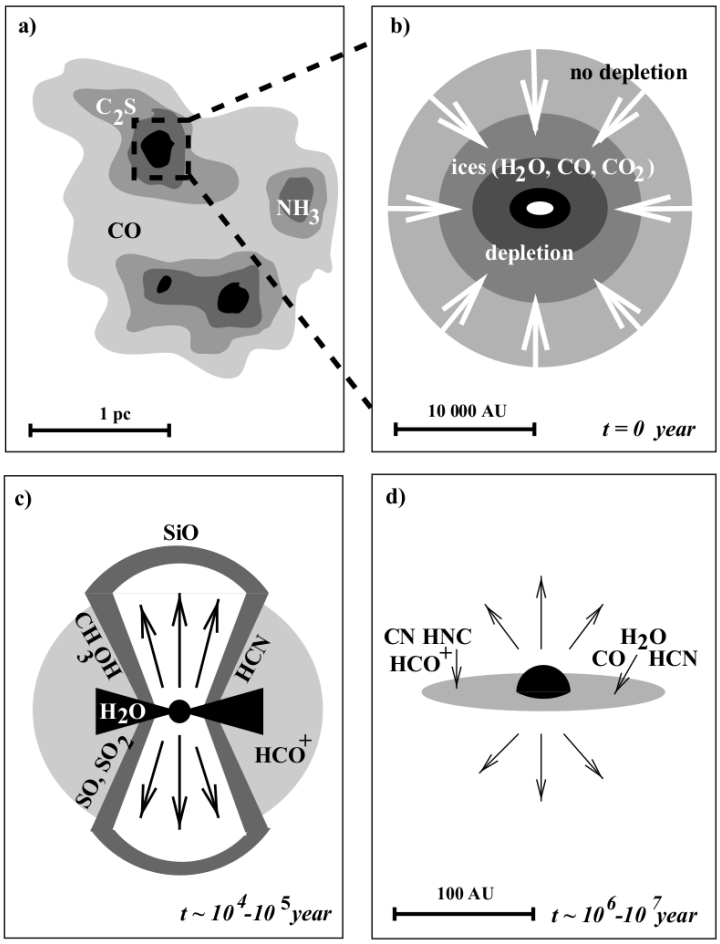

Figure 1.2: Evolutionary stages of LMSF, taken from van Dishoeck & Blake (1998). The sub-panels are detailed as follows:

a) Within a molecular cloud, a core of gas and dust (a compact substructure with typical sizes of 1 parsec and densities of 10^5 molecules of hydrogen per cubic centimetre) is unable to support its internal pressure against gravitational self-collapse, also known as the Jeans instability (Jeans 1902);

b) Matter within the core falls into a focus, via a procedure termed 'inside-out collapse'. The most central part of the core collapses inwards fastest, followed by the surrounding shell, and so on, until the material is exhausted (Shu 1977);

c) The focus of the core becomes a young stellar object (YSO), which is fed by an accretion disk and exhibits perpendicular outflows. These features are necessary to remove the excess angular momentum of in-falling material;

d) Through a combination of the disk being exhausted and blown away by the outflows, accretion halts. Eventually, the internal temperature of the YSO rises to begin hydrogen fusion, at which point the star joins the main sequence. The remaining accretion disk may become a protoplanetary disk.

stars. They are also rare: Wood & Churchwell (1989) imply that there are roughly 20000 O-type stars in the Galaxy. Magnetic fields resist the self-gravity collapse of clouds (Pillai et al. 2015). Therefore, witnessing HMSF 'in the act' is difficult, in addition to all the above.

Parallels do exist between LMSF and HMSF. As with LMSF, molecular clouds fragment to form similar substructures (clumps and cores; see Table 1.1), and there is overwhelming evidence of outflows occurring in HMSF (Moscadelli & Goddi 2014; Yu & Wang 2014; Navarete et al. 2015). The presence of outflows also hints at the existence of accretion disks. However, the traditional inside-out collapse model (*core accretion*) (McKee & Tan 2003) may not be the solution to accretion within HMSF; an alternate theory of *competitive accretion* (Bonnell 2008) asserts that gas is drawn over larger spatial scales within molecular clouds, because the surrounding low-mass YSOs are formed simultaneously, and are also able to accrete gas. Recent observations show HMSF occurring along filaments within GMCs (Molinari et al. 2010), supporting models such as Smith et al. (2014). Additionally, if the density of YSOs is high enough, high-mass YSOs may be formed by mergers (Bonnell et al. 1998). Mergers are proposed due to the difficulty of accretion being efficient enough to yield high-mass YSOs. While mergers remain a possibility for generating high-mass stars, it is unlikely to affect typical HMSF; modelling shows that mergers are efficient mechanisms in high-population star clusters, and that one or two extreme objects result (Moeckel & Clarke 2011).

Currently, HMSF studies have allowed us to understand how to generate stars up to $20\,M_{\odot}$, yet we see stars in excess of $100\,M_{\odot}$ in nature. How are these stars created? There are many directions of study to help answer this question. In the following sections, evolutionary stages of HMSF and tools used to identify them are discussed.

1.2 A general timeline of HMSF

All star formation occurs within molecular clouds (MCs), but HMSF typically occurs within giant molecular clouds (GMCs), with masses exceeding $10^4\,M_{\odot}$. In an attempt to understand HMSF, we must categorise the various evolutionary stages. Table 1.1 lists some properties of these stages, although these should be treated with care. The remainder of this section describes each evolutionary stage in further detail.

Table 1.1: Properties of various structures associated with HMSF. These values serve as 'rules of thumb' for classification. Temperatures of H II regions refer to molecular gas, rather than the ionised regions.

	Size (pc)	Density (n_{H_2} cm^{-3})	Temperature (K)	Reference
Molecular cloud	∼10	∼10^2	∼10	Kim & Koo (2001)
Molecular clump	∼1	∼10^5	∼30	Kim & Koo (2001)
Hot molecular core	<0.1	>10^7	>100	de Villiers et al. (2015)
HC H II region	<0.1	>10^6	>200	Lizano (2008)
UC H II region	<0.5	>10^5	100-200	Churchwell (2002)

Table 1.2: Properties of various molecular cloud types, taken from Stahler & Palla (2005).

Cloud type	A_V (mag)	n_{tot} (cm^{-3})	Diameter (pc)	Temp. (K)	Mass ($M_\odot$)	Examples
Diffuse	1	500	3	50	50	
GMCs	2	100	50	15	10^5	Orion
Dark clouds						
Complexes	5	500	10	10	10^4	Taurus-Auriga
Individual	10	10^3	2	10	30	B1
Dense cores/Bok globules	10	10^4	0.1	10	10	TMC-1/B335

1.2.1 Molecular clouds and Infrared dark clouds

MCs are regions of the ISM both sufficiently cold and dense for molecules to survive. The neutral H I population is allowed to form covalent bonds with one another, yielding the primary component H_2. However, MCs also contain heavier molecules; because H_2 is difficult to detect, the amount of H_2 present is usually estimated in terms of the heavier molecules using so-called '$\mathcal{X}$-factors'. The archetypal example is carbon monoxide (CO); it is easily excited and very abundant, making it useful for probing MCs. Table 1.2 gives some typical properties of MCs. As the ISM contains energetic photons (ultraviolet or shorter wavelength) which are able to dissociate H_2, a molecular cloud might not survive longer enough to allow star formation to occur. Clouds with sufficient mass are resistant to destruction via a process called self-shielding; simply put, H_2 on the exterior of a MC is dissociated, leaving the internal H_2 intact.

Dust grains also contribute to shielding of molecules by absorbing some of the ultraviolet radiation. By mass, grains are mostly made up of silicon (Draine 2003), and are important for the chemistry within MCs. In addition to gas-phase chemistry, sufficiently dense regions allow the various molecules present to react with one another by using electrostatic forces on dust grain surfaces, which yield more complicated molecular species. This is especially useful for the study of HMSF, as the signatures of these molecules allow us to diagnose the conditions within MCs. In young regions of star formation, certain species experience 'freeze-out' (depletion) on to the dust grains; as the density increases and temperature remains low, the observed molecular emission decreases, as molecules freeze onto dust grains. Other species are resistant to depletion, which allow diagnosis of evolutionary state. Depleted species may be released later by shocks or radiation from newly formed stars, which further detail the evolutionary state. Eventually, dust grains may be destroyed by shocks, providing further useful species for study, such as silicon monoxide (SiO).

Is there an analogue of LMSF core collapse in HMSF? Relatively new objects of study, infrared dark clouds (IRDCs), may provide it. Discovered by Egan et al. (1998) and Carey et al. (1998), IRDCs are the densest parts of GMCs, and are identified as extinction features against the bright infrared emission of the Galaxy; a beautiful example can be seen in Fig. 1.3. They are thought to be the birthplaces of high-mass stars and star clusters, with typical masses 10^2-10^4 $M_\odot$, densities 10^2-10^4 cm^{-3} and temperatures 10-20 K (Rathborne et al. 2006). Space-based observations have provided relevant infrared imagery in various wavelengths,

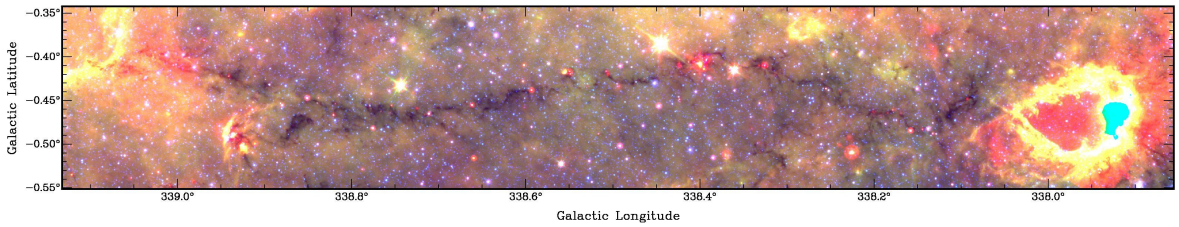

Figure 1.3: An exceptional example of an infrared dark cloud, Fig. 1a of Jackson et al. (2010): *A false three-colour image of the Nessie Nebula. The 3.6 µm (blue) and 8.0 µm (green) emission is from GLIMPSE, and the 24 µm (red) emission is from MIPSGAL.*

including the Galactic Legacy Infrared Mid-Plane Survey Extraordinaire (GLIMPSE). Using infrared imagery, large catalogues of IRDC candidates have been formed (Simon et al. 2006; Peretto & Fuller 2009). However, there are multiple ways to define what an IRDC is, and therefore different methods will highlight different objects; large differences exist between the catalogues presented by Simon et al. (2006) and Peretto & Fuller (2009). Nonetheless, exciting results have come from the study of these objects, including an extremely dense cloud that may form a stellar cluster similar to Orion (SDC335.579−0.272; Peretto et al. 2013). Improvements in isolating IRDCs are on-going, utilising the *Herschel* space telescope (Battersby et al. 2011; Wang et al. 2015).

1.2.2 Cold molecular core

HMSF begins within MCs and IRDCs, which are readily detected across the Galaxy. An accreting high-mass YSO disrupts its environment, and is reasonably obvious when doing so, detectable by its advanced chemistry, higher temperatures and infrared emission. By contrast, finding the evolutionary phase between a cold molecular cloud and a hot molecular core is difficult, but important, as the properties of these cold molecular cores determine the initial conditions for HMSF, such as the distribution of mass among resulting stars. Observations of ammonia and deuterated ammonia have proven successful at finding 'pre-protoclusters', although this branch of star formation is largely waiting for a thorough investigation through observations with the upcoming ALMA* Pillai et al. (2011).

1.2.3 Hot molecular core

As accretion is on-going, the high-mass YSO becomes hot, irradiating its environment with thermal energy. Additionally, the outflows from an accretion disk shock and further inject thermal energy into the medium. Hot molecular cores are distinct from earlier stages of HMSF, given their tiny sizes (<0.1 pc), high densities (>10^7 cm^{-3}) and high temperatures (>100 K) (Churchwell 2002). These conditions allow unique chemistry to occur, signposting this relatively evolved stage of HMSF. Evidence does exist for accretion disks in HMSF (Yen et al. 2014), but it still remains somewhat of a 'Holy grail' to observe. An effective technique of inferring the presence of a disk is using highly-excited molecular transitions, which are

*The Atacama Large Millimeter/submillimeter Array, a 66-element interferometer located on the Chajnantor plateau, Chile.

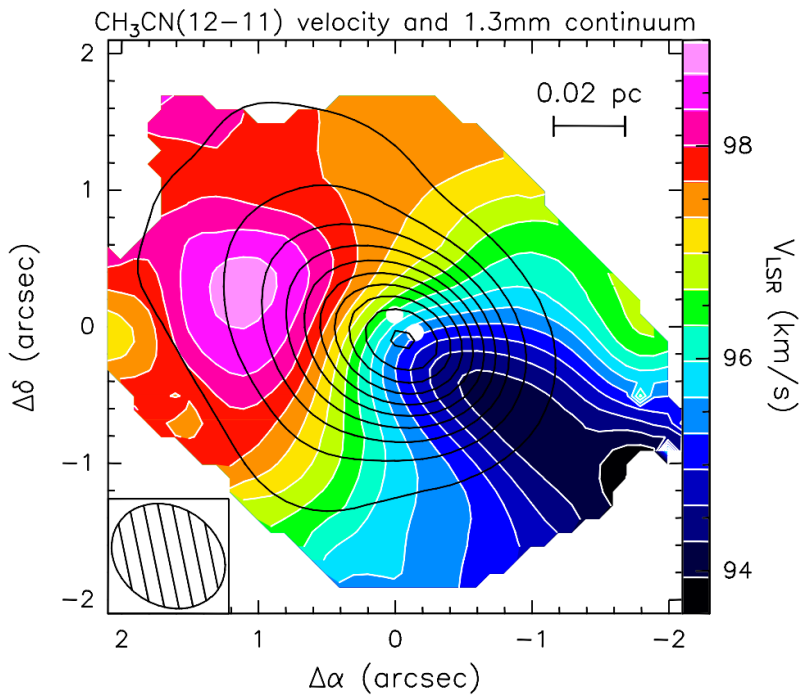

Figure 1.4: Fig. 5 of Cesaroni et al. (2011) shows evidence of a circumstellar disk: *Overlay of the map of the 1.3 mm continuum emission (contours) on that of the CH_3CN (12–11) line velocity (colour scale). Contour levels range from 0.1 to 2 in steps of 0.2 Jy/beam. Offsets are measured with respect to the phase centre. The two white dots denote the free-free continuum sources detected by Cesaroni et al. (2010). The synthesized beam is shown in the bottom left.*

rare, powered by high temperatures and require high densities of gas. One successful case of detection is via methyl cyanide (CH_3CN): it traces extremely dense gas (critical density, $n_c > 10^5\,\mathrm{cm}^{-3}$) and is excited in relatively warm regions >100 K (Purcell et al. 2006). Using emission from this molecule, Cesaroni et al. (2011) were able to map a velocity gradient across a well-studied hot molecular core; see Fig. 1.4.

Recently, a H_2O maser line with high excitation temperature (>3000 K) was used to identify a circumstellar disk in Orion Source I (Hirota et al. 2012). This complements other studies done in this region, including the detection of SiO maser emission highlighting the interface between disk and outflow (Niederhofer et al. 2012).

Outflows are relatively obvious, typical signatures of star formation. As mass collapses on to a YSO via an accretion disk, the built-up angular momentum is shed as perpendicular outflows. Interaction between the core medium, accretion disk and outflow is difficult to model; an example schematic attempting to quantify all mass flows can be seen in Fig. 1.5. One study finds that outflowing mass is a useful indicator of core mass (derived from 1.2 mm dust emission), with a first-order linear relation (Beuther et al. 2002b). The same study also finds that the physical processes are largely the same as in LMSF. While outflows are commonly seen in LMSF and HMSF, evidence for extremely low mass examples exist, such as toward brown dwarfs (Whelan et al. 2012). However, outflows from HMSF are empirically not as neatly collimated as in LMSF (Beuther et al. 2002a). Identification of outflows is commonly done by observing H_2 and SiO, as well as high-level transitions of CO, although heavier molecules such as HCO^+ and CS help to identify regions of HMSF (Gibb et al. 2003;

Garay et al. 2007; López-Sepulcre et al. 2009).

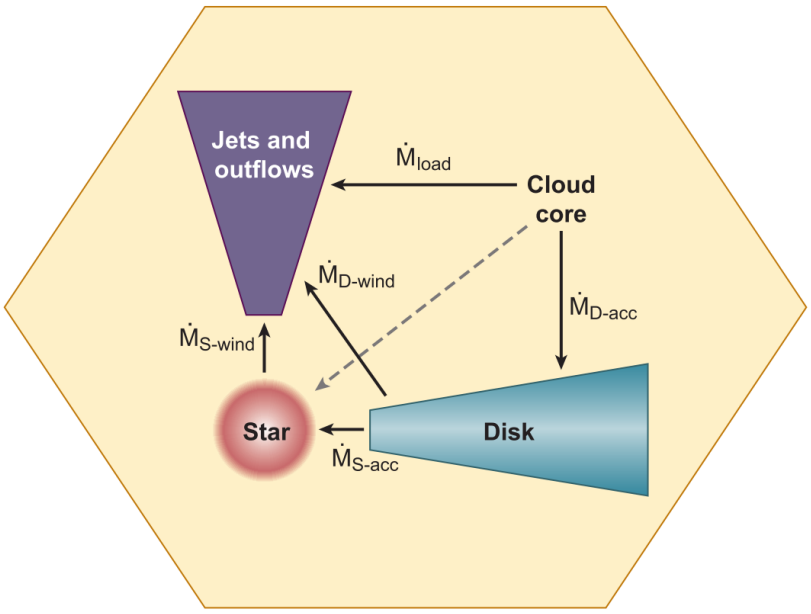

Figure 1.5: Fig. 1 of Zinnecker & Yorke (2007): *Accretion and mass loss as exchange between components: the accretion disk is the reservoir and interface between the molecular cloud core and the forming star.*

1.2.4 H II region

Eventually, a high-mass YSO is hot and luminous enough to ionise the surrounding natal gas. As well as converting molecular hydrogen to H II, the ultraviolet radiation effectively destroys many of the complex molecules in the vicinity, such as CH_3OH, by disassociation. The brightest of these can appear spectacular and even to the naked eye; see Fig. 1.6. Young H II regions are important because they signpost a late stage of HMSF.

H II regions evolve over time, and can be roughly classified by their size. Empirically, ultra-compact H II (UC H II) regions have sizes $\leq$0.1 pc and densities $\geq 10^4\,\mathrm{cm}^{-3}$ (Hoare et al. 2007). Observations reveal that hyper-compact H II (HC H II) regions have sizes $\leq$0.01 pc and densities $\geq 10^6\,\mathrm{cm}^{-3}$; these are clearly much more extreme than their UC H II relatives (Beuther et al. 2007). The Coordinated Radio and Infrared Survey for High-Mass Star Formation (CORNISH) complements the plethora of Galactic plane surveys with arcsecond resolution at 5 GHz, in a direct effort to detect H II regions, especially UC H II regions (Hoare et al. 2012). However, CORNISH is insensitive to HC H II regions, due to their tiny spatial sizes and optical thickness at 5 GHz (Purcell et al. 2013); higher frequencies are required to observe HC H II regions.

They can be detected in a few ways, but primarily through radio continuum observations as well as the presence of radio recombination lines. Ultra-compact H II (UC H II) regions are best detected at frequencies $\geq$5 GHz, where free-free continuum emission is optically thin (Purcell et al. 2013).

HC H II regions are younger, more extreme objects that will evolve into UC H II regions. One useful probe for identifying these are radio recombination lines, as these have been demon-

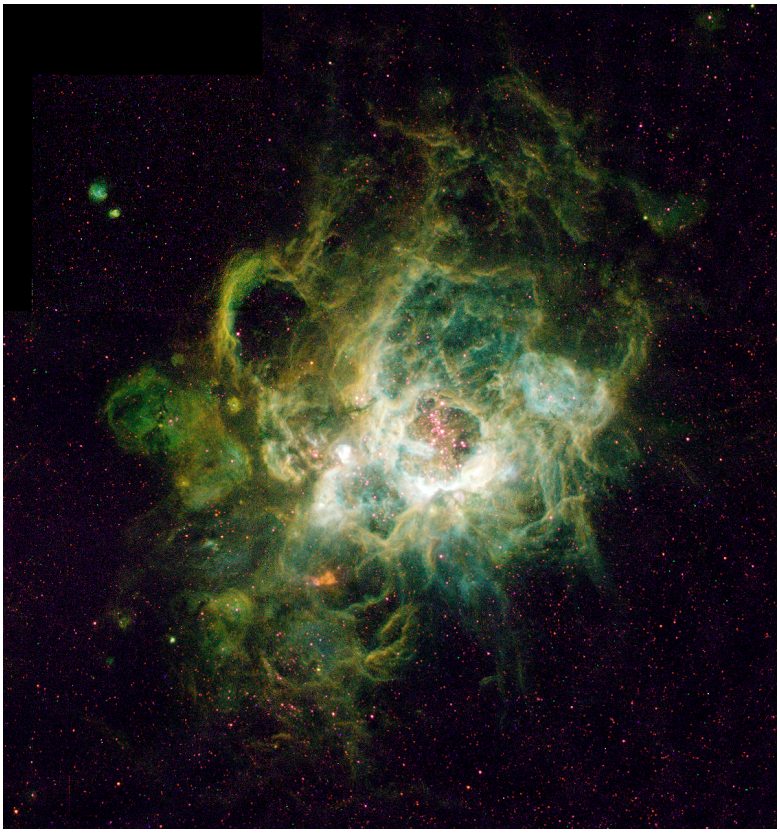

Figure 1.6: The giant H II complex, NGC 604, as viewed by the Hubble space telescope. Contained in the nearby galaxy M33, it contains several OB and WR stars (Eldridge & Relaño 2011).

strated to have linewidths in excess of $40\,\mathrm{km\,s^{-1}}$; UC H II regions typically have linewidths up to $30\,\mathrm{km\,s^{-1}}$ (Lizano 2008). Another useful tool for identification could be bright H_2O masers, which are powered in strongly shocked regions.

1.2.5 Summary

The different stages of HMSF have quite different properties. To understand the whole picture, it is important to discriminate and identify each evolutionary stage. The following section describes commonly used probes and techniques to do so.

1.3 Astrophysical diagnostics

1.3.1 Spectral lines

Hydrogen is the most abundant element in the universe, mostly existing in the atomic form, designated H I. The 'H I line' serves as a useful introduction to spectral lines, and is perhaps the most important astronomical spectral line; in practice, H I emission is easily detected, because it is ubiquitous in our Galaxy as well as others. H I is primarily useful for galactic structure and ISM studies. H I is produced by the quantum mechanical interaction between proton and election, and because energy shift is so small in magnitude, is termed hyperfine; see Fig. 1.7 for a schematic. Such low-energy photons are emitted within the radio regime

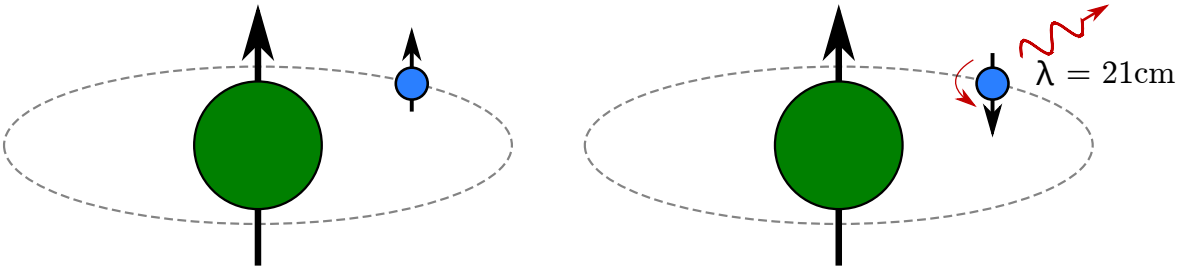

Figure 1.7: A schematic of the hyperfine H I transition. The arrow of the proton (green) and electron (blue) indicates the direction of quantum mechanical spin. If the spins are aligned, the energy configuration of the system is slightly higher than a mis-aligned pair; when the transition to this lower state occurs, a weak photon is produced at 21 cm.

($\lambda \approx 21\,\mathrm{cm}$, $f \approx 1420\,\mathrm{MHz}$). Additionally, this transition is highly forbidden, given the Einstein A coefficient:

$$A_{10} \simeq 2.85 \times 10^{-15}\,\mathrm{s}^{-1}$$

and the half-life time:

$$\begin{aligned} \tau_{\frac{1}{2}} &= A_{10}^{-1} \\ &\simeq 11\,\text{million years} \end{aligned}$$

This type of transition is termed *spontaneous emission*, and is characterised by Einstein A coefficients. Despite the long half-life time of H I, this hyperfine line is easily detected due to the extremely high abundance of hydrogen. Indeed, it is readily detectable in other galaxies at high redshifts, and instruments are currently searching for this spectral signature during the epoch of reionization.

To study star formation, it is important to identify dense regions of gas in space. Similar to H I, all atoms and molecules exhibit spectral lines by quantum mechanical transitions. These transitions have various methods of being triggered, such as total angular momentum loss, or inversion (tunnelling), but the technical components are largely unimportant in this thesis. What matters are the conditions to cause the emission (or absorption); for example, the ground-state transition of carbon monoxide (CO $J = 1 \rightarrow 0$, shorthand (1–0)) is easily excited by low temperatures:

$$\begin{aligned} \Delta E\,(J = 1 \rightarrow 0) \equiv E(J=1) - E(J=0) &= \frac{h^2}{4\pi^2 \mathcal{I}_{\mathrm{CO}}} \\ &\simeq 7.6 \times 10^{-23}\,\mathrm{J} \\ &\simeq k\,[5.5\,\mathrm{K}] \\ &\simeq h\,[115\,\mathrm{GHz}] \\ &\simeq hc\,[2.6\,\mathrm{mm}]^{-1} \end{aligned} \tag{1.1}$$

where $\mathcal{I}_{\mathrm{CO}} \simeq 1.5 \times 10^{-46}\,\mathrm{kg\,m^2}$ (Ward-Thompson & Whitworth 2011). This means that, with sufficient amounts of CO present, this transition is excited in cold regions of the ISM. Higher transitions refer to further excited states, such as (2–1), and can pinpoint hotter, denser regions; however, practical limitations exist, such as the resilience of a molecule in hot or photon-dominated regions. CO, as well as other diatomic molecules (such as OH and CS), are useful for studying star formation because of the permanent electric dipole

moment between both atoms. Unfortunately, despite being the most abundant molecule in the universe, H_2 is almost invisible to observers due to its small dipole moment; both atoms are identical. H_2 has a few ground-state transitions, but most require temperatures exceeding 100 K, which likely destroys H_2 before the line can be exhibited (Bolatto et al. 2013). As star formation occurs in dense gas, we must infer the presence of dense gas through other means.

As seen in Equation 1.1, the ground-state transition of CO emits at radio frequencies. This is fortunate, given that longer wavelengths suffer less extinction in dense regions, allowing detection of these molecules within MCs. To relate various molecules back to H_2, and thus total mass, conversion factors ($\mathcal{X}$-factors) are used to estimate the amount of H_2. As star formation requires very dense gas, knowledge of MC densities is useful. However, $\mathcal{X}$-factors are difficult to determine and vary depending on optical depth or abundance. Throughout this thesis, instead of using the mass of a MC to determine the density of its gas, the density of gas is inferred by critical density:

$$n_c(jk) = \frac{A_{jk}}{\gamma_{jk}} \tag{1.2}$$

where A_{jk} is the Einstein A coefficient and γ_{jk} is the collisional de-exciatation rate per molecule in level j. In essence, the critical density of a species estimates the density of gas required before the emission of that species is detectable. Evans (1999) list common spectral lines in star-forming regions along with critical densities at 10 and 100 K; for example, the detection of CS (1–0) implies a gas density of at least 4.6×10^4 H_2 molecules per cm^{-3} at 10 K. Critical densities are useful for a qualitative estimate of density, but rigorous analysis is needed to determine the true density of gas within MCs. For example, the abundance of CS will vary between MCs, and therefore the critical density will inaccurately reflect the amount of H_2 present.

Other molecules, despite their rarity compared to H_2, can become so abundant in regions of HMSF that the emission saturates, which is referred to as optically thick emission. This effect is obvious in spectral line emission from CO, as it very abundant and easily excited. Optically thick emission can be identified by a 'flat-top' in the spectrum; see Fig. 1.8. To avoid optically thick emission, less abundant molecules and rarer isotopes are better at probing properties such as mass, column density and temperature. Other molecules can highlight specific mechanisms within star-forming regions, such as outflows or accretion disks, which are useful for determining evolutionary sequences. Common molecules associated with star formation and their diagnostics, especially applicable to this thesis, are discussed in §1.4.

1.3.2 Continuum

Brightness temperature acts as a classic probe of continuum radiation; given an observed intensity I_ν at frequency ν, the temperature of a blackbody may be inferred. In the same way, continuum measurements can be used to determine the age of a star-forming region, based on its spectral energy distribution, which are not purely blackbody spectra. Protoclusters have strong sub-millimetre continuum emission, while older regions have brighter mid-infrared emission.

This thesis is primarily concerned with spectral line emission rather than continuum properties. However, there are a few continuum properties of particular interest. The GLIMPSE

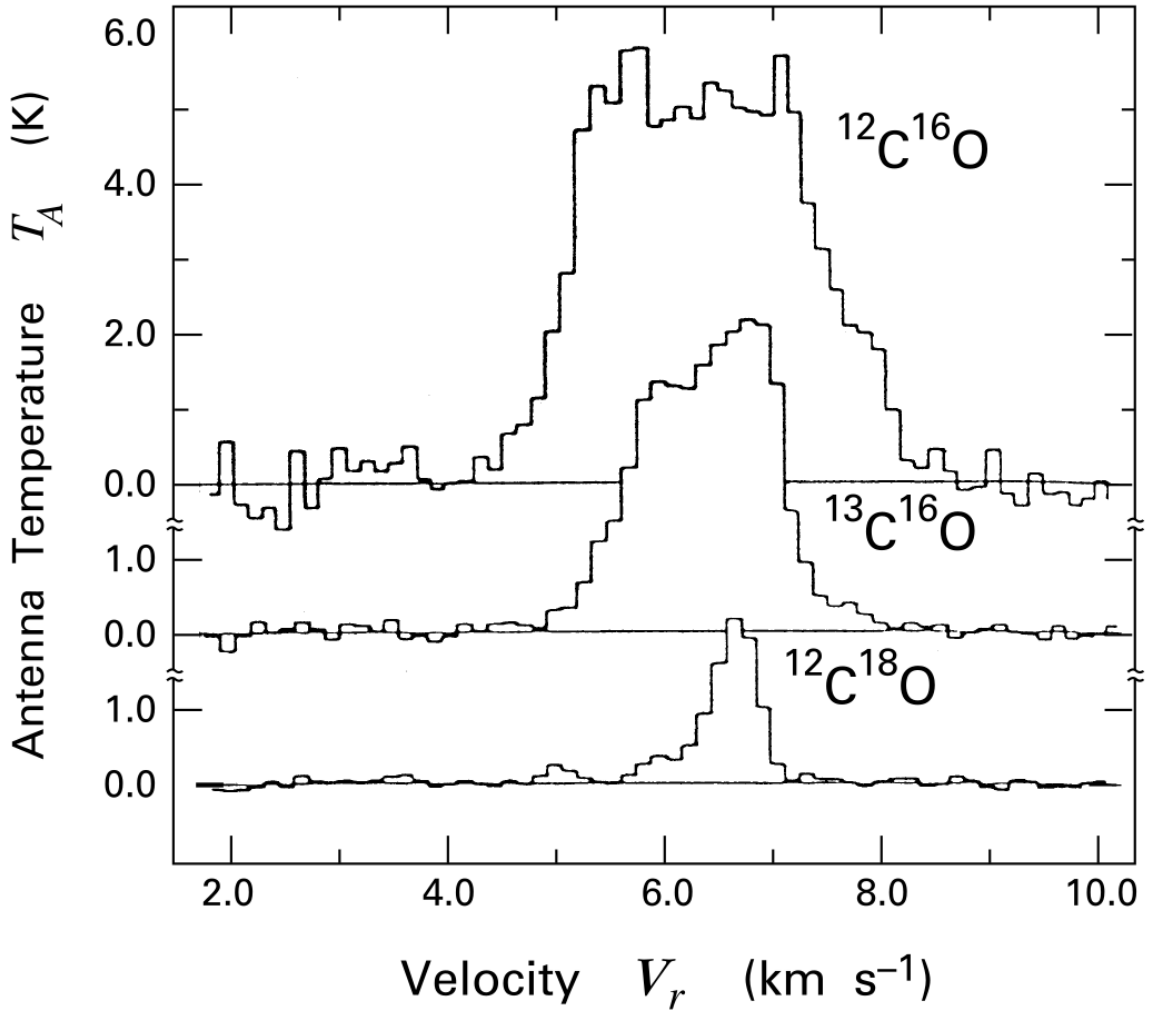

Figure 1.8: Rare molecules and isotopologues help to isolate the most dense regions of gas, Fig. 6.1 of Stahler & Palla (2005): *Intensity profiles of the* $J = 1 \rightarrow 0$ *line in three CO isotopologues, observed toward Taurus-Auriga.*

survey maps the Galactic plane in 3.6, 4.5, 5.4 and 8.0 μm continuum bands, which reveal intriguing properties. The 8.0 μm band primarily traces the 7.7μm feature of polycyclic aromatic hydrocarbon (PAH) molecules, which have some similarity with dust grains contained in star-forming regions. An extensive review of PAH molecules is given in Tielens (2008). The 4.5 μm band of emission is usually attributed to strongly shocked gas, such as H_2 and CO in outflows (Cyganowski et al. 2008); however, this may not be true in all regions (De Buizer & Vacca 2010). The 3.6 μm band of emission is sensitive to the 3.3 μm feature from PAH molecules (Benjamin et al. 2003) and can be used to determine the stellar-mass distribution of old stars (Meidt et al. 2012). Star-formation study often combines these *Spitzer* bands into three-colour images, with red pertaining to 8.0 μm emission, green to 4.5 μm and blue to 3.6 μm. Most notably, an excess of 4.5 μm emission relative to the others manifests as bright green objects, which have successfully identified HMSF; see Fig. 1.9. We use GLIMPSE images to show the infrared emission toward the regions of HMSF studied.

Sub-millimetre continuum highlights thermal dust emission from a wide range of temperatures, including very cold dust. Additionally, this kind of emission is optically thin, which

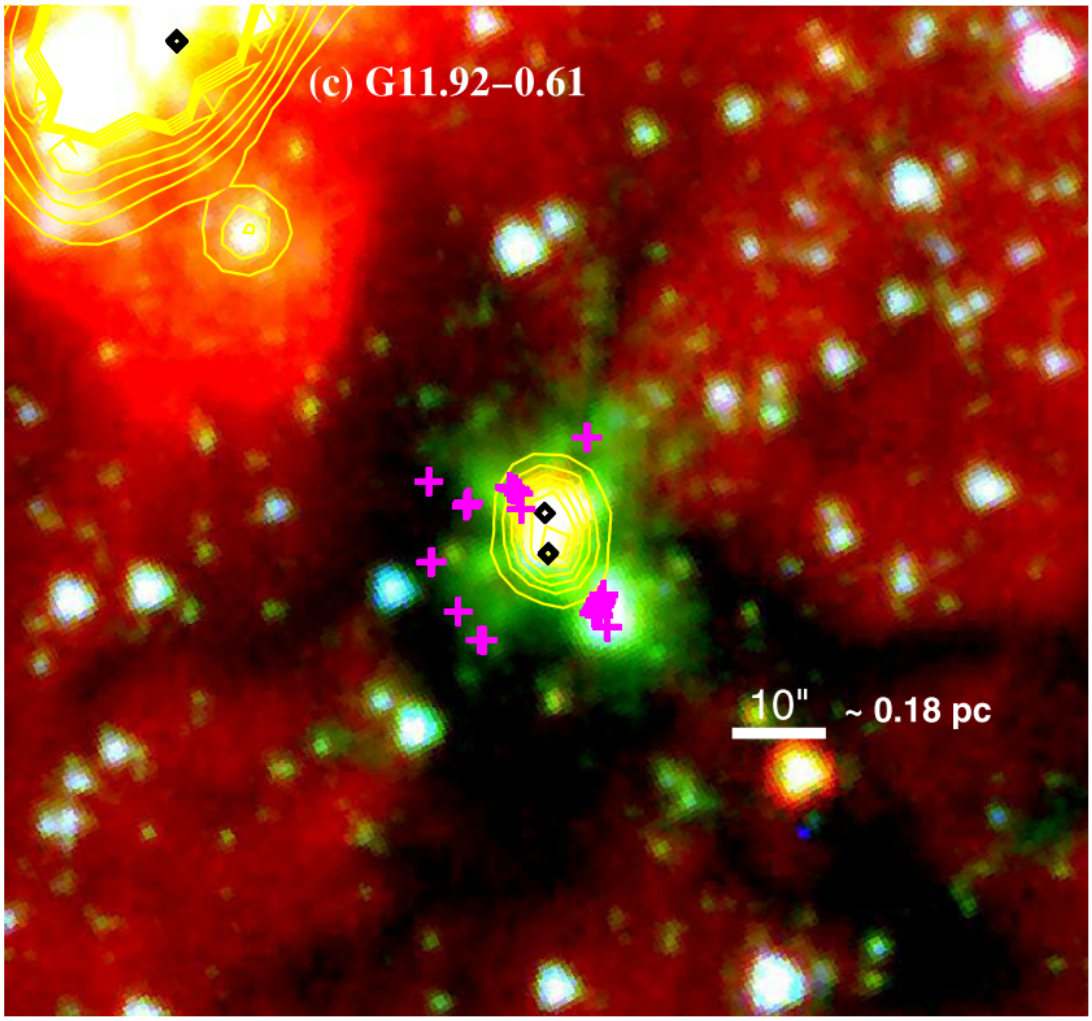

Figure 1.9: Sample of Fig. 1 of Cyganowski et al. (2009). The image is constructed from three infrared GLIMPSE bands, *rgb* → 8.0, 4.5 and 3.6 μm. The study of Extended Green Objects (i.e. an excess of 4.5 μm emission, which highlights shocked H_2) has been successful in identifying HMSF. A strong correlation between Extended Green Objects and CH_3OH maser emission has been observed in regions such as this one; 6.7 GHz class II CH_3OH masers are marked with diamonds, and 44 GHz class I CH_3OH masers are marked with magenta crosses. Yellow contours show 24 μm MIPSGAL emission.

helps to calculate column densities, and is associated with all stages of HMSF. To this end, the APEX Telescope Large Area Survey of the GALaxy (ATLASGAL) maps a large area of the Galactic plane in 870 μm emission (Schuller et al. 2009). Similarly, the Bolocam Galactic Plane Survey (BGPS) maps a large fraction of the Galactic plane at 1.1 mm (Aguirre et al. 2011). Finally, the *Herschel* space observatory images other wavebands, such as 70 μm. Results from this instrument are still forthcoming, but recent observations used *Herschel* 70 μm emission to map high-mass YSOs (Olguin et al. 2015).

1.4 Tracers of star formation

In this section, spectral lines and their relation to HMSF are discussed. Spectral lines are powerful tools for diagnosing the ISM, due to the relative ease of detection, and the informa-

tion gleaned by their presence (density, temperature, morphology etc.). Gas kinematics and structure may also be obtained by observing the Doppler shift of spectral lines.

1.4.1 Hydrogen

Despite being the most abundant molecule in MCs, H_2 is mostly undetectable due to its lack of dipole moment; the ground-state transition requires extreme temperatures (>300 K; Habart et al. 2005) to be excited, but likely destroys the molecule. Fortunately, H_2 can survive and emit, tracing very hot, shocked gas, including supernova remnants (SNRs), expanding H II regions and outflows (Habart et al. 2005). The presence of H_2 can also be inferred indirectly; it was first detected through Lyman-alpha (Lyα) absorption toward the star ξ Persei, and acted as a probe for optical depth (Carruthers 1970). Concerning star formation, H_2 is useful as a shocked gas tracer, emitting in the 4.5 μm infrared band (along with CO). Study of star-forming regions with pronounced 4.5 μm emission (so called Extended Green Objects, or EGOs, due to 4.5 μm emission being displayed as green) has revealed evolved regions of HMSF (Cyganowski et al. 2008, 2009); see Fig. 1.9.

As discussed, the final evolutionary state of HMSF is a H II region. These arise when a YSO is hot enough to produce ultraviolet radiation, which requires a high-mass YSO. As the H II region expands by radiative and outflow processes, the neutral H I is constantly being ionised and pairing with electrons. This procedure produces recombination lines, often referred to as radio recombination lines (RRLs), as they are brightest around 8 GHz. The detection of RRLs is a bona-fide method of inferring the presence of a H II region; because HMSF occurs in high-density gas, surveys for RRLs have been productive in identifying dense gas in spiral arms, and therefore Galactic structure (Bania et al. 2010, Brown et al. *in prep.*).

1.4.2 Carbon monoxide (CO)

As discussed in §1.3.1, CO is an abundant and easily excited molecule in cold, dense regions of the ISM. Therefore, CO is important for studying both star formation and Galactic structure, as it readily highlights MCs. This motivated the CO surveys of Dame et al. (1987) and Dame et al. (2001), which mapped large areas of the sky (∼7700 square-degrees and the entire Galactic plane, respectively). The cost of conducting such surveys is huge, but yields a wealth of important information, including the global properties of MCs both in our Galaxy and others, where MCs are located and resolving kinematic distance ambiguities.

CO requires relatively low densities before becoming optically thick ($<10^3$ cm^{-3}), owing to its low critical density ($\sim 10^2$ cm^{-3}). Additionally, CO suffers depletion in high-density regions. This renders the most abundant $^{12}C^{16}O$ isotopologue unusable to diagnose the interiors of very dense MCs. However, useful properties of MCs may be obtained by using optically thick spectral lines of $^{12}C^{16}O$, when observed with less abundant species such as ^{13}CO and $C^{18}O$. For example, with an optically thick line of $^{12}C^{16}O$, and assuming a constant ratio between the abundance of $^{12}C^{16}O$ and ^{13}CO, the optical depth, column density, mass and temperature can be calculated. Analysis of several isotopologues (fractionation) is particularly important, given that observations of other J-transitions may not be possible on the same instrument. For example, CO (1–0) has a rest frequency of 115 GHz, while (2–1) is

at 231 GHz. An instrument such as Mopra* cannot observe the (2–1) line, but can observe other (1–0) transitions (such as ^{13}CO), and has many significant CO results published from the (1–0) transition (Braiding et al. 2015; Barnes et al. 2015).

1.4.3 Ammonia (NH_3)

The first polyatomic molecule detected in interstellar space, NH_3 was discovered by Cheung et al. (1968) toward Sgr A. These authors were able to calculate the kinetic temperature and optical depth of the gas using the intensities of the observed (1,1) and (2,2) transitions. These results are useful and important for the study of star formation, and so demonstrated the the value of NH_3 detections.

The (1,1) inversion line of NH_3 is easily detected in star-forming regions, and has a critical density of $\sim 10^3\,\mathrm{cm}^{-3}$ (Evans 1999). This formed part of the motivation of the H_2O Galactic Plane Survey (HOPS; Walsh et al. 2011), which searched for many spectral lines pertaining to star formation, including NH_3 (1,1), (2,2) and (3,3). Higher inversion transitions are more forbidden than the (1,1) line; their presence indicate hotter, further excited regions. While the critical density of NH_3 is useful for probing high densities of gas, other diagnostics may be obtained from the same data. The optical depth of NH_3 can be calculated using relation of intensities between hyperfine transitions (Ho & Townes 1983). For the (J, K) inversion line:

$$\frac{\Delta T_a^*(J,K,m)}{\Delta T_a^*(J,K,s)} = \frac{1 - e^{-\tau(J,K,m)}}{1 - e^{-a\tau(J,K,m)}} \tag{1.3}$$

where ΔT_a^* is the observed brightness temperature, m and s refer to the main and satellite hyperfine components, $\tau(J,K,m)$ is the optical depth of the main component, and a is the ratio of the intensity for the satellite compared with the main component. This equation assumes equal beam-filling factors and excitation temperatures for the different hyperfine components; fortunately, this is not problematic because there is a only a small difference in frequency between hyperfine components and they are likely excited within the same gas. Additionally, the temperature of gas may be estimated via:

$$T_{rot} = -41\,\mathrm{K} \Big/ \ln\left(\frac{9}{20}\frac{\tau_{2,2}}{\tau_{1,1}}\right) \tag{1.4}$$

where T_{rot} is the rotational temperature (Purcell 2006). Note that this equation assumes $\Delta\nu_{2,2}/\Delta\nu_{1,1} \approx 1$. Finally, the column density may be estimated via:

$$N \approx N_{(1,1)} \left[\frac{1}{3}e^{23.26/T_{rot}} + 1 + \frac{5}{3}e^{41.18/T_{rot}} + \frac{14}{3}e^{-100.25/T_{rot}} + \frac{9}{3}e^{-177.21/T_{rot}} + \frac{11}{3}e^{-272.02/T_{rot}} + \frac{26}{3}e^{-284.67/T_{rot}} + \ldots\right] \tag{1.5}$$

where N is the total column density of H_2, and $N_{(1,1)}$ is the column density of the NH_3 (1,1) line (Purcell 2006).

Observations of NH_3 have provided numerous scientific discoveries. NH_3 observations from HOPS helped isolate one of the most extreme examples of a protocluster, G0.253+0.016, with

*A 22 m radio telescope near Coonabarabran, New South Wales, Australia.

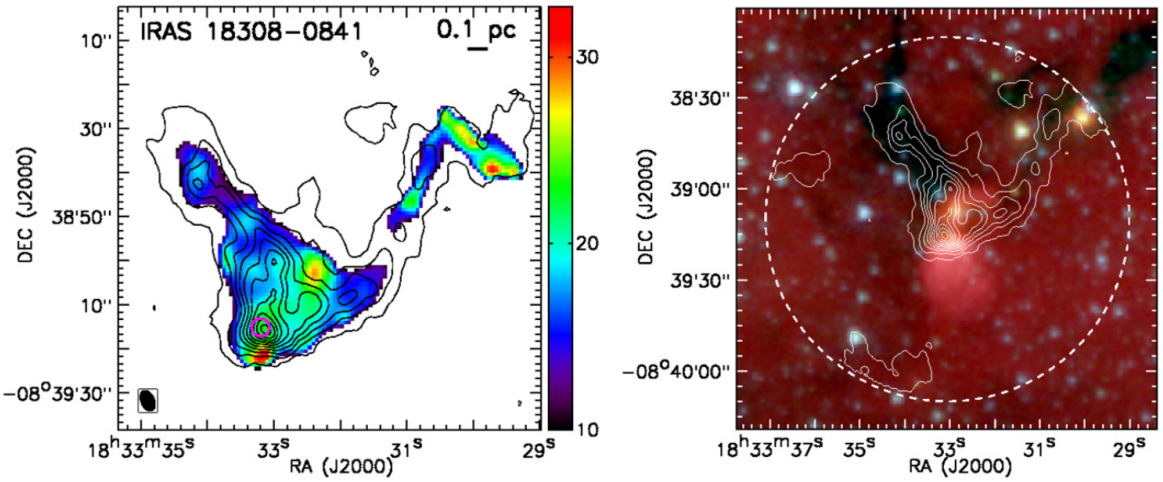

Figure 1.10: A sample figure from Lu et al. (2014): *Rotational temperature and IRAC three-colour images of* IRAS *18308−0841. Left: Rotational temperatures are presented in colour scales. The black contours are the integrated intensities of NH_3 (1,1) main hyperfine line, from 5 to 95 per cent of the peak intensity in steps of 10 per cent. Maser detections with interferometers are marked with either circles (water maser), crosses (class II methanol maser), or triangles (hydroxyl maser). The synthesized beam of the integrated intensities is shown in the lower-left corner, while the beam of the rotational temperatures should be slightly larger given that the temperatures are derived from the smoothed data. Right: The* Spitzer *IRAC composite image, with 8 µm (red), 4.5 µm (green) and 3.6 µm (blue) emission. The NH_3 (1,1) integrated intensity contours are identical to those in the left panels. The dashed circle shows the 2′ FWHM primary beam of the VLA.*

a high mass ($\sim 10^5\,M_\odot$) and low temperature ($\sim$20 K) (Longmore et al. 2012); ALMA has revealed unprecedented detail of this molecular cloud, which is thought to be on the verge of star formation (Rathborne et al. 2015). A recent interferometric survey of NH_3 toward bright ($L_{bol} > 10^3\,L_\odot$) high-mass star-forming regions reveals gas flowing toward the focus of star formation over large distances; see Fig. 1.10 (Lu et al. 2014). Another survey of NH_3 in the Galactic centre finds that dust is necessary to form detectable NH_3 (Ott et al. 2014).

1.4.4 Carbon monosulfide (CS)

As discussed earlier, CS traces dense gas, with a critical density $n_c = 4.6 \times 10^4\,\mathrm{cm}^{-3}$ at 10 K (Evans 1999). Overall, CS is not as useful for diagnostics as NH_3, but can be used to determine optical depth when combined with rarer isotopes (e.g. $C^{34}S$), i.e.:

$$\frac{T(\mathrm{C^{34}S})}{T(\mathrm{CS})} = \frac{1 - e^{-\tau}}{1 - e^{-a\tau}} \tag{1.6}$$

where $T(x)$ is the brightness temperature of x, τ is the $C^{34}S$ optical depth and a is the abundance ratio of $^{32}S/^{34}S$ (Bergin et al. 2001). Chin et al. (1996) quote the relative abundance of CS to $C^{34}S$ in the solar system value of 22.5±5.5, and 24.4±5.0 for 20 star-forming regions they observed. However, in the process of statistically modelling the density of H_2 by observations of CS isotopologues, Pratap et al. (1997) claim that a $^{32}S/^{34}S$ ratio between 12 and 14 provided better fits than a ratio of 22. Care must be taken when assuming relative abundance values.

Wu et al. (2010) performed CS observations towards dense clumps associated with H_2O masers. The authors note that most clumps are associated with compact or UC H II regions, highlighting relatively evolved star formation. Given the late evolutionary status of these objects, and the presence of H_2O masers, outflow activity is expected (see §1.5.4). Unsuprisingly, these observations find that the (2–1) transition of CS traces a larger area than (7–6); however, the linewidths of (7–6) is greater than that of (2–1). As (7–6) is more compact, the increased linewidth compared to (2–1) is attributed to outflow activity (and/or expanding H II regions). Subsequent modelling of hot cores shows CS to be one of the best tracers of very dense gas (Bayet et al. 2011).

Comparing the distribution of CS and NH_3 can yield information on the evolutionary stage of a HMSF region. Despite having a higher critical density than NH_3, CS has been observed to be more extended in emission; specifically, observations performed by Lopez et al. (1994) identify extended CS emission over star-forming regions where NH_3 emission is typically confined to an outflow. Taylor et al. (1998) attempt to resolve this phenomenon with a model, classifying CS (and other carbon-bearing species) as 'early-type' molecules and NH_3 (and other nitrogen-bearing species) as 'late-type'. Tafalla et al. (2004) observed two starless cores for CO, CS, NH_3 and N_2H^+ (another molecule resilient against depletion similar to NH_3); N_2H^+ was observed at constant abundance in each targeted core, while CS and CO depleted as a function of density. Tafalla et al. (2004) also observed an increased abundance of NH_3 in the centre of these cores. The Taylor et al. (1998) categories of early- and late-type star formation appear be separated by molecular cloud fragmentation, before core collapse occurs. Corroborating, Lee et al. (2013) targeted starless cores in Orion, and did not detect N_2D^+ (2–1) alongside detections of CS (2–1) and (3–2); they assume that the target cores are chemically young.

Given that high transitions of CS have large linewidths compared to lower transitions within hot cores, CS molecules are apparently sublimating from dust grains. Therefore, 'late-type' molecules postulated by Taylor et al. (1998) (i.e. nitrogen-bearing species) refer to an evolutionary stage before the hot core phase, upon when carbon-bearing species are comparably abundant (e.g. CO, CS). In essence:

i) Very early, dense regions that will become or are HMSF regions are dominated by emission from carbon-bearing species;

ii) Cold, dense regions of HMSF (cold molecular cores) are dominated by nitrogen-bearing species;

iii) Hot cores of HMSF allow the carbon-bearing species back into the gas phase.

1.4.5 Silicon monoxide (SiO)

Thermal emission from SiO is well understood to trace shocked regions, especially outflows (Martin-Pintado et al. 1992; Leurini et al. 2014). It is greatly enhanced in hot core chemistry, signposting a specific evolutionary stage. Dust grains within dense cores, being primarily composed of silicates, are destroyed by collisions and liberate Si into the gas phase. SiO can then be produced by oxidation (Schilke et al. 1997):

$$\mathrm{Si} + \mathrm{O_2} \longrightarrow \mathrm{SiO} + \mathrm{O} \tag{1.7}$$

$$\mathrm{Si} + \mathrm{OH} \longrightarrow \mathrm{SiO} + \mathrm{H} \tag{1.8}$$

A recent investigation discusses the possibility of SiO emission being triggered by weaker shocks (Nguyen-Lu'o'ng et al. 2013). As the SiO (2–1) emission has the same velocity as N_2H^+ and CO, as well as the lack of an outflow profile, the authors speculate that the SiO emission is driven by low-velocity shocks.

SiO masers can also be found in the ISM, but these usually trace very different conditions to the thermal emission discussed above, and are usually found toward evolved stars with vibrational mode $v = 1, 2, 3$. However, Orion-KL provides one of the very few known SiO masers in a star-forming region, even in the $v = 0$ mode (Cho et al. 2005). Further discussion of SiO masers is contained in §1.5.6.

1.5 Masers associated with star formation

Masers were first described in 1952 and created in the laboratory in 1953. However, the astrophysical community appeared to have no notion to believe that masers could (or would) naturally exist outside of laboratories. This is evident after their discovery and subsequent disbelief of the strong spectral lines observed. Due to the exponential amplification process, maser emission can be detected across vast distances, from the other side of our Galaxy (Green et al. 2012), to mega-masers in other galaxies (Wang et al. 2014). This makes masers invaluable lines to observe, particularly in surveys, given their great intensities.

Weaver et al. (1965) are credited with the discovery of the first interstellar masers. This publication reported unusual results from a search for hydroxyl (OH) within the Galaxy. The authors discuss the presence of 'strong, unidentified emission lines' towards the Orion nebula and radio continuum sources W3, W49, W51 and W75. Dubbed 'Mysterium', the authors note that it is found towards some strong H II regions, but not all. Very quickly, more observations were conducted to detect Mysterium toward other regions. Linewidths of Mysterium implied a temperature of 10^2 K, but the brightness temperature was at least 10^3 K. Eventually, Mysterium was confirmed as masing OH in the ISM.

Masers are commonly seen in regions of star formation, due to the special conditions and high energies required for their excitation. In this review, an overview of maser theory is given, as well as a discussion on typical HMSF masers and their currently understood characteristics.

1.5.1 Theory

Most of the thermal line emission discussed in §1.4 is generated through spontaneous emission. The mechanism governing maser emission is *stimulated emission*. A simple scenario for stimulated emission is as follows:

i) An excess of molecules is in a higher energy state E_2 with respect to a lower state E_1. This is referred to as an inverted population;

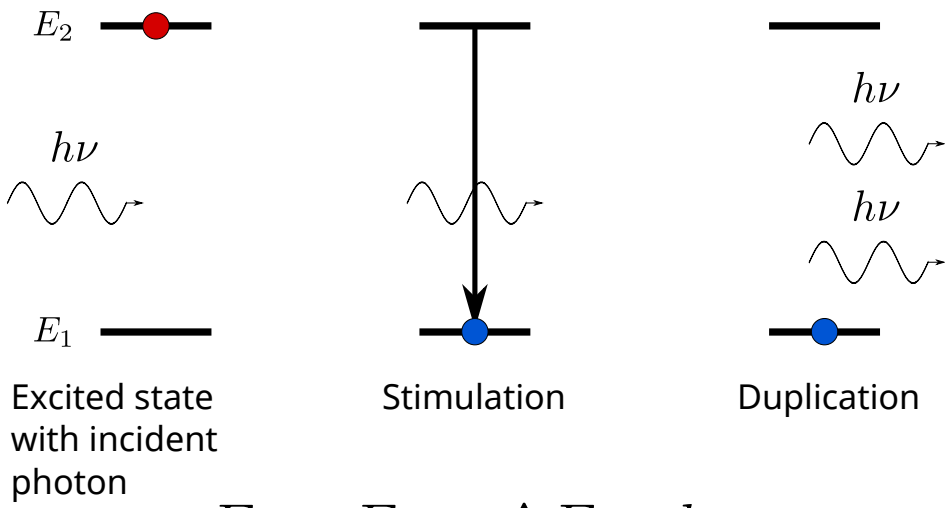

$$E_2 - E_1 = \Delta E = h\nu$$

Figure 1.11: A typical simplified schematic of stimulated emission. An inverted population exists with energy E_2 (panel 1). A molecule in this elevated energy state is stimulated by a photon of characteristic energy $E_2 - E_1 = h\nu$ (panel 2), duplicating the photon and leaving the atom or molecule depressed state (panel 3).

ii) A photon with an energy of (or close to) $E_2 - E_1 = h\nu$ interacts with a member of the elevated species. This photon induces stimulated emission;

iii) This photon and the original photon continue to interact with other molecules in state E_2, producing an exponential amplification of emission. This procedure continues until there is no longer a population inversion and the maser is said to be saturated.

This procedure is outlined in Fig. 1.11. The population inversion is usually achieved via excitation to state higher than E_2, either radiatively (typically infrared absorption) or collisionally. Masing is favoured if there are more pathways allowing thermal decay from higher states to E_2.

One can think of the 'stimulation' step as negative absorption; rather than absorbing the incident photon, another is emitted. The optical depth τ normally measures attenuation by photon absorption, but when the stimulation is combined with the population inversion, an exponential amplification of emission is observed along the path of inverted species. This explains the extreme brightness temperatures that are measured from interstellar masers. Masers are well characterised by their compact, unresolved spatial structure as well as very small linewidths.

1.5.2 Class II methanol (CH_3OH)

Interstellar CH_3OH masers were discovered by Barrett et al. (1971) towards Orion-KL in 25 GHz lines ($J = \{4,5,6,7,8\}$, $\Delta J = 0$, $K = 2 \rightarrow 1$; a compilation of CH_3OH maser transitions mentioned in this thesis are included in Table 1.3.). Quickly, many more CH_3OH maser lines were discovered, but the next important discovery was by Wilson et al. (1984), who detected CH_3OH masers in the 9_2–10_1 A^+ transition. Their results note unusual absorption of CH_3OH toward W31, but are otherwise unaware of the importance of this transition; being the first to find CH_3OH emission beyond Orion-KL, these observations demonstrated how

Table 1.3: Methanol maser transitions mentioned within this thesis. The transitions are indicated as being radiatively or collisionally excited by a 'R' or 'C' character. Rest frequencies are taken from the Cologne Database for Molecular Spectroscopy (CDMS; Müller et al. 2005), and are rounded to the third decimal place.

Transition	Frequency (GHz)	Radiatively or collisionally excited?
5_1–6_0 A^+	6.669	R
2_0–3_{-1} E	12.178	R
9_2–10_1 A^+	23.121	C
4_2–4_1 E	24.933	C
5_2–5_1 E	24.959	C
6_2–6_1 E	25.018	C
7_2–7_1 E	25.125	C
8_2–8_1 E	25.294	C
4_{-1}–3_0 E	36.169	C
7_{-2}–8_{-1} E	37.704	R
7_0–6_1 A^+	44.069	C
8_0–7_1 A^+	95.169	C

bright CH_3OH masers could be (9.5 Jy). The publication by Batrla et al. (1987) made an important distinction by classifying CH_3OH masers into two groups: class I and class II. Most observations at that point had focused on class I, which is collisionally excited, but could occur at large spatial offsets from H_2O and OH masers. More observations were conducted toward the 2_0–3_{-1} E line, revealing a tight correlation with H II regions and OH masers (Norris et al. 1987). At this point, depending on the class, it was evident that class I and class II CH_3OH masers traced very different gas conditions.

The discovery of the 6.7 GHz 5_1–6_0 A^+ line has proven to be one of the most important for star formation (Menten 1991). Since its discovery, this line (as well as all class II CH_3OH species) have been determined to occur exclusively towards regions of HMSF (Breen et al. 2013). This was established by the absence of CH_3OH masers toward low-mass YSOs (Minier et al. 2003). We now understand class II CH_3OH masers are powered by mid-infrared radiation from YSOs, seemingly only powerful enough in HMSF. A very recent investigation finds that 6.7 GHz CH_3OH masers must appear after outflows are generated (de Villiers et al. 2015).

In the 1990s, UC H II regions were rich objects for star formation study. Naturally, the connection with class II CH_3OH masers was investigated, which revealed a surprisingly small overlap of ∼20 per cent (Walsh et al. 1998). This small association is explained by differing evolutionary phases; class II CH_3OH masers turn on earlier than the appearance of an UC H II region, and the masers turn off relatively quickly after the UC H II region is apparent. The age of YSOs and brightness of associated class II CH_3OH masers is thought to be correlated (Breen et al. 2011; Bartkiewicz et al. 2014; de Villiers et al. 2015). Notably, the presence of the 37.7 GHz 7_{-2}–8_{-1} E class II CH_3OH maser line was found toward brighter 6.7 GHz lines; if brighter 6.7 GHz masers occur toward relatively evolved YSOs, the presence of 37.7 GHz masers is thought to indicate the 'apocalypse' of all class II CH_3OH maser activity (Ellingsen

et al. 2011). Clearly, constraints exist for when class II CH_3OH maser emission could occur, but when do class II CH_3OH masers turn on?

It is currently well understood that class II CH_3OH masers occur very near to a YSO. Profoundly, there are many examples of rings surrounding YSOs (see Fig. 1.12). Very-long-baseline interferometry (VLBI) observations of such rings reveals radii of order a few hundred to ∼1000 AU (Bartkiewicz et al. 2009). Bartkiewicz et al. (2009) also suggest that these maser morphologies occur at the interface of the ring and outflow, highlighting a relatively evolved class II CH_3OH stage of HMSF. However, not all class II CH_3OH morphologies are rings; further observations by Bartkiewicz et al. (2014) observe linear, ring-like and 'complex' morphologies within their sample. Linear morphologies were speculated as edge-on ring features, although this idea has been largely rejected. An investigation of the geometry of infrared emission toward four 'maser rings' at ∼150 milliarcsec resolution argues that the masers do not behave as if they lie within a circumstellar disk (De Buizer et al. 2012). Other investigations also tested circumstellar disk-like class II CH_3OH masers using the outflow tracers H_2 and SiO; if the outflows were perpendicular to the masers, the masers might be considered circumstellar. However, this was shown not to be the case (De Buizer 2003; De Buizer et al. 2009).

1.5.3 Hydroxyl (OH)

The most commonly detected hydroxyl spectral lines are at 18 cm (1612, 1665, 1667 and 1720 MHz). The energy-level diagram of these OH lines can be seen in Fig. 1.13. The presence of this molecule in the ISM was confirmed by Weinreb et al. (1963); detected in absorption, the 1665 and 1667 MHz lines were found toward the SNR Cassiopeia A. Since the discovery, OH has also been seen in emission and absorption for all 18 cm lines, and can have been characterised in relative intensity as 1:5:9:1, in order of increasing frequency (Townes & Schawlow 1955). By observing the relative strengths of each hyperfine line, one can determine optical depth and excitation temperatures of the gas (Guibert et al. 1978). Similar to CO, OH traces low-density gas, but is susceptible to Zeeman splitting; stronger magnetic fields spread the hyperfine lines further apart, allowing diagnosis of local magnetic fields. OH is a versatile molecule, not just for probing star-forming regions.

Surveys in the 1990s for OH masers revealed that, in almost all cases, their positions coincided with class II CH_3OH masers within errors, clearly signposting star formation (Caswell 1997). At the same time, Caswell (1997) noted the preference for OH masers to be associated with UC H II regions, especially compared to class II CH_3OH masers. This study was one of the first to isolate HMSF sequencing through only maser emission, which began a new motivation of study in HMSF - can we identify and diagnose an evolutionary timeline of HMSF purely through maser emission?

The 18 cm OH maser lines can be produced through non-star-forming mechanisms. In particular, 1612 MHz masers primarily occur from so-called OH/IR stars, shedding mass during their transition along the asymptotic giant branch Sevenster et al. (1997). The outflowing mass powers the maser via radiation, which in turn is powered by the stellar radiation. This proved useful for a large survey of 1612 MHz masers, conducted by (Sevenster et al. 1997) to investigate Galactic kinematics and the evolution of stellar populations. Other maser lines,

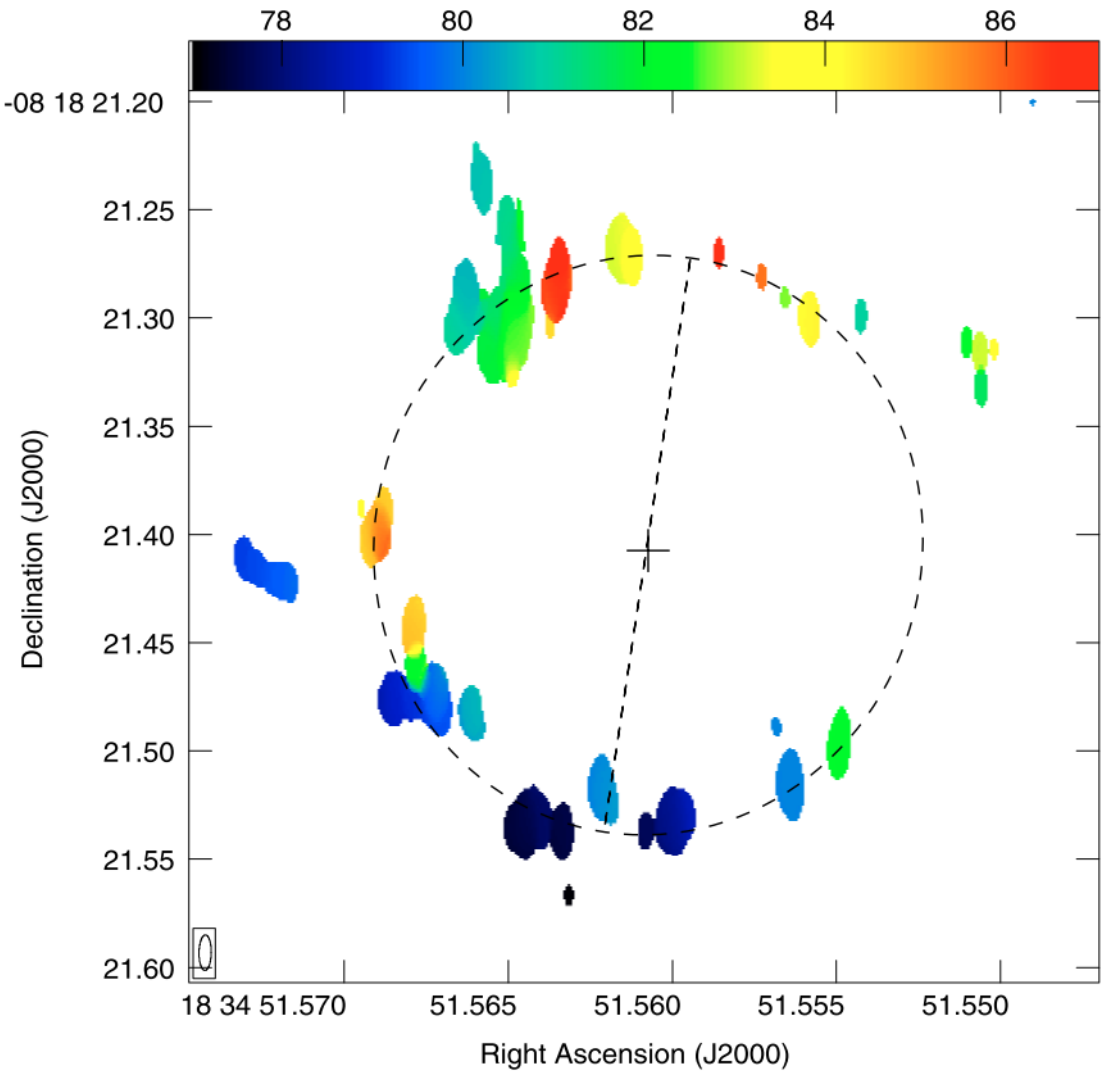

Figure 1.12: Class II CH_3OH masers in a ring morphology, Fig. 1 from Bartkiewicz et al. (2005): *Velocity field of maser components (first moment map). The colour scale varies linearly from 77.0 to 87.0 km s^{-1}. The beam is indicated by the ellipse in the bottom left-hand corner of the image. The cross indicates the inferred position of a central object.*

such as 1665 and 1667 MHz, have been used to diagnose polarisation (Gonidakis et al. 2014) toward AGB and post-AGB stars. The rare 1720 MHz maser, unlike the others, is collisionally excited; although it commonly occurs toward star-forming regions, it has been detected towards SNRs (Green et al. 1997) and planetary nebulae (Gómez 2007; Qiao et al. 2016). More recently, 1720 MHz OH masers are claimed as signposts of SNR and molecular cloud interactions (Brogan et al. 2013). Results of the Southern Parkes Large Area Survey in Hydroxyl (SPLASH) project, surveying a large portion of the Galactic plane for OH, will reveal more detail in all 18 cm maser lines (Dawson et al. 2014).

1.5.4 Water (H_2O)

Frozen H_2O forms a major component of dust grains within star-forming regions (di Francesco et al. 2007). Once sublimated, thermal emission from this line can be produced, although detection of this emission is difficult due to the presence of H_2O in Earth's atmosphere.

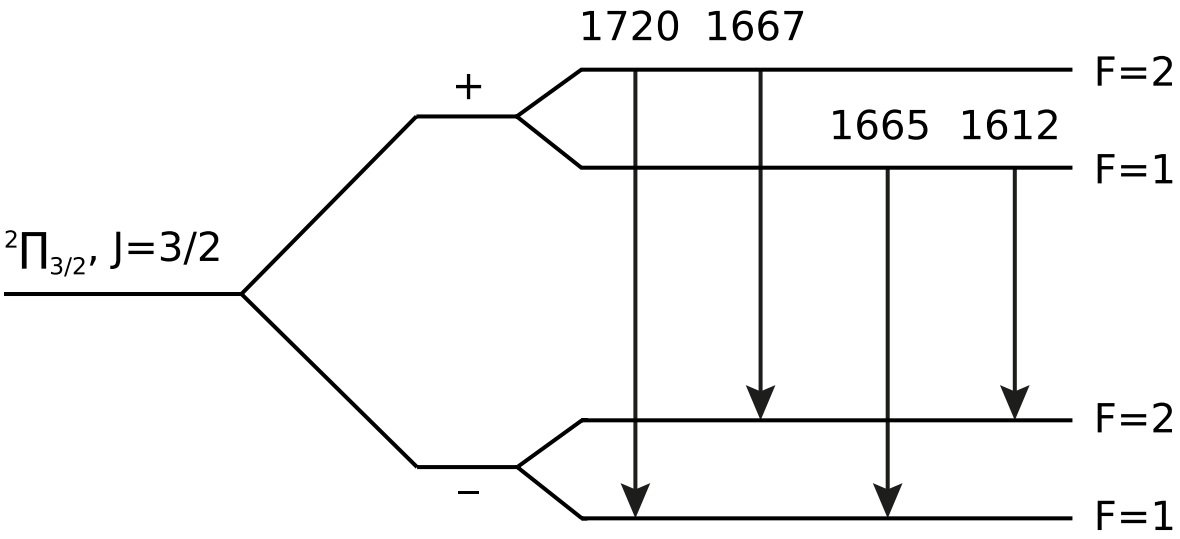

Figure 1.13: Fig. 1 from Dawson et al. (2014): *Energy level diagram of the ground-state hyperfine structure transitions of OH. Here F is the total angular momentum quantum number, including the nuclear spin. Frequencies are in MHz.*

Instead, almost all interest of interstellar H_2O lies with its 22 GHz maser line. H_2O masers are classic tracers of outflows; they are created and pumped by a mass outflow from a central star or YSO with clumps or inhomogeneities in the surrounding cloud (Elitzur 1992). There are endless examples of H_2O masers tracing outflows, in both LMSF and HMSF (Moscadelli et al. 2005, 2006; Goddi & Moscadelli 2006; Felli et al. 1992). Extreme examples exist, with velocity spans of nearly $300\,\mathrm{km\,s^{-1}}$ (Titmarsh et al. 2013). Results from VLA observations reasoned that of H_2O masers may be arising from accretion disks (Goddi et al. 2005); however, follow-up VLBI observations revealed that water masers close to YSOs are arranged in circular, expanding arcs (Goddi & Moscadelli 2006). This suggests that water masers found very near (within hundreds of AU) to YSOs are associated with their outward winds, rather than a rotating structure.

As for when H_2O masers appear in an evolutionary timeline, a survey towards high-mass YSOs and UC H II regions shows that H_2O masers are equally likely to be detected in either state; the 'high-mass YSO state' is taken to mean a class II CH_3OH maser phase, before a UC H II is apparent (Urquhart et al. 2009). Recent evidence affirms the overlap between a class II CH_3OH maser dominated phase and H II region phase (Titmarsh et al. 2014).

Similar to CO and NH_3, H_2O is formed through gas-phase reactions. Within shocked cloud regions, the major sequence for production is:

$$\mathrm{H_2 + O \longrightarrow OH + H} \tag{1.9}$$

$$\mathrm{OH + H_2 \longrightarrow H_2O + H} \tag{1.10}$$

This also helps to explain why OH can detected through collisions. One might expect the occurrence of H_2O masers to overlap with 1720 MHz OH masers. However, at least in the case of SNRs, 1720 MHz OH masers are found without H_2O maser counterparts. This imposes constraints upon the gas densities that allow for both species to pump masers; Claussen et al. (1999) find that the density of the post-shock region is $10^5\,\mathrm{cm^{-3}}$, and that densities of four

orders of magnitude higher are required to produce 22 GHz H_2O masers.

1.5.5 Class I methanol (CH_3OH)

For the period between the discovery of the 6.7 GHz class II CH_3OH maser and a decade ago, class I CH_3OH masers had not been well-studied. There are a few reasons for this, but perhaps primarily because of its relatively tenuous association with star formation compared to class II masers. Also, finding new class I masers was difficult; while the 44 GHz line is the brightest, even when targeting known regions of star formation, a survey of these masers suffers a poor detection rate. Broadening our understanding of these masers requires finding them away from obvious star-forming regions, as well as a much larger catalogue.

Unlike class II masers, class I masers can occur in LMSF, albeit rarely. Kalenskii et al. (2010) targeted LMSF outflows for 44 and 36 GHz class I masers, finding a weak association. Gan et al. (2013) confirms this by observing outflows from both LMSF and HMSF, finding a 9 and 38 per cent association rate, respectively. Clearly, there is a good relation with outflows, but the certainty of finding class I masers is not high. EGOs have a stronger connection with class I masers; Cyganowski et al. (2009) and Chen et al. (2011) report a 90 and 55 per cent detection rate of masers toward EGOs, respectively. The large difference between these rates might be explained by the lines targeted; Cyganowski et al. (2009) observed 44 GHz lines, whereas Chen et al. (2011) used 95 GHz lines. Val'tts et al. (2000) find the ratio between peak flux densities, i.e. $^{P(44\,GHz)}/_{P(95\,GHz)}$ is approximately 3. The relatively weak line used by Chen et al. (2011) may explain the low detection rate. Gan et al. (2013) also used the 95 GHz line, which may mean their statistics are under-represented.

The publication by Voronkov et al. (2014) acts as one of the most comprehensive reviews of class I CH_3OH masers. The authors observed 71 known maser sources and find a few important results:

i) The number of class I maser spots falls exponentially with spatial offset from a class II maser;

ii) Class I CH_3OH masers have higher spatial offsets when associated with an OH maser;

iii) The velocities of class I masers are good tracers of cloud systemic velocities.

Point i) suggests that the shocked gas from a high-mass YSO originates near the class II maser, and class I masers are more likely to be excited at smaller spatial offsets. Point ii) confirms this, as OH masers turn on after class II CH_3OH masers, suggesting an older region of HMSF; an older region has had more time to influence its environment, which could produce class I maser emission at larger spatial offsets. Point iii) may suggest that class I masers are powered by weak shocks, as strongly shocked gas is expected to have a significantly different velocity from the systemic velocity. Another result by Voronkov et al. (2010a) finds a high-velocity class I maser, potentially contradicting this assertion. However, this high-velocity feature is speculated as arising from a molecular outflow permeating the surrounding molecular gas, which can still agree with weak shocks as being the powering mechanism.

Through modelling, Cragg et al. (1992) predict the collisionally-excited nature of class I masers. Given their strong association with outflows discussed above, this seems clear. Class I CH_3OH masers have also been observed within SNRs (Pihlström et al. 2014) and an extra-galactic merger (Chen et al. 2015), which further hint collisional excitation for these masers.

However, very little is known about when class I masers turn on. Without an untargeted survey for these masers, identifying them in the earliest stages of HMSF will be difficult.

1.5.6 Silicon monoxide (SiO)

SiO masers are not usually associated with the thermal SiO emission seen in star-forming regions. The masers at 43 GHz, (as well as 86 GHz, 129 GHz etc.) arise from rotational transitions in vibrationally-excited states and are found towards asymptotic giant branch (AGB) and red super-giant (RSG) stars (Elitzur 1992; Gonidakis et al. 2013). As these stars shed large amounts of mass (10^{-7} to $10^{-4}\,M_{\odot}$), there exists a so-called circumstellar envelope. SiO masers can be powered in the densities and temperatures just beyond these envelopes, within the 'extended atmosphere'. The morphology of these masers can appear as a shell, presumably centred on a star, and reveal in-falling as well outflowing motions (Assaf et al. 2011).

Concerning star formation, the SiO maser appears to be extremely rare. Zapata et al. (2009) conducted sensitive interferometric observations towards 60 high- or intermediate-mass star-forming regions for SiO maser emission. Despite this extensive search, only three regions, all previously known, had detectable SiO masers (Orion-KL, W51 North and Sgr B2). Observations of Orion-KL are particularly exciting, revealing a bi-polar wind, likely driven by an accretion disk (Goddi et al. 2009). The SiO results are augmented with observations of high-frequency H_2O masers, which appear to trace a disk (Hirota et al. 2014); see Fig. 1.14. Hence, the value of detecting interstellar SiO masers in star-forming regions cannot be understated.

1.5.7 An evolutionary timeline of HMSF with masers

Given the range of evolutionary phases that masers can trace in star formation, many surveys have been conducted to identify HMSF purely through maser emission. Three prominent surveys include HOPS, for H_2O masers; the Methanol MultiBeam (MMB), for class II CH_3OH masers; and SPLASH, for OH masers. The wealth of data available led to comparisons between these three types of maser, and found strong associations (Breen et al. 2010a). Another publication by Breen et al. (2010b) attempts to quantify HMSF through maser emission with a graphical timeline; see Fig. 1.15.

Since this timeline has been published, it has been refined; class I CH_3OH masers are not unusual toward OH masers, for example. One useful way to improve this timeline is through a large-scale survey for class I CH_3OH maser emission. Such a survey could determine if these masers occur earlier than other masers in a HMSF timeline, and how they relate to other masers. With this knowledge, the detection of class I CH_3OH masers can then reveal basic properties of the host region, such as evolutionary phase.

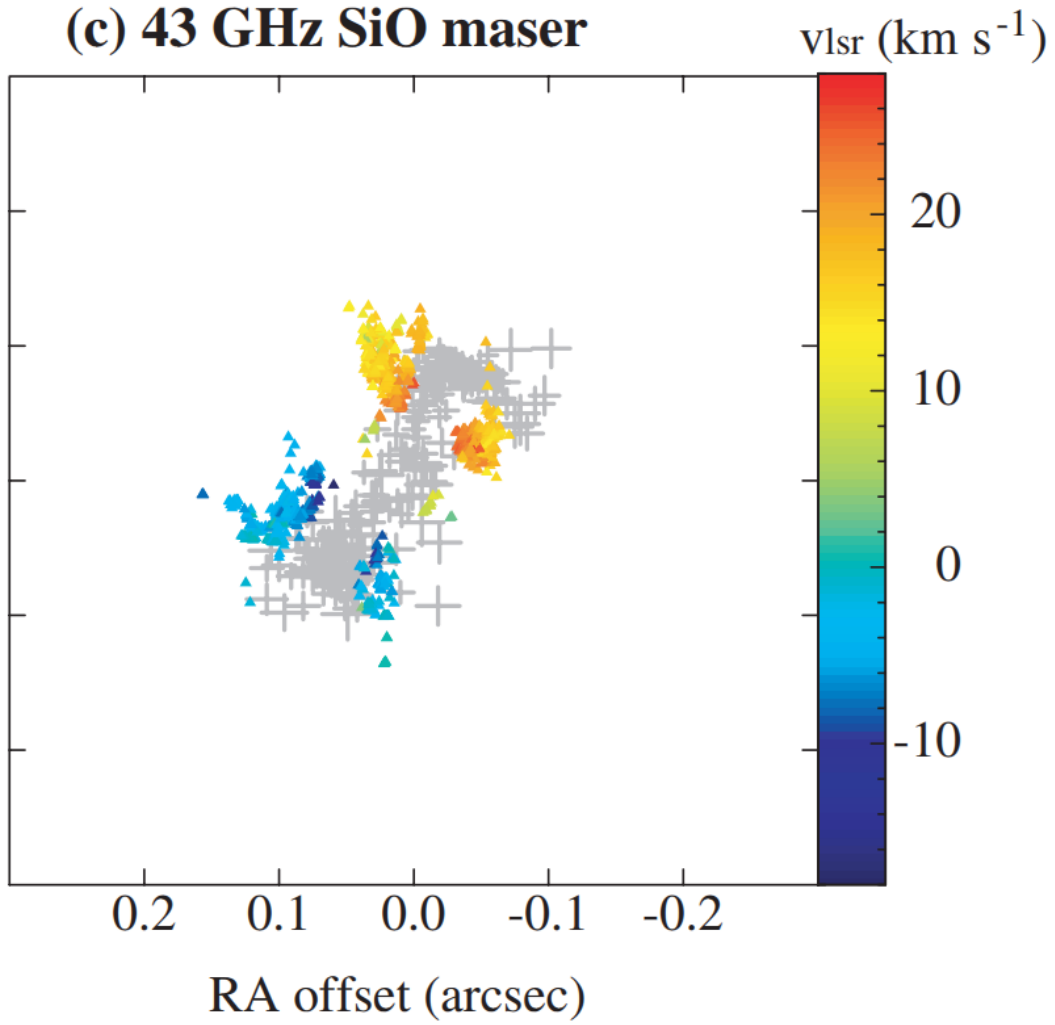

Figure 1.14: Fig. 3c from Hirota et al. (2014), showing maser emission toward Orion-KL. The SiO maser emission from Kim et al. (2008) is given in colour, with 336 GHz H_2O maser emission in grey. These results are some of the best evidence for accretion disk HMSF.

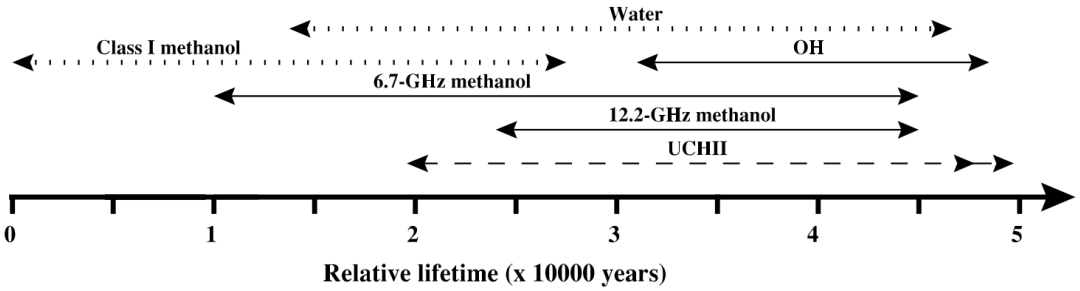

Figure 1.15: Fig. 6 of Breen et al. (2010b): *Evolutionary sequence for masers associated with high-mass star formation. Lifetimes represented by dotted lines indicate that they have been estimated from the literature along with unpublished data. The lifetime of the UC H II region is represented by a dashed line as the onset of radio continuum emission is particularly dependent on the mass of the associated star. The double arrow head on the far end of the UC H II region lifetime is to show that it will persist past the end of the range of the plot.*

1.6 Motivation of this thesis

There are many intermediate stages to HMSF, each with unique ways of being identified. In recent years, improvements in technology have allowed large-scale astronomical surveys to identify some of these stages of HMSF. A few prominent examples include cold dust (e.g. BOLOCAM, ATLASGAL), warm dust (e.g. GLIMPSE, MIPSGAL), masers (e.g MMB, HOPS) and dense gas (HOPS). By comparing these statistically-complete surveys with one another, typical attributes of HMSF can be determined, such as the spectral lines present across an evolutionary timeline.

The last decade has been extremely productive in mapping evolutionary stages of HMSF, but detail could be improved in some areas. For example, identifying the earliest stages of HMSF is challenging, but we know that cold dense gas is required. The only large-scale survey for dense gas is HOPS, which observed NH_3 inversion transitions, and in turn are useful for determining the temperature of gas within molecular clouds (see §1.4.3). However, because HOPS was conducted with Mopra, a small (22 m) dish, the survey has limited resolution and sensitivity.

CS is an excellent dense gas tracer, due to its ease of detection and probing of very high-density gas (see §1.4.4). The $J = 1 - 0$ transition, also the easiest to detect, lies in the 7 mm wavelength range accessible to the ATCA*. Other interesting spectral lines pertaining to HMSF lie in the 7 mm waveband. Class I CH_3OH masers are the least well understood of the masers observed toward star-forming regions, and the 44 GHz transition is typically the brightest (see §1.5.5). To date, there have not been any large-scale untargeted searches for these masers, limiting our understanding of the astrophysical objects and conditions they trace. Additionally, the ground state transitions of SiO lie in the 7 mm waveband. The $v = 0$ vibrational mode transition is a classic shocked-gas tracer, highlighting active regions of HMSF (see §1.4.5). The $v = 1, 2, 3$ transitions are typically masing and are observed toward evolved stars, although a few examples exist toward star formation (see §1.5.6).

A large-scale, untargeted survey in the 7 mm waveband with the ATCA opens the opportunity to sensitively observe each of these spectral lines with modest resolution, along with a large number of other interesting molecular and recombination line transitions. The MALT-45 survey, which this thesis presents, is the realisation of a 7 mm survey with the ATCA and aims to address a range of scientific questions:

i) What is the distribution of the dense gas in the Galaxy and how does it compare to the cold and warm dust and diffuse gas tracers such as CO (1–0)? What differences do we observe between a carbon-bearing dense gas tracer (CS) and a nitrogen-bearing dense gas tracer (NH_3), which is thought to be less susceptible to 'freeze-out' in the coldest, densest cores? Are there significant Galactic dense gas structures which were not detected by HOPS due to sensitivity?

ii) How do class I CH_3OH masers fit into the HMSF timeline? What is the full population of class I CH_3OH masers and how many class I masers are not associated with any other maser species? Can we predict the presence of class I CH_3OH masers in a star-forming region, based

*Australia Telescope Compact Array, a six-element radio interferometer located near Narrabri, New South Wales, Australia.

on the presence of another spectral transition? Class I CH_3OH masers are typically known toward select regions featuring class II CH_3OH masers; by finding new class I CH_3OH masers in the same regions with class II CH_3OH masers, can we find a connection to class II CH_3OH masers that has not been seen before?

iii) When observed in a large-scale survey, do we find SiO (1–0) $v = 0$ only toward active regions of HMSF (i.e. outflows) or somewhere else? Does SiO (1–0) $v = 0$ only trace outflows? Can we find new examples of SiO masers in the $v = 1, 2, 3$ transitions toward star-forming regions?

1.6.1 Thesis overview

Chapter 2 details the pilot observations and techniques conducted for MALT-45, to determine the feasibility of the survey. The auto-correlation pipeline is also detailed, as non-standard techniques are required. The data quality of the pilot survey was poor for a few reasons, including poor weather, but this ultimately improved the final survey by identifying weaknesses in the techniques of the pilot survey. Despite the sub-optimal conditions of the pilot survey, emission in CS is detected, as well as class I CH_3OH and SiO masers, vindicating the auto-correlation data reduction. The CS emission matches HOPS NH_3 over the region, and highlights an IRDC. Seven class I CH_3OH masers were identified along with three SiO $v = 1$ masers toward evolved stars. Refinement of the survey technique is suggested.

Chapter 3 details the MALT-45 survey conducted within $330° \leq l \leq 335°$, $b = \pm 0.5°$. The improved mapping procedure since the pilot observations greatly enhances the sensitivity to emission, revealing extended CS emission across the entire survey region, as well as detecting 77 class I CH_3OH masers and 47 SiO maser regions. A comparison between CS emission from MALT-45 and NH_3 emission from HOPS shows that CS emission experiences a combination of being depleted and becoming optically thick in the centres of gas clumps, while NH_3 is enhanced. Class I CH_3OH masers are found to possess similar peak velocities to that of CS emission, highlighting their value as systemic velocity tracers. Furthermore, most of the other masers associated with star formation known in the survey region have an identified MALT-45 class I CH_3OH maser counterpart, yet a large population of class I CH_3OH masers have no other maser association. Finally, all SiO masers appear to be associated with evolved stars, and a few regions curiously have stronger emission in their $v = 2$ lines compared to $v = 1$.

In an effort to further the understanding of class I CH_3OH masers, **Chapter 4** details interferometric follow-up observations toward each of the class I CH_3OH masers detected by MALT-45, in Chapter 3. Within the maser regions observed, a total of 238 maser spots are found, and compared to other tracers of star formation. In particular, the typical projected linear distances between class I CH_3OH masers and other masers does not exceed 0.5 pc. Relatively evolved regions of star formation tend to have more class I CH_3OH maser spots, larger velocity spreads and larger spatial distributions. The brightness of class I CH_3OH masers do not have strong correlations in any comparison, although the CS (1–0) emission detected in each maser region has a strong correlation with 870 μm dust emission.

Chapter 5 details additional investigations with CS emission detected by MALT-45, detailed in Chapter 3. The temperature of molecular gas is derived from HOPS NH_3 (1,1)

and (2,2), which is then compared against the distribution of CS emission. Projected linear distances from peaks of CS emission to class I CH_3OH masers and 870 μm dust emission point sources are also investigated.

Chapter 6 summarises and concludes the thesis, with a scope for long- and short-term projects derived from this work.

Chapter 2

Pilot observations and techniques for MALT-45

This chapter includes a co-authored publication. The bibliographic details of the paper are: Jordan, C. H., Walsh, A. J., Lowe, V., Lo, N., Purcell, C. R., Voronkov, M. A. and Longmore, S. N., Monthly Notices of the Royal Astronomical Society, 429, 469. doi: 10.1093/mnras/sts350. The published paper is referenced by this thesis as Jordan et al. (2013).

The auto-correlation methodology is expanded, to further detail this procedure. The introduction and discussion sections have been modified to streamline the discussed literature, to avoid unnecessary overlap with Chapter 1.

Abstract

We introduce the MALT-45 (Millimetre Astronomer's Legacy Team - 45 GHz) Galactic plane survey and describe pilot survey results with the Australia Telescope Compact Array (ATCA). The pilot survey was conducted to test the instrumentation and observational technique of MALT-45, before commencing the full survey. We mapped two half-square degree regions within the southern Galactic plane around the G333 giant molecular cloud, using fast mosaic mapping. Using the new Compact Array Broadband Backend (CABB) on the ATCA, we were able to observe two 2048 MHz spectral windows, centred on frequencies 43.2 and 48.2 GHz. Although only a coarse spectral resolution of around 7 $\mathrm{km\,s^{-1}}$ was available to us, we detect widespread, extended emission in the CS (1–0) ground state transition. We also detect eight class I CH_3OH masers at 44 GHz and three SiO masers in vibrationally excited (1–0) transitions. We also detect the H53α radio recombination line, non-vibrationally excited SiO (1–0) and emission in the CH_3OH 1_0–0_0 A^+ line.

2.1 Introduction

High mass star formation (HMSF) is a poorly understood process due to the rapid evolution of high mass stars, the rarity of high mass stars, and high levels of dust extinction toward

the regions in which they are born (Zinnecker & Yorke 2007). HMSF does not occur in isolation, thus making it difficult to disentangle mechanisms involved with HMSF from other sites of star formation in the vicinity. HMSF is known to occur within dense regions of giant molecular clouds (GMCs; e.g. Lo et al. 2011). In order to comprehend the earliest stages of HMSF, a catalogue of their regions must be identified and mapped through high density tracers.

Previous surveys have been productive in identifying many sites of HMSF, but emphasise signposts that pick out only a subsection of the various stages, are typically targeted toward known regions. For example, methanol maser surveys (e.g. Walsh et al. 1998; Green et al. 2009) pick out hot cores and young ultra-compact H II regions; infrared dark clouds (IRDCs; e.g. Rathborne et al. 2006) are only seen when they are close to us (typically $\sim$5 kpc), and projected against a bright infrared background from the Galaxy and may not always identify sites of high mass star formation (Kauffmann & Pillai 2010); radio continuum sources are only found once a high mass star has had time to reach the main sequence and push its ionising wind through the surrounding material (e.g. Purcell & Hoare 2010).

Untargeted Galactic plane surveys not only give us an opportunity to address these concerns, but they also allow us to study aspects of HMSF on a Galaxy-wide scale, with higher resolution and sensitivity than is achievable in external galaxies. For example, we can study the structure of the Galaxy through CO surveys (e.g. Dame & Thaddeus 2008) and H I surveys (e.g. McClure-Griffiths et al. 2005). The nature of CO and H I mean that these tracers typically pick out low density gas (critical density $\approx 10^1$-$10^2\,\mathrm{cm}^{-3}$) that is not directly related to HMSF. These tracers are also sensitive to inter-spiral arm gas, making it difficult to identify spiral structure in the Galaxy. Higher density gas tracers, such as NH_3 and HC_3N, observed as part of the H_2O southern Galactic Plane Survey (HOPS; Walsh et al. 2008, 2011), do trace gas directly associated with HMSF and may more clearly trace spiral structure. However, HOPS is a shallow survey, sensitive to typical HMSF regions within a few kpc. In order to study the spiral structure of the Galaxy, as well as the gas associated with HMSF, we have devised the MALT-45 survey. This paper introduces the MALT-45 survey design and outlines the auto-correlation results of pilot survey. MALT is the Millimetre Astronomer's Legacy Team - the result of a successful meeting of star formation astronomers to collaborate on major southern hemisphere millimetre surveys. MALT currently consists of the MALT-90 (Foster et al. 2011) and MALT-45 surveys.

2.2 MALT-45 design

MALT-45 is an untargeted Galactic plane survey to be conducted on the Australia Telescope Compact Array (ATCA) with a Galactic latitude width of $\pm0.5^\circ$ (the longitude range is yet to be determined). The survey will focus on the dense gas tracer CS (1–0), and identify previously unknown sources of both class I CH_3OH and SiO (1–0) masers, which occur towards sites of star formation and evolved stars, respectively. The survey region of MALT-45 will be a subsection of HOPS (which covers a range $l = 290^\circ$ through $l = 0^\circ$ to $l = 30^\circ$, $b = \pm0.5^\circ$), allowing comparison with 12 mm tracers of star formation, particularly NH_3 (1,1) and H_2O masers. Other lines of possible interest are outlined in Table 2.1.

2.2.1 Australia Telescope Compact Array characterisation

The ATCA is an interferometer composed of six 22 m antennas, CA01 through CA06. In recent years, the ATCA correlator has been upgraded to the Compact Array Broadband Backend (CABB; Wilson et al. 2011), which provides auto-correlation spectra. In addition to this upgrade, the ATCA obtained on-the-fly (OTF) mosaicing capabilities. We are particularly interested in the auto-correlations, as combining the six antennas in this way is similar to observing six times longer with an individual 22 m antenna such as Mopra. By using the ATCA auto-correlations for 7 mm surveying, we obtain an excellent metric on sensitivity versus survey speed. Note that cross-correlations are collected simultaneously with the auto-correlations, although the interferometric data provided by MALT-45 observations are not discussed in this thesis.

For the results presented in this thesis, only data from antennas CA01 through CA05 are presented. CA06 has a higher surface root-mean-square (RMS) and poorer sensitivity in the 7 mm wavelength range. In future MALT-45 observations, it may be possible to include CA06 data by weighting its contribution accordingly, but it is ignored at present.

2.2.1.1 CABB zoom modes

The ATCA provides two simultaneously observing broadband windows, each with 2048 MHz of bandwidth, and 2048 channels (i.e. 1 MHz channel resolution). For the observing frequencies of MALT-45, this corresponds to a velocity resolution of approximately 6.8 $\mathrm{km\,s^{-1}}$ per channel, which is quite coarse. Fortunately, the CABB provides 'zoom modes', which allow observing with a small channel resolution, ideal for spectral line observations. MALT-45 uses the 64M-32k zoom mode configuration, which provides up to 16 simultaneous observing 'zoom' windows in each 2048 MHz broadband window. Each of these zoom windows has 64 MHz of spectral coverage over 2048 channels (i.e. 32 kHz channel resolution). At observing frequencies, this corresponds to a velocity resolution of approximately 0.2 $\mathrm{km\,s^{-1}}$ per channel.

For pilot observations for MALT-45, the broadband windows were centred on frequencies of 43.2 and 48.2 GHz, and were placed to observe SiO (1–0) masers, class I CH_3OH masers and CS (1–0) thermal emission. These spectral lines and hence the 2 GHz band placements have been selected as being easiest to detect without sacrificing too many other lines of interest, and therefore some lines are neglected (e.g. HC_3N (5–4) at 45.49031 GHz).

At the time of observation for the pilot observations of MALT-45 (data described within this chapter), the CABB was unable to provide the 64M-32k zoom mode configuration, providing only broadband mode windows. The CABB was also unable to provide OTF mapping. The survey observations of MALT-45 detailed in Chapter 3 make use of the 64M-32k mode.

2.3 Auto-correlation

Interferometers, such as the ATCA, are popular in radio astronomy for their increased spatial resolution over a single dish. The quality of the images produced by an interferometer is determined by the *uv*-coverage over the observations, as interferometers sample the *uv*-plane. The *uv*-coverage is determined by the interferometer configuration, which provides baselines

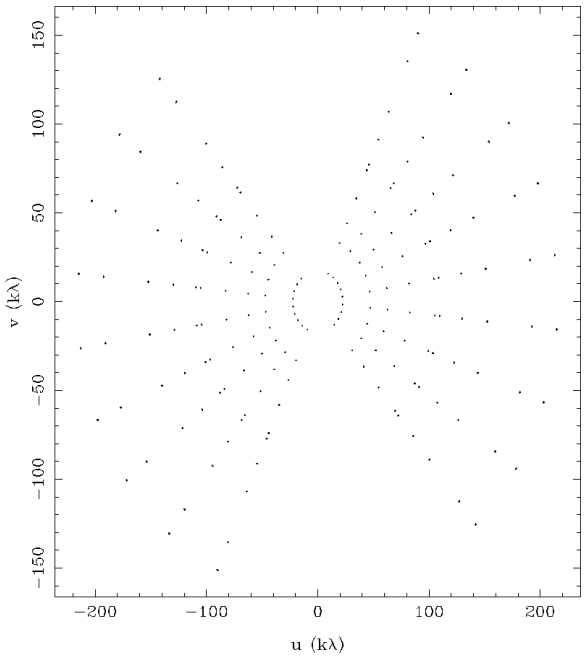

Figure 2.1: An example of ATCA baselines in the 1.5A array configuration. Note the lack of data in the centre of the plot, typical of an interferometer.

(the distance between any two antennas); see Fig. 2.1 for an example of *uv*-coverage. One problem that will always occur in interferometry is the lack of spatial coverage at short *uv*-distances; the distance between two antennas is limited by their physical size. For example, observations with the ATCA cannot have a pair of antennas closer than 22 m to each other, as each antenna is 22 m in diameter (in reality, the smallest baseline available is 31 m). This is known as the 'short-spacing problem'.

Short *uv*-distances are important, because they contain the total-power measurements, where the longer distances are sensitive to emission on small spatial scales. Emission (or absorption) with a smooth spatial distribution will appear absent without short baseline information; such extended emission is 'resolved out'. Single-dish observations avoid short *uv*-distance considerations, because there is no short-spacing problem. Thus, they are very useful for providing total-power measurements, ideal for detecting extended emission such as CS (1–0).

Cross-correlation is a measure of similarity between separate signal. The correlator response of an interferometer is the cross-correlation of antennas. By contrast, auto-correlation is simply the cross-correlation of a signal with itself. Throughout this thesis, auto-correlation refers to the processing of single-dish data. Each single-dish spectrum provided can be correlated with one another (stacking) to diminish noise and identify features in the spectra. This stacking technique is not restricted to spectra from the same antenna; we use the single-dish data from each of antennas in the ATCA together to achieve a high sensitivity in a short amount of observing time.

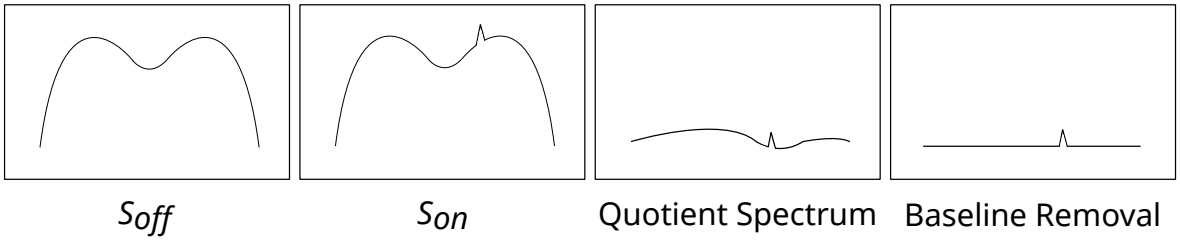

Figure 2.2: An example of the baselining procedure used to identify spectral lines.

2.3.1 Procedure

Observations with a single dish are typically divided between sources and reference calibrators. When reducing data to identify spectral lines, a quotient spectrum is formed from the source (on) and reference (off) spectra:

$$T_{Source} = \left(\frac{S_{on} - S_{off}}{S_{off}} \right) T_{ref} \tag{2.1}$$

where T is an antenna temperature, and S is a spectrum. T_{ref} refers to the system temperature of the reference source; this is used to calibrate antenna temperatures and flux densities. This procedure is referred to as baselining; a graphical representation can be seen in Fig. 2.2. Baselining relies on the system response between a source and reference being very similar, such that what remains after performing the subtraction and quotient is only source emission or absorption. Because the system response varies with pointing position, and the atmosphere intervening, resulting spectra may have significant variation in intensity with frequency, rather than being flat. Post-baselining fits to the spectra, such as polynomials, are utilised to remove any additional variations. Note that depending on the capabilities of the receiver system, observed continuum emission within the spectrum may have a significant slope, which is hard to distinguish from instrumental effects; extra care must be taken when subtracting polynomials in these cases.

As auto-correlation data reduction with the ATCA has not been conducted previously, standard single-dish data reduction techniques were employed. For each observing run of MALT-45, interferometric calibrators were observed as part of standard ATCA procedure, although these were not used in the resulting auto-correlation data. Over the course of the observations, reference scans were observed between source scans, as is standard with a single dish. These reference scans provide the calibration used for MALT-45 auto-correlation data.

2.3.2 Software

CSIRO Astronomy and Space Science (CASS), in addition to running and maintaining the ATCA, Mopra and Parkes* radio telescopes, provides various software packages to process raw data. Mopra raw data files are formatted and immediately ready to be processed by LiveData, which performs the baseline procedure outlined above. It also removes a polynomial of user specified order. If imaging is desired, LiveData products may be processed by Gridzilla, which regrids the spectra to form a data cube.

*A 64 m antenna near Parkes, New South Wales, Australia.

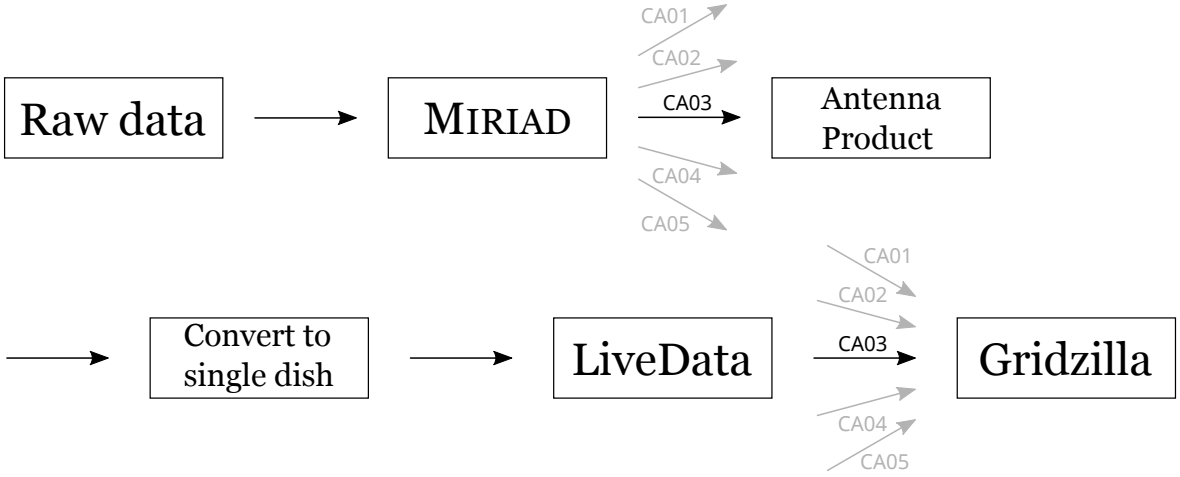

Figure 2.3: A diagram outlining the auto-correlation data reduction pipeline used for MALT-45.

ATCA raw data files are not ready to be processed in such a fashion. Our pipeline strategy of auto-correlation with the ATCA was as follows:

(i) MIRIAD, another software package provided by CASS, is used to interpret ATCA raw data, using tasks ATLOD and UVAVER to isolate auto-correlations for every antenna, and select specific channel ranges of the data applicable to emission;

(ii) A specifically-designed program, developed by Maxim Voronkov, is used to convert products into a LIVEDATA readable format. This involves correctly designating a reference scan and performing rest frequency frame conversions;

(iii) LIVEDATA performs the baselining routine for each antenna product, followed with a linear subtraction to the spectra;

(iv) GRIDZILLA takes all antenna products, and produces a data cube.

The procedure is outlined graphically in Fig. 2.3. LIVEDATA parameters and GRIDZILLA parameters were tweaked for optimal results. LIVEDATA used a referenced method with a mean estimator, a robust linear fit for post-baselining subtraction, and a Doppler frame of LSRK. GRIDZILLA parameters include a beam full-width at half-maximum (FWHM) of 1 arcmin, a kernel FWHM of 1.5 arcmin, a cutoff radius of 0.8 arcmin and a mean gridding statistic.

Flux density calibration was achieved with antenna efficiencies and T_B-to-Jy conversion factors taken from Urquhart et al. (2010). Antenna efficiencies of 0.53 and 0.43 were used for the lower and upper broadband windows of the ATCA, respectively. For the maser lines, a T_B-to-Jy conversion factor of 14.1 was used. By using these values, we assume that the 7 mm antenna and receiver response from Mopra is similar to the ATCA. Once the data cubes were gridded, the factors were applied to provide appropriate flux density scaling.

2.3.3 The G333 GMC

The MALT-45 pilot survey was conducted partially over the GMC associated with the H II region RCW 106. RCW106 has a centre located roughly at $l = 333°$, $b = -0.5°$. We are particularly interested in this GMC, commonly referred to as the G333 complex, located at

a distance of 3.6 kpc (Lockman 1979). The G333 GMC has been thoroughly investigated for molecular spectral lines relevant to star formation (Bains et al. 2006; Wong et al. 2008; Lo et al. 2009), and has shown evidence of HMSF (Lo et al. 2011). See Bains et al. (2006), Wong et al. (2008) and Lo et al. (2009) for a detailed description of the G333 complex. G333 is an ideal location to test MALT-45 before commencing the full survey, as we can expect extended CS thermal emission and Class I CH_3OH masers to be detected (Slysh et al. 1994).

2.4 Observations

The first observations for MALT-45 were conducted on the ATCA over 36 hours from the 18th to 20th of March 2010, using the H168 array configuration. Additional MALT-45 observations were conducted on the 7th and 8th of June 2010, using the 6C array configuration. These observations were necessary to test the feasibility of MALT-45, as conducting an untargeted survey at this frequency will be demanding on time, and may yield poor data if not observed optimally.

A mosaic of source pointings was constructed to observe over one square-degree, with interleaved points spaced on a square grid of 42 arcsec, which is slightly larger than Nyquist sampled at the highest frequency (29 arcsec, assuming a beam of 57 arcsec). The mosaic contained roughly 12,000 points, and thus required short exposure times for each point to be completed within the allocated observation time, hence only 6 seconds of observation was allowed for each pointing. Prior testing to the pilot survey revealed that the ATCA required nominally 1.5 seconds settling time between adjacent points, thus leaving at most 4.5 seconds per pointing. This pilot survey was also necessary to test the 6 second cycle time used instead of the ATCA default 10 seconds.

Due to software limitations, a single mosaic of 12,000 discrete pointings was not possible on the ATCA. Instead, it was split into two half-mosaics, observed one after the other. However, an unfortunate miscalculation on the position of each half-mosaic caused an approximate half-degree gap between each mosaic. Nevertheless, an entire square-degree was mapped as planned. The centres of each half-mosaic are approximately 333.4° and 334.1° in Galactic longitude. This region was selected for its known rich star-forming regions, including the G333 GMC. The reference position used for auto-correlation processing was G334.0−1.0, and was observed for 5 cycles (30 seconds) approximately every 34 minutes.

It was found that data from antenna 6 of the ATCA (CA06) had increased noise levels by a factor of 3.5. The removal of CA06 data from the other antenna data improved the quality of images substantially, and therefore no data with CA06 is presented here. The poorer performance of CA06 is due to its different dish surface, yielding poor sensitivity to 7 mm emission. Furthermore, at the time of observation, the CABB also had bad channel issues with the broadband windows, specifically, on the channel range 250-500, and all multiples of 512.

Table 2.1: Bright spectral lines in the 42.2 to 49.2 GHz range. Radio recombination lines (RRL) are taken from Lilley & Palmer (1968). All other rest frequencies are taken from CDMS (Müller et al. 2005).

Spectral line	Frequency (GHz)	Pilot survey detection	Maser or thermal?	Beam size (arcsec)
SiO (1–0) $v = 3$	42.51934	N	Maser	66
SiO (1–0) $v = 2$	42.82048	Y	Maser	66
H53α (RRL)	42.95197	Y	Thermal	65
SiO (1–0) $v = 1$	43.12203	Y	Maser	65
SiO (1–0) $v = 0$	43.42376	Y	Thermal	65
CH_3OH 7(0,7)–6(1,6) A^+	44.06941	Y	Maser (Class I)	64
H51α (RRL)	48.15360	N	Thermal	58
$C^{34}S$ (1–0)	48.20694	Y	Thermal	58
CH_3OH 1_0–0_0 A^+	48.37246	Y	Thermal	58
CH_3OH 1_0–0_0 E	48.37689	N	Thermal	58
OCS (4–3)	48.65160	N	Thermal	58
CS (1–0)	48.99095	Y	Thermal	57

2.5 Results

Auto-correlated data cubes were produced for each of the lines listed in Table 2.1 from the ATCA broadband data. We detected emission in CS (1–0) (Fig. 2.4), class I CH_3OH masers at 44 GHz (Figs 2.5 and 2.6), vibrationally excited SiO masers (Figs 2.6 and 2.7), as well as occasional detections of H53α, SiO (1–0) $v = 0$ and CH_3OH 1_0–0_0 A^+. Radio recombination lines H53α and H51α were anticipated detections, as the brightest H69α detection in the Galactic plane found by HOPS is located at G333.609−0.211. The survey region of this pilot survey did not cover the known regions of emission, but some H53α recombination line emission was found cospatial with the class I CH_3OH maser G333.281−0.382.

As only the broadband modes were available at the time of observation, the results provide a coarse spectral resolution of about 6.8 km s^{-1}. Fortunately, some observing time was permitted on the Mopra radio telescope to briefly follow-up some of the detected class I CH_3OH and SiO masers. Observations on Mopra were carried out using a standard position-switch mode, where each on-source position was observed for 5 minutes, resulting in a higher sensitivity than the ATCA observations. Maser emission characteristics are detailed in Table 2.2 and Figs 2.8 and 2.9.

The sensitivity of auto-correlated data varies greatly with the different days of observation. The MIRIAD task IMSTAT calculates a mean RMS of 15 mK per channel in antenna temperature, although this seems vastly too small. We feel that the true sensitivity of these data is approximately 40 mK per channel, although with good weather, this may improve. The size of the primary beam at the rest frequency of each of the spectral lines mapped by MALT-45 is included in Table 2.1.

By comparing the positions of the same maser feature in G333.227−0.057, the estimated astrometric errors are derived from new ATCA data from Voronkov et al. (2012). We find an offset of 9 arcsec and so ascribe the estimated astrometric error of the auto-correlated data from the pilot survey work to be 10 arcsec.

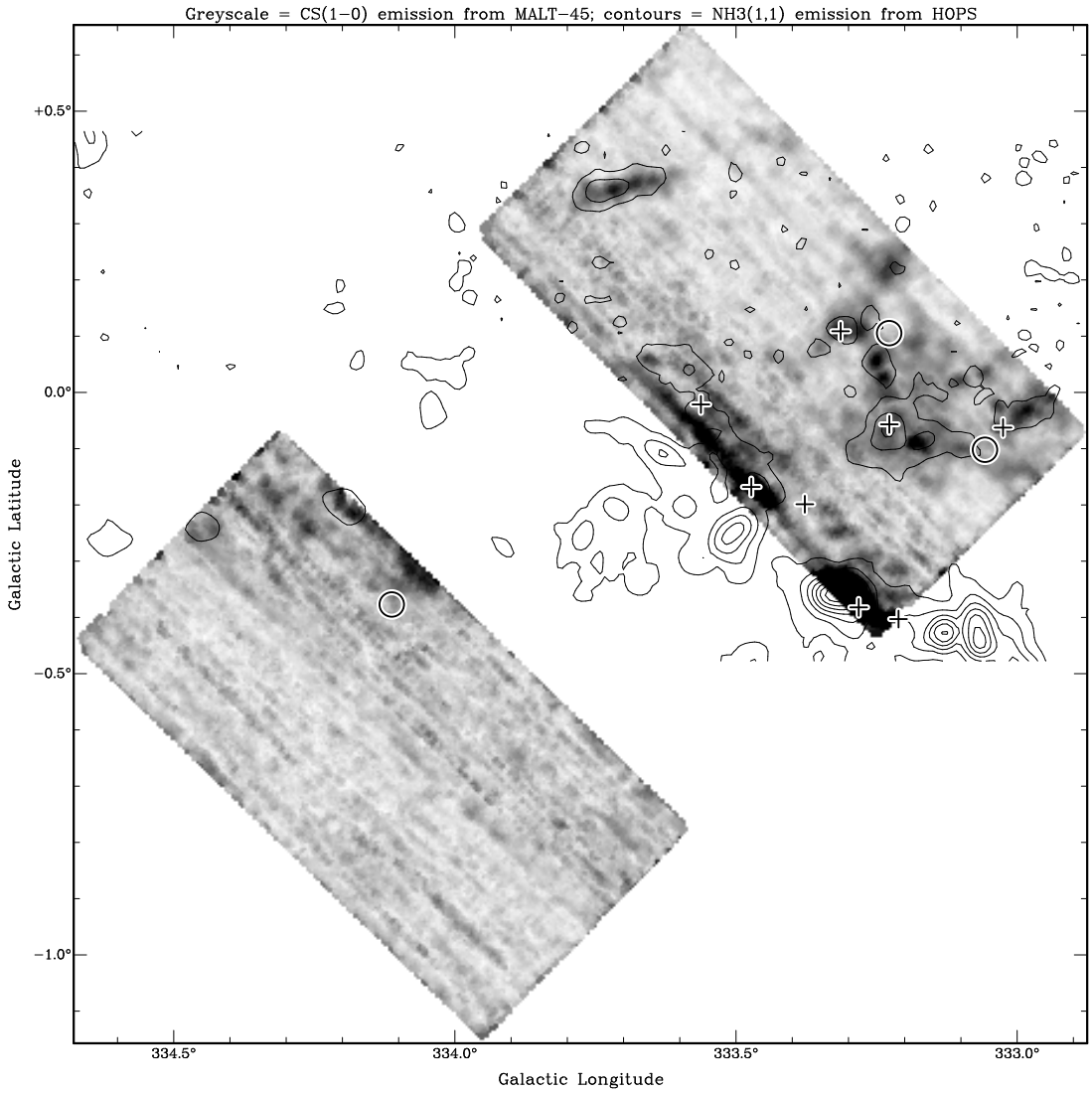

Figure 2.4: Auto-correlated CS peak-intensity map, overlaid with HOPS thermal NH_3 (1,1) contours. Contour levels are 10, 20, ..., 90 per cent of 1.09 K in units of antenna temperature. Circle symbols represent SiO $v = 2$ maser positions, while plus symbols designate class I CH_3OH maser positions. The major tick labels are 333.0°, 333.5°, ..., 334.5° and −1.0°, −0.5°, ..., +0.5° for Galactic longitude and latitude, respectively.

2.5.1 CS (1–0) at 48.990 GHz

The main isotopologue of CS was detected in extended emission across a large portion of the survey region (Fig. 2.4). Also shown in Fig. 2.4 is NH_3 (1,1) emission, as detected in HOPS (Purcell et al. 2012). The CS emission appears to closely follow the NH_3 emission, as might be expected from the two quiescent dense gas tracers (e.g. Purcell et al. 2009). The strongest CS emission occurs cospatial with the G333 GMC, which is close to the edge of the surveyed area around G333.3−0.4.

Extended CS emission is seen between Galactic longitudes of 329.9° and 333.3° and Galactic latitudes −0.2° and +0.3°. NH_3 emission is detected within this region, but covers a much smaller area than the CS emission, possibly highlighting differences in the distribution of each dense gas tracer.

At G333.70+0.35, we see a filamentary CS structure that is oriented close to the Galactic

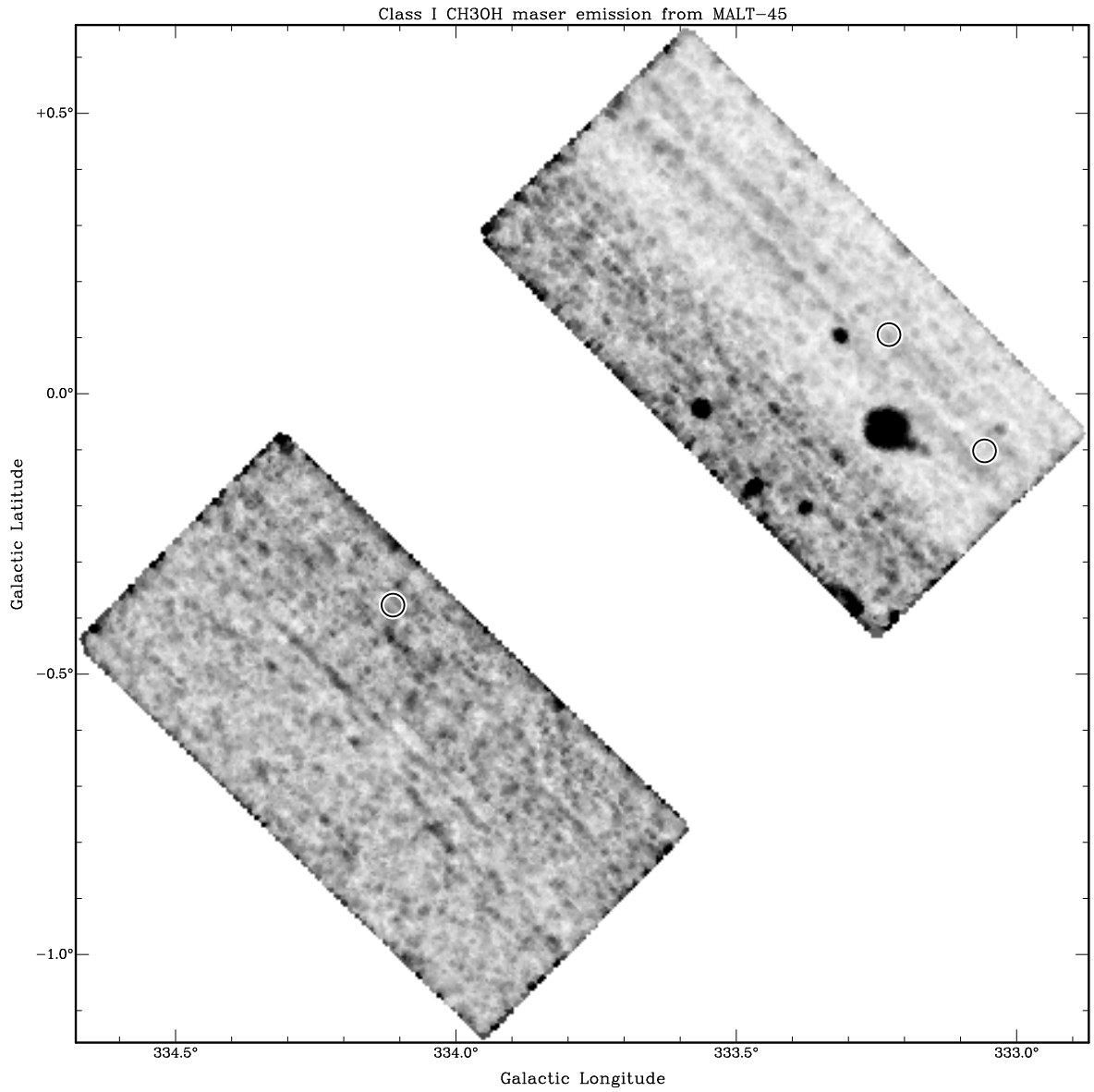

Figure 2.5: Auto-correlated class I CH_3OH maser peak-intensity map. Circles represent SiO $v = 2$ maser positions. The major tick labels are 333.0°, 333.5°, ..., 334.5° and −1.0°, −0.5°, ..., +0.5° for Galactic longitude and latitude, respectively.

plane. This structure is also seen in NH_3 emission (Fig. 2.4), as well as an infrared dark cloud (Fig. 2.10). See §2.6.3 for more details.

2.5.2 Class I CH_3OH 7(0,7)–6(1,6) A^+ masers at 44.069 GHz

In the survey region, we found eight possible class I CH_3OH masers, whose properties are listed in Table 2.2 and shown as greyscale emission in Fig. 2.5, and positions are shown in Figs 2.4, 2.7, 2.10 and 2.11 as plus symbols. Most of the masers (5 of 8) are cospatial with the G333 GMC and have line of sight velocities within $10\,\mathrm{km\,s^{-1}}$ of the GMC systemic velocity. They are thus likely to be associated with the star formation occurring in and around the GMC. The other three appear cospatial with extended CS emission. The CABB broadband spectra for each maser are provided in Fig. 2.6. For each of these detections, we managed to acquire time on the Mopra radio telescope to re-observe the CH_3OH spectra, as shown

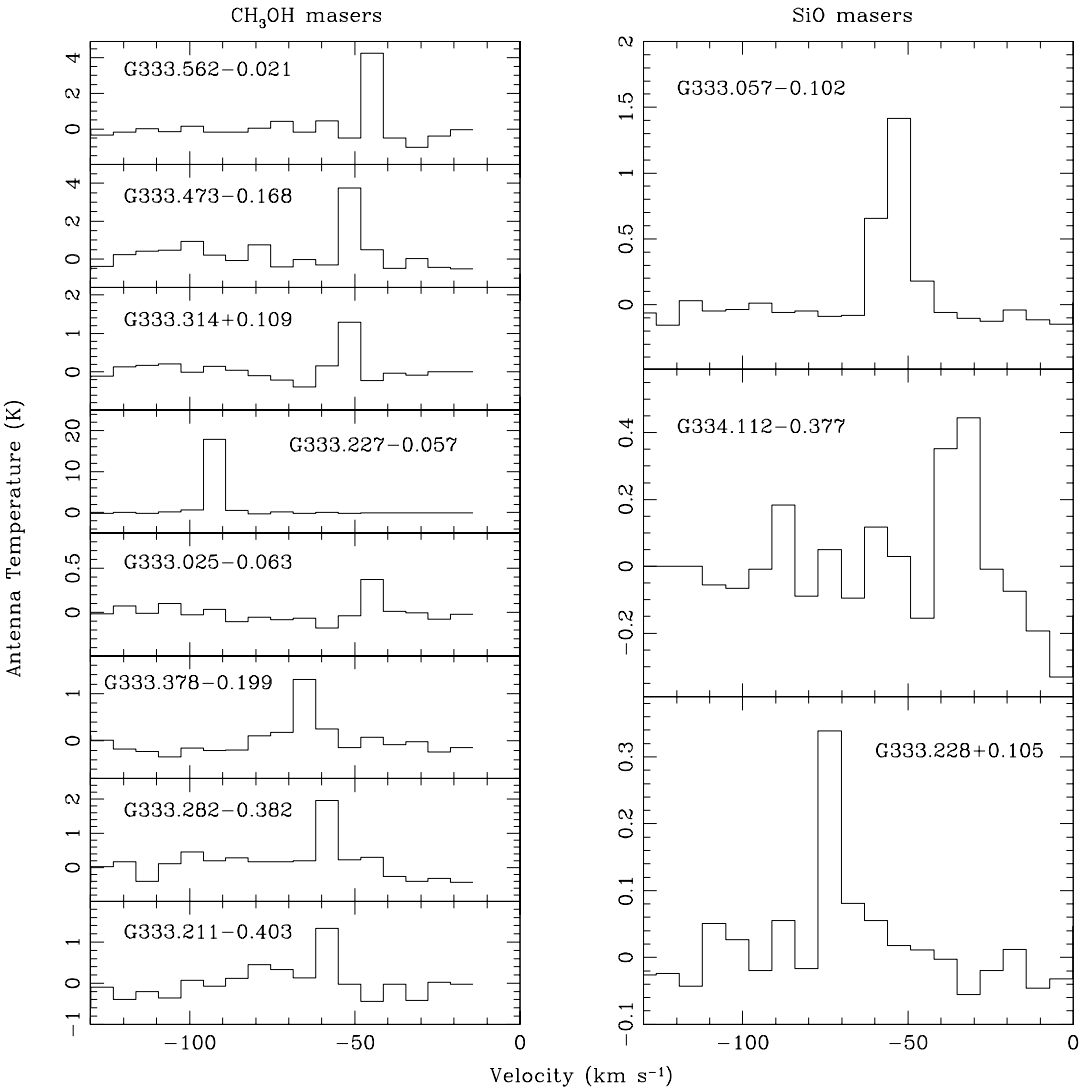

Figure 2.6: Auto-correlated spectra for each class I CH_3OH (left) and SiO $v = 2$ maser (right) detected. The deviations in the baselines are a result of poor weather. The channel width is approximately 6.8 km s^{-1}.

in Fig. 2.8. With the superior spectral resolution of Mopra, more convincing detections are made and finer velocity detail becomes apparent. Of all the CH_3OH detections, only G333.227−0.057 and G333.473−0.168 have been previously reported at 44 GHz by Slysh et al. (1994) and Voronkov et al. (2012), respectively.

2.5.3 SiO (1–0) $v = 1, 2$ masers at 43.122 and 42.820 GHz

SiO emission in the vibrationally excited transitions, which are known to show maser activity, was tentatively detected towards three positions, shown as circles in Figs 2.4, 2.5, 2.10, and 2.11, and as greyscale in Fig. 2.7. All three positions appear to exhibit emission in the $v = 2$ transition and two of the three in the $v = 1$ transition (the exception being G333.228+0.105). Spectra for the $v = 2$ transition are shown in Fig. 2.6. Again, emission is restricted to a small number of channels, using the CABB broadband mode. Each of the three tentative masers

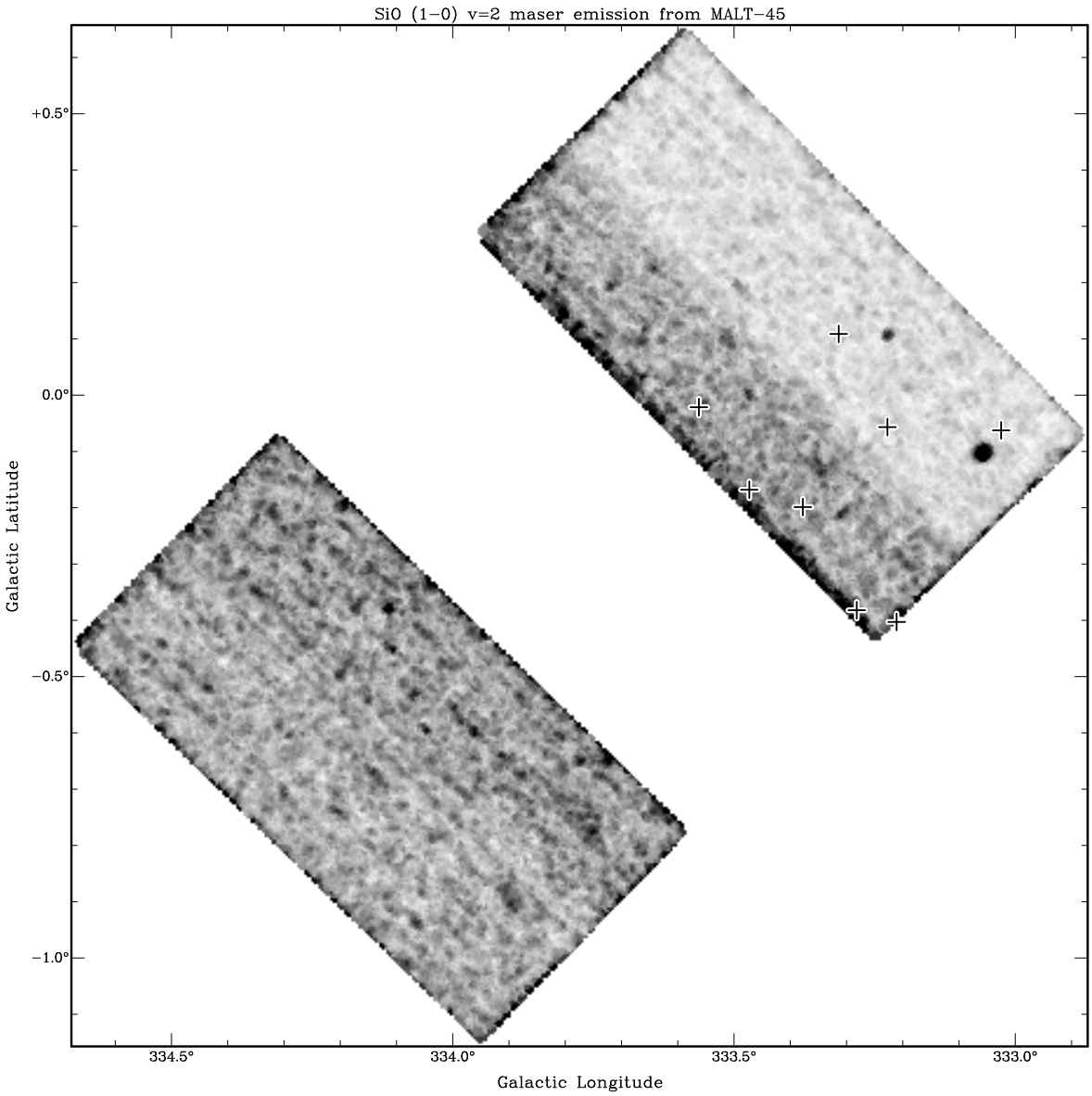

Figure 2.7: Auto-correlated SiO (1–0) $v = 2$ maser peak-intensity map. Class I CH_3OH maser positions are designated by plus symbols. The major tick labels are 333.0°, 333.5°, ..., 334.5° and −1.0°, −0.5°, ..., +0.5° for Galactic longitude and latitude, respectively.

were re-observed with Mopra and high-resolution spectra are provided for two in Fig. 2.9, where more detail of the spectra can be seen. The maser at G333.228+0.105 was not detected by Mopra, leaving its detection status by the CABB as tentative. Figs 2.10 and 2.11 show the locations of the SiO masers with respect to infrared emission from GLIMPSE. Each SiO maser is cospatial with a bright infrared star which is likely to be an evolved star in each case.

2.5.4 Other detected lines

In addition to the main lines mentioned above, we made tentative detections in the SiO (1–0) $v = 0$ and CH_3OH 1_0–0_0 A^+ lines. The SiO was detected towards G333.227−0.057, which is cospatial with a class I CH_3OH maser. The CH_3OH 1_0–0_0 A^+ and E lines are thermally emitting lines that are close in frequency (equivalent to $27.5\,\mathrm{km\,s^{-1}}$). We detect

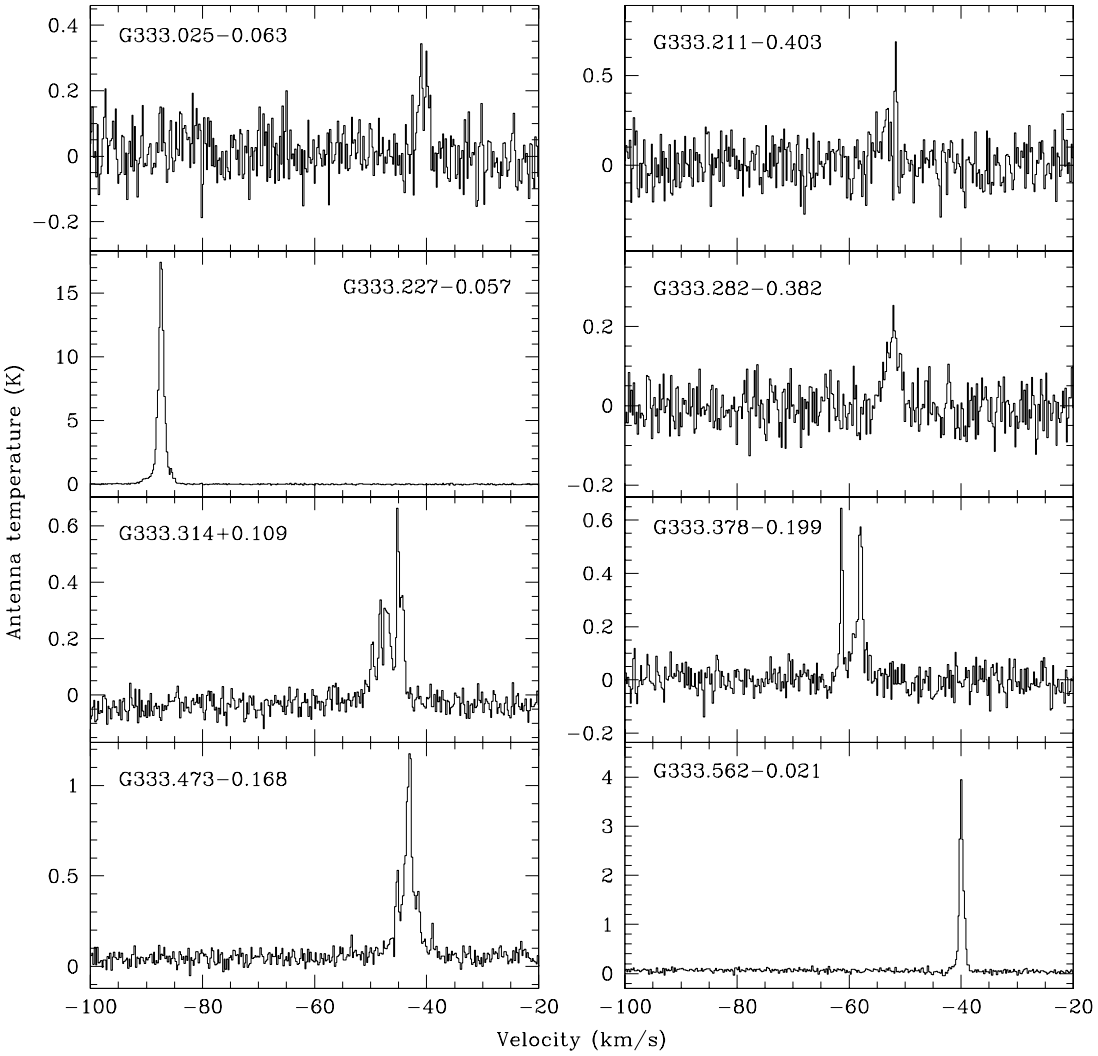

Figure 2.8: Follow-up class I CH_3OH maser spectra from Mopra.

thermal emission at G333.227−0.057 and G333.314+0.109 in the A^+ transition, but not the E transition. Kalenskii & Sobolev (1994) indicate that the E-CH_3OH transition may require higher densities to produce line strengths comparable to A^+-CH_3OH. The emission at G333.227−0.057 is cospatial with the thermal SiO source above and thermal methanol at G333.314+0.109 is cospatial with another class I CH_3OH maser, leading to a likely star formation origin for both thermal CH_3OH sources.

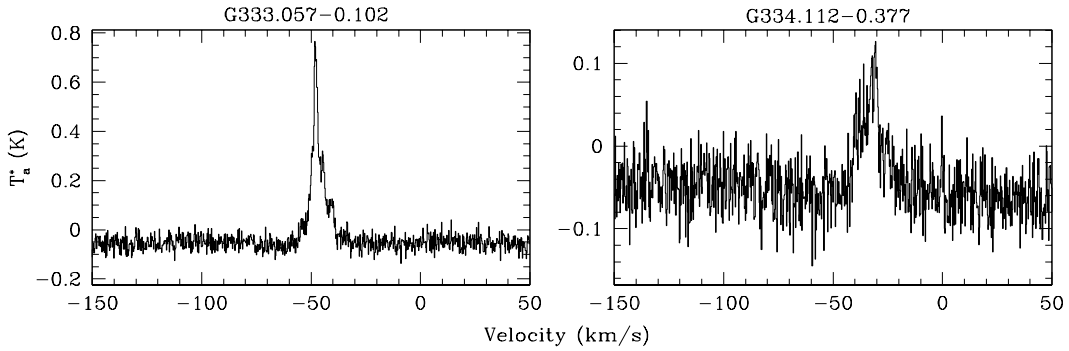

Figure 2.9: Follow-up SiO maser spectra from Mopra.

Table 2.2: Properties of detected MALT-45 maser emission as determined by Mopra.

Source Name	RA (J2000) (h m s)	Dec (J2000) (° ′ ″)	Peak antenna temperature (K)	Peak velocity ($km\,s^{-1}$)	Velocity range Min. ($km\,s^{-1}$)	Max.	Maser detected
G333.025−0.063	16 18 55.6	-50 24 03.6	0.34	−41	−42	−39	Class I CH_3OH
G333.057−0.102	16 19 15.0	-50 24 12.1	0.84	−48	−45	−50	SiO $v = 1, 2$
G333.211−0.403	16 21 15.6	-50 30 45.1	0.69	−52	−54	−51	Class I CH_3OH
G333.227−0.057	16 19 48.6	-50 15 17.2	18	−87	−86	−88	Class I CH_3OH
G333.282−0.382	16 21 29.0	-50 26 52.0	0.25	−52	−55	−50	Class I CH_3OH
G333.314+0.109	16 19 28.8	-50 04 45.0	0.70	−45	−45	−48	Class I CH_3OH
G333.378−0.199	16 21 05.8	-50 15 00.9	0.65	−61	−62	−56	Class I CH_3OH
G333.473−0.168	16 21 22.7	-50 09 42.6	1.1	−43	−42	−44	Class I CH_3OH
G333.562−0.021	16 21 08.1	-49 59 47.8	3.8	−40	−39	−41	Class I CH_3OH
G334.112−0.377	16 25 06.7	-49 51 28.5	0.14	−30	−29	−34	SiO $v = 1, 2$

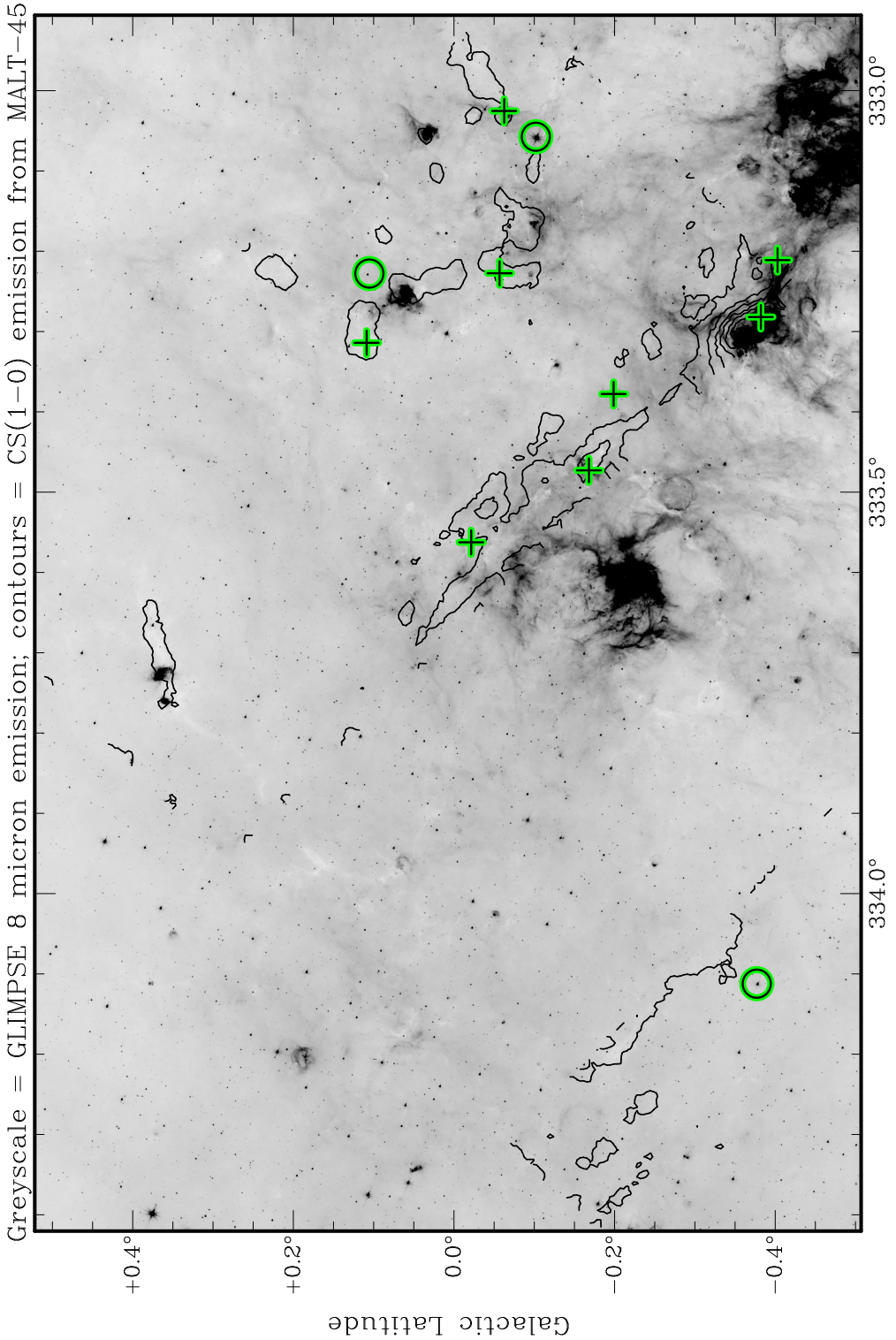

Figure 2.10: *Spitzer* GLIMPSE 8.0 μm greyscale image with MALT-45 pilot survey CS (1–0) thermal emission in black contours, with the positions of detected CH_3OH and SiO masers designated by plus symbols and circles, respectively. Contour levels are 7, 17, ..., 87 per cent of 0.72 K, in units of antenna temperature. Dark regions in the infrared greyscale image indicate emission, while light regions indicate a lack of emission, such as the IRDC near G333.7+0.4.

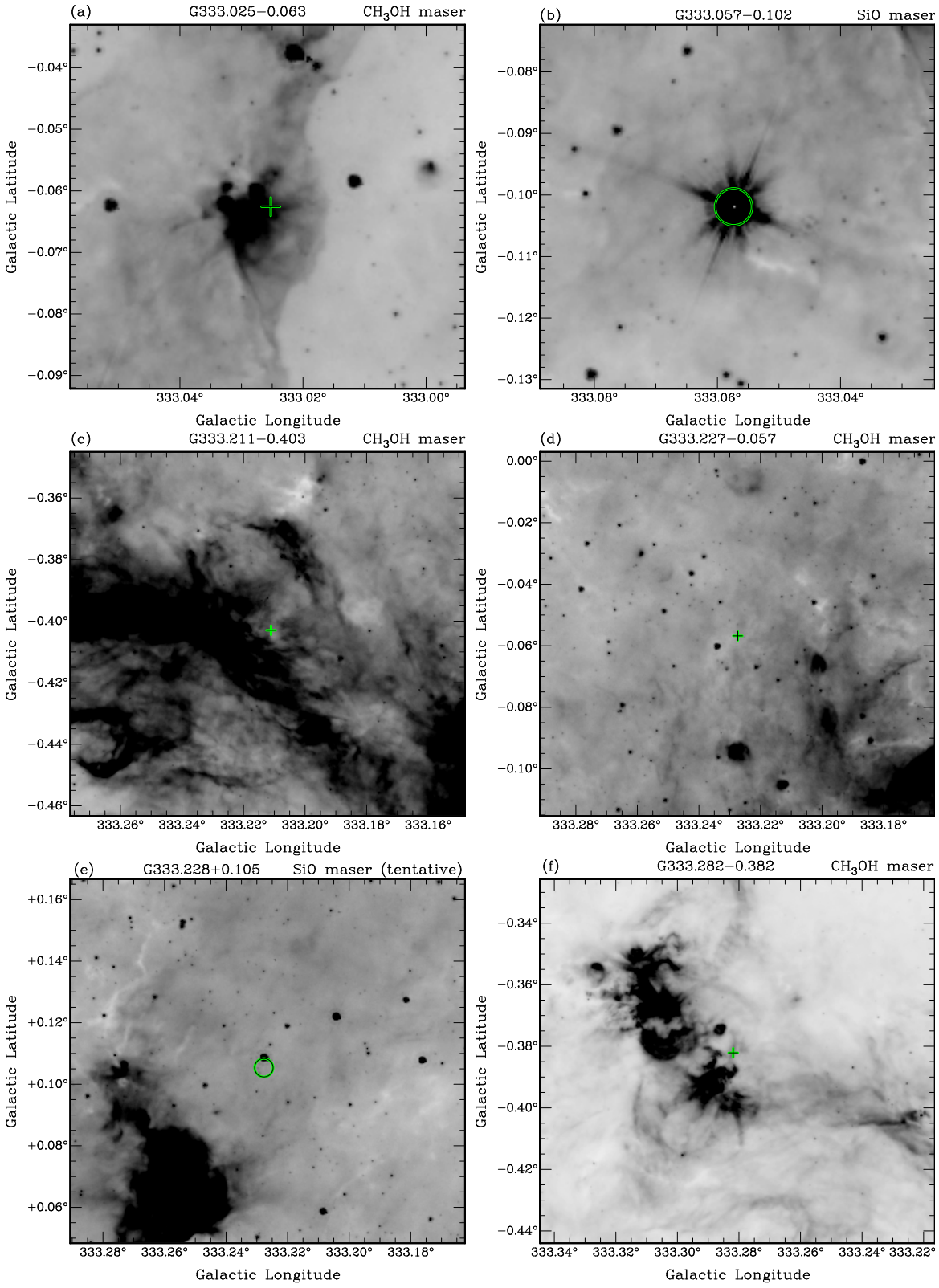

Figure 2.11: GLIMPSE 8 μm images of maser detection regions. Plus symbols designate positions of class I CH_3OH masers, and circles represent SiO maser positions. (k) contours are CS (1–0) emission at 7, 9 and 11 per cent of 0.72 K, in units of antenna temperature. Dark regions in the infrared greyscale images indicate emission, while light regions indciate a lack of emission.

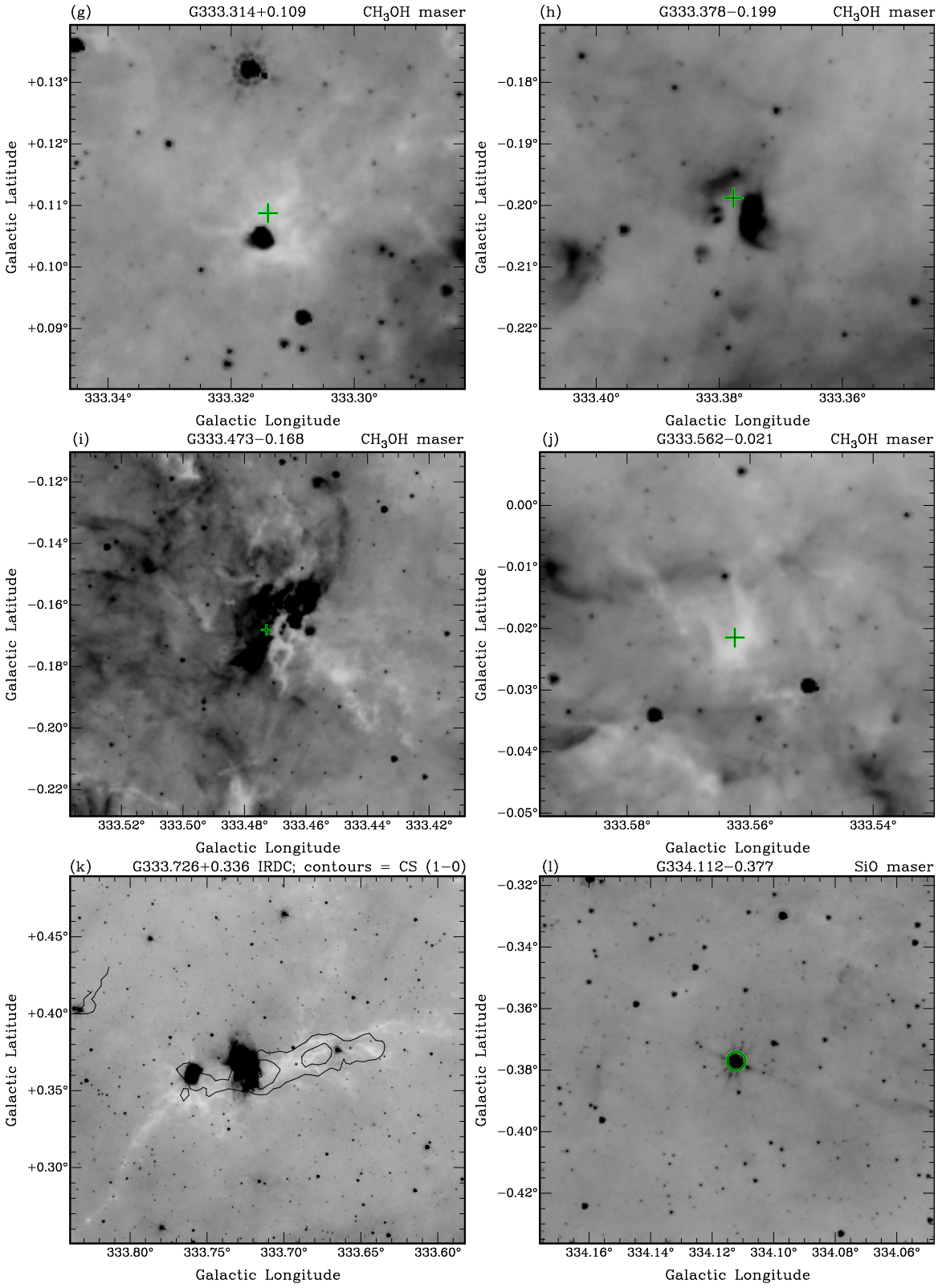

Figure 2.11: *continued*

2.6 Discussion

2.6.1 Weather effects

As can be seen in Fig. 2.4, significant 'striping' artifacts exist in the data. The stripes coincide with the scanning direction of the observations. One contributing factor to the poor data is the fast-mosaic method; due to the fast slewing times between pointings, antennas were occasionally unable to keep up and thus did not contribute data. However, the main factor in poor data is the inclement weather experienced during observations. The most prominent stripes seen in Fig. 2.4 coincide with periods of light rain. Lagging antennas serve to decrease our sensitivity to emission, but the weather hampers our ability at determining real astrophysical emission from noise. This weather introduced noise into both broadband spectral windows, but has affected some frequencies more than others. See Fig. 2.6 for CH_3OH and SiO spectra. Examples of species with poor spectra include CH_3OH 1_0–0_0 A^+ (and its E species), H53α and H51α. The noise is apparent on all relevant frequencies of emission, but fortunately has permitted reasonable detections for the primary lines of interest (CS, class I CH_3OH and SiO masers).

It must be mentioned that the problems experienced in the pilot will not plague the overall MALT-45 survey, as the pilot survey merely seeks to provide a proof-of-concept on the techniques used and reveal potential problems before committing to the full observation.

2.6.2 Limitations of the observations

Given the demands of our observational setup, we found some limitations to the ATCA that have affected the outcome of our pilot observations. Initially we found software limitations that meant changes to the intended survey design. These included: mosaic scans in Right Ascension and Declination coordinates only, rather than Galactic coordinates; no more than 999 pointings per mosaic file; no more than 2000 individual commands in a schedule file. These limitations resulted in a survey region that is at an angle to the Galactic plane, as can be seen in Fig. 2.4, and a complicated mosaicing system.

During the observations, zoom modes with the CABB were not available, so we used the broadband mode. This had the unfortunate effect of greatly limiting the amount of spectral detail seen, as described in §2.4. We also expect that the broadband mode is less sensitive to narrow-line emission (e.g. masers) by a factor of up to three. Also as mentioned previously, we found that some of the antennas had difficulty in keeping up with the demanding 6-second pointing regime. Indeed we found that RMS errors on the position of antenna 3 were typically 20 arcsec, which has reduced the sensitivity of the resulting data. We believe these excessive pointing errors can be eliminated with OTF mapping, where the antennas are driven smoothly and subsequent testing of this method suggests OTF mapping will resolve this issue for the full survey.

2.6.3 Comparison with other observations

In this subsection, we compare selected sources within the MALT-45 pilot survey region to observations from previous surveys. In particular, we compare our results with the mid-infrared

Spitzer Galactic Legacy Infrared Mid-Plane Survey Extraordinaire (GLIMPSE; Benjamin et al. 2003), for a visual correlation with infrared structures and objects. Mid-infrared extended emission is typically seen towards regions of active star formation, where the interstellar dust has been heated by newly formed stars. In addition to infrared emission, GLIMPSE also reveals prominent regions of infrared absorption, projected against the bright infrared background emission from the Galaxy (IRDCs; Rathborne et al. 2006).

Infrared emission can also arise from a variety of other astrophysical objects. One such example is emission from evolved stars, that may also give rise to SiO masers, which appear as bright infrared stars in the GLIMPSE images (Robitaille et al. 2008). The evolved stars appear unresolved in the GLIMPSE images, which may occasionally be confused with confined sites of star formation. A useful, but not entirely robust, method to distinguish between evolved and young stars is that an infrared star is likely to be evolved if it is not associated with extended infrared emission or an IRDC and has a 4.5 μm magnitude brighter than 7.8 (Robitaille et al. 2008). Young stars are more likely to be fainter and associated with either extended emission or IRDCs.

A comparison of MALT-45 CS to HOPS NH_3 would be a valuable scientific addition to this paper, providing insight into star formation within these clouds. However, the data being presented is not of a sufficient quality to merit an accurate analysis. A variation in the CS/NH_3 ratio may be apparent in a region such as G333.24+0.21, where there appears to be an over-abundance of CS, relative to NH_3, as can be seen in Fig. 2.4. A thorough analysis will instead be performed with data from the full MALT-45 survey.

2.6.3.1 G333.227−0.057

GLIMPSE images in Figs 2.10 and 2.11 reveal that the region at G333.227−0.057 is on the edge of extended emission, but does not appear to be closely associated with a prominent infrared feature. We note there is an infrared source located approximately 15 arcsec to the lower left of the maser position in Fig. 2.11(d), which could be the powering source for an outflow that creates the maser. The class I CH_3OH maser spectrum (Fig. 2.8) is dominated by a single peak at around $-87\,\mathrm{km\,s^{-1}}$. This region has been studied previously, and contains OH maser emission (Sevenster et al. 1997), class II CH_3OH maser emission (Ellingsen et al. 1996) and water maser emission (Kaufmann et al. 1976; Breen et al. 2010a). The spectra of all maser species are remarkably similar, with a peak close to $-87\,\mathrm{km\,s^{-1}}$, indicating a likely common origin for all masers. This velocity is significantly different from velocities of gas found associated with the G333 GMC, which are more typically around $-45\,\mathrm{km\,s^{-1}}$. Lockman (1979) calculate a distance of 3.6 kpc to G333. Based on a kinematic model of Galactic rotation, we estimate the distance to G333.227−0.057 is 5.1 kpc, putting it at a significant distance behind G333.

The class I CH_3OH maser associated with G333.227−0.057 was first detected by Slysh et al. (1994), with a peak flux density over 300 Jy. Using the high velocity resolution Mopra observations (Fig. 2.8), we see that the spectrum shows weaker emission, with a peak flux density 250 Jy, assuming a Jy/K conversion factor of 14.1 (Urquhart et al. 2010). This difference may be partially due to intrinsic variability of the maser, but can likely be attributed

to calibration uncertainties which are at the 20 per cent level.

We have detected unresolved SiO (1–0) $v = 0$ emission coincident with G333.227−0.057. This emission is seen in a single channel in the CABB data, but also as a well-defined single peak in the Mopra follow up data. Based on the Mopra spectrum at this position, the SiO emission has an integrated intensity of $2.2\,\mathrm{K\,km\,s^{-1}}$, a peak velocity of $-88.6\,\mathrm{km\,s^{-1}}$ and line FWHM of $12.7\,\mathrm{km\,s^{-1}}$. The velocity of the SiO emission is within $2\,\mathrm{km\,s^{-1}}$ of the peak of the class I CH_3OH maser, suggesting that the two are associated. As previously discussed, this ground state thermal transition is known to trace outflows associated with star formation. Using the CABB data, we also tentatively detect thermal CH_3OH emission in the 1_0–0_0 A^+ transition. Since this transition was not covered by the Mopra follow up observations, we cannot be certain that this is a real detection. If this is a real detection, then we can expect occasional detection of these thermal lines throughout the main MALT-45 survey, which will be useful to compare the thermal and masing properties of CH_3OH in such regions.

2.6.3.2 G333.726+0.366

The CS image shows a clear elongated structure at this position. Comparison with the GLIMPSE 8 μm image indicates that there is an IRDC, whose morphology closely follows that of the CS emission (Fig. 2.11). HOPS NH_3 emission also closely follows the CS emission and IRDC. The NH_3 emission is strongest at $-34.9\,\mathrm{km\,s^{-1}}$ and the CS emission appears to peak close to this, although the velocity of the peak is not known accurately due to the broad-band channels of the CABB. The close velocity and shape suggests both CS and NH_3 arise from the IRDC. The IRDC is cospatial with bright, extended emission at 8 μm which lies at the peak of both CS and NH_3 emission. The extent of the CS and NH_3 emission is almost 0.2°, which, assuming a distance of 3.6 kpc (Lockman 1979), is equivalent to a projected distance of 10 pc. The GLIMPSE image indicates that the IRDC may extend significantly beyond this.

2.6.3.3 G333.314+0.109

We detect both CS and a class I CH_3OH maser emission at this position. The GLIMPSE image of this region shows a faint IRDC, with an extended and reddened emission feature within the IRDC. The peak of weak NH_3 emission appears at this position, as well as a water maser, detected in HOPS. All spectral features appear to peak around $-45\,\mathrm{km\,s^{-1}}$, which is similar to the velocity of the G333 GMC. It is likely that this cloud and the G333 GMC are located a similar distance from us.

2.7 Future work and refinement of the MALT-45 survey

The pilot survey has been successful in many ways, perhaps most notably with the successful auto-correlation data reduction for each of the spectral lines relevant to MALT-45. The pilot has detected extended CS emission, as well as eight class I CH_3OH masers, two SiO masers in the $v = 1$ and 2 transitions, and another tentative detection in the $v = 2$ transition. We have

Table 2.3: MALT-45 parameters from the pilot survey and full survey. Both the broadband and zoom windows provide 2048 channels. The velocity coverage of a single 64 MHz zoom window is approximately 400 $\mathrm{km\,s^{-1}}$.

MALT-45	Correlator configuration	Channel resolution ($\mathrm{km\,s^{-1}}$)	Cycle time (seconds)	Targeted spectral lines	On-the-fly mapping	Orthogonal scans / Nyquist sampling
Pilot survey	2× 2048 MHz broadband windows	∼7	6	12	No	No
Full survey	32× 64 MHz zoom windows	∼0.2	6	12	Yes	Yes

also detected thermal emission in CS, SiO $v = 0$ and CH_3OH 1_0–0_0 A^+ detections, with CS emission being extended across a large fraction of the surveyed area. However, we anticipate great improvements for the main survey, based on the results of this work, and the expected completion of the CABB upgrade on the ATCA.

With CABB 64M-32k zoom modes available, we expect to achieve spectral channel resolution of $\sim$0.2 $\mathrm{km\,s^{-1}}$, which will not only allow us to identify more spectral features, but will also effectively increase our sensitivity to narrow-lined emission, such as from masers. For a maser of line 1 $\mathrm{km\,s^{-1}}$ FWHM, we expect to gain a factor of $\sim$2.5 in sensitivity.

We expect to employ an OTF mapping technique, which will eliminate problems with the antenna drive systems not being able to keep up with the rigorous 6 second pointing we have used in this work. Early tests using OTF have indeed proven this to be the case. Overall, this could increase sensitivity by a factor of about 2, as some mapped regions had only three antennas sufficiently close to the desired pointing position to have usable data.

Early problems with the CABB blocks that cause noisy channels to be flagged out (as mentioned in §2.6.2) should be greatly reduced, as the cause of such problems become identified. We are currently aware that the problems with some blocks have already been addressed.

The ATCA scheduler now allows us to write schedule files in Galactic coordinates, as well as allowing many more pointings per mosaic and commands per schedule file. This will allow for a much smoother running schedule, as well as a smoother final mapped region, without jagged edges that would be a result of RA/Dec scans.

We will employ a method of scanning in two orthogonal directions (Galactic longitude and latitude). We expect that this will greatly reduce stripe features that are evident in the current data. Such stripes are mainly caused by varying weather conditions, but can also be affected by the changing elevation of the observations. Our experience in the pilot work is that observations should not be undertaken under heavy cloud, light rain or worse weather conditions. Scanning in two directions has proven very successful for OTF mapping with the Mopra radio telescope, such as those used in HOPS. Scanning in two directions will also increase the sensitivity. Furthermore, the combination of both OTF mapping and orthogonal scans will produce data that is effectively Nyquist sampled with closest spacing between adjacent observations of 30 arcsec. The differences between both surveys are highlighted in Table 2.3.

Chapter 3

Spectral line data from MALT-45

This chapter includes a co-authored publication. The bibliographic details of the paper are: Jordan, C. H., Walsh, A. J., Lowe, V., Voronkov, M. A., Ellingsen, S. P., Breen, S. L., Purcell, C. R., Barnes, P. J., Burton, M. G., Cunningham, M. R., Hill, T., Jackson, J. M., Longmore, S. N., Peretto, N. and Urquhart, J. S., Monthly Notices of the Royal Astronomical Society, 448, 2344. doi: 10.1093/mnras/stv178. The published paper is referenced by this thesis as Paper I.

The introduction section has been modified to streamline the discussed literature, to avoid unnecessary overlap with Chapter 1.

Abstract

We present the first results from the MALT-45 (Millimetre Astronomer's Legacy Team - 45 GHz) Galactic Plane survey. We have observed 5 square-degrees ($330° \leq l \leq 335°$, $b = \pm 0.5°$) for spectral lines in the 7 mm band (42–44 and 48–49 GHz), including CS (1–0), class I CH_3OH masers in the 7(0,7)–6(1,6) A^+ transition and SiO (1–0) $v = 0, 1, 2, 3$. MALT-45 is the first unbiased, large-scale, sensitive spectral line survey in this frequency range. In this paper, we present data from the survey as well as a few intriguing results; rigorous analyses of these science cases are reserved for future publications. Across the survey region, we detected 77 class I CH_3OH masers, of which 58 are new detections, along with many sites of thermal and maser SiO emission and thermal CS. We found that 35 class I CH_3OH masers were associated with the published locations of class II CH_3OH, H_2O and OH masers but 42 have no known masers within 60 arcsec. We compared the MALT-45 CS with NH_3 (1,1) to reveal regions of CS depletion and high opacity, as well as evolved star-forming regions with a high ratio of CS to NH_3. All SiO masers are new detections, and appear to be associated with evolved stars from the *Spitzer* Galactic Legacy Infrared Mid-Plane Survey Extraordinaire (GLIMPSE). Generally, within SiO regions of multiple vibrational modes, the intensity decreases as $v = 1, 2, 3$, but there are a few exceptions where $v = 2$ is stronger than $v = 1$.

3.1 Introduction

The mechanism of high-mass star formation (HMSF) remains an important unsolved problem in astrophysics. Understanding HMSF is difficult for a number of reasons: the rarity of HMSF regions, high dust extinction within molecular clouds, rapid evolution, and large distances from our Solar System (Zinnecker & Yorke 2007) all combine to hinder our understanding. HMSF is known to begin within Giant Molecular Clouds (GMCs) and eventually end with star clusters or associations (Lada & Lada 2003). To understand the various stages of HMSF, an inventory of regions must be compiled in a range of known tracers.

Large area surveys of molecular gas are ideal for identifying HMSF regions across a broad range of evolutionary phases. In particular, the critical density of a gas tracer can act as a probe for Galactic structure and star formation. Critical density (n_c) is a measure of the density required to produce detectable emission (Evans 1999). Previous surveys for star formation in external galaxies, typically for low-density gas tracers ($n_c < 10^3\,\mathrm{cm}^{-3}$), suffer from poor resolution (on the order of kpc) and sensitivity. Untargeted Galactic plane surveys avoid these issues, while simultaneously offering the ability to detect new, less obvious regions of star formation within our Galaxy. Other untargeted surveys have been productive in identifying extended emission, such as in CO (Dame et al. 2001; Jackson et al. 2006; Burton et al. 2013), OH (Dawson et al. 2014) and H I (McClure-Griffiths et al. 2005). However, HMSF occurs in regions of dense molecular gas, and so mapping higher density tracers serves well to identify target regions. Examples include NH_3 (1,1) ($n_c \approx 10^3\,\mathrm{cm}^{-3}$; Evans 1999) and HC_3N (4–3) ($n_c \approx 10^4\,\mathrm{cm}^{-3}$; Fuller & Myers 1993), which have been mapped by the H_2O Galactic Plane survey (HOPS; Walsh et al. 2011). HOPS has been successful in identifying previously unknown sites of star formation, as well as probing the structure of the Milky Way's spiral arms.

Another, even higher density gas tracer useful for detecting HMSF and mapping the structure of our Galaxy is CS. The ground state transition $J = 1 \rightarrow 0$ for CS lies within the 7 mm waveband, and has an effective critical density $n_c = 4.6 \times 10^4\,\mathrm{cm}^{-3}$ at 10 K (Evans 1999). Previous large scale observations towards specific regions, such as RCW 106 (Rodgers et al. 1960) for CS and other high-critical-density molecules have been productive in HMSF research (Lo et al. 2009). Untargeted observations of CS over bright infrared regions such as RCW 106 and regions without infrared emission reveal the full population of star-forming candidates above a small sensitivity limit.

The 7 mm waveband also contains the 44 GHz 7(0,7)–6(1,6) A^+ class I methanol maser line, which is the brightest of the class I species. Previous observations of the class I maser have almost always been targeted (e.g. Slysh et al. 1994; Voronkov et al. 2014), which limits and biases our understanding of this astrophysical phenomenon. The 7 mm waveband includes other spectral lines detailed in Table 3.1. To help develop our understanding of HMSF using the diagnostics in the 7 mm waveband, we have devised the MALT-45 untargeted Galactic plane survey.

Presently, the MALT-45 survey has only been conducted within the Galactic plane region $330° \leq l \leq 335°$, $b = \pm 0.5°$. Hence, within this part of the Galaxy, we present the survey results of CS (1–0), class I CH_3OH masers and SiO (1–0) thermal and maser emission. This

Table 3.1: Bright spectral lines mapped by MALT-45 between 42.2 and 49.2 GHz. Column 1 lists the spectral line. Column 2 lists the rest frequency of the line. Column 3 lists the uncertainty of the rest frequency. Column 4 classifies the line as either a maser or thermal line. Column 5 gives the ATCA primary beam size at this frequency. Column 6 indicates whether this line is discussed in this paper ('Y') or not ('N'). Columns 7 and 8 detail the local standard of rest velocity range covered by the CABB zoom band for this spectral line. Column 9 lists the median RMS noise level per spectral channel, with errors representing the standard deviation. The RMS noise is given to two significant figures. Radio recombination line (RRL) frequencies are taken from Lilley & Palmer (1968). All other rest frequencies are taken from CDMS (Müller et al. 2005). The velocity resolution ranges from 0.225 km s^{-1} (lowest rest frequency) to 0.195 km s^{-1} (highest rest frequency) per channel.

Spectral line	Frequency (GHz)	Uncertainty (kHz)	Maser or thermal?	Beam size (arcsec)	Detailed in this paper?	Velocity range Min. (km s^{-1})	Max. (km s^{-1})	Median RMS noise level
SiO (1–0) $v = 3$	42.51934	1	Maser	66	Y	−287	167	0.85±0.07 Jy
SiO (1–0) $v = 2$	42.82048	1	Maser	66	Y	−194	257	0.82±0.06 Jy
H53α (RRL)	42.95197		Thermal	65	N			
SiO (1–0) $v = 1$	43.12203	2	Maser	65	Y	−321	127	0.83±0.06 Jy
SiO (1–0) $v = 0$	43.42376	2	Thermal	65	Y	−224	221	27±1.7 mK
CH_3OH 7(0,7)–6(1,6) A^+	44.06941	10	Maser (Class I)	64	Y	−183	256	0.90±0.09 Jy
H51α (RRL)	48.15360		Thermal	58	N			
$C^{34}S$ (1–0)	48.20694	2	Thermal	58	N			
CH_3OH 1_0–0_0 A^+	48.37246	0.7	Thermal	58	N			
CH_3OH 1_0–0_0 E	48.37689	10	Thermal	58	N			
OCS (4–3)	48.65160	1	Thermal	58	N			
CS (1–0)	48.99095	2	Thermal	57	Y	−157	237	34±6.8 mK

section of the Galaxy was selected because it contains the G333 GMC. Future MALT-45 observations, if any, will observe more of the Galactic plane.

3.2 Observations

3.2.1 Survey parameters

The MALT-45 results presented here observed 5 square-degrees within the region bounded by $330° \leq l \leq 335°$, $b = \pm 0.5°$ over eight months on the ATCA. The first set of observations were conducted on 2012 September 21-23, 28 and 30, and October 1-13. The second set of observations were conducted from 2013 April 10-19. All observations were conducted in the H214 array configuration. The region $330° \leq l \leq 333°$, $b = \pm 0.5°$, and part of $333.0° \leq l \leq 333.5°$, $0° \leq b \leq 0.5°$ were surveyed in the first observing run. The remainder ($333° \leq l \leq 335°$, $b = \pm 0.5°$) was completed during the second observing run. Weather conditions across all observations were generally good, with typical path noises below 300 μm. Path noise is a measure of the weather quality, based on the phase delay between successive measurements of a geosynchronous satellite. Values above 500 μm are considered poor, but conditions only affect interferometric data.

All observations were conducted with the same surveying technique. Scans were observed in quarter-square-degree regions in Galactic coordinates, in both latitude and longitude directions. For both latitude and longitude scans, the mosaics are represented by 'long' and 'short' interleaved pointings. See Fig. 3.1 for an illustrative example. Within a mosaic row, consecutive pointing centres are separated by 1.045 beams, and centres of each mosaic row are separated by 0.45 beams. Each beam (pointing) is observed for 6 seconds in OTF mode observing. The frequency used to calculate the size of the primary beam is 49.2 GHz (the highest observed frequency), thus the beam used was 57.13 arcsec, and separation parameters are 59.7 and 25.7 arcsec, respectively. When combined, the scans provide a fully Nyquist-sampled spatial map.

Each quarter square-degree region required approximately 14 hours observation time, including the typical setup and calibration. Pointing corrections were determined using PMN J1646−5044 and applied approximately every 70 minutes. The reference position G334.0−1.0 was observed every 45 minutes for calibration of the auto-correlation data. In addition, to allow interferometric calibration, bandpass calibration was derived from PKS B1253−055, phase calibration from PMN J1646−5044 and flux density from PKS 1934−63.

3.2.1.1 CABB zoom modes

These MALT-45 observations make use of the 64M-32k zoom mode configuration, which provides 64 MHz of spectral coverage over 2048 channels (i.e. a channel resolution of 32 kHz). Each spectral line listed in Table 3.1 was observed with a 64M-32k zoom window (with the exception of the thermal CH_3OH 1_0–0_0 A^+ and E lines, which are separated by 4 MHz and were simultaneously observed within one zoom), using a total of 11 zooms. The channel resolution at observed frequencies is approximately 0.2 $\mathrm{km\,s^{-1}}$ per channel. Each zoom window is ideally placed upon the spectral line centre frequency, although the exact placement de-

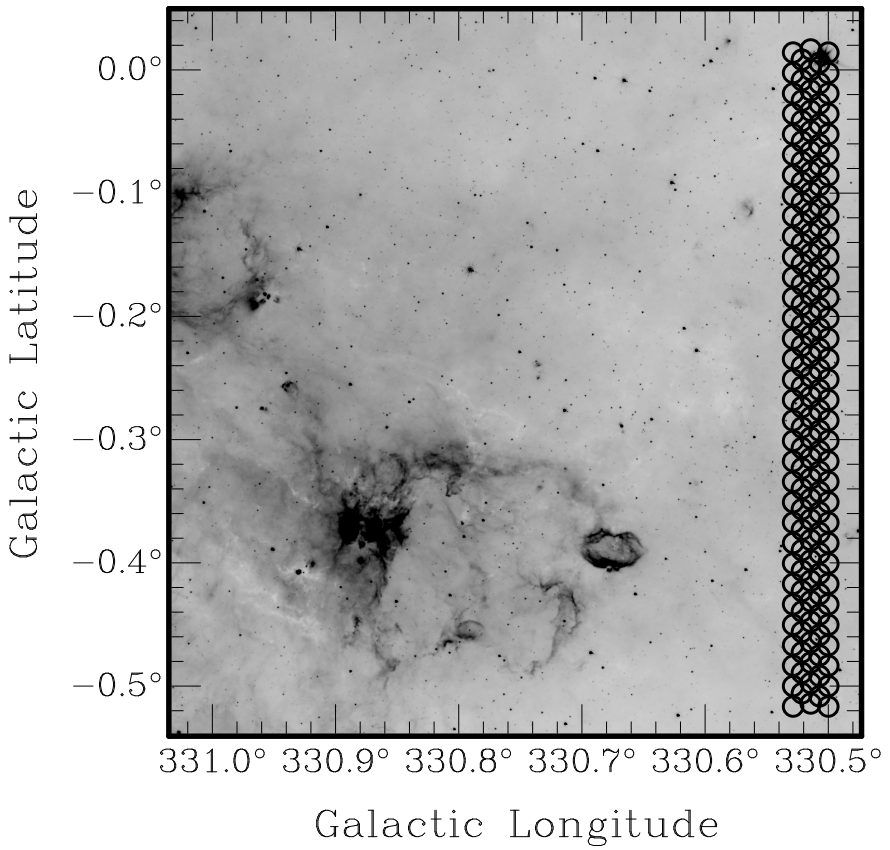

Figure 3.1: GLIMPSE 8.0 μm emission overlaid with part of a MALT-45 mosaic. Each circle represents the primary beam of the ATCA at 49.2 GHz, and is a pointing of the mosaic. Every quarter-square-degree region mapped by MALT-45 is built up of pointing 'rows' seen here. These five rows represent the start of the Galactic latitude scans for the G330.5−0.5 region. A similar mosaic is made for each region in Galactic longitude. When both Galactic latitude and longitude mosaics are combined, a fully Nyquist sampled map is obtained. Rows are classified as either 'long' or 'short'; in this figure, the three long rows have two short rows interleaved.

pends on the way the correlator distributes the zooms. Every zoom provides approximately 400 km s^{-1} of velocity coverage, and is detailed in Table 3.1.

3.2.2 Data reduction

Data reduction was undertaken in a similar manner to that of the MALT-45 pilot survey (Jordan et al. 2013). Unlike the pilot survey data reduction, the LiveData products were processed by more robust baselining using the ATNF Spectral line Analysis Package (ASAP). ASAP averages each of the antenna auto-correlations together before performing further baseline smoothing. ASAP then provides both XX and YY polarisation products, which are used by Gridzilla to create data cubes.

The average RMS noise levels were calculated for each data cube. The median values and their errors are listed in Table 3.1. Values are calculated by using the MIRIAD task imstat, which determines RMS values for each channel in a cube. The errors in the medians represent the standard deviation of all RMS values. RMS noise maps may be seen in Appendix A.1, Figs 1 through 6.

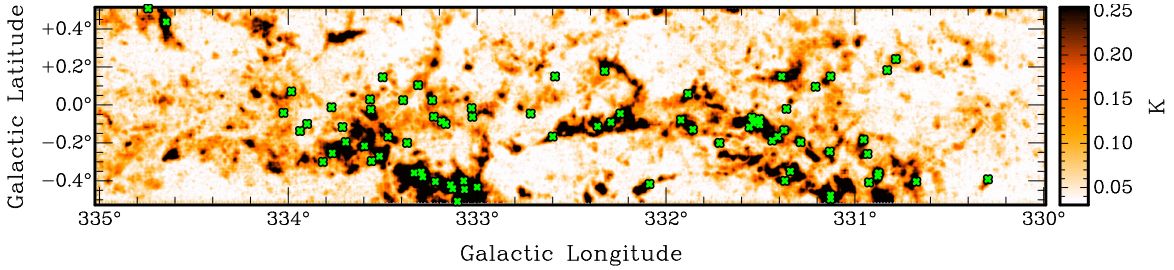

Figure 3.2: Auto-correlated CS (1–0) peak-intensity map overlaid with positions of detected class I CH_3OH masers (green cross symbols). A main-beam temperature of 0.1 K represents a 5σ peak of emission; note that the RMS of this image is less than that stated in Table 3.1 (10 mK vs. 34mK), because this image has been produced by binning channels into groups of 10.

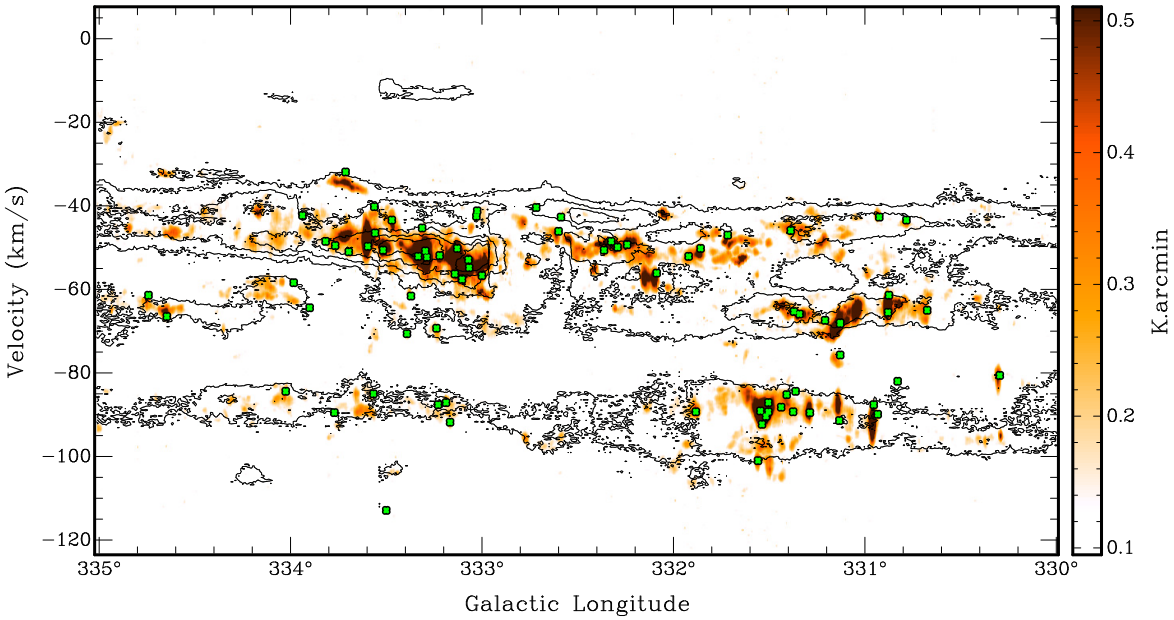

Figure 3.3: Integrated CS (1–0) emission from MALT-45 overlaid with CO contours from Barnes et al. (2015), presented as a *p-v* diagram. Contour levels are 90, 180, ..., 450 K arcmin in units of main-beam temperature, integrated over Galactic latitude. There is excellent agreement in regions of concentrated CO with CS emission. Green cross symbols represent MALT-45 class I CH_3OH masers, which generally occur in bright regions of CS; only 4 of the 77 masers (5 per cent) have a CS peak intensity less than 0.11 K ($\sim 3\sigma$) at their peak position.

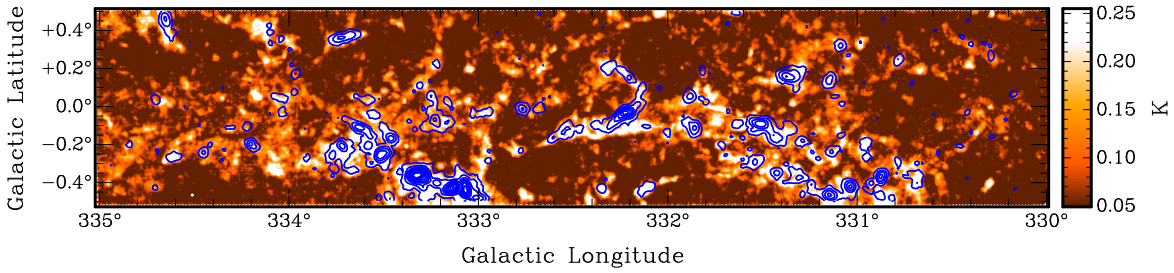

Figure 3.4: Auto-correlated CS (1–0) peak-intensity map overlaid with blue HOPS NH_3 (1,1) peak-signal-to-noise contours. Contour levels are 8, 18, ..., 88 per cent of 11.13 K in units of main-beam temperature. The white circle seen at G334.5−0.45 is the size of the beam.

3.3 Results

For this paper, auto-correlated data cubes were produced for CS (1–0), class I CH_3OH masers, each of the SiO (1–0) $v = 1, 2, 3$ maser lines and SiO (1–0) $v = 0$ thermal emission. Emission was detected in each data cube. The absolute scale of intensity calibration is not well established, and can be affected by systematic effects such as the bandpass subtraction. However, comparing the peak flux densities of MALT-45 class I methanol masers with Voronkov et al. (2014), we ascribe 20 per cent as the uncertainty of the intensities in MALT-45 data.

Class I CH_3OH masers detected in interferometry by Voronkov et al. (2014) were used to analyse the spatial offset from their masers to those detected by MALT-45 (discussion of detected class I CH_3OH masers is given in §3.3.2). Within the MALT-45 survey region, all 14 class I CH_3OH maser regions detected by Voronkov et al. (2014) were also detected by MALT-45. The masers detected in each survey were considered the same based on their angular spatial offset being within 20 arcsec. We compared the position of each MALT-45 maser with that of the corresponding maser in Voronkov et al. (2014) to derive a survey astrometric error. The median is 15 arcsec, and so we ascribe a 15 arcsec astrometric error to MALT-45.

3.3.1 CS (1–0) at 48.990 GHz

The most abundant isotopologue of CS ($^{12}C^{32}S$) was detected in extended emission across the entire survey region, as shown in Figs 3.2, 3.3 and 3.4. Also shown in Fig. 3.4 is NH_3 (1,1) emission, as detected in HOPS (Purcell et al. 2012). Bright CS emission is largely coincident with HOPS NH_3 (1,1) emission, but despite having a higher critical density, the CS appears to be more extended than the NH_3; this is discussed further in §3.4.1. A p-v plot reveals a few velocity components to the CS data, which trace the spiral arms of the Galaxy over the survey region; see Fig. 3.3.

$C^{34}S$ (1–0) at 48.20694 GHz is also detected across the survey region, but is not detailed in this paper due to an incomplete data reduction. However, a preliminary reduction has been conducted for analysis in §3.4.1. $C^{34}S$ data will be presented in future publications.

3.3.2 Class I CH_3OH 7(0,7)–6(1,6) A^+ masers at 44.069 GHz

Within the survey region, 77 class I CH_3OH masers were detected. Class I CH_3OH maser catalogues from Slysh et al. (1994); Val'tts et al. (2000); Ellingsen (2005); Chen et al. (2011) and Voronkov et al. (2014) were used to determine previously known masers. The published positions of class I CH_3OH masers were within 20 arcsec of MALT-45 detections, and all 19 previously known masers within the MALT-45 survey region were re-detected. Note that these articles report findings of 95 GHz class I CH_3OH masers, rather than 44 GHz masers (except Slysh et al. 1994); if a 44 GHz maser has not been reported in a position where a 95 GHz maser has been detected, we still deem this class I maser as a previously known detection. Therefore, 58 of the 77 detections are previously unknown (hereinafter new masers). A histogram of these populations can be seen in Fig. 3.5, revealing the number of new masers for various peak flux densities. Images showing the locations of class I CH_3OH masers with respect to thermal molecular gas are shown in Figs 3.2, 3.3 and 3.6. The properties of each class I

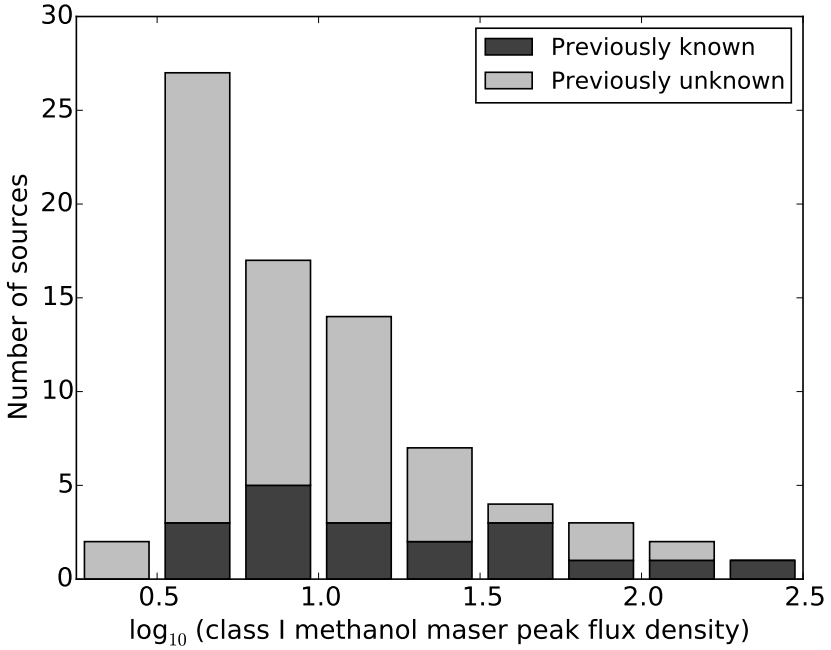

Figure 3.5: A stacked histogram of known and new class I CH_3OH maser peak flux densities. Previously known masers have a near even spread of flux densities, but the new MALT-45 population favours the weaker bins.

maser spectrum is classified in Table 3.2. Each un-smoothed maser spectrum can be seen in Appendix A.2, and a peak signal-to-noise map is presented in Appendix A.3.

Masers were identified by visual inspection of the data by analysing various binned versions of the cube, such as 0.4, 0.6, 0.8, 1.0 and 2.0 $\mathrm{km\,s^{-1}}$ bins. This is effective at highlighting weak but broad maser emission; see for example G330.83+0.18 in Appendix A.2. Any peak of emission exceeding 3σ in the various binned cubes with at least two adjacent channels of 2σ was considered for candidacy. The position of each maser reflects the brightest pixel within the neighbourhood of bright maser pixels. We compared the velocity of weaker maser candidates with CS and SiO $v = 0$ emission at the same location to strengthen their candidacy. In future work, we will re-observe each maser candidate to greater sensitivity and spatial resolution to confirm (or otherwise) its existence. The velocity range of each maser is determined by a 1.5σ cutoff in intensity from the peak velocity. As the channel resolution is approximately 0.2 $\mathrm{km\,s^{-1}}$, velocities are specified to 0.1 $\mathrm{km\,s^{-1}}$. All flux densities are specified with two significant figures. Intrinsic variation of masers along with calibration uncertainties place peak flux density errors within 20 per cent.

Using the program supplied by Reid et al. (2009), kinematic distances have been calculated and are included for each maser in Table 3.2. Parameters used for determining revised velocities and kinematic distances were taken from Green & McClure-Griffiths (2011), and the V_{LSR} uncertainty from Voronkov et al. (2014): $\Theta_0 = 246\,\mathrm{km\,s^{-1}}$, $R_\odot = 8.4\,\mathrm{kpc}$, $U_\odot = 11.1\,\mathrm{km\,s^{-1}}$, $V_\odot = 12.2\,\mathrm{km\,s^{-1}}$, $W_\odot = 7.25\,\mathrm{km\,s^{-1}}$, $U_s = 0\,\mathrm{km\,s^{-1}}$, $V_s = -15.0\,\mathrm{km\,s^{-1}}$, $W_s = 0\,\mathrm{km\,s^{-1}}$, $\sigma(V_{LSR}) = 3.32\,\mathrm{km\,s^{-1}}$. All distances are assumed to be kinematically 'near', unless the distance prescribed by Green & McClure-Griffiths (2011) is 'far'.

Table 3.2: Properties of detected MALT-45 class I CH_3OH maser emission. Each maser was detected within a 64 MHz zoom window. Column 1 lists the source name, derived from Galactic coordinates of the brightest peak. Columns 2 and 3 give the coordinates of the maser. Column 4 lists the source peak flux density. Column 5 lists the RMS noise level of the peak. Columns 6 and 7 list the velocity range of maser emission, within a 1.5σ cutoff. Column 8 lists the velocity at the peak. Column 9 lists kinematic distance calculated, based on position and peak velocity. Columns 10 and 11 list the errors for the kinematic distance. Columns 12 and 13 list the integrated intensity of CS (1–0) and SiO (1–0) $v = 0$ at the brightest peak. Column 14 gives additional remarks, mentioned in the footnotes[a]. Column 15 lists associations with other masers and EGOs, and is detailed in the footnotes[b]. Association is credited for any presence within 60 arcsec of the class I CH_3OH maser peak position. All velocities are specified to $0.1\,km\,s^{-1}$, and all flux densities are specified to two significant figures. Kinematic distances are derived using the kinematic distance model of Reid et al. (2009). All distances are assumed to be kinematically 'near', unless labelled otherwise.

Source name	RA (J2000) (h m s)	Dec. (J2000) (° ′ ″)	Peak flux density (Jy)	RMS noise level	Velocity Min. ($km\,s^{-1}$)	Velocity Max. ($km\,s^{-1}$)	Velocity Peak ($km\,s^{-1}$)	Kinematic distance (kpc)	Distance error (kpc)		Integrated intensity ($K\,km\,s^{-1}$) CS	Integrated intensity ($K\,km\,s^{-1}$) SiO	Remarks[a]	Other masers and EGOs[b]
G330.30−0.39	16 07 37.8	−52 30 52.1	4.4	4.9	−80.8	−79.5	−80.6	4.90	0.16	−0.16	3.1			W
G330.67−0.40	16 09 31.2	−52 16 03.9	5.3	5.6	−65.9	−64.6	−65.0	4.16	0.15	−0.15	2.5			
G330.78+0.24	16 07 12.8	−51 43 03.4	3.7	4.3	−43.8	−43.1	−43.4	3.12	0.17	−0.17	1.2			
G330.83+0.18	16 07 41.1	−51 43 48.0	3.1	3.8	−82.3	−79.7	−82.0	4.95	0.16	−0.16				
G330.87−0.36	16 10 16.6	−52 05 54.3	10	15	−67.0	−58.0	−61.4	4.00	0.15	−0.16	8.0	0.42	C	
G330.88−0.38	16 10 22.3	−52 06 28.1	7.8	10	−67.4	−58.0	−65.5	4.19	0.15	−0.15	8.6	0.56	C	MWSCG
G330.92−0.41	16 10 44.3	−52 06 04.0	28	33	−44.0	−41.0	−42.7	3.09	0.17	−0.17	1.4			
G330.93−0.26	16 10 06.9	−51 59 07.3	5.0	5.9	−91.4	−89.3	−89.9	5.33	0.17	−0.16	1.4			
G330.95−0.18	16 09 53.1	−51 54 57.9	4.0	4.7	−94.8	−86.7	−87.6	5.21	0.16	−0.16	9.6	1.4		MWCG
G331.13−0.48	16 12 00.3	−52 00 38.5	5.6	7.5	−69.1	−66.7	−68.0	4.30	0.15	−0.15	5.3	0.15		
G331.13−0.50	16 12 05.9	−52 01 33.3	8.6	11	−68.7	−67.8	−68.2	4.31	0.15	−0.15	4.5			
G331.13−0.25	16 11 00.7	−51 50 24.8	71	88	−92.9	−82.5	−91.4	5.39	0.17	−0.16	4.4	0.49	SVE	MWCG
G331.13+0.15	16 09 15.5	−51 33 08.1	68	60	−79.1	−74.6	−75.7	4.65	0.15	−0.15	1.2			MW
G331.21+0.10	16 09 52.2	−51 32 18.6	3.5	3.3	−67.8	−67.0	−67.4	4.27	0.15	−0.15				
G331.29−0.20	16 11 31.3	−51 41 54.8	15	20	−95.7	−85.0	−89.5	5.29	0.16	−0.16	3.7	0.17		MWC
G331.34−0.35	16 12 27.4	−51 46 26.9	32	37	−67.2	−65.0	−65.9	4.21	0.15	−0.15	2.1		SVE	MWCG
G331.36−0.02	16 11 06.4	−51 31 09.7	4.7	5.8	−84.6	−84.2	−84.4	5.05	0.16	−0.15				
G331.37−0.40	16 12 48.9	−51 47 26.2	5.9	7.3	−65.9	−65.0	−65.3	4.18	0.15	−0.15	1.6		C	G
G331.37−0.13	16 11 39.5	−51 35 35.3	3.7	4.5	−89.5	−88.8	−89.3	5.28	0.16	−0.16	1.6			
G331.39+0.15	16 10 28.7	−51 22 37.6	6.5	5.8	−46.5	−45.5	−45.9	3.26	0.16	−0.17	2.5	0.19		
G331.41−0.17	16 11 57.8	−51 35 40.6	4.9	6.6	−86.3	−84.8	−85.2	5.08	0.16	−0.15	2.7			
G331.44−0.19	16 12 11.4	−51 35 24.1	14	18	−92.5	−86.3	−88.2	9.53	0.16	−0.16	2.3	0.25	VF	MWC
G331.50−0.08	16 12 00.6	−51 27 44.3	38	49	−92.7	−86.7	−89.3	5.27	0.16	−0.16	4.1	0.14	P3	
G331.50−0.10	16 12 08.2	−51 29 01.0	11	14	−101.8	−86.1	−87.1	5.17	0.16	−0.15	6.5	0.31		WSC
G331.52−0.08	16 12 06.3	−51 27 35.5	20	18	−94.0	−88.0	−90.4	5.33	0.16	−0.16	5.8	0.13	P1	
G331.54−0.10	16 12 15.4	−51 27 17.1	77	77	−94.2	−89.1	−92.3	5.42	0.17	−0.16	7.4	0.29	P2	
G331.55−0.07	16 12 10.1	−51 25 39.9	4.9	5.3	−92.9	−86.3	−89.1	5.26	0.16	−0.16	4.9	0.15		MC

Table 3.2: *continued*

Source name	RA (J2000) (h m s)	Dec. (J2000) (° ′ ″)	Peak flux density (Jy)	RMS noise level	Velocity Min. (km s^{-1})	Velocity Max. (km s^{-1})	Peak	Kinematic distance (kpc)	Distance error (kpc)		Integrated intensity (K km s^{-1})		Remarks[a]	Other masers and EGOs[b]
											CS	SiO		
G331.56−0.12	16 12 26.8	−51 27 20.4	14	16	−104.8	−98.2	−101.0	5.87	0.19	−0.18	2.9			MWC
G331.72−0.20	16 13 33.1	−51 24 28.0	4.1	3.8	−47.2	−46.8	−47.0	3.32	0.16	−0.17	2.0			
G331.86−0.13	16 13 54.0	−51 15 32.1	5.6	6.5	−51.4	−49.5	−50.2	3.48	0.16	−0.16	2.6	0.44		
G331.88+0.06	16 13 11.6	−51 06 19.8	10	13	−90.1	−85.9	−89.3	5.26	0.16	−0.15	2.4	0.45		
G331.92−0.08	16 13 58.2	−51 10 46.7	5.8	6.4	−52.7	−51.6	−52.1	3.57	0.16	−0.16	1.5			
G332.09−0.42	16 16 13.7	−51 18 30.7	17	21	−59.5	−55.5	−56.1	3.76	0.15	−0.16	3.6			MW
G332.24−0.05	16 15 18.1	−50 56 03.2	140	180	−51.2	−45.9	−49.3	3.44	0.16	−0.16	3.4	0.32		
G332.30−0.09	16 15 43.9	−50 55 57.8	41	37	−52.5	−45.9	−49.9	3.47	0.16	−0.16	3.0		VE	MWG
G332.32+0.18	16 14 42.0	−50 42 50.2	9.3	11	−51.0	−48.0	−48.5	3.40	0.16	−0.16	1.2			W
G332.36−0.11	16 16 08.8	−50 53 55.2	9.8	12	−51.2	−49.9	−50.6	3.51	0.16	−0.16	1.7		C	MWCG
G332.59+0.15	16 16 01.3	−50 33 12.6	3.4	4.0	−43.6	−42.5	−42.7	11.79	0.17	−0.17			CF	MG
G332.60−0.17	16 17 28.1	−50 46 21.2	15	18	−47.6	−45.5	−46.1	3.29	0.16	−0.17	2.2		V	MWG
G332.72−0.05	16 17 27.9	−50 36 16.5	6.4	7.3	−41.0	−39.1	−40.4	3.01	0.17	−0.17				
G333.00−0.43	16 20 27.1	−50 40 58.3	6.6	9.8	−57.2	−56.1	−56.7	3.80	0.15	−0.15	4.8			W
G333.02−0.06	16 18 55.5	−50 24 04.3	6.8	7.9	−41.7	−39.7	−41.2	3.06	0.17	−0.17	1.2		E	MW
G333.03−0.02	16 18 44.6	−50 21 56.0	5.6	7.0	−42.9	−42.1	−42.5	3.12	0.17	−0.17				M
G333.07−0.44	16 20 48.4	−50 38 41.3	2.7	3.2	−55.3	−54.8	−54.8	3.72	0.15	−0.16	6.5	0.20		MW
G333.07−0.40	16 20 37.3	−50 36 33.5	4.1	4.6	−54.4	−52.7	−52.9	3.63	0.15	−0.16	4.2	0.21		
G333.10−0.51	16 21 15.1	−50 39 45.6	14	8.1	−58.9	−57.0	−57.6	3.85	0.15	−0.15	4.2			M
G333.13−0.44	16 21 04.0	−50 35 52.0	120	150	−57.2	−45.5	−50.2	3.50	0.16	−0.16	11	0.64	SVE P2	MWC
G333.14−0.42	16 21 01.8	−50 34 27.1	16	18	−56.7	−45.9	−56.3	3.79	0.15	−0.15	10	0.51	P1	W
G333.16−0.10	16 19 43.4	−50 19 43.0	5.6	7.7	−92.9	−91.2	−91.8	5.33	0.15	−0.14	1.3		E	M
G333.18−0.09	16 19 45.7	−50 18 18.3	5.6	7.1	−88.4	−85.7	−87.1	5.13	0.14	−0.14	1.7		E	MG
G333.22−0.40	16 21 18.6	−50 30 23.5	17	19	−55.3	−51.0	−51.9	3.59	0.15	−0.16	2.7			
G333.23−0.06	16 19 50.3	−50 15 28.9	250	310	−92.3	−84.4	−87.6	5.15	0.14	−0.14	1.0	0.25	SVE	MWSC
G333.24+0.02	16 19 29.5	−50 11 23.5	3.9	5.4	−69.5	−67.8	−69.3	4.37	0.14	−0.14	1.4			
G333.29−0.38	16 21 29.7	−50 26 30.3	5.4	6.3	−53.6	−50.6	−52.3	3.61	0.15	−0.16	11	0.27		
G333.30−0.35	16 21 25.3	−50 25 05.4	3.5	3.6	−53.1	−49.5	−50.8	3.54	0.16	−0.16	9.8	0.18		
G333.31+0.10	16 19 28.7	−50 04 50.9	7.7	13	−50.6	−43.8	−45.3	11.74	0.17	−0.16	2.1	0.12	ECF	MWG
G333.33−0.36	16 21 36.4	−50 23 40.6	22	22	−53.8	−49.5	−52.1	3.60	0.15	−0.16	6.0	0.27		
G333.37−0.20	16 21 04.4	−50 15 21.6	13	16	−62.3	−57.6	−61.6	4.03	0.15	−0.15				W
G333.39+0.02	16 20 10.6	−50 04 53.7	4.1	6.5	−72.9	−69.7	−70.6	10.60	0.14	−0.14			F	MWC
G333.47−0.16	16 21 22.1	−50 09 42.5	21	23	−46.1	−41.4	−43.4	3.18	0.16	−0.17	3.6		E	MWCG
G333.50+0.15	16 20 07.6	−49 55 10.1	3.5	5.9	−114.4	−112.0	−112.9	6.35	0.21	−0.19				
G333.52−0.27	16 22 01.9	−50 12 11.2	6.4	8.7	−51.2	−50.2	−50.6	3.53	0.16	−0.16	3.5			
G333.56−0.30	16 22 19.6	−50 11 28.6	7.8	11	−48.0	−45.9	−46.5	3.33	0.16	−0.17	2.4			
G333.56−0.02	16 21 09.0	−49 59 48.3	54	63	−41.7	−39.1	−40.2	12.02	0.17	−0.17	1.8		EF	M

Table 3.2: *continued*

Source name	RA (J2000) (h m s)	Dec. (J2000) (° ′ ″)	Peak flux density (Jy)	RMS noise level	Velocity Min.	Velocity Max. (km s^{-1})	Velocity Peak	Kinematic distance (kpc)	Distance error (kpc)		Integrated intensity (K km s^{-1}) CS	Integrated intensity (K km s^{-1}) SiO	Remarks[a]	Other masers and EGOs[b]
G333.57+0.03	16 20 55.9	−49 57 19.4	6.2	6.4	−85.7	−84.8	−85.0	5.04	0.14	−0.14	0.95			
G333.59−0.21	16 22 08.5	−50 06 31.7	26	34	−51.2	−47.6	−49.7	3.49	0.16	−0.16	11	0.31	SV	WSC
G333.70−0.20	16 22 29.4	−50 01 23.8	4.4	6.1	−51.2	−50.8	−51.0	3.55	0.16	−0.16	2.4			
G333.71−0.12	16 22 12.8	−49 57 20.1	6.6	6.9	−32.3	−31.2	−31.9	2.58	0.18	−0.19				
G333.77−0.01	16 22 00.7	−49 50 26.5	16	20	−90.5	−88.8	−89.5	5.22	0.14	−0.14	2.3			
G333.77−0.25	16 23 03.5	−50 00 51.0	6.4	8.0	−50.2	−49.3	−49.5	3.49	0.16	−0.16	2.4	0.12		
G333.82−0.30	16 23 28.8	−50 00 39.2	19	24	−49.5	−47.8	−48.5	3.44	0.16	−0.16	1.3			
G333.90−0.10	16 22 57.7	−49 48 39.2	3.4	4.1	−65.3	−62.9	−64.4	10.92	0.15	−0.14			F	M
G333.94−0.14	16 23 17.4	−49 48 38.4	4.6	4.9	−43.1	−42.3	−42.3	3.14	0.17	−0.17				MW
G333.98+0.07	16 22 34.6	−49 37 52.8	4.5	5.7	−60.8	−58.0	−58.4	3.90	0.15	−0.15				
G334.03−0.04	16 23 15.0	−49 40 51.7	11	14	−84.8	−84.0	−84.4	5.01	0.14	−0.14	2.0			
G334.64+0.44	16 23 50.4	−48 54 08.7	5.7	6.4	−67.2	−66.5	−66.5	4.27	0.14	−0.14	2.2			
G334.74+0.51	16 23 56.6	−48 47 03.7	18	6.7	−65.5	−61.4	−61.4	4.05	0.14	−0.15	1.1	0.17		

[a]S - 44 GHz detection from Slysh et al. (1994); V - 95 GHz detection from Val'tts et al. (2000); E - 95 GHz detection from Ellingsen (2005); C - 95 GHz detection from Chen et al. (2011); P - indicates a blended spectrum of emission. P1 contains a strong peak of emission at a spatially distinct position, with a different velocity to nearby strong masers (but not as strong as the neighbour), P2 is the strong neighbour, and P3 is the next strongest neighbour; F - this maser has been labelled as being kinematically 'far', due to a class II CH_3OH maser being labeled as such by Green & McClure-Griffiths (2011). Note that a source without a S, V, E or C remark is a new detection.

[b]M - presence of a 6.7 GHz class II methanol maser (Caswell et al. 2011); W - presence of a 22 GHz H_2O maser (Walsh et al. 2011, 2014; Breen et al. 2010a); G - presence of an EGO classified by Cyganowski et al. (2008); S - presence of a 1612 OH maser (Sevenster et al. 1997); C - presence of a 1665 or 1667 MHz OH maser (Caswell 1998).

Table 3.3: Properties of detected MALT-45 SiO (1–0) maser emission. Each maser was detected within a 64 MHz zoom window. Column 1 lists the source name, derived from Galactic coordinates of the brightest peak. Columns 2 and 3 give the coordinates of the maser. Columns 4 through 15 are categorised into $v = 1$, $v = 2$ and $v = 3$. For each category, there are four columns, listing the peak flux density within this vibrational mode (if detected), and the minimum, maximum and peak velocities. Column 16 lists the RMS noise level, which indicates the most statistically significant maser peak detected among the three modes. Column 17 lists the kinematic distance calculated, based on position and peak velocity. Columns 18 and 19 list the errors for the kinematic distance. Column 20 gives additional remarks, clarified in the footnotes[a]. If data are not available in one of the lines for a source, it was not detected by MALT-45. Velocity ranges (between minimum and maximum) are determined by a 1.5σ cutoff. All velocities are specified to 0.1 km s^{-1}, and all flux densities are specified to two significant figures. Association is credited if the source position is within 30 arcsec of the peak SiO maser position. Kinematic distances are derived using the kinematic distance model of Reid et al. (2009). All distances are assumed to be kinematically 'near', except for G330.14−0.39, G331.08+0.17, G332.40−0.33 and G334.20+0.22; when assumed to be near, unphysical distances and errors are generated.

Source name	RA (J2000) (h m s)	Dec. (J2000) (° ′ ″)	SiO $v = 1$ properties				SiO $v = 2$ properties				SiO $v = 3$ properties				RMS noise level	Kinematic distance (kpc)	Distance error (kpc)		Remarks[a]
			Peak flux density (Jy)	Velocity Min.	Velocity Max. (km s^{-1})	Peak	Peak flux density (Jy)	Velocity Min.	Velocity Max. (km s^{-1})	Peak	Peak flux density (Jy)	Velocity Min.	Velocity Max. (km s^{-1})	Peak					
G330.12−0.31	16 06 24.3	−52 34 33.5					3.5	−65.8	−61.2	−61.4					4.8	3.46	0.23	−0.23	
G330.14−0.39	16 06 52.6	−52 37 04.9	6.3	−2.6	4.5	3.5	7.5	−3.0	5.5	3.6					11	5.05	0.45	−0.41	W
G330.47+0.03	16 06 36.7	−52 05 15.6	23	−59.5	−48.3	−53.7	13	−59.7	−51.6	−54.4	2.5	−56	−52.7	−53.8	26	3.12	0.24	−0.24	W
G330.51+0.01	16 06 53.2	−52 04 19.6	11	−13.7	−9.8	−12.2	19	−15.5	−10.2	−12.8					19	0.76	0.34	−0.36	
G330.55+0.15	16 06 28.1	−51 56 41.6	4.0	−68.7	−67.8	−68.0	2.7	−69.7	−68	−69.3					4.9	3.80	0.22	−0.23	
G330.75+0.20	16 07 15.2	−51 46 25.6	2.9	−66.1	−65.2	−65.8	2.7	−64.0	−67.1	−63.8					3.8	3.63	0.22	−0.23	
G330.85−0.44	16 10 29.3	−52 10 34.9	3.4	−32.0	−30.7	−31.7									4.3	1.98	0.28	−0.29	W
G331.08+0.17	16 08 55.8	−51 34 14.6	4.9	−6.1	−3.9	−5.2	3.8	−6.9	−3.7	−5.8					7.3	4.45	0.40	−0.37	
G331.13−0.27	16 11 06.2	−51 51 19.7	4.6	−31.5	−30.0	−30.7	4.7	−32.1	−30.3	−31.0					7.7	1.94	0.28	−0.29	
G331.21+0.25	16 09 10.8	−51 25 19.1	2.9	−36.7	−34.6	−36.1	3.0	−37.1	−36.0	−36.3					4.4	2.24	0.27	−0.28	
G331.24−0.02	16 10 32.2	−51 36 05.6	2.7	−90.0	−89.1	−89.1									3.2	4.69	0.22	−0.21	
G331.48−0.03	16 11 43.7	−51 26 46.0	7.0	−69.5	−66.3	−68.0	5.7	−69.7	−62.9	−68.4					9.1	3.80	0.22	−0.22	
G331.58+0.07	16 11 44.5	−51 18 06.2	2.7	−33.7	−32.4	−32.8									3.4	2.06	0.28	−0.29	
G331.60−0.14	16 12 42.8	−51 26 42.7	2.8	−96.5	−93.9	−95.6	7.8	−97.3	−94.0	−96.0	2.7	−96.3	−94.6	−95.9	9.9	4.98	0.22	−0.21	CS
G331.65−0.25	16 13 28.8	−51 29 34.6	4.4	−38.3	−34.8	−36.5	3.5	−39.1	−35.4	−36.5					5.7	2.27	0.27	−0.28	S
G331.70−0.03	16 12 43.5	−51 17 20.4	3.1	−26.1	−25.2	−25.4	1.7	−25.5	−24.7	−25.3					3.6	1.63	0.30	−0.31	
G331.72+0.45	16 10 43.2	−50 55 38.7	4.2	18.9	21.1	20.0	3.6	18.2	21.3	19.8					4.9	6.97	0.62	−0.57	S
G331.76−0.33	16 14 19.0	−51 28 22.3	28	−36.1	−23.9	−29.1	24	−34.1	−24.2	−29.7	3.6	−30.4	−24.5	−25.6	40	1.79	0.29	−0.30	W
G331.95+0.08	16 13 23.5	−51 02 50.8	2.8	−102.8	−98.4	−101.9	2.5	−99.7	−102.5	−99.7					4.2	5.19	0.22	−0.21	
G331.96−0.24	16 14 52.6	−51 16 07.2	3.0	−81.5	−80.2	−80.8									3.9	4.35	0.21	−0.21	W
G331.99−0.04	16 14 05.7	−51 06 12.7	2.9	−99.1	−97.1	−98.0	2.8	−98.2	−98.6	−98.2					3.9	5.07	0.21	−0.21	
G332.14−0.51	16 16 52.0	−51 20 23.1	5.1	−36.7	−35.2	−36.5	6.9	−36.9	−35.4	−36.3					4.5	2.28	0.27	−0.28	
G332.22+0.36	16 13 25.5	−50 39 30.7	3.4	−121.2	−120.6	−121.0	2.1	−122.2	−122.7	−122.2					4.4	6.17	0.32	−0.27	
G332.30+0.44	16 13 27.9	−50 32 16.3	6.2	−56.3	−54.1	−55.4	3.6	−56.4	−54.4	−55.3					8.4	3.24	0.23	−0.24	
G332.40−0.33	16 17 16.5	−51 01 21.2					2.7	−7.4	−5.0	−5.6					3.8	4.61	0.41	−0.38	
G332.83+0.19	16 16 57.1	−50 21 10.2	4.8	−34.3	−31.7	−33.7									5.1	2.15	0.27	−0.29	
G332.90−0.37	16 19 41.3	−50 42 31.2	2.2	−102.1	−99.7	−101.0	3.4	−101.7	−102.5	−101.7					4.9	5.20	0.21	−0.20	
G333.06−0.10	16 19 14.4	−50 24 16.6	4.4	−48.9	−43.3	−45.4	6.8	−48.5	−43.7	−45.7					9.5	2.79	0.25	−0.26	W
G333.44−0.07	16 20 49.1	−50 06 52.0	3.3	−96.9	−95.4	−96.3	2.7	−97.1	−98.6	−97.1					4.2	5.00	0.20	−0.20	
G333.46−0.34	16 22 06.3	−50 17 29.4	4.3	−63.0	−56.7	−58.5	4.3	−64.7	−58.6	−64.3					5.4	3.55	0.22	−0.23	
G333.53+0.41	16 19 06.9	−49 42 21.9	3.3	−145.1	−144.7	−144.9									4.0	7.52	0.77	−0.77	
G333.60−0.49	16 23 21.6	−50 18 09.7	4.1	−16.1	−15.0	−15.7	3.0	−16.3	−15.7	−15.9					4.8	1.06	0.34	−0.36	
G333.64−0.37	16 22 59.3	−50 11 06.3	4.1	−70.6	−67.8	−69.5	4.5	−70.8	−69.1	−70.2					6.3	3.93	0.21	−0.21	W

Table 3.3: *continued*

Source name	RA (J2000) (h m s)	Dec. (J2000) (° ′ ″)	SiO $v = 1$ properties				SiO $v = 2$ properties				SiO $v = 3$ properties				RMS noise level	Kinematic distance (kpc)	Distance error (kpc)		Remarks[a]
			Peak flux density (Jy)	Velocity Min.	Velocity Max. ($km\,s^{-1}$)	Peak	Peak flux density (Jy)	Velocity Min.	Velocity Max. ($km\,s^{-1}$)	Peak	Peak flux density (Jy)	Velocity Min.	Velocity Max. ($km\,s^{-1}$)	Peak					
G333.72−0.39	16 23 25.8	−50 08 36.6	5.2	−44.3	−40.4	−43.3	5.0	−45.7	−41.5	−43.5					7.1	2.71	0.25	−0.26	
G333.78−0.36	16 23 35.6	−50 04 53.2	2.1	−93.4	−92.1	−92.4	1.6	−93.1	−92.7	−92.9					3.1	4.85	0.20	−0.20	
G333.90−0.09	16 22 56.6	−49 48 07.4	3.8	−126.0	−123.2	−123.9	4.0	−123.8	−122.9	−123.1					4.5	6.12	0.26	−0.23	S
G334.01−0.02	16 23 06.3	−49 40 30.9	3.3	−94.3	−93.0	−93.4	3.3	−95.5	−93.6	−93.8					3.9	4.89	0.19	−0.19	
G334.11−0.37	16 25 05.0	−49 50 58.6	3.9	−32.8	−30.9	−31.5									4.7	2.08	0.28	−0.30	
G334.20+0.22	16 22 49.6	−49 22 18.8	2.7	−7.4	−7.0	−7.2	2.8	−5.2	−7.4	−5.2					4.4	4.78	0.42	−0.39	
G334.35−0.36	16 26 03.3	−49 40 15.0	3.2	−22.8	−21.5	−22.6									4.1	1.54	0.31	−0.33	
G334.35+0.06	16 24 13.2	−49 22 24.8	3.8	−82.6	−81.9	−82.1									3.8	4.44	0.20	−0.20	
G334.41+0.22	16 23 44.6	−49 13 15.1	3.9	−32.8	−31.7	−32.2	3.0	−32.5	−32.1	−32.3					4.7	2.13	0.28	−0.30	
G334.49−0.37	16 26 41.1	−49 34 40.5	3.8	−9.8	−8.5	−9.1	2.7	−10.2	−8.9	−10.0					4.7	0.62	0.38	−0.41	
G334.61−0.43	16 27 29.9	−49 32 14.1	5.0	−139.5	−138.2	−138.8	3.3	−139.7	−138.9	−139.3					5.7	6.97	0.36	−0.36	
G334.68+0.44	16 23 57.9	−48 52 53.8	3.6	−96.9	−95.2	−95.2									3.8	4.96	0.19	−0.19	
G334.68+0.35	16 24 22.8	−48 56 34.8	4.0	−55.6	−55.2	−55.2	2.6	−55.9	−56.4	−55.9					4.4	3.34	0.23	−0.23	
G334.68+0.13	16 25 20.5	−49 05 30.2	5.1	−94.5	−89.1	−91.1	2.2	−93.4	−91.8	−92.5					6.1	4.83	0.19	−0.19	W

[a]C - presence of a 1665 MHz OH maser from Caswell (1998); S - presence of a 1612 MHz OH maser from Sevenster et al. (1997); W - presence of a H_2O maser from Walsh et al. (2011, 2014).

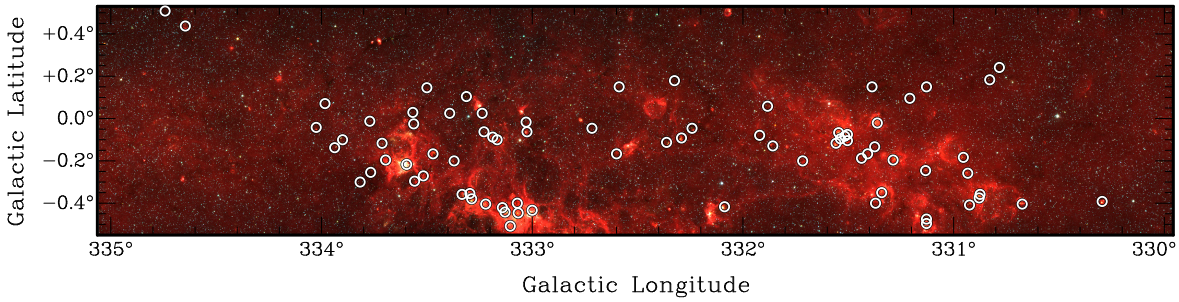

Figure 3.6: *Spitzer* GLIMPSE 3-colour (RGB = 3.6, 4.5 and 8.0 μm) image with MALT-45 positions of class I CH_3OH masers (circle symbols).

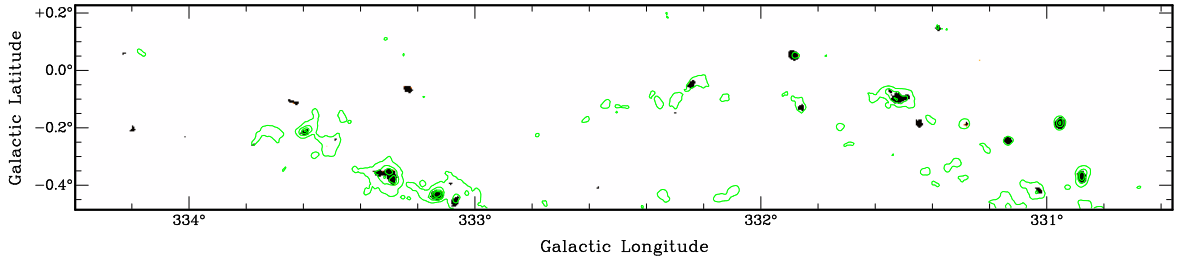

Figure 3.7: Auto-correlated map of SiO (1–0) $v = 0$ shown in greyscale, overlaid with CS (1–0) thermal emission contours. This image shows SiO emission at and above 0.04 K ($\sim$1.5σ). Contour levels are 14, 34, ..., 74 per cent of 2.62 K. The lowest contour corresponds to 10.8σ.

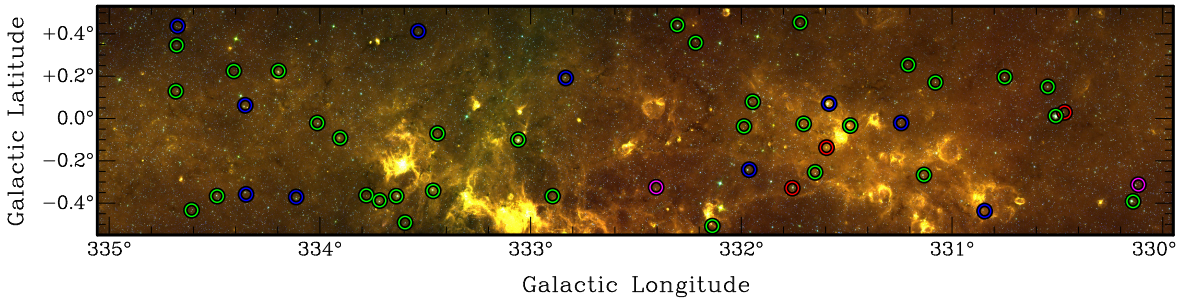

Figure 3.8: *Spitzer* GLIMPSE 3-colour (RGB = 3.6, 5.8 and 8.0 μm) image with MALT-45 positions of detected SiO (1–0) $v = 1, 2, 3$ masers (circle symbols). The circles have been colour-coded by the vibrational modes within each region. Red: region containing $v = 1, 2, 3$ maser emission; green: $v = 1, 2$; blue: $v = 1$; magenta: $v = 2$. The GLIMPSE bands presented here were chosen to help reveal evolved stars.

The positions of class I CH_3OH masers have been compared with the published positions of class II CH_3OH, H_2O and OH masers to establish associations. When considering the maximum distance between masers that still constitute an association, we use 60 arcsec from the class I position as suitable for defining associations. An analysis of the velocities of these masers finds that their velocities are similar (within 10 km s^{-1}), so the spatial offset alone is robust at identifying associations, at least within the MALT-45 survey region. Csengeri et al. (2014) analysed a large distribution of clumps associated with HMSF in their source sample, and find that all clumps have effective radii within 55 arcsec. Additionally, we note that increasing the maximum offset beyond 60 arcsec does not increase the number of unique associations. These findings suggest for our purposes that 60 arcsec is sufficient to group

masers within a single star-forming region. We have chosen not to define an association based on source distance or size, as it is difficult to implement across a wide range of objects, kinematic distances may be erroneous, and maser geometry may be wide-spread. An angle of 60 arcsec on the sky corresponds to approximately 1.5 pc at a distance of 5 kpc.

There are two targets where the spread of class I CH_3OH maser emission is large and these have been considered as two separate maser regions. The weaker masers (G331.52−0.08 and G333.14−0.42) near to each of these bright masers (G331.50−0.08 and G333.13−0.44) possess a distinct spectral velocity component and are sufficiently spatially offset to be considered a different site (54 and 87 arcsec, respectively). See the spectra in Appendix A.2. These sources are marked with a 'P' in Table 3.2.

Integrated intensity values for CS and SiO $v = 0$ have been included for each maser, where possible, in Table 3.2. Emission was integrated $\pm 10\,\mathrm{km\,s^{-1}}$ from the peak velocity of the maser. Values were not included if the emission was not significant ($<3\sigma$).

3.3.3 SiO (1–0) $v = 0$ thermal emission at 43.424 GHz

Extended SiO $v = 0$ emission is detected in some regions, as shown in Fig. 3.7, which shows that SiO $v = 0$ emission tends to be associated with bright peaks of CS emission. Note that emission from the SiO $v = 0$ is typically weaker than for CS, hence the signal-to-noise is lower for this transition; Fig. 3.7 shows all emission above 1.5σ. Discussion on the relation between class I CH_3OH masers and SiO $v = 0$ emission is contained in §3.4.3.

3.3.4 SiO (1–0) $v = 1, 2, 3$ masers at 43.122, 42.820 and 42.519 GHz

The vibrationally excited SiO (1–0) lines were detected towards 47 regions, as shown in Fig. 3.8. The properties of each maser region are classified in Table 3.3. The search procedure for SiO masers was the same as with CH_3OH masers; they were identified by visual inspection of the data, and had velocities categorised by a 1.5σ cutoff from the peak velocity. Velocities are specified to $0.1\,\mathrm{km\,s^{-1}}$, and flux densities to two significant figures. Many masers have low signal-to-noise values, but are considered real detections based on their association in GLIMPSE, and simultaneous detection of emission in another SiO maser transition. The positions of SiO masers have been compared with OH and H_2O masers; see Table 3.3 and §3.4.7. CH_3OH maser species were searched at these positions, but none were found, implying that any class I CH_3OH maser emission associated with the SiO masers has a peak flux density <4.5 Jy. Peak intensity maps are presented in Appendix A.3, and each un-smoothed maser spectrum can be seen in Appendix A.4.

Fig. 3.8 shows the locations of SiO masers detected by MALT-45 with respect to infrared emission from GLIMPSE. All SiO masers are detected towards point-like, isolated regions that appear to arise from evolved stars, based on their infrared colours and lack of obvious associations with star formation, such as IRDCs or extended infrared emission. Fig. 3.9 shows the relative locations of three SiO masers compared to infrared stars; these masers were chosen as they show various colours of infrared stars towards all SiO masers. It can be seen that the maser locations are not identical to the stars, but are within one beam. Therefore, we cannot conclusively argue that each SiO maser site is coincident with an evolved star, although the

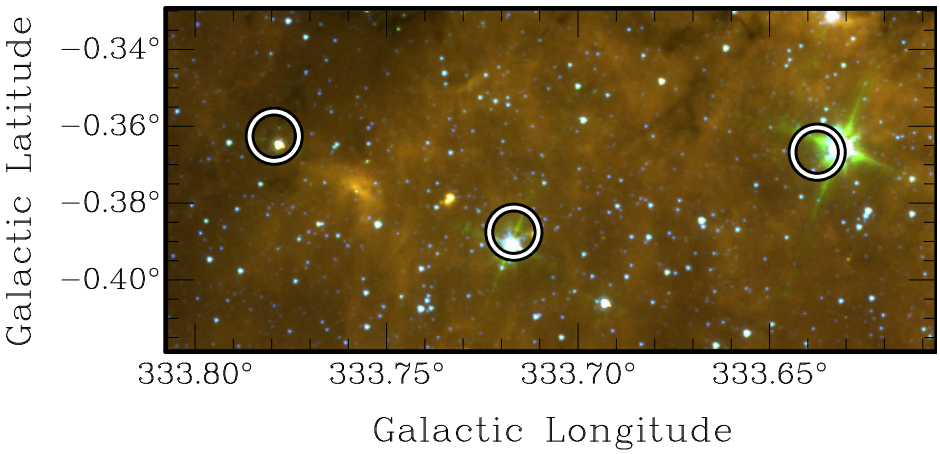

Figure 3.9: *Spitzer* GLIMPSE 3-colour (RGB = 3.6, 5.8 and 8.0 μm) image with examples of detected SiO masers towards infrared stars. Circles are centred on the peak position of maser emission, and are beam sized (≈1 arcmin). All three of these SiO maser regions contain the $v = 1$ and $v = 2$ lines, but all other maser region variants have similar infrared colours.

evidence we have suggests this is the case. Further higher spatial resolution observations of the maser sites will be able to demonstrate conclusively whether or not each SiO maser is associated with an evolved star.

Of the 47 SiO maser regions, 45 contain $v = 1$ emission, 37 contain $v = 2$, and only 3 have $v = 3$ emission. We have found no previously published data for any of these SiO masers and consider them all to be new detections. Some SiO maser regions have greater $v = 2$ emission than $v = 1$, and two have no detected emission $v = 1$; this is discussed further in §3.4.7. There are also 12 SiO maser regions with an associated OH or H_2O maser; see §3.4.7.

Parameters used in determining kinematic distances are the same as those found in §3.3.2, except for a more generous velocity uncertainty $\sigma(V_{LSR}) = 5.0\,\mathrm{km\,s^{-1}}$, and $V_s = 0\,\mathrm{km\,s^{-1}}$. Four masers are labelled at the far kinematic distance, because the position and errors for a near distance are unrealistic; see Table 3.3.

3.3.5 Survey completeness

By analysing the RMS noise values per pixel distributed across the MALT-45 region, we find that the noise levels may vary by up to a factor of three due to some data being flagged or insufficient time on the telescope to complete the observations. However, we determine that approximately 95 per cent are consistent with the values listed in Table 3.1, and only 5 per cent show RMS levels worse than these values. Thus, we assess that to first order the survey has uniform sensitivity and only a small fraction of the area has sensitivity poorer than nominal.

Tables 3.2 and 3.3 include the RMS value for each detected maser peak, which help to identify the completeness of the MALT-45 survey. We detect many masers at less than 5σ significance. However, we consider the survey complete at the 5σ level for 95 per cent of the survey area. This completeness limit is equivalent to 4.5 Jy for class I CH_3OH masers, and approximately 4.3 Jy for each SiO maser line.

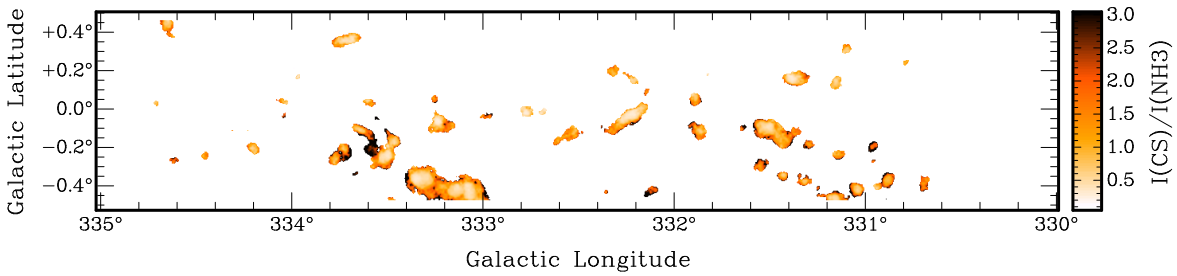

Figure 3.10: A ratio image of integrated MALT-45 CS (1–0) to HOPS NH_3 (1,1) emission. The clumps visible here contain at least $0.5\,\mathrm{K\,km\,s^{-1}}$ of integrated NH_3 (1,1) emission. The edges of most clumps typically have ratios around 2, and centres of clumps can have ratios as low as 0.4.

3.4 Discussion

3.4.1 Comparing MALT-45 CS (1–0) emission with HOPS NH_3 (1,1) emission

Fig. 3.4 shows that NH_3 (1,1) emission from HOPS is closely correlated with bright CS (1–0) emission, but with prominent exceptions; examples include G330.30−0.40, G332.17−0.10 and G334.17+0.06. We calculate that MALT-45 is more sensitive to CS (1–0) emission than HOPS is to NH_3 (1,1) emission by a factor approximately 9, therefore regions of CS without NH_3 in Fig. 3.4 may be due to the superior sensitivity of MALT-45 over HOPS. However, it is also likely attributable to the phenomena described by Taylor et al. (1998), who reason that CS is a molecule associated with 'early-type' star formation, tracing quiescent gas, while NH_3 is 'late-type', associated with dense cores. For this reason, despite having a higher effective critical density, CS without NH_3 may be tracing molecular clouds before cold, dense cores have formed. Additionally, Bergin et al. (2001) and Tafalla et al. (2002) indicate that CS tends to deplete in core collapse. This means a relatively high abundance of NH_3 to CS should reflect a cold, dense core, which is a Taylor et al. (1998) 'late-type' scenario. As results indicate later in this section, NH_3 is not persistent in even further developed stages of HMSF, as it is not detected or very faint. We distinguish 'late-type' sources from these evolved sources through bolometric luminosities and the presences of infrared features, such as stars or H II regions.

We produced a map of the ratio between the integrated intensities of CS and NH_3 in order to highlight the differences between their distributions. Before performing the quotient of integrated intensity, the CS data were smoothed to the HOPS NH_3 resolution ($\sim$2 arcmin). We used a cutoff at $0.5\,\mathrm{Km\,s^{-1}}$ (3σ) of the less sensitive NH_3 data; CS data is $>3\sigma$ everywhere NH_3 is $>3\sigma$. Integration of emission was taken between -100 and $-40\,\mathrm{km\,s^{-1}}$, to eliminate subtle baseline effects which decrease the robustness of analysis; this velocity range is where most of the emission in this part of the Galaxy lies (see Fig. 3.3 for the longitude-velocity plot). Quotients use units of main-beam temperature for both CS and NH_3. See Fig. 3.10 for the full ratio map.

Moving inward from the clump edges, the CS/NH_3 ratio quickly changes. We observe the amount of both CS and NH_3 to increase, with the NH_3 intensity increasing more 'quickly'.

Edge values are mostly about 2, while clump centres are usually between 1 and 0.5, but can be as low as 0.4.

We now discuss the ratio map qualitatively, reserving radiative transfer modelling for future work. In almost every clump, the centre is dominated by NH_3 over CS. This could be due to any or a combination of enhanced NH_3, depleted CS, or both species being enhanced but CS becoming optically thick. The hyperfine line structure of NH_3 means that it remains optically thin at higher column densities than CS. To test for optically thick CS, we compared CS with MALT-45 $C^{34}S$.

We conducted the analysis of CS against $C^{34}S$ in a similar manner to that of CS against NH_3. Both integrated maps were smoothed to the same resolution, the velocity range of integration was -100 to $-40\,\mathrm{km\,s^{-1}}$, and emission was limited to detectable $C^{34}S$ ($0.15\,\mathrm{K\,km\,s^{-1}}$). A preliminary analysis of the $C^{34}S$ data was undertaken only to investigate the CS optical depth within these clumps.

Fig. 3.11 shows contours of the ratio of $C^{34}S$/CS overlaid on GLIMPSE images, with contours of CS/NH_3. Progressively higher levels of $C^{34}S$/CS indicate CS self-absorption, but appear to be slightly offset from the lowest CS/NH_3 ratios. This implies that the relatively fainter CS emission in the presence of an abundance of NH_3 is due to both depletion and optical thickness. Additionally, the higher ratios of $C^{34}S$/CS appear to be associated with bright infrared emission, and correlate well with thermal SiO emission. We speculate that high $C^{34}S$/CS ratios may be due to high CS optical depth as a result of high CS relative abundance in the presence of an outflow or shocked gas. $C^{34}S$ is not detected in other regions of these clumps; aside from having poor signal-to-noise, this is likely due to the isotopologue depleting similar to CS, and emission is only apparent in hotter, shocked regions where these molecules have been released into the gas phase.

A similar analysis to the one we have conducted was performed in Tafalla et al. (2004) towards two cold, dense cores. Their results indicate significant depletion of CS and $C^{34}S$ towards the core centres, while NH_3 peaks in abundance. We have not undertaken a detailed analysis of the temperature or mass of the MALT-45 molecular gas clumps in this paper; this will be investigated in a future publication focusing on the CS emission. In future work, we will present radiative transfer modelling (including depletion, time-dependant chemistry and the relative sensitivity limits of the various surveys) of the dust, CS and NH_3 emission to quantitatively understand the physical reason for these effects.

The following subsections briefly discuss three unusual clumps, which have the largest CS/NH_3 ratios.

3.4.1.1 G330.95−0.19

This source is one of the brightest in CS across the MALT-45 survey region (peak of 1.5 K), and is the brightest in thermal SiO emission (peak of 0.17 K). The source also contains all the common star formation masers: class I and II CH_3OH, H_2O and OH. The CS spectrum has a broad profile of $\sim$10 $\mathrm{km\,s^{-1}}$ FWHM, possibly due to a powerful molecular outflow. A strong outflow would not be surprising given the strength of the thermal SiO detected, relative to all other SiO sources in MALT-45.

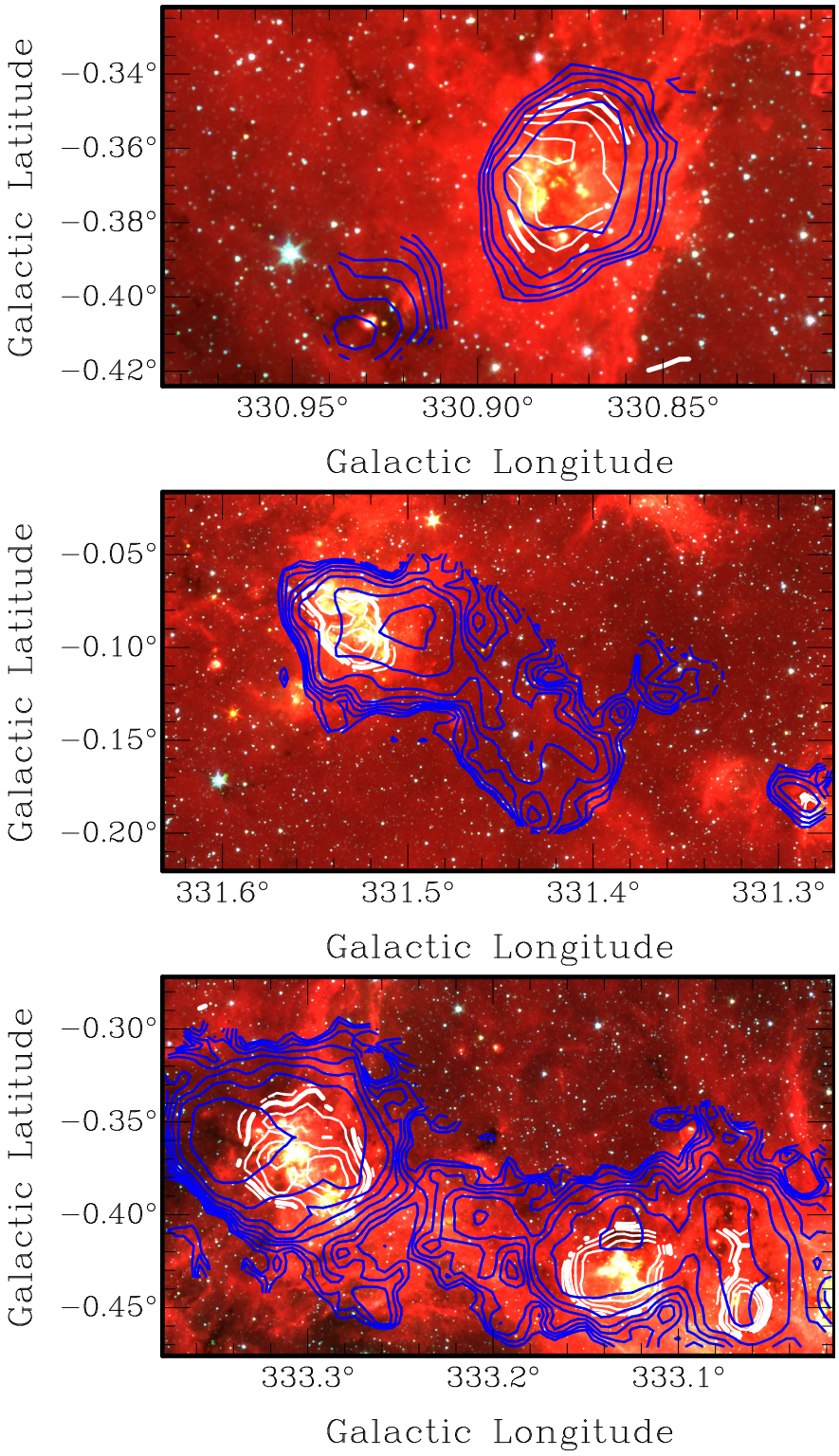

Figure 3.11: Examples of significant $C^{34}S/CS$ ratios within CS/NH_3 clumps. *Spitzer* GLIMPSE 3-colour (RGB = 3.6, 4.5 and 8.0 μm) image with contours of $I(C^{34}S)/I(CS)$ (white) and contours of $I(CS)/I(NH_3)$ (blue). $I(C^{34}S)/I(CS)$ contour levels are 0.08, 0.10, ..., 0.16, and $I(CS)/I(NH_3)$ contour levels are 0.3, 0.5, ..., 1.9. Note that contour levels for $I(CS)/I(NH_3)$ move from large to small, outside-in. The lowest CS/NH_3 and highest $C^{34}S/CS$ ratios appear to be slightly offset. High $C^{34}S/CS$ ratios appear to occur with bright infrared emission; this is likely due to $C^{34}S$ is only detectable where the overall CS abundance is enhanced in hotter, shocked regions where these molecules have been released into the gas phase.

Garay et al. (2010) have targeted this source which has a high *IRAS* far-infrared luminosity, as well as detection of CS (2–1) by Bronfman et al. (1996). Garay et al. (2010) present data for SiO (2–1) and note that of the four sources they discuss, this source is brightest in SiO, and conclude that an outflow is present due to the spectral profiles of CS and SiO. Garay et al. (2010) also discuss the requirement of OB stars to produce the ionised gas seen in other observations. The evolved nature of the source is the likely reason for the faint NH_3, because it is being destroyed or dispersed by outflows or young stellar objects.

3.4.1.2 G332.10−0.42

The CS/NH_3 ratio of this source is approximately 3. Of the three unusual sources discussed in this section, this is the only one without detected thermal SiO emission. A small region (∼30 arcsec) of the clump has a constant $C^{34}S/CS$ ratio of 0.08, and is coincident with a H_2O and class II CH_3OH maser, as well as what appears to be a star in GLIMPSE. A new class I CH_3OH maser is detected by MALT-45, but is slightly offset from this position (∼30 arcsec).

This source has been targeted by Ilee et al. (2013) to determine disc properties through CO observations, and is listed with a very high bolometric luminosity (1.8×10^5 $L_\odot$). The Red MSX Source (RMS; Lumsden et al. 2013) survey also lists a K-band magnitude of 5.9. These values suggest that the source is not embedded. As a star is visible in GLIMPSE and the source is not embedded, it may be assumed that the star (and the region) are post star-forming. However, we are confident that the associated star is not evolved (beyond the main-sequence), as a near-infrared (NIR) spectrum of the source contains Brγ, indicating the presence of an H II region. The spectrum is taken from the RMS survey, although the data remain unpublished; Cooper et al. (2013) present detailed analysis of the NIR spectroscopy, but note that it does not cover this specific source. We conclude that this source is somewhat evolved because of its exposure from natal clouds, but is pre-main-sequence because of the class II CH_3OH maser emission. Again, the evolved nature of this region is the likely reason for the relatively faint NH_3.

3.4.1.3 G333.60−0.20

This region is the brightest H II region within the MALT-45 survey, and appears to harbour evolved sources. $C^{34}S$ emission is detected within this source, and the $C^{34}S/CS$ ratio varies from 0.09 to 0.14. Thermal SiO emission is also detected towards the source. As well as a previously known class I CH_3OH maser, this region is associated with 1612-, 1665- and 1667-MHz OH masers (Sevenster et al. 1997; Caswell 1998), and many H_2O masers from HOPS (Walsh et al. 2014). The peak velocity of the class I CH_3OH maser is $-49.7\,km\,s^{-1}$, $-51\,km\,s^{-1}$ for OH, and -75.5 to $-43.1\,km\,s^{-1}$ for the H_2O masers. MALT-45 CS also has a double-peak profile in this region; a strong, broad peak is associated with $-48.1\,km\,s^{-1}$ and a weaker one at $-89.8\,km\,s^{-1}$, both at the same position ($16^h22^m06^s$, $-50°06'17''$ J2000).

Fujiyoshi et al. (2006) conducted observations of H90α towards this source, which also reveal two peaks of emission, and reason that it contains many O-type stars. The peak velocity of each H90α component varies greatly over the region, from -78.5 to $-52.9\,km\,s^{-1}$ and -42.8 to $-22.8\,km\,s^{-1}$, where the second peak is weaker and not present across the

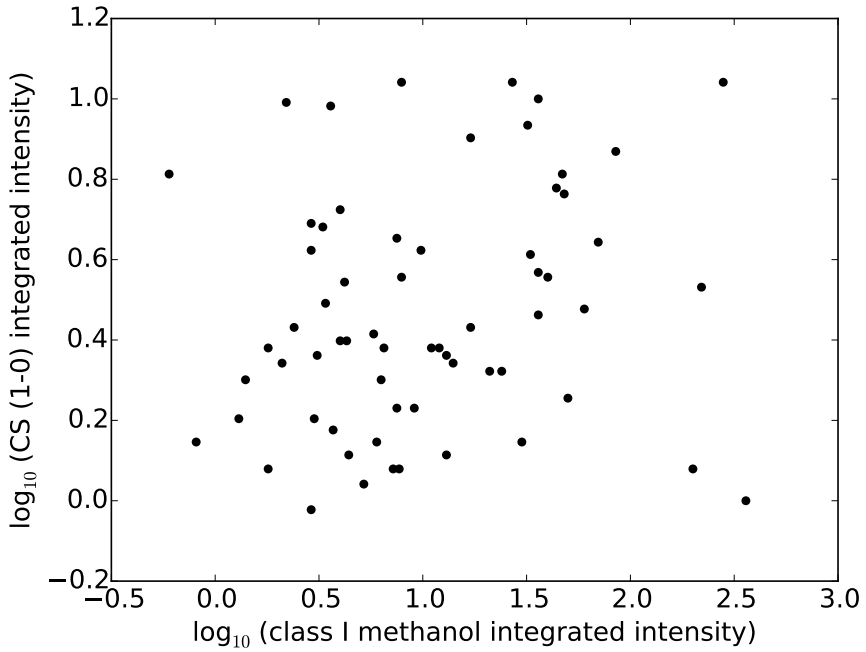

Figure 3.12: A log-log scatter plot of class I CH_3OH and CS integrated intensities. Units of integrated intensity are $Jy\,km\,s^{-1}$ for class I CH_3OH, and $K\,km\,s^{-1}$ for CS. There is no significant correlation observed.

observed area. Note that the position of peak MALT-45 CS is outside of the data presented in Fujiyoshi et al. (2006); it is possible that the spatial resolution of our CS data is limiting our ability to interpret the physics of this region. However, it is interesting that the peak velocities of CS are quite different to H90α; this may indicate complex structure of the source, and indeed this is discussed in Fujiyoshi et al. (2006).

The weak presence of NH_3 (1,1) emission is mysterious. The high CS/NH_3 ratio may be attributable to the region being at a higher temperature, preventing CS depletion. Lowe et al. (2014) attempted a NH_3 (1,1) and (2,2) analysis of this clump, but were unable to detect significant emission. They suggested that the relatively faint NH_3 emission could be due to extreme self-absorption. Lo et al. (2009) comment that in general, CS (2–1) and HCO^+ (1–0) have similar velocity structure, except at this location; the HCO^+ has a strong self-absorption feature. However, given that the source is clearly evolved, it is consistent with the other sources discussed in having little NH_3 emission.

3.4.1.4 Summary

The cause for the high ratios (CS/NH_3 > 3) in our analysis appears to stem from evolved regions of HMSF. The other clumps are more difficult to classify - are they less evolved? Do they have significantly different temperatures or column densities? More analysis is needed, and will be presented in a future MALT-45 paper with CS clump analysis.

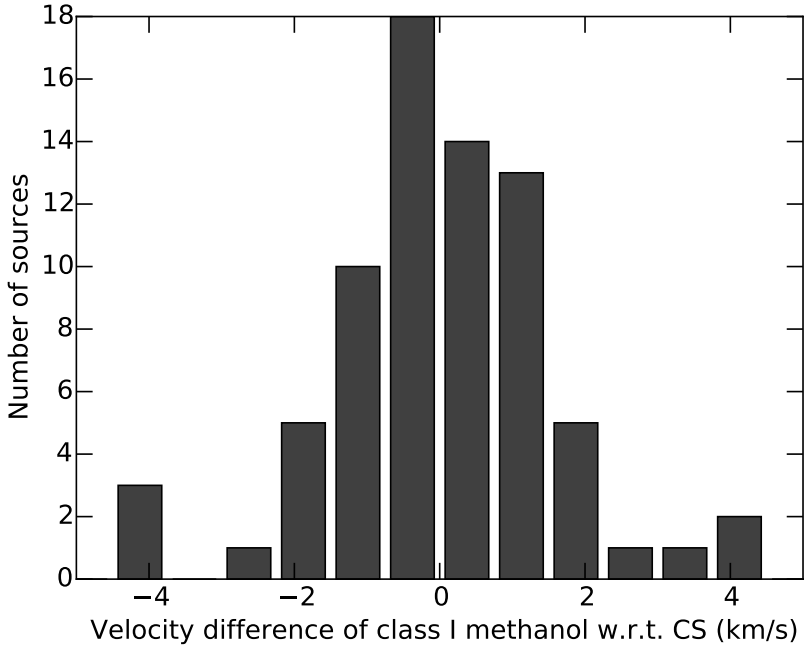

Figure 3.13: The distribution of velocity offsets between the peak velocity of class I CH_3OH and CS (1–0). The bin size was chosen to be $0.75\,\mathrm{km\,s^{-1}}$. The histogram is approximated by a Gaussian with a mean velocity $0.0\pm0.2\,\mathrm{km\,s^{-1}}$ and standard deviation $1.5\pm0.1\,\mathrm{km\,s^{-1}}$.

3.4.2 Comparing CS (1–0) emission with class I CH_3OH maser regions

Table 3.2 includes the integrated flux density of CS (1–0) in each maser region. The kinematic distance calculated for each source is used to determine the luminosities. Fig. 3.12 compares the integrated CS intensity with the integrated class I CH_3OH maser intensity.

Fig. 3.2 shows that most class I CH_3OH masers appear to be associated with a bright peak of CS emission (73/77 masers with $>0.11\,\mathrm{K}$ of peak intensity CS). This is quantified (using integrated intensity) in Fig. 3.12. However, there is no correlation observed between the relative intensity of a class I CH_3OH maser and its associated CS.

A class I CH_3OH maser with CS emission suggests association with a star-forming region, because sufficient gas and shocks exist to power their emission. However, without being able to associate these lines with other diagnostics of star formation, it is not certain that the masers are stimulated by star formation; cloud-cloud collisions have been found to stimulate class I CH_3OH emission (Sjouwerman et al. 2010). While the possibility of being a non-star-forming maser extends to all candidates without additional tracers (such as class II CH_3OH masers), we expect that these are exceptional cases, and that the majority if not all class I CH_3OH masers in the MALT-45 sample are associated with star formation.

A comparison between the peak velocities of class I and class II CH_3OH masers was undertaken by Voronkov et al. (2014), and found a broad Gaussian distribution of velocity differences. We have performed a similar analysis with the peak velocities of both CS and class I CH_3OH masers from the MALT-45 data. The resulting histogram of the velocity difference of CH_3OH with respect to CS is found in Fig. 3.13. The distribution is approximated by a Gaussian with statistics $\mu = 0 \pm 0.2\,\mathrm{km\,s^{-1}}$ and $\sigma = 1.5 \pm 0.1\,\mathrm{km\,s^{-1}}$ (where μ is the mean

and σ the standard deviation). The median velocity difference is $-0.1\,\mathrm{km\,s^{-1}}$.

The statistics of the class I and class II CH_3OH maser velocity difference distribution presented by Voronkov et al. (2014) are $\mu = -0.57 \pm 0.07\,\mathrm{km\,s^{-1}}$ and $\sigma = 3.32 \pm 0.07\,\mathrm{km\,s^{-1}}$. Thus, the variance of class I and class II CH_3OH maser velocity differences is larger than that of class I CH_3OH maser and CS emission velocity differences. Because CS is a dense gas tracer, it will occur in cloud cores and thus trace systemic motions accurately. Given the resulting Gaussian of velocity differences, this means that class I CH_3OH masers are also good indicators of systemic velocities. Voronkov et al. (2010b) discuss class I CH_3OH masers having similar velocities to the quiescent gas, due to a small amount of gas actually being shocked in these regions. As is noted in Voronkov et al. (2014), Garay et al. (2002) indicate that CH_3OH emission arising without thermal SiO emission is due to mild shocks, destroying dust grain mantles but not dust grain cores. Hence the dispersion in class I CH_3OH maser velocities is thought to be small, and is reflected here. This also indicates that the large dispersion seen by Voronkov et al. (2014) is likely due to the large class II CH_3OH maser velocity spread. This is readily explained by class II CH_3OH maser emission radiating from close to a high-mass young stellar object, and therefore having a higher dispersion.

The histogram in Fig. 3.13 appears to have a slight blueshifted component. This is also discussed in Voronkov et al. (2014) as perhaps due to maser emission being easier to detect on the near-side of a cloud to the observer. While the median velocity offset is negative, it is statistically insignificant. A larger data set is required to determine if the blueshift phenomena is real or not.

3.4.3 Comparing class I CH_3OH maser regions with thermal SiO (1–0) emission

As discussed in Chapter 1, SiO $v = 0$ is a good tracer of shocked gas and outflows. Regions of thermal SiO emission and positions of class I CH_3OH masers correlate weakly; 23 of 77 masers (30 per cent) have at least a 2σ peak of SiO emission. As class I masers are collisionally excited, it is perhaps not surprising to find some association with thermal SiO. However, the majority of masers are detected without SiO $v = 0$ emission. This could be due to: insufficient sensitivity to extended SiO emission; class I CH_3OH masers having stronger intensity than thermal SiO; or not all class I CH_3OH masers being associated with SiO $v = 0$ emission. Garay et al. (2002) found that thermal CH_3OH emission may be triggered by less energetic shocks, which destroy dust grain mantles but not their cores, which explains a lack of SiO emission. In more energetically shocked regions (such as a jet or molecular outflow), CH_3OH may not survive, which may explain SiO emission without CH_3OH.

Three regions with strong SiO emission (0.04 K) are not associated with any maser species: G331.02−0.42, G333.63−0.11 and G334.20−0.20. Each of these regions has a CS peak of at least 0.4 K ($>10\sigma$), but no obvious infrared emission. Table 3.2 lists 28 class I CH_3OH masers with detected SiO emission, implying that these three regions without masers are in the minority. This could be due to the variability of any masers making them undetectable during observations, or that conditions in these regions are unfavourable for masers to exist.

It is clear that sensitivity to CH_3OH and/or SiO will play a part in the detectability of each. However, the fact that we see regions with both CH_3OH and SiO, regions with

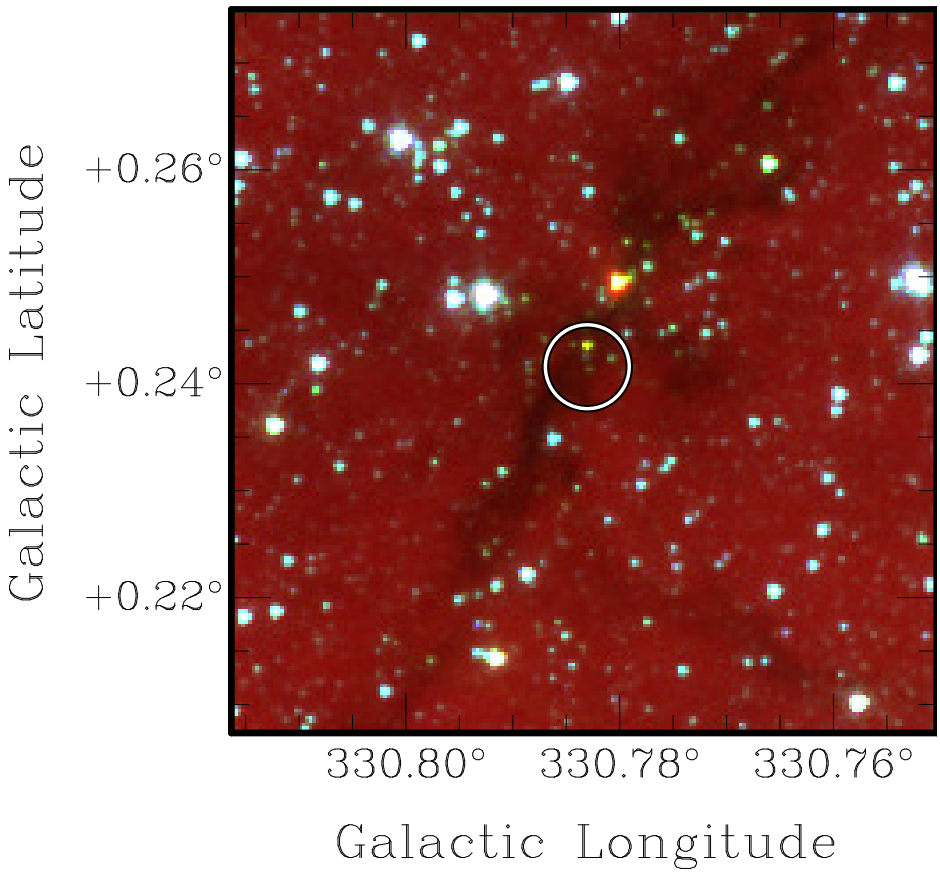

Figure 3.14: An example of a class I CH_3OH maser with associated 'green' emission. This region is not classified as an EGO by Cyganowski et al. (2008), but may have similar properties. The circle represents 15 arcsec centred on the peak of the class I CH_3OH maser emission, which is the expected positional error.

only CH_3OH masers and regions with only SiO emission suggests that there are multiple conditions under which each of these will exist. If we assume that all class I CH_3OH masers are associated with star formation, then given that the majority of masers are not associated with thermal SiO emission, these masers may be tracing weaker shocks that do not produce detectable SiO emission. 30 per cent of CH_3OH masers also show thermal SiO emission. It is not clear whether the masers and SiO are physically connected, although a reasonable interpretation is that the SiO originates in a jet, where as the masers are associated with the surrounding outflow. In a subsequent paper for MALT-45, maser follow-up observations will be conducted at high spatial resolution. We will simultaneously observe SiO with greater sensitivity, and using this data we will more thoroughly investigate the association of class I CH_3OH masers and thermal SiO emission.

3.4.4 Class I CH_3OH maser comparison with 3-8 μm emission

GLIMPSE mapped the Galactic plane in four infrared bands (3.6, 4.5, 5.8 and 8.0 μm). These images are useful for investigating potential relationships between infrared emission and MALT-45 detections. A common example of how GLIMPSE data is used is by combining the 3.6, 4.5 and 8.0 μm bands in a three-colour image (blue, green and red, respectively) to reveal EGOs (extended green objects). As discussed in Cyganowski et al. (2008), EGOs have

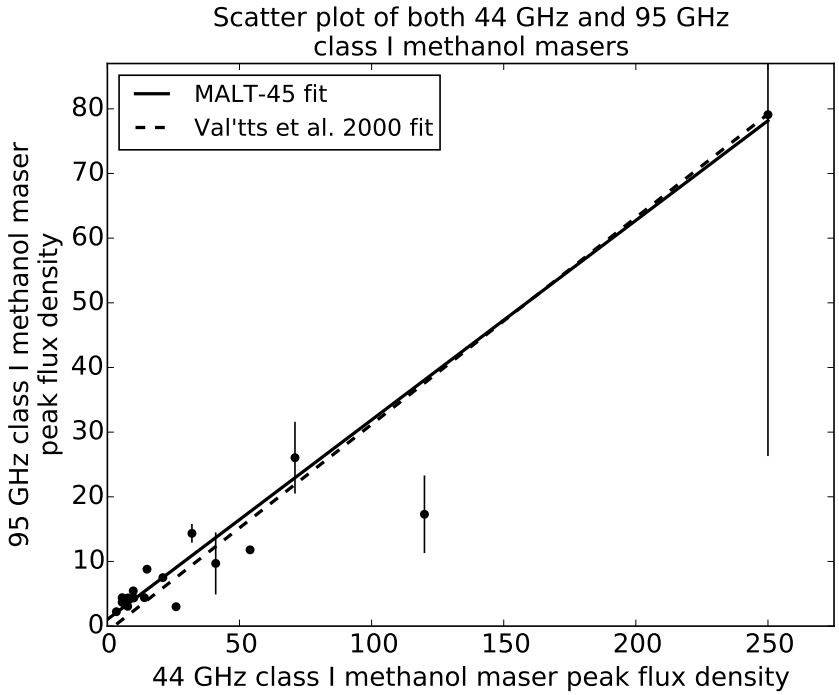

Figure 3.15: A scatter plot of 44 GHz class I CH_3OH masers from MALT-45 with known 95 GHz class I CH_3OH maser emission. There are 19 masers with both 44 and 95 GHz emission. The line of best fit for these data is plotted alongside the line of best fit presented by Val'tts et al. (2000). Vertical lines indicate the minimum and maximum recorded values for 95 GHz masers, if available, on top of the plotted average. Units of peak flux density are in Jy.

a strong correlation with class I CH_3OH maser regions.

The catalogue provided by Cyganowski et al. (2008) was used to investigate the presence of EGOs over the survey region. The catalogue covers $10° \leq l \leq 65°$ and $295° \leq l \leq 350°$, $b = \pm 1.0°$, and lists 22 candidate EGOs within the MALT-45 survey region. Of the 77 class I masers found by MALT-45, 12 are associated with an EGO. Association is credited for any spatial overlap within 60 arcsec. Of the 12 EGO-associated class I CH_3OH masers, 11 were previously known (G330.95−0.18 is new). EGOs are classified by visual inspection and as such are intrinsically subjective. However, it is clear that many of the new class I CH_3OH maser detections are associated with GLIMPSE sources with 'green' (i.e. 4.5 μm excess) emission; see Fig. 3.14 for an example source. Cyganowski et al. (2009) explains that the green emission band of GLIMPSE contains both H_2 and CO (1–0) lines, which are excited by shocks. Indeed, some of the new masers detected by MALT-45 have similar 'green' emission as with EGOs, although less prominently so. This shows a close association between shocks traced by EGOs and class I CH_3OH masers.

3.4.5 95 GHz class I CH_3OH masers

Val'tts et al. (2000) found a relationship between the peak flux density of the 95 and 44 GHz class I methanol masers (which come from the same transition family). They found that the peak flux density of 44 GHz masers is approximately three times greater than the 95 GHz masers.

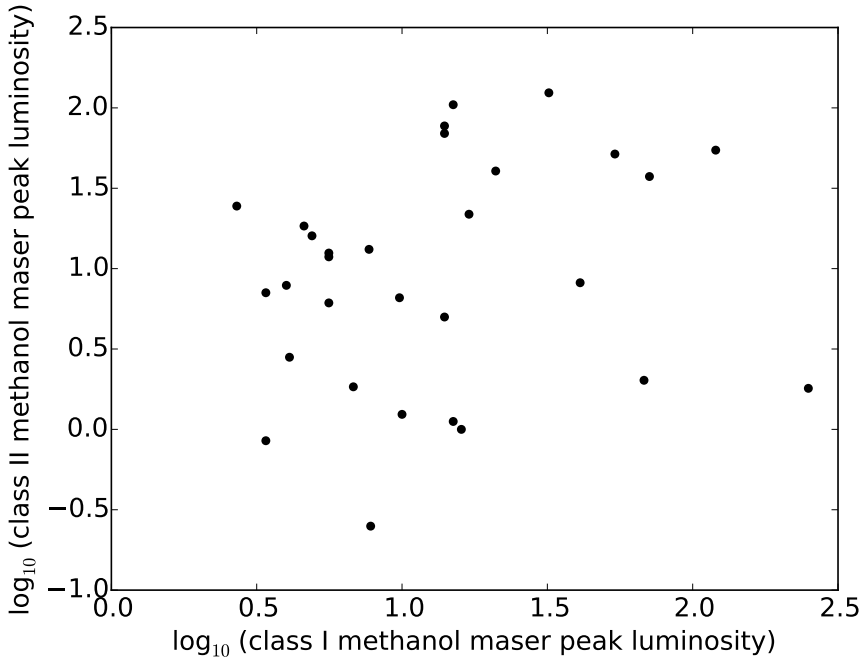

Figure 3.16: The luminosities of associated class I and class II CH_3OH masers plotted against each other. No significant correlation is observed. Units of luminosity for the masers are $Jy\,kpc^2$, using peak flux densities.

Information for 95 GHz class I CH_3OH masers towards MALT-45 44 GHz masers are obtained from Val'tts et al. (2000); Ellingsen (2005) and Chen et al. (2011). In total, we have 19 class I maser sources with both 44 and 95 GHz peak flux densities. When faced with more than one peak flux density over various epochs, we use the average of all values. Analysing the distribution in Fig. 3.15, we find that our results agree with those of Val'tts et al. (2000). Our line of best fit is $P_{95} = 0.31 \times P_{44} + 1.0$, with an r^2-value of 0.98, while the Val'tts et al. (2000) fit is $P_{95} = 0.32 \times P_{44} - 8.1$, with an r^2-value of 0.53. The uncertainty of our fitted slope is ± 0.01. Note that our fit does not use the 44 GHz maser with 120 Jy; if we do include it, our fit becomes $P_{95} = 0.28 \times P_{44} + 1.0$, with an r^2-value of 0.91 and uncertainty ± 0.02. This is not significantly different, but our slope closely agrees with Val'tts et al. (2000) when the outlier is omitted.

Four of the five brightest masers in this comparison also have the largest variation. A reasonable explanation is that the flux density of these masers is varying with time, although variations with class I CH_3OH masers are not well characterised. Many observational epochs of these masers are required to identify if the maser flux density varies with time or otherwise.

3.4.6 Class I CH_3OH maser associations

In this section, we discuss other maser species and transitions and their association with the class I CH_3OH masers detected in MALT-45. Association with each maser is credited if the emission in question is within 60 arcsec of the class I maser position.

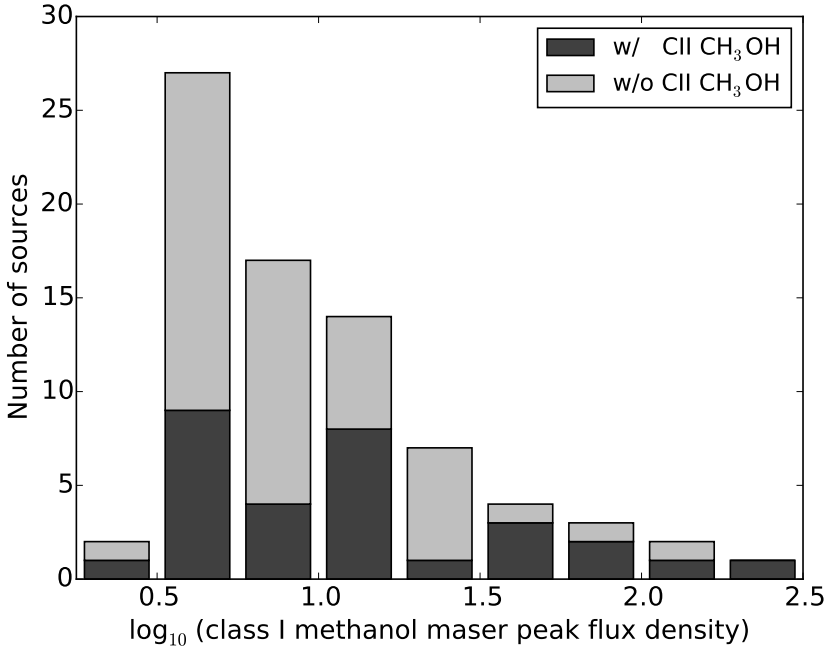

Figure 3.17: A stacked histogram of class I CH_3OH masers with and without class II methanol masers. This plot shows that class II masers can be associated with a wide range of class I intensities.

3.4.6.1 Class II masers from the MMB

In the past, class I methanol masers have been identified from targeted searches towards class II maser sites (Ellingsen 2005). For the first time, we are able to make an unbiased comparison of the rate at which each class of methanol maser occurs and their degree of overlap.

Within the MALT-45 survey region, 54 6.7 GHz class II methanol masers have been detected by the MMB (Caswell et al. 2011). To compare against MALT-45 class I maser regions, 7 class II masers have been grouped together into 'clusters', as they are close together (within 60 arcsec). The clusters containing grouped masers are G330.88−0.37, G331.54−0.07, G332.30−0.09, G333.13−0.44 and G333.23−0.06. While the velocities of each maser site grouped together may be different, there is significant overlap in the range of emission (not greater than 9 km s^{-1} apart). Without high-resolution positions, inferring which class II maser is associated with the class I emission is difficult, and it is more practical to only compare their clustered position, especially as a class I CH_3OH maser is almost certainly associated with the class II source. Therefore, we compare 47 class II methanol masers positions against the 77 class I sources detected in MALT-45. There are 28 class I CH_3OH masers associated with the clusters, and 16 of these class I masers are new; see Table 3.2. An association exception is made for G331.13−0.25, where the class II CH_3OH maser is slightly further offset than 60 arcsec from the MALT-45 class I CH_3OH maser position, but is well studied and known to be related (Ellingsen 2005; Voronkov et al. 2014). Additionally, the next closest class I and class II CH_3OH maser pair is approximately 100 arcsec, which aids to rule out mis-association. Thus, 60 per cent of class II masers have a class I counterpart (28/47), while

approximately 36 per cent of class I masers have a class II counterpart (28/77).

Ellingsen (2005) reports a 38 per cent association of class II sources with a 95 GHz class I maser counterpart. Given that the 44 GHz species is typically stronger than the 95 GHz transition, and that the MALT-45 sensitivity is better, we perhaps expect our reported class II-to-class I association to be greater. As discussed in §3.4.5, Val'tts et al. (2000) finds the relative peak flux density of 95 GHz class I CH_3OH masers to 44 GHz class I CH_3OH masers to be approximately one-third. Assuming Ellingsen (2005) had a sensitivity cutoff for 95 GHz masers at 3 Jy, we can limit the results of the 44 GHz population by a 9 Jy cutoff. There are 17 44 GHz masers with a peak flux density greater than 9 Jy associated with a class II CH_3OH maser (36 per cent), which is only slightly lower than the proportion of associations found by Ellingsen (2005). Therefore, our results are reasonably consistent. Considering that the MALT-45 sensitivity to class I CH_3OH masers is better than that of Ellingsen (2005) by approximately a factor of 2, and that we search for 44 GHz masers instead of 95 GHz masers, we are assured that there is a higher association rate than previously reported.

The luminosities of class I and class II CH_3OH masers were compared, but no correlation was found (r^2-value of 0.03); see Fig. 3.16. The relative populations for class I masers with and without a class II source are compared in Fig. 3.17; the histogram reveals that class II sources are associated with a wide range of class I brightnesses, which reaffirms the lack of correlation. With sensitive, targeted 44 GHz observations of class II masers, more data can be collected for a better analysis. Note that the search radius should be at least an arcmin to cover the range of separations between class I and class II masers; see §4.2 of Voronkov et al. (2014).

3.4.6.2 H_2O masers from HOPS

22 GHz water masers are another maser species that are collisionally excited. Therefore, we might expect a close association between class I methanol and water masers. HOPS has found H_2O masers in an untargeted way, and catalogues their findings into three association groups: star formation, evolved star, and 'unknown' (Walsh et al. 2014). Breen et al. (2010a) also presents a catalogue of H_2O masers, typically associated with class II CH_3OH masers and/or OH masers.

HOPS has detected a total of 48 H_2O masers within the MALT-45 survey region (Walsh et al. 2011, 2014). Of these, HOPS has classified 10 as being associated with an evolved star, leaving 38 as star formation or 'unknown'. Including the Breen et al. (2010a) detections brings the total to 71, but there is a large overlap with the HOPS catalogue, as well as many H_2O masers near to others (within 60 arcsec). Similar to the MMB class II CH_3OH masers, after grouping masers into clusters, we compare MALT-45 class I CH_3OH masers against a total of 43 H_2O maser clusters.

Of these 43 H_2O maser clusters, 27 are associated with a class I CH_3OH maser (63 per cent). It is possible that the class I CH_3OH population have more H_2O maser associations, but have not been found yet. Breen et al. (2010a) targeted observations towards known sources, and HOPS has a lower-bound sensitivity between 5 and 10 Jy. Follow-up observations for H_2O masers towards new class I CH_3OH masers may be productive in identifying new H_2O masers.

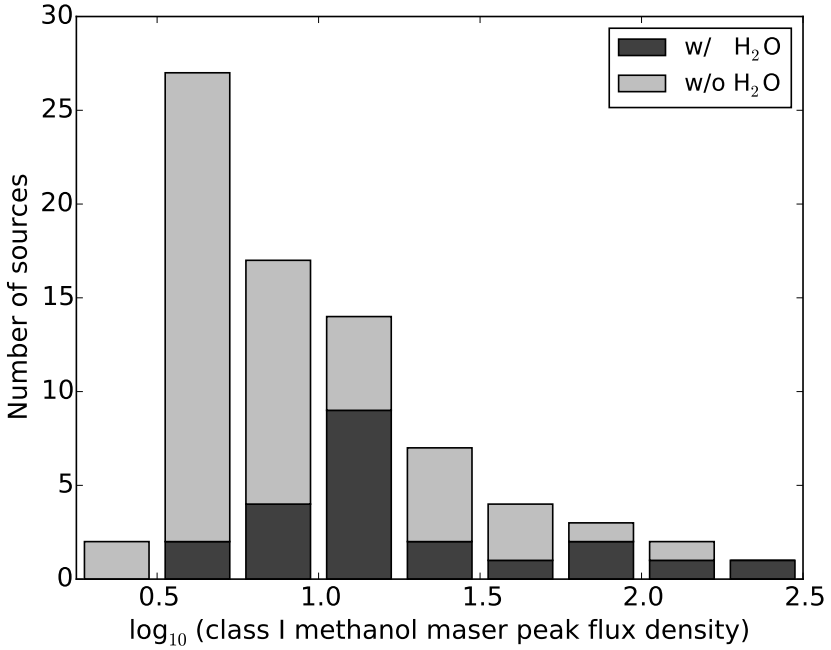

Figure 3.18: A stacked histogram of class I CH_3OH masers with and without H_2O masers. This plot shows that H_2O masers tend to be associated with brighter class I methanol masers.

In the HOPS catalogue recently published (Walsh et al. 2014), the water masers G331.86+0.06 and G333.46−0.16 were not redetected in the high-resolution follow-up survey. The G333.46−0.16 water maser is associated with a MALT-45 class I CH_3OH maser, but this was a known class I CH_3OH maser region (along with other maser species). The G331.86+0.06 water maser, however, is slightly offset from a new class I CH_3OH maser. The offset is enough to not be included as an association, but it lends credence that this variable water maser is likely highlighting star-forming activity.

3.4.6.3 OH masers from Sevenster et al. (1997) and Caswell (1998)

Voronkov et al. (2010b) discuss the positioning of class I methanol maser emission on a HMSF evolutionary timeline, especially compared to other masers. Class II methanol masers have been characterised well in terms of their position in a HMSF timeline, associated with millimetre sources, but typically not H II regions. Unlike class II masers, class I masers are currently thought to be associated with both early- and late-type HMSF. This stems from finding class I masers associated with outflows, but also with OH masers.

To date, no unbiased comparison between OH and class I methanol masers has been performed. With the first unbiased sample of class I masers, we are able to analyse the relative populations and perhaps refine class I masers on an evolutionary timeline. Voronkov et al. (2010b) mentions that class I masers associated with OH masers are known primarily due to the class II methanol maser emission present, as most class I sources have been found toward class II sources. Caswell (1997) discuss how OH favoured maser regions have a greater number of associated H II regions than class II masers, indicating that OH masers typically signpost later stages of an evolutionary timeline than class II masers. Combining the OH

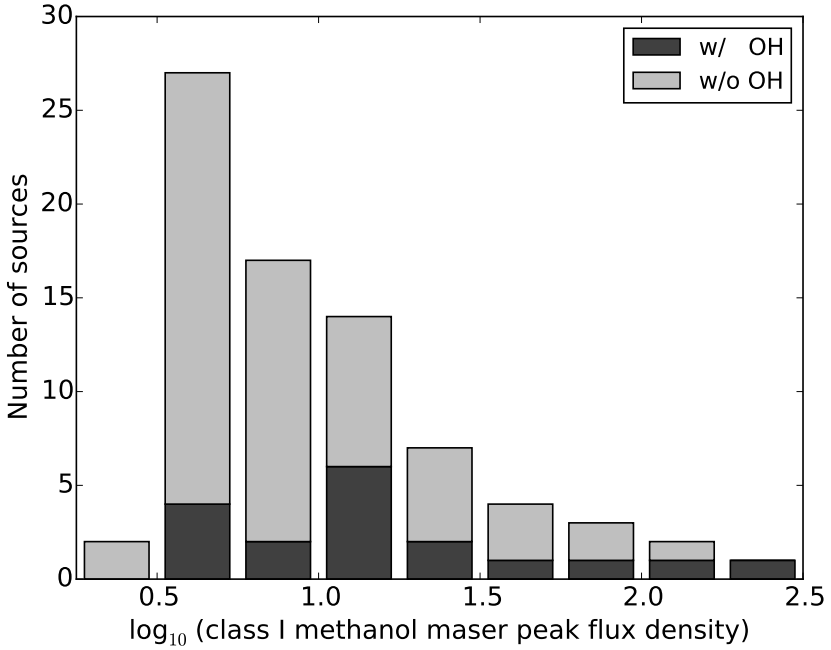

Figure 3.19: A stacked histogram of class I CH_3OH masers with and without OH (1612, 1665, or 1667 MHz) masers. OH masers appear to be associated with a wide range of class I methanol masers.

masers found by Sevenster et al. (1997) and Caswell (1998), there are 16 star formation OH masers within the MALT-45 survey region. The other OH masers in Sevenster et al. (1997) and Caswell (1998) are associated with evolved OH/IR stars, determined from SIMBAD and individual source descriptions within Caswell (1998). 94 per cent (15/16) of star formation OH masers are associated with a class I CH_3OH maser. Of these 15, only 2 masers are without a 6.7 GHz class II methanol maser (13 per cent; G331.50−0.10 and G333.59−0.21). It is difficult to contrast maser regions containing OH but not class II methanol, as almost every OH maser in the survey region is associated with a class II CH_3OH maser. If a population of OH masers without class II CH_3OH was isolated, a better comparison with class I CH_3OH could be established. The MALT-45 survey results merely indicate that class I CH_3OH is associated with all maser species found.

There are 30 class I CH_3OH maser regions with associated class II CH_3OH or OH maser emission, indicating late stages of star formation. The remaining 47 masers are unaccounted for; if these are all associated with early-type star-formation, then class I CH_3OH masers appear to be more closely associated with earlier stages in an evolutionary timeline.

3.4.6.4 Summary of star-formation maser associations

A Venn diagram of the maser associations can be seen in Fig. 3.20. There appears to be a strong overlap between class I and class II CH_3OH masers, with and without the presence of H_2O and/or OH masers. This may suggest that the majority of class II CH_3OH masers are associated with class I CH_3OH masers because of an abundance of CH_3OH. The smaller population of class II CH_3OH masers without class I CH_3OH emission (40 per cent; 19/47)

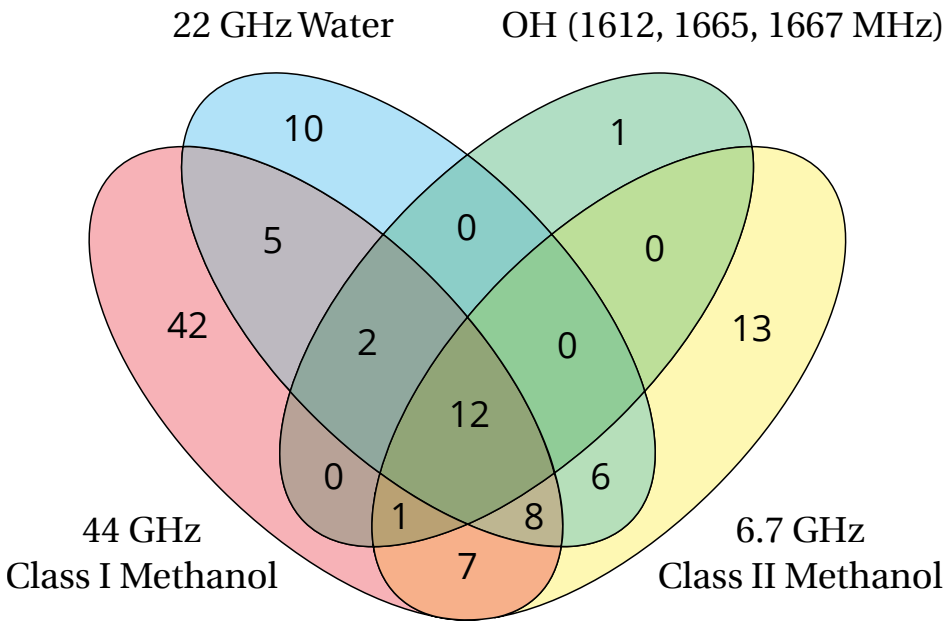

Figure 3.20: Venn diagram of all discussed maser region associations. The majority of maser regions have a class I CH_3OH component, particularly with class II CH_3OH as well, but there is a large population of class I masers without any associations.

may indeed have no association, or even weaker class I CH_3OH emission than is detected by MALT-45.

There is a large population of class I CH_3OH masers without any other maser counterpart. As discussed, these may highlight non-star-forming phenomena, young regions of HMSF, or low mass star-forming regions. However, given the strong association with CS seen in Fig. 3.3 and with other HMSF masers seen in Fig. 3.20, the majority of class I CH_3OH masers are likely associated with HMSF.

Figs 3.17, 3.18 and 3.19 show the luminosity population of class I CH_3OH masers as stacked histograms. Generally, the presence or absence of other maser transitions does not appear to correlate with the class I CH_3OH maser luminosity.

Titmarsh et al. (2014) discuss the placement of H_2O masers within an evolutionary timeline for HMSF, and concluded that they are not likely to be associated with any specific phase of a timeline, but rather dependant on the environment. As H_2O masers are collisionally excited like class I CH_3OH masers, and class I masers are associated with a wide range of other species (with and without class II CH_3OH, OH), we tend to agree that a dusty or active star-forming environment plays perhaps the predominant role in determining the likelihood of a region having an associated class I CH_3OH maser rather than the evolutionary phase.

Investigation of the peak flux densities and luminosities of class I CH_3OH masers versus class II CH_3OH, H_2O and OH masers does not reveal any relation. Investigation will be performed again in a subsequent MALT-45 maser follow-up paper, where maser regions can be better associated and flux density calibration is able to be more accurately determined.

3.4.7 SiO $v = 1, 2, 3$ maser associations

MALT-45 has detected 47 regions with at least one of the vibrationally excited lines $v = 1, 2, 3$ of SiO (1–0) maser emission. Of these, 4 are associated with a OH maser (all 1612 MHz, G331.60−0.14 has an additional 1665 MHz), and 8 are associated with a H_2O maser. OH and H_2O masers are common companions with evolved infrared stars (Caswell 1998; Walsh et al. 2014), and indeed GLIMPSE reveals that all SiO maser regions have an infrared star associated within 30 arcsec of the peak maser position. There is no overlap of SiO masers associated with both an OH and H_2O maser. The population presented in this paper associated with OH and H_2O masers is insufficient to perform correlation tests upon. None of the SiO masers detected have been reported previously; thus, MALT-45 is a productive survey for identifying evolved stars not found in other searches.

The SiO $v = 1$ line generally appears to be the strongest of the three maser lines, and is the most common detection. There are eleven cases where the $v = 2$ line is stronger than $v = 1$, and two regions contain only $v = 2$ emission. This result is somewhat unexpected, as generally the lower v transitions should be brighter than the higher v transitions. Gray et al. (2009) predict that SiO masers should have brightness decreasing with $v = 1, 2, 3$, and the $v = 2$ is often weaker due to overlap with a water line. Neither of the two regions with only SiO $v = 2$ emission have other masers associated, but the sub-population of SiO regions with brighter $v = 2$ than $v = 1$ have three H_2O masers and two OH masers associated. This is almost half of all masers associated with SiO regions. However, we currently cannot explain why some $v = 2$ masers are stronger than their $v = 1$ counterparts. Only three $v = 3$ lines are detected, and these are all quite weak, especially compared to the $v = 1, 2$ lines within the same region; it appears that this line is difficult to detect without sensitive observations.

The only SiO maser with nearby CH_3OH masers is G333.90−0.09, but is separated by 33 arcsec. The same SiO maser is 13 arcsec from a Sevenster 1612 MHz OH maser, which is cospatial with a star in GLIMPSE. As the nearby class I and class II CH_3OH masers are only 4 arcsec apart but separated from the star, we consider both pairs of masers to not be associated.

3.5 Summary

MALT-45 has successfully probed the Galactic plane for CS (1–0), 44 GHz class I methanol masers, and the SiO (1–0) family of $v = 0, 1, 2, 3$ lines. This is the first survey to produce a large scale unbiased map of CS, and is the first untargeted search of class I CH_3OH masers and SiO emission. Further publications will reveal other properties of the 7 mm star-forming environment, through the remaining lines mapped by this survey. With time, MALT-45 could be extended to map more of the Galactic plane, revealing more about the nature of star formation within our Galaxy. With the current survey, we have determined:

(i) Across the survey region, the CS/NH_3 ratio is low in the centres of many clumps, but higher at the edges. This is likely due to a combination of increased NH_3 abundance and CS being depleted and/or becoming optically thick in the centres of clumps;

(ii) A large population of class I methanol masers are not associated with other masers (55 per cent). In addition, 61 per cent of class I methanol masers are not associated with

either a class II methanol or hydroxyl maser, which indicates that class I methanol masers are preferentially associated with earlier phases of HMSF;

(iii) Class I methanol masers are good indicators of systemic velocities;

(iv) Class I methanol masers are found towards most known class II methanol, water and hydroxyl masers within the survey region. Thus, positioning class I methanol on a maser timeline of HMSF is difficult, and the occurrence of class I methanol masers is perhaps more likely due to environmental factors;

(v) Silicon monoxide masers associated with evolved stars are most commonly detected in their $v = 1$ vibrational mode. When a region contains more than one vibrational mode, the intensity typically descends with vibrational mode ($v = 1, 2, 3$). However, we find two cases where we only detect $v = 2$ and eleven cases where both $v = 1$ and $v = 2$ are detected, but the $v = 2$ is stronger.

Chapter 4

MALT-45 - II. Follow-up observations of 44 GHz class I methanol masers

This chapter details an in-progress, co-authored publication. The authors of this paper are: Jordan, C. H., Walsh, A. J., Ellingsen, S. P., Voronkov, M. A., Breen, S. L. When complete, this work will be submitted to the Monthly Notices of the Royal Astronomical Society.

The introduction section has been modified to streamline the discussed literature, to avoid unnecessary overlap with Chapter 1.

Abstract

We detail interferometric observations of 44 GHz class I methanol masers detected by MALT-45. We detect 238 maser spots across 77 maser regions. Using high-resolution positions, we compare the detected masers to other star formation maser species. The simultaneously collected cross- and auto-correlated data provided by these observations are for brightness comparisons, identifying quasi-thermal emission in the 44 GHz line. We find that the majority of class I methanol masers have small spatial and velocity spreads, and closely trace the systemic velocities of associated clouds. Using 870 μm dust continuum emission from the ATLASGAL survey, we determine clump masses associated with class I masers, and find they are generally associated with clumps between 1000 and 3000 $M_{\odot}$. For each class I methanol maser region, we use the presence of class II CH_3OH masers, OH masers and radio recombination lines to distinguish older regions of high-mass star formation; we find that regions without these associations have lower luminosities and appear toward dark infrared regions.

4.1 Introduction

Methanol masers are excellent tracers of high-mass star-formation. Empirically, they are divided into two groups: class I and class II. Class II CH_3OH masers are exclusively associated

with high-mass star formation (HMSF) and signpost a distinct evolutionary stage (Minier et al. 2003; Green et al. 2012; Breen et al. 2013). The connection between HMSF and class I CH_3OH masers is less certain; observations have shown that these masers can be found towards many star-forming regions and evolutionary stages, but not consistently, and not necessarily with or without the presence of class II masers (Ellingsen 2006; Voronkov et al. 2010b; Breen et al. 2010a; Ellingsen et al. 2013). Additionally, class I maser emission has been found towards low-mass star formation (Kalenskii et al. 2010), supernova remnants (Pihlström et al. 2014; McEwen et al. 2014) and the centres of galaxies (Yusef-Zadeh et al. 2013; Ellingsen et al. 2014).

Within the MALT-45 survey (Jordan et al. 2015; hereafter Paper I) region $330^\circ \leq l \leq 335^\circ$, $b = \pm 0.5^\circ$, 77 class I CH_3OH masers were detected, 58 of which were new detections. For the first time, with a flux-density limited sample of class I sources, we are able to test the bulk-properties of these masers. Paper I in this series of MALT-45 publications briefly investigated the association of methanol masers with other detected spectral lines, but was ultimately limited by the spatial resolution of the data ($\sim$1 arcmin). In order to derive accurate positions for each of the class I CH_3OH masers observed in Paper I, interferometric follow-up observations were conducted using the ATCA. In this chapter, the results of these observations are detailed.

4.2 Observations

Observations were conducted on 2013 September 7 and 8 using the Australia Telescope Compact Array. The array configuration was 1.5A, which has 5 antennas distributed in the East-West direction with baselines ranging from 153 m to 1.5 km.*

As with other MALT-45 observations, the correlator was programmed in the 64M-32k mode, which provides a 32 kHz channel resolution over 64 MHz. However, unlike Paper I, these observations made use of 'stitched zooms'; rather than using individual zoom windows, multiple may be joined, albeit non-linearly, to increase frequency coverage over a spectral line. Each spectral line in these observations was observed with a zoom window covering 96 MHz (except for the zoom window containing H51α and $C^{34}S$ (1–0), which covers 224 MHz). For observations at 7 mm, the 32 kHz channel resolution results in a spectral resolution of approximately 0.2 km s^{-1} per channel. The spectral lines observed are identical to that of Paper I. The list of observed lines and velocity coverage information is contained in Table 4.1. Since Paper I, the rest frequencies of the SiO (1–0) molecular lines have been updated (Müller et al. 2013).

The targets for these observations were chosen for their class I CH_3OH maser emission, and used a source list extracted from a preliminary MALT-45 data reduction. Consequently, not all masers listed in Paper I are discussed in this chapter. The targets of these observations are listed in Table 4.2. The additional sources detailed in this chapter that are not included within Paper I are G331.44−0.14, G331.44−0.16, G333.01−0.46, G333.12−0.43. The sources not detailed in this chapter but listed in Paper I are G331.36−0.02 and G334.64+0.44. For

*The maximum baseline is 4.5 km including antenna 6 (CA06), however, CA06 has a different surface to the others, and suffers poor sensitivity at 7 mm. Consequently, data from CA06 is not included in this chapter.

Table 4.1: Bright spectral lines between 42.2 to 49.2 GHz, targeted by MALT-45 and these observations. Column 1 lists the spectral line. Column 2 lists the rest frequency of the line. Column 3 classifies the line as either a maser or thermal line. Column 4 gives the ATCA pointing beam size at this frequency. Column 5 indicates whether this line is detailed in this chapter ('Y') or not ('N'); this refers to the inclusion of Gaussian fits to the emission from these lines. Column 6 lists the median RMS noise level per spectral channel, with errors representing the standard deviation. The RMS noise is given to two significant figures. Radio recombination line (RRL) frequencies are taken from Lilley & Palmer (1968). All other rest frequencies are taken from CDMS (Müller et al. 2005). Note that RMS noise levels are specified for auto-correlation data; cross-correlation noise levels are given in Table 4.2.

Spectral line	Frequency (GHz)	Maser or thermal?	Beam size (arcsec)	Detailed in this chapter?	Median RMS noise level
SiO (1–0) $v = 3$	42.51938	Maser	66	N	
SiO (1–0) $v = 2$	42.82059	Maser	66	N	
H53α (RRL)	42.95197	Thermal	65	N	8.7±1.5 mK
SiO (1–0) $v = 1$	43.12207	Maser	65	N	
SiO (1–0) $v = 0$	43.42385	Thermal	65	Y	5.9±0.67 mK
CH_3OH 7(0,7)–6(1,6) A^+	44.06941	Maser (Class I)	64	Y	170±62 mJy
H51α (RRL)	48.15360	Thermal	58	N	
$C^{34}S$ (1–0)	48.20694	Thermal	58	N	8.1±0.85 mK
CH_3OH 1_0–0_0 A^+	48.37246	Thermal	58	Y	7.7±1.8 mK
CH_3OH 1_0–0_0 E	48.37689	Thermal	58	N	
OCS (4–3)	48.65160	Thermal	58	N	
CS (1–0)	48.99095	Thermal	57	Y	8.9±1.3 mK

more details, refer to §4.3. Hence, a total of 79 targets were observed over the two days of observations. To obtain good *uv*-coverage, each target was observed multiple times over a single observing shift. Each individual observation of a target lasted one minute (one 'cut'), and each target has at least seven cuts, but some have up to ten; the noise levels for each target are also listed in Table 4.2.

Bandpass calibration was derived from PKS B1253−055, phase calibration from PMN J1646−5044 and flux-density calibration from PKS 1934−638. The assumed flux-density of PKS 1934−638 was 0.39 Jy at the rest frequency of the 44 GHz class I CH_3OH maser line.

4.2.1 Data reduction

4.2.1.1 Cross-correlation

Class I CH_3OH maser data were reduced using standard interferometric techniques with MIRIAD. These steps are:

i) ATLOD - to convert raw observational data to a *uv*-visibility MIRIAD format. Parameters specified were `options=noauto,rfiflag,birdie,xycorr,opcorr,unflag`;

ii) QVACK - to remove data that is recorded near an observing setup change. Parameters specified were `interval=0.1 force=0 mode=source`;

iii) ATFIX - to apply offline corrections to data, such as elevation effects. No parameters were specified;

iv) UVFLAG - to flag known bad channels in CABB data. The flagged channels were 1025

and 2049;

v) MFCAL - to determine bandpass calibration. PKS B1253−055 was used for this purpose, and MFCAL was run with parameters `interval=0.1 refant=2`

vi) GPCAL - to determine flux calibration, then phase calibration. Normally, observations in the 7 mm waveband use a planet such as Uranus, but these observations used PKS 1934−63. Parameters used for flux calibration were `interval=0.1 options=xyvary refant=2`. PMN J1646−5044 was used as the phase calibrator, and parameters used for this purpose were `interval=0.1 options=xyvary,qusolve,nopol refant=2`.

vii) GPBOOT - to apply the flux calibration to the phase calibration data;

viii) MFBOOT - to apply the bandpass calibration to the phase calibration data.

The dataset containing the phase calibration is then applied to all target source data with GPCOPY.

For all data cubes reduced, the synthesised beam is approximately 0.5×1 arcsec in right ascension and declination, respectively. Voronkov et al. (2014) observed many 44 GHz class I CH_3OH masers with the ATCA; similar to that publication, the results presented in this chapter make use of self-calibrated data cubes. Self-calibration arbitrarily affects the absolute positional accuracy of data; to remove this effect, a reference maser feature was used. The position of this reference feature was determined before and after self-calibration and the measured difference was used to determine the absolute positions for all spectral features in the self-calibrated data cube. Ideally, the reference position before and after self-calibration has not shifted significantly (>0.5 arcsec), but some significant offsets were unavoidable in these data ($\gg$10 arcsec). Prior experience with the ATCA in this waveband suggests that the absolute positional accuracy is around 0.5 arcsec (Voronkov et al. 2014). However, given that we experience non-ideal self-calibration offsets and the synthesised beam for each region is approximately 0.5×1 arcsec, the absolute positional error for any maser spot should be considered as being ∼1 arcsec.

In this chapter, a maser spot refers to a spatial and spectral peak of emission that comes from a single well-defined position on the sky. Data cubes were produced for each of the target regions, then maser spots were identified by visual inspection. Spots were classified if the spectrum contained at least three consecutive channels of 3σ emission, with a peak of at least 5σ. We employ this conservative approach of maser identification to be confident that all identified maser spots are real. A small number of weaker, narrow features may have been missed using these criteria; however, from past experience and comparison of our cubes with previous observations (where available), these features are rare. The requirement of three consecutive channels has the effect of limiting our maser detections to a velocity width of at least 0.65 $\mathrm{km\,s^{-1}}$. Similar to Voronkov et al. (2014), dynamic range limitations exist for channels containing extremely bright maser emission. This reduces the ability to identify real maser emission at a similar velocity to the bright feature; emission was not extracted if it was thought to be the product of such dynamic range artefacts.

Once each maser spot was identified, positions in right ascension and declination were fitted with the MIRIAD task IMFIT. For each channel of emission in a maser spot, IMFIT used a 3×3 arcsec box to generate a position. Each channel-fitted position is then flux-weighted and is listed in Appendix B.1. Uncertainties of the resulting position reflects the 1σ of all

channel-fitted positions. In some cases, the maser spot positions have uncertainties of a few tens of milliarcsec. We caution that we are unlikely to determine relative positions to this accuracy for these observations, as dynamic range and calibration uncertainties become limiting, considering that the absolute positional accuracy of the observations is around 1 arcsec. In general, we found the class I maser spots were spatially separated by our observations, with separations of 1 arcsec or greater, but occasionally spots were very near to a bright neighbour. In these cases, positions were manually assigned by using the brightest pixel, with a more generous position uncertainty of 100 milliarcsec in right ascension and 200 milliarcsec in declination. Such maser spots are designated with an asterisk ($*$) in Appendix B.1. Maser spots at slightly larger offsets to bright masers required altered procedures to fit a position. To accurately fit these masers, either the velocity range of emission was altered for position fitting, or the size of the box for fitting was decreased. Decreasing the size of the box used by IMFIT was not found to significantly affect resultant positions, so we do not identify the maser spots using these modified procedures.

Spectral information for each maser spot were derived from image cubes using the MIRIAD task IMSPEC, which were then characterised with Gaussian fits. These fits provide the peak flux density, FWHM and peak velocity of the emission in each maser spot. Each Gaussian was fitted to minimise residuals, but in many cases it was not possible to match the root-mean-square (RMS) noise of the spectrum. This is partially due to many masers having only a few channels of emission, resulting in Gaussian fits with relatively large uncertainties. However, all fitting residuals are within 10 per cent of the fitted peak intensity. Coupled with uncertainties in calibration, we ascribe a 20 per cent uncertainty to all quoted flux-density values.

4.2.1.2 Auto-correlation

For each targeted maser region, the observations simultaneously provide coverage of the CS (1–0), SiO (1–0) $v = 0$ and CH_3OH 1_0–0_0 A^+ transitions. However, due to the extended nature and low surface brightness of these thermal spectral lines and the limited uv-coverage of the observations, these lines were not detectable in the cross-correlation data. However, auto-correlation data is available, which provides detail for these extended, thermal lines. To report on these properties, a RUBY script was written to assist with the analysis of the auto-correlated data. These observations were not designed with auto-correlation processing in mind; unlike Paper I, no dedicated reference position was observed. Instead, data collected at the location where the emission is known to be weak and have a simple spectral profile was used as the reference location for auto-correlations. The script routine pipeline was as follows:

(i) For each source, a raw auto-correlation spectrum was produced for each antenna and each cut;

(ii) For each antenna source cut, a quotient spectrum was formed from the source and reference cut data;

(iii) A first-order polynomial was fitted to and removed from the spectra. The velocity range of the fit was restricted to -160 and $20\,\mathrm{km\,s^{-1}}$, covers the velocity range of emission from the Galaxy at this longitude, and constraining the fit improves the quality of the resulting

spectra;

(iv) All quotient spectra from an antenna are averaged together, before averaging all antennas together;

(v) The flux-density calibration is achieved by using values from Paper I.

This procedure is graphically outlined in Fig. 4.1, with the CS emission of G330.95−0.18. Existing software solutions for auto-correlation processing were inadequate for the data collected, however, the auto-correlation script developed for this work is robust at producing publication quality results.

For each of the auto-correlated CS, SiO and CH_3OH thermal lines, spectra are spectrally smoothed with a Hanning window of 9 spectral channels, and up to two Gaussians were fitted to characterise the spectral feature. This smoothing results in a velocity resolution of $\sim$0.39 km s^{-1} for CS, $\sim$0.44 km s^{-1} for SiO $v = 0$ and $\sim$0.40 km s^{-1} for CH_3OH 1_0–0_0 A^+. As with the cross-correlation data, Gaussians are fitted to minimise residuals; however, after fitting Gaussians, all residuals were less than 10 per cent of the fitted peak intensity. Combined with uncertainties in flux-density calibration, we place a 20 per cent uncertainty on all intensity values derived from auto-correlated data.

This auto-correlation procedure was also used for class I CH_3OH masers, which is used to determine the integrated intensities, luminosities, and comparison with the cross-correlation data in §4.4.5.

4.3 Results

The basic properties of each observed target (the region name, pointing centre, observed date, RMS noise level, spatial extent of emission and velocity range of emission) are listed in Table 4.2. Note that five sources were not detected in the cross-correlation data, but three of these five were detected in the auto-correlation data (G331.44−0.14, G331.72−0.20 and G333.24+0.02). Their non-detection in the cross-correlation data is likely caused by the emission being too extended; the maximum detectable scale is roughly double the length of the shortest baseline, which for these observations corresponds to a synthesised beam of approximately 4.6 arcsec. This is likely too large to resolve out any compact maser emission. Poor phases may also affect the lack of maser spots detected. Extended CH_3OH emission at 44 GHz could be caused by quasi-thermal rather than masing mechanisms, or even broad but weak maser components. Differences between cross-correlation spectra and auto-correlation spectra are discussed further in §4.4.5.

The remaining two sources (G330.83+0.18 and G331.21+0.10) may have varied in their intensity, resulting in them not being detected by these observations in cross- and auto-correlation. However, false-positives listed by Paper I are more probable; the auto-correlation sensitivity of the observations reported in this chapter is $\sim$170 mJy, and the Paper I peak flux densities are 3.1 and 3.5 Jy, observed at October 2013. Our non-detection therefore requires a flux-density variation in these masers of a factor of 20. Additionally, each of these masers appear to have only a single feature. Given that class I CH_3OH maser variability is not well characterised, and that the flux-densities of other masers detected in Paper I and these observations are largely consistent, we deem these two regions as false-positives of Paper I.

For the remainder of this chapter, we discuss the 77 regions containing 44 GHz class I CH_3OH emission.

The auto-correlation sensitivity of these observations is approximately a factor of 5 better than that of Paper I, and has improved the detection rate of thermal lines towards the class I CH_3OH masers. Paper I had detectable CS emission towards 95 per cent of class I CH_3OH masers, whereas these data have detectable CS towards every maser. Thermal SiO emission detection statistics are greatly improved; these data have detectable SiO towards 83 per cent of regions (64/77), which is a significant increase over Paper I (30 per cent). The thermal 1_0–0_0 A^+ line of CH_3OH was not characterised in Paper I, but auto-correlations have also been produced for this chapter. MALT-45 had a similar detection rate between thermal CH_3OH and thermal SiO, but here it is detected towards almost all regions (75/77; 97 per cent). Additionally, we list detections of H53α and $C^{34}S$ with the targeted maser regions, along with median RMS noise levels in Table 4.1, but do not list their properties for conciseness. The thermal lines are used for various comparisons in §4.4.

Associations between detected class I CH_3OH masers and other maser transitions, as well as selected HMSF tracers, are detailed in Table 4.3. Association between maser species is credited if the angular offset between the two is less than one arcmin. Each region is compared with published positions of class II CH_3OH (Caswell et al. 2011), water (H_2O) (Breen et al. 2010a; Walsh et al. 2014) and hydroxyl (OH) masers (Sevenster et al. 1997; Caswell 1998), as well as ATLASGAL clumps (Contreras et al. 2013). The presence of each thermal line is determined by the method described in §4.2.1.2, using data from these observations. The Gaussian parameters determined for each of the thermal lines are listed in Appendix B.2. Uncertainties for each of the fitted parameters are quoted, however, we remind the reader to consider the 20 per cent uncertainty placed upon all intensity values.

Kinematic distances are also contained in Table 4.3. Like Paper I, distances were calculated using the program supplied by Reid et al. (2009); however, all distances in this chapter have been calculated using a 'near' kinematic distance, whereas Paper I used a 'far' distance when prescribed by Green & McClure-Griffiths (2011). Given the similar velocities to other nearby masers and how well the class I CH_3OH masers trace the dense gas, we abandon the far distance prescription; see Fig. 3.3 of Paper I. The affected masers are G332.583+0.147, G333.313+0.106, G333.387+0.031, G333.562−0.025 and G333.900−0.098. The need for accurate near/far selection arises in analysis conducted later in this chapter, particularly with mass calculation in §4.4.4. All distances presented in this chapter use the same parameters as Paper I, specifically: $\Theta_0 = 246\,\mathrm{km\,s^{-1}}$, $R_\odot = 8.4\,\mathrm{kpc}$, $U_\odot = 11.1\,\mathrm{km\,s^{-1}}$, $V_\odot = 12.2\,\mathrm{km\,s^{-1}}$, $W_\odot = 7.25\,\mathrm{km\,s^{-1}}$, $U_s = 0\,\mathrm{km\,s^{-1}}$, $V_s = -15.0\,\mathrm{km\,s^{-1}}$, $W_s = 0\,\mathrm{km\,s^{-1}}$, $\sigma(V_{LSR}) = 3.32\,\mathrm{km\,s^{-1}}$.

The complete collection of Gaussian fits to class I CH_3OH spots are included in Appendix B.1, and Gaussian fits to thermal emission are included in Appendix B.2. Maser positions overlaid on infrared images from the *Spitzer* Galactic Legacy Infrared Mid-Plane Survey Extraordinaire (GLIMPSE; Benjamin et al. 2003) can be seen in Appendix B.3.

Table 4.2: Targeted class I CH_3OH masers, as well as their parameters. Column 1 lists the region name taken from Paper I. Column 2 lists the refined region name, based on the average position of maser spots found within that region, and takes into account the more accurate position based on the follow-up observations. The refined region names are used throughout this chapter instead of the Paper I names. A refined name is not supplied if no maser emission was detected in interferometry. Columns 3 and 4 list the targeted position for these observations. Column 5 gives the date on which the region was observed (7 or 8 September 2013). Column 6 lists the median RMS noise value for the self-calibrated cube. Column 7 lists the smallest radius of a circle to encompass all emission of the region. Column 8 lists the velocity range of emission detected in auto-correlation data. All maser regions were observed with an approximate local standard of rest velocity coverage between -353 and $195\,\mathrm{km\,s^{-1}}$. Note that regions with a radius of <1 arcsec contain either only one maser spot, or spots very close together. Regions without a radius were not detected in interferometry. Regions without a velocity range were not detected in interferometry or auto-correlation (likely false-positives; see §4.3). Regions labelled with an asterisk (∗) were not listed by Paper I, but have class I CH_3OH maser emission detected by these observations. Regions labelled with a dagger (†) are designated as 'non-evolved'; see §4.4.1.

Paper I region name	Refined region name	Pointing centre α_{2000} (h:m:s)	Pointing centre δ_{2000} (°:′:″)	Obs. date (Sep. 2013)	Median RMS noise level (mJy)	Radius (arcsec)	Velocity range ($\mathrm{km\,s^{-1}}$)
G330.30−0.39	G330.294−0.393	16:07:37.0	−52:30:59	8	46	4	−82 to −76
G330.67−0.40	G330.678−0.402	16:09:30.6	−52:16:08	8	42	< 1	−69 to −60
G330.78+0.24†	G330.779+0.249	16:07:12.2	−51:43:07	8	42	< 1	−46 to −41
G330.83+0.18		16:07:40.6	−51:43:54	8	44		
G330.87−0.36	G330.876−0.362	16:10:16.6	−52:05:50	8	45	22	−66 to −57
G330.88−0.38	G330.871−0.383	16:10:21.1	−52:06:42	8	44	< 1	−67 to −57
G330.92−0.41†	G330.927−0.408	16:10:44.2	−52:05:56	8	45	3	−44 to −40
G330.93−0.26†	G330.931−0.260	16:10:06.6	−51:59:23	8	43	1	−91 to −87
G330.95−0.18	G330.955−0.182	16:09:52.0	−51:54:59	8	46	< 1	−98 to −84
G331.13−0.48†	G331.131−0.470	16:11:59.8	−52:00:32	8	44	< 1	−70 to −65
G331.13−0.25	G331.132−0.244	16:10:59.7	−51:50:25	8	46	10	−93 to −78
G331.13−0.50	G331.134−0.488	16:12:05.9	−52:01:33	8	37	< 1	−68 to −68
G331.13+0.15	G331.134+0.156	16:09:14.8	−51:32:47	8	46	4	−79 to −73
G331.21+0.10		16:09:50.8	−51:32:39	8	44		
G331.29−0.20	G331.279−0.189	16:11:27.0	−51:41:54	8	45	21	−95 to −84
G331.34−0.35	G331.341−0.347	16:12:25.6	−51:46:16	8	46	< 1	−67 to −64
G331.37−0.40†	G331.370−0.399	16:12:48.2	−51:47:26	8	44	< 1	−66 to −64
G331.37−0.13†	G331.371−0.145	16:11:40.3	−51:35:52	8	47	< 1	−89 to −86
G331.39+0.15†	G331.380+0.149	16:10:26.2	−51:22:52	8	46	< 1	−47 to −43
G331.41−0.17†	G331.409−0.164	16:11:59.2	−51:35:33	8	45	< 1	−85 to −85
G331.44−0.14*†		16:11:57.9	−51:33:08	8	45		−87 to −84
G331.44−0.19	G331.440−0.187	16:12:11.5	−51:35:02	8	44	5	−92 to −85
G331.44−0.16*†	G331.442−0.158	16:12:05.0	−51:33:45	8	40	< 1	−87 to −85
G331.50−0.08	G331.492−0.082	16:11:59.6	−51:28:14	8	46	22	−93 to −84
G331.50−0.10	G331.503−0.109	16:12:10.5	−51:29:23	8	44	17	−101 to −86
G331.52−0.08	G331.519−0.082	16:12:07.5	−51:27:25	8	44	8	−93 to −85
G331.54−0.10	G331.530−0.099	16:12:14.5	−51:27:34	8	45	19	−95 to −85
G331.55−0.07	G331.544−0.067	16:12:11.3	−51:25:29	8	45	7	−92 to −85
G331.56−0.12	G331.555−0.122	16:12:26.7	−51:27:41	8	44	3	−104 to −97
G331.72−0.20†		16:13:34.4	−51:24:25	8	46		−49 to −45
G331.86−0.13†	G331.853−0.129	16:13:52.3	−51:15:42	8	46	< 1	−52 to −48
G331.88+0.06†	G331.887+0.063	16:13:10.5	−51:06:09	8	44	12	−91 to −84
G331.92−0.08†	G331.921−0.083	16:13:58.0	−51:10:56	8	46	< 1	−53 to −51
G332.09−0.42	G332.092−0.420	16:16:15.6	−51:18:31	8	46	7	−59 to −54
G332.24−0.05†	G332.240−0.044	16:15:17.6	−50:55:59	8	47	8	−51 to −46
G332.30−0.09	G332.295−0.094	16:15:46.0	−50:55:54	8	46	8	−55 to −45
G332.32+0.18†	G332.318+0.179	16:14:40.0	−50:43:11	8	45	10	−50 to −44
G332.36−0.11	G332.355−0.114	16:16:07.3	−50:54:16	8	45	< 1	−51 to −49
G332.59+0.15	G332.583+0.147	16:15:58.5	−50:33:22	8	45	< 1	−45 to −42
G332.60−0.17	G332.604−0.167	16:17:28.1	−50:46:20	8	46	2	−48 to −44
G332.72−0.05†	G332.716−0.048	16:17:28.6	−50:36:34	8	45	2	−41 to −38
G333.00−0.43	G333.002−0.437	16:20:27.7	−50:41:06	8	45	< 1	−57 to −55
G333.01−0.46*	G333.014−0.466	16:20:37.1	−50:41:31	7	41	< 1	−55 to −52
G333.02−0.06	G333.029−0.063	16:18:55.9	−50:24:03	8	43	1	−43 to −39
G333.03−0.02	G333.029−0.024	16:18:45.9	−50:22:21	7	41	< 1	−43 to −41
G333.07−0.44	G333.068−0.446	16:20:49.6	−50:38:51	7	46	< 1	−55 to −51
G333.07−0.40	G333.071−0.399	16:20:37.0	−50:36:33	7	42	6	−54 to −51
G333.10−0.51	G333.103−0.502	16:21:13.4	−50:39:56	7	41	11	−60 to −53
G333.12−0.43*	G333.121−0.433	16:20:58.5	−50:35:41	7	54	3	−57 to −44
G333.13−0.44	G333.126−0.439	16:21:02.3	−50:35:53	7	55	12	−57 to −42
G333.14−0.42	G333.137−0.427	16:21:03.0	−50:34:59	7	49	17	−57 to −43
G333.16−0.10	G333.162−0.101	16:19:41.4	−50:19:55	7	35	4	−93 to −90
G333.18−0.09	G333.184−0.090	16:19:45.2	−50:18:45	7	37	10	−89 to −84
G333.22−0.40	G333.220−0.402	16:21:16.9	−50:30:17	7	42	4	−57 to −49
G333.23−0.06	G333.233−0.061	16:19:49.4	−50:15:17	7	42	14	−96 to −81
G333.24+0.02†		16:19:26.0	−50:11:29	7	42		−71 to −66
G333.29−0.38	G333.284−0.373	16:21:28.1	−50:26:35	7	43	< 1	−55 to −49
G333.30−0.35	G333.301−0.352	16:21:24.5	−50:24:47	7	40	< 1	−54 to −48
G333.31+0.10	G333.313+0.106	16:19:27.6	−50:04:45	7	55	8	−51 to −43
G333.33−0.36	G333.335−0.363	16:21:36.4	−50:23:53	7	44	18	−55 to −46
G333.37−0.20†	G333.376−0.202	16:21:05.2	−50:15:18	7	44	5	−63 to −56
G333.39+0.02	G333.387+0.031	16:20:08.2	−50:04:49	7	39	3	−73 to −68
G333.47−0.16	G333.467−0.163	16:21:19.5	−50:09:42	7	40	12	−49 to −38

Table 4.2: *continued*

MALT-45 region name	Refined region name	Pointing centre α_{2000} (h:m:s)	Pointing centre δ_{2000} (°:′:″)	Obs. date (Sep. 2013)	Median RMS noise level (mJy)	Radius (arcsec)	Velocity range ($\mathrm{km\,s^{-1}}$)
G333.50+0.15†	G333.497+0.143	16:20:06.5	−49:55:25	7	42	2	−115 to −111
G333.52−0.27	G333.523−0.275	16:22:03.4	−50:12:08	7	42	< 1	−52 to −49
G333.56−0.30	G333.558−0.293	16:22:19.2	−50:11:28	7	42	27	−47 to −44
G333.56−0.02	G333.562−0.025	16:21:07.9	−49:59:49	7	44	< 1	−43 to −37
G333.57+0.03†	G333.569+0.028	16:20:55.4	−49:57:25	7	42	< 1	−86 to −81
G333.59−0.21	G333.595−0.211	16:22:06.2	−50:06:30	7	45	4	−52 to −44
G333.70−0.20	G333.694−0.197	16:22:27.7	−50:01:22	7	41	9	−52 to −49
G333.71−0.12†	G333.711−0.115	16:22:10.8	−49:57:21	7	41	5	−32 to −30
G333.77−0.01†	G333.772−0.010	16:21:59.6	−49:50:20	7	42	< 1	−91 to −88
G333.77−0.25†	G333.773−0.258	16:23:02.8	−50:00:31	7	40	< 1	−50 to −47
G333.82−0.30†	G333.818−0.303	16:23:29.5	−50:00:40	7	41	1	−50 to −46
G333.90−0.10	G333.900−0.098	16:22:56.3	−49:48:43	7	41	4	−66 to −61
G333.94−0.14	G333.930−0.133	16:23:14.1	−49:48:40	7	44	5	−43 to −39
G333.98+0.07†	G333.974+0.074	16:22:31.0	−49:38:08	7	40	< 1	−62 to −57
G334.03−0.04†	G334.027−0.047	16:23:16.7	−49:40:57	7	41	< 1	−85 to −83
G334.74+0.51†	G334.746+0.506	16:23:57.9	−48:46:40	7	38	4	−66 to −59

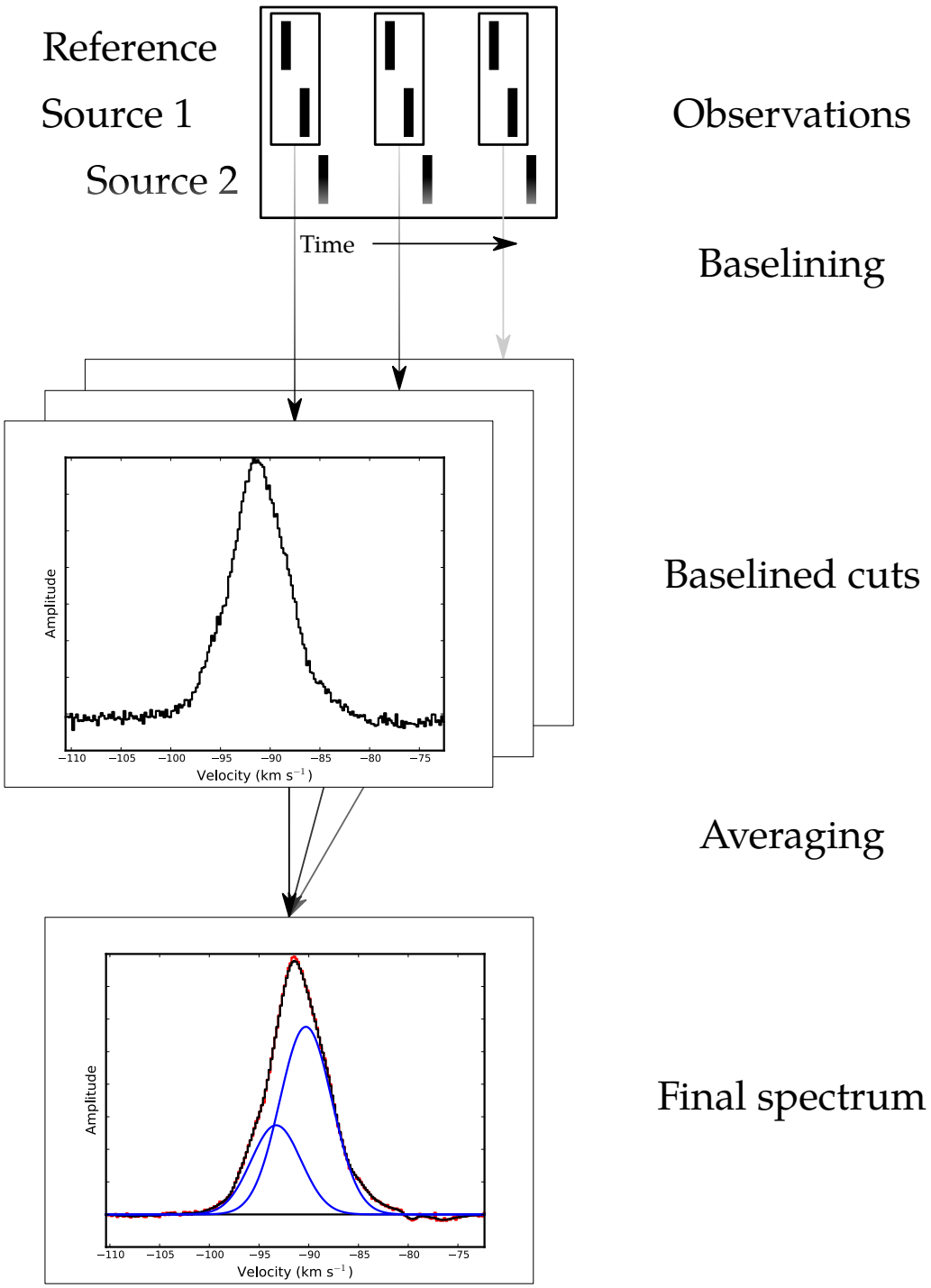

Figure 4.1: A graphical representation of the reduction procedure for auto-correlated data used in this chapter. The data from each one minute observation is combined with the nearest reference cut in time to produce a baselined cut. All baselined cuts are then averaged to produce an auto-correlation product. This procedure is performed for each antenna of the ATCA, and all products are then averaged together for a final product. The final panel contains the raw spectrum (red) and the Hanning-smoothed (black). This example shows the two Gaussian profiles (blue) that were fit simultaneously to the spectrum.

Table 4.3: Associations with each of the targeted class I CH_3OH masers. Column 1 lists the average position of all maser emission in Galactic coordinates. Columns 2 and 3 list the same average position in right ascension and declination. Column 4 lists the kinematic distance. Uncertainties are expressed in units of the least significant figure. Column 5 lists the presence of other masers and ATLASGAL clumps within 1 arcmin of the centre position. If there is more than one of a type of association, the number is listed as a subscript. Columns 6 through 10 list whether thermal CS (1–0), SiO (1–0) $v = 0$, CH_3OH 1_0–0_0 A^+, H53α and $C^{34}S$ (1–0) emission is detected ('Y') or not ('N'). Regions labelled with a dagger (†) are designated as 'non-evolved'; see §4.4.1.

Region name	Centre of maser emission α_{2000} (h:m:s)	δ_{2000} (°:′:″)	Kinematic distance (kpc)	Associations within 1 arcmin[1]	Presence of CS (1–0)?	Presence of SiO (1–0) $v = 0$?	Presence of CH_3OH 1_0–0_0 A^+?	Presence of H53α?	Presence of $C^{34}S$ (1–0)?
G330.294−0.393	16:07:37.9	−52:30:58.29	4.9 (2)	WA	Y	N	Y	Y	Y
G330.678−0.402	16:09:31.7	−52:15:50.68	4.1 (2)	A	Y	Y	Y	Y	Y
G330.779+0.249†	16:07:09.8	−51:42:53.76	3.1 (2)	A	Y	Y	Y	N	Y
G330.871−0.383	16:10:22.1	−52:07:08.28	4.1 (2)	MA	Y	Y	Y	Y	Y
G330.876−0.362	16:10:17.9	−52:05:59.37	4.0 (2)	$MWSCGA_2$	Y	Y	Y	Y	Y
G330.927−0.408†	16:10:44.7	−52:05:57.33	3.1 (2)	A	Y	Y	Y	N	Y
G330.931−0.260†	16:10:06.7	−51:59:18.13	5.3 (2)	A	Y	N	Y	N	Y
G330.955−0.182	16:09:53.0	−51:54:52.84	5.5 (2)	MWCA	Y	Y	Y	Y	Y
G331.131−0.470†	16:11:59.4	−52:00:19.88	4.3 (2)	GA	Y	Y	Y	N	Y
G331.132−0.244	16:10:59.8	−51:50:21.78	5.4 (2)	WCGA	Y	Y	Y	N	Y
G331.134−0.488	16:12:05.1	−52:01:01.37	4.3 (2)	A	Y	Y	Y	Y	Y
G331.134+0.156	16:09:15.1	−51:32:39.79	4.6 (2)	MWA	Y	Y	Y	N	Y
G331.279−0.189	16:11:27.2	−51:41:57.04	5.3 (2)	MWCA	Y	Y	Y	Y	Y
G331.341−0.347	16:12:26.4	−51:46:20.50	4.2 (2)	MWCGA	Y	Y	Y	Y	Y
G331.370−0.399†	16:12:48.5	−51:47:24.39	4.2 (2)	GA	Y	N	Y	N	Y
G331.371−0.145†	16:11:41.2	−51:36:15.36	5.2 (2)		Y	N	Y	N	Y
G331.380+0.149†	16:10:26.8	−51:22:58.46	3.2 (2)	A	Y	Y	Y	N	Y
G331.409−0.164†	16:11:57.4	−51:35:32.03	5.1 (2)	A_3	Y	Y	Y	N	Y
G331.44−0.14†	16:11:57.9	−51:33:07.81	5.1 (2)	A	Y	Y	Y	N	N
G331.440−0.187	16:12:11.9	−51:35:15.76	5.2 (2)	MWCA	Y	Y	Y	N	Y
G331.442−0.158†	16:12:04.8	−51:33:55.74	5.1 (2)		Y	Y	Y	N	Y
G331.492−0.082	16:11:59.0	−51:28:34.01	5.3 (2)	A_2	Y	Y	Y	Y	Y
G331.503−0.109	16:12:09.3	−51:29:14.95	5.2 (2)	$WSCA_3$	Y	Y	Y	Y	Y
G331.519−0.082	16:12:06.6	−51:27:25.69	5.3 (2)	A	Y	Y	Y	Y	Y
G331.530−0.099	16:12:14.3	−51:27:44.11	5.4 (2)	A	Y	Y	Y	Y	Y
G331.544−0.067	16:12:09.7	−51:25:44.35	5.2 (2)	MCA	Y	Y	Y	Y	Y
G331.555−0.122	16:12:27.1	−51:27:42.69	5.8 (2)	MW_2CA_2	Y	Y	Y	N	Y
G331.72−0.20†	16:13:34.4	−51:24:24.91	3.3 (2)	A	Y	Y	Y	N	Y
G331.853−0.129†	16:13:52.5	−51:15:46.63	3.4 (2)	A	Y	Y	Y	N	Y
G331.887+0.063†	16:13:11.2	−51:05:58.39	5.2 (2)	A	Y	Y	Y	N	Y
G331.921−0.083†	16:13:59.2	−51:10:56.00	3.5 (2)	A	Y	Y	Y	N	Y
G332.092−0.420	16:16:15.7	−51:18:27.64	3.7 (2)	MWA	Y	Y	Y	N	Y
G332.240−0.044†	16:15:17.2	−50:56:01.32	3.4 (2)	A	Y	Y	Y	N	Y
G332.295−0.094	16:15:45.3	−50:55:54.87	3.5 (2)	MWGA	Y	Y	Y	Y	Y
G332.318+0.179†	16:14:40.1	−50:43:07.07	3.4 (2)	WA	Y	Y	Y	N	Y
G332.355−0.114	16:16:07.2	−50:54:19.92	3.5 (2)	MWCGA	Y	N	Y	N	Y
G332.583+0.147	16:16:01.0	−50:33:30.96	3.1 (2)	MGA	Y	N	N	N	Y
G332.604−0.167	16:17:29.3	−50:46:12.92	3.3 (2)	MWGA	Y	Y	Y	N	Y
G332.716−0.048†	16:17:28.5	−50:36:23.32	3.0 (2)	A	Y	N	Y	N	Y

[1]M - 6.7 GHz CH_3OH maser from Caswell et al. (2011); W - 22 GHz H_2O maser from any of Breen et al. (2010a); Walsh et al. (2014); S - 1612 MHz OH maser from Sevenster et al. (1997); C - 1665 or 1667 MHz OH maser from Caswell (1998); G - EGO from Cyganowski et al. (2008); A - ATLASGAL point source from Contreras et al. (2013).

Table 4.3: *continued*

Region name	Centre of maser emission α_{2000} (h:m:s)	δ_{2000} (°:′:″)	Kinematic distance (kpc)	Associations within 1 arcmin[1]	Presence of CS (1–0)?	Presence of SiO (1–0) $v = 0$?	Presence of CH_3OH 1_0–0_0 A^+?	Presence of H53α?	Presence of $C^{34}S$ (1–0)?
G333.002−0.437	16:20:28.7	−50:41:00.91	3.8 (2)	WA_3	Y	Y	Y	Y	Y
G333.014−0.466	16:20:39.5	−50:41:47.45	3.6 (2)	A	Y	Y	Y	Y	Y
G333.029−0.063	16:18:56.7	−50:23:54.64	3.0 (2)	MWA	Y	N	Y	N	Y
G333.029−0.024	16:18:46.6	−50:22:14.57	3.1 (2)	MA_2	Y	Y	Y	N	Y
G333.068−0.446	16:20:48.7	−50:38:38.68	3.7 (2)	MWA	Y	Y	Y	Y	Y
G333.071−0.399	16:20:37.2	−50:36:30.13	3.6 (2)	A	Y	Y	Y	Y	Y
G333.103−0.502	16:21:13.1	−50:39:31.37	3.8 (2)	MA	Y	Y	Y	Y	Y
G333.121−0.433	16:20:59.5	−50:35:51.03	3.4 (2)	$M_4W_6C_2A_2$	Y	Y	Y	Y	Y
G333.126−0.439	16:21:02.6	−50:35:52.44	3.5 (2)	$M_4W_6C_2A_2$	Y	Y	Y	Y	Y
G333.137−0.427	16:21:02.2	−50:34:56.03	3.5 (2)	MWC_2A	Y	Y	Y	N	Y
G333.162−0.101	16:19:42.5	−50:19:56.29	5.3 (2)	MA_2	Y	N	Y	Y	Y
G333.184−0.090	16:19:45.5	−50:18:34.59	5.1 (1)	MGA	Y	Y	Y	Y	Y
G333.220−0.402	16:21:17.9	−50:30:19.97	3.6 (2)	A	Y	Y	Y	Y	Y
G333.24+0.02†	16:19:26.0	−50:11:29.26	4.4 (1)	A	Y	Y	Y	N	Y
G333.233−0.061	16:19:50.8	−50:15:15.94	5.1 (1)	M_2W_3SCA	Y	Y	Y	N	Y
G333.284−0.373	16:21:27.3	−50:26:22.48	3.6 (2)	A	Y	Y	Y	Y	Y
G333.301−0.352	16:21:25.9	−50:24:46.26	3.5 (2)	A_2	Y	Y	Y	Y	Y
G333.313+0.106	16:19:28.5	−50:04:45.61	3.2 (2)	MWGA	Y	Y	Y	Y	Y
G333.335−0.363	16:21:38.0	−50:23:46.78	3.6 (2)	A	Y	Y	Y	Y	Y
G333.376−0.202†	16:21:06.2	−50:15:13.21	4.0 (2)	WA	Y	Y	Y	N	Y
G333.387+0.031	16:20:07.5	−50:04:49.51	4.4 (1)	MWCA	Y	Y	Y	N	Y
G333.467−0.163	16:21:20.2	−50:09:41.70	3.1 (2)	MWCGA	Y	Y	Y	Y	Y
G333.497+0.143†	16:20:07.6	−49:55:26.21	6.3 (2)	A_2	Y	Y	Y	N	Y
G333.523−0.275	16:22:04.5	−50:12:05.32	3.5 (2)	A	Y	Y	Y	Y	Y
G333.558−0.293	16:22:18.7	−50:11:23.38	3.1 (2)	A_2	Y	Y	Y	Y	Y
G333.562−0.025	16:21:08.7	−49:59:48.85	3.0 (2)	MA	Y	Y	Y	N	Y
G333.569+0.028†	16:20:56.6	−49:57:15.91	5.0 (1)	A	Y	Y	Y	N	Y
G333.595−0.211	16:22:06.7	−50:06:21.28	3.5 (2)	WSCA	Y	Y	Y	Y	Y
G333.694−0.197	16:22:29.1	−50:01:31.84	3.5 (2)	A_2	Y	Y	Y	Y	Y
G333.711−0.115†	16:22:12.1	−49:57:20.77	2.5 (2)	A	Y	N	N	N	Y
G333.772−0.010†	16:22:00.3	−49:50:15.79	5.2 (1)		Y	N	Y	N	Y
G333.773−0.258†	16:23:06.2	−50:00:43.31	3.5 (2)	A	Y	Y	Y	N	Y
G333.818−0.303†	16:23:30.0	−50:00:41.97	3.4 (2)		Y	N	Y	N	Y
G333.900−0.098	16:22:57.3	−49:48:35.60	4.2 (2)	MSA	Y	Y	Y	N	Y
G333.930−0.133	16:23:14.5	−49:48:45.94	3.1 (2)	MWA	Y	Y	Y	N	Y
G333.974+0.074†	16:22:31.4	−49:38:08.31	3.9 (2)	A	Y	N	Y	N	Y
G334.027−0.047†	16:23:16.7	−49:41:00.19	5.0 (1)	A_2	Y	N	Y	N	Y
G334.746+0.506†	16:23:58.0	−48:46:59.12	4.2 (1)	A	Y	Y	Y	N	Y

4.4 Discussion

4.4.1 Class I CH_3OH masers on a HMSF evolutionary timeline

In this subsection, we attempt to divide class I CH_3OH masers into 'non-evolved' or 'evolved' categories. Paper I briefly discusses class I CH_3OH masers with associated class II CH_3OH or OH masers; class I CH_3OH masers associated with either or both of these types of maser was assumed to be in a relatively late stage of HMSF. Paper I notes that the majority of class I CH_3OH masers lack these associations and therefore seem more likely to be associated with earlier stages of HMSF. With the additional sensitivity provided by the follow-up observations discussed in this chapter, we may also use radio recombination line (RRL) data to help discriminate HMSF regions between evolved and non-evolved stages. RRLs are associated with H II regions, which in turn tend to signpost further evolved stages of HMSF than class II CH_3OH masers (Walsh et al. 1998). Class I CH_3OH maser regions with detected H53α emission are listed in Table 4.3. We use the presence or absence of class II CH_3OH masers, OH masers and H53α emission to deem a 'region' as evolved or 'non-evolved'.

Fig. 4.2 shows the populations of class I masers with and without these tracers of evolved stages of star formation. Due to the additional discrimination provided by the presence of H53α, we find that class I CH_3OH masers tend to appear in more evolved regions, unlike Paper I. A large number of regions (17/77, 22 per cent) featuring H53α emission are all without class II CH_3OH and OH masers. Are there un-detected masers at these locations? The population of OH masers within the MALT-45 survey region are primarily from the catalogue of Caswell (1998); this survey allows detections to approximately 0.16 Jy, but Caswell (1998) note that the survey is not complete at this level, requiring emission across several channels or corroboration with other data. Additional masers from the SPLASH survey may reveal new associations (Dawson et al. 2014). Across the MALT-45 survey region, class II CH_3OH masers from the Methanol MultiBeam survey are complete to 0.17 Jy (Caswell et al. 2011). Given the good sensitivity of these surveys, it seems unlikely that undiscovered class II CH_3OH and OH masers are associated with these class I CH_3OH masers, but follow-up observations at these transitions may prove effective for finding new detections.

The population of class I CH_3OH maser regions without any evolved tracer is about a third of this sample; clearly, class I CH_3OH masers are still strongly associated with younger star-forming regions. In order to help identify relatively non-evolved regions of star formation, we discuss the properties of this sub-population.

In the following text, we qualitatively discuss infrared associations with non-evolved class I CH_3OH maser regions. Appendix B.3 shows infrared images toward each of the detected masers. It can be seen that many masers are cospatial with IRDCs. IRDCs are known sites of star formation, even HMSF, thus it is not surprising to find a large population of class I CH_3OH masers towards these locations. However, some slight differences appear between evolved and non-evolved regions. The non-evolved population appears to be more closely associated with dark infrared features, have less bright infrared counterparts, and generally have only one maser spot. A good example of the differences in the typical infrared properties of non-evolved and evolved sources can be seen on the same page in Appendix B.3 between G331.279−0.189 (evolved) and G331.370−0.399, G331.371−0.145, G331.380+0.149

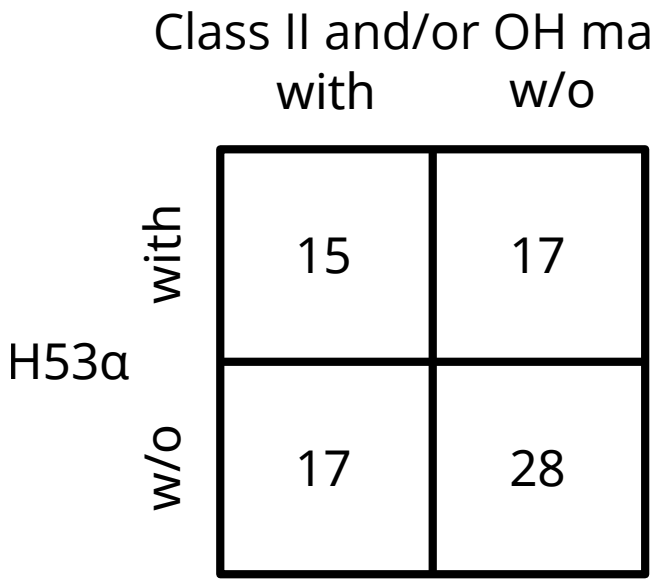

Figure 4.2: A diagram depicting the relative populations of evolved species associated with class I CH_3OH masers; in this chapter, evolved regions of class I CH_3OH are associated with a class II CH_3OH or OH maser, or H53α emission. The majority of sources are evolved (49/77, 64 per cent).

and G331.409−0.164 (non-evolved). G331.279−0.189 appears to have dark infrared lanes coalescing into a region with excess extended green emission, coincident with class II CH_3OH, H_2O and OH masers, surrounded by class I CH_3OH masers. In contrast, the four non-evolved regions are all associated with dark infrared regions, although there is little else in the infrared to pin-point or identify these as masing regions.

One extreme exception is G330.931−0.260; two maser spots are detected towards the end of what appears to be an extended and diffuse photon-dominated region. No other masers are detected, and no dark infrared regions apparent, but an infrared feature at G330.938−0.255 might be the powering source.

The three regions with class I CH_3OH maser emission detected in auto- but not cross-correlation data are also within the non-evolved population. G331.72−0.20 and G333.24+0.02 appear to be typically associated with dark infrared regions, but G331.44−0.14 lacks any obvious infrared feature; it may be an example of a region without star-forming activity.

Fig. 4.3 shows that 31 of 74 (42 per cent) of class I CH_3OH masers have an associated OH maser, and that maser regions featuring only one or two class I CH_3OH maser spots are particularly unlikely to have an OH association. Those with eleven, twelve or thirteen spots all have an association. To check if there is a significant difference between class I CH_3OH maser regions with and without an associated OH maser, we have performed a Kolmogorov-Smirnov (KS) test on the two samples, and find there is a 2.6 per cent probability that they are drawn from the same distribution. This supports the assertion that class I CH_3OH masers with more spots tend to be associated with OH masers. This relationship between class I CH_3OH maser spot counts and OH maser association helps to explain why evolved class I CH_3OH maser regions have larger projected linear sizes and velocity spreads in Fig. 4.4; more spots indicate more maser activity, presumably driven by a relatively evolved region of HMSF.

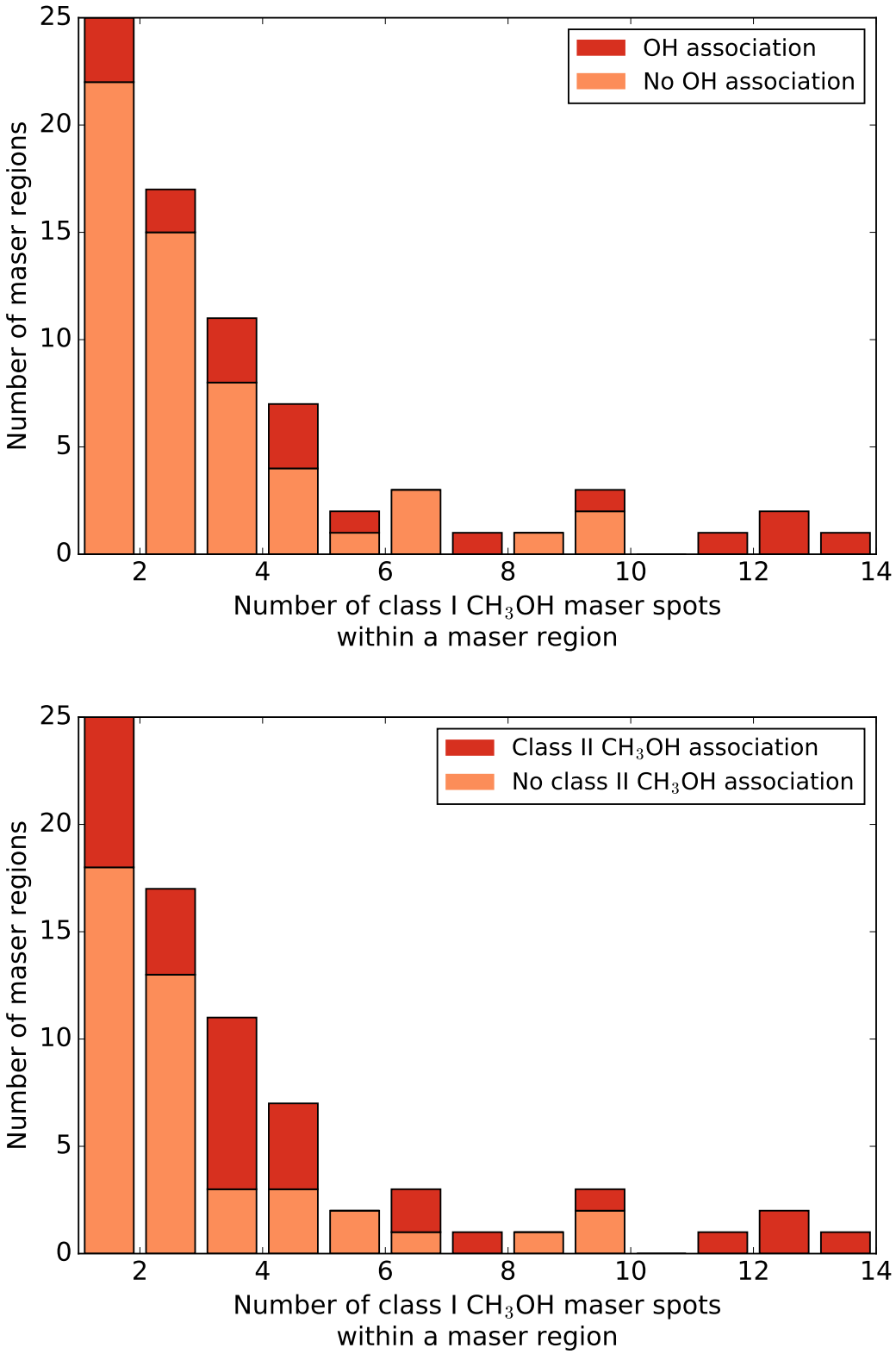

Figure 4.3: Histograms of class I CH_3OH maser spot counts within each maser region, highlighting associations with and without an OH or class II CH_3OH maser. The majority of class I CH_3OH maser regions with only one or two spots do not have an associated OH or class II CH_3OH maser, but there is a tendency for more associations in regions with more class I CH_3OH maser spots. A KS test on the samples with and without an OH maser association has a 2.6 per cent probability that the two samples are drawn from the same underlying population. Another KS test using the samples with and without an associated class II CH_3OH maser shows a 1 per cent probability of not being distinct.

This type of comparison was also performed with class II CH_3OH masers. Another KS test finds that there is 1 per cent probability that the samples of class I CH_3OH masers with and without an associated class II CH_3OH maser are not distinct. It seems that the number of detected class I CH_3OH maser spots is a good indication of the presence of other masers, and hints at the evolutionary phase of the host region (evolved enough to feature class II CH_3OH or OH masers, or neither).

MALT-45 observations provided the initial detections of the class I CH_3OH masers detailed in this paper. With only a few possible exceptions, each of the class I CH_3OH masers identified by MALT-45 appear to be associated with HMSF. Further observations will isolate more non-evolved star-forming regions, and purely through masers, identify HMSF in its early stages. In addition to isolating a non-evolved population, the number of class I CH_3OH maser spots detected can hint at the evolutionary stage of the region.

4.4.2 Properties of detected class I CH_3OH masers

Using the information gathered from these observations, we conduct analyses of the basic properties of class I CH_3OH masers. Fig. 4.4 shows the luminosities, projected linear sizes and velocity spreads of these masers. Luminosities are determined from the integrated intensity of auto-correlated emission, calculated by Gaussian fits to maser spectra. The projected linear size is calculated using the angular size of maser emission across a region and its derived kinematic distance. Velocity spread simply refers to the difference between the most redshifted and blueshifted emission within a single region.

The histogram in Fig. 4.4 presents luminosities of class I CH_3OH masers, highlighting the evolved and non-evolved regions. The distribution of luminosities has a peak around $10^{-6.25}\,L_\odot$. There are 57 maser regions with luminosities less than $10^{-5.75}\,L_\odot$, of which 26 are classified non-evolved (46 per cent). The remainder of the histogram ($L > 10^{-5.75}\,L_\odot$) has only 2 non-evolved maser regions out of 20 (10 per cent). Thus, class I CH_3OH masers in non-evolved regions tend to have lower luminosities.

G332.240−0.044 is the outlying non-evolved maser region with a high luminosity ($L > 10^{-5}\,L_\odot$); unlike other non-evolved regions, there are many maser spots associated with this region, concentrated about a bright infrared feature embedded in an IRDC. This may be an example of a region about to produce class II CH_3OH maser emission, given the infrared appears similar to other regions with class II CH_3OH masers.

Fig. 4.4 compares the projected linear sizes and velocity spreads of class I CH_3OH masers. The majority of sources have small projected linear sizes (<0.5 pc) and small velocity spreads ($<5\,\mathrm{km\,s^{-1}}$). Non-evolved sources have particularly small projected linear sizes and velocity spreads (mostly <0.2 pc and $<3\,\mathrm{km\,s^{-1}}$). KS tests were performed on both samples of projected linear sizes and velocities; the probability that each sample is drawn from the same distribution is 0.3 per cent and 1.5 per cent, respectively. Voronkov et al. (2014) also perform this comparison for a sample of class I CH_3OH masers, and observe a similar distribution to ours (Fig. 5 of their paper). However, one large difference between the comparison presented here and that of Voronkov et al. (2014) is that average velocity spread of Voronkov et al. (2014) is between 5 and $10\,\mathrm{km\,s^{-1}}$. This is likely due to the sample of class I CH_3OH masers used by Voronkov et al. (2014) being typically biased toward class II CH_3OH masers.

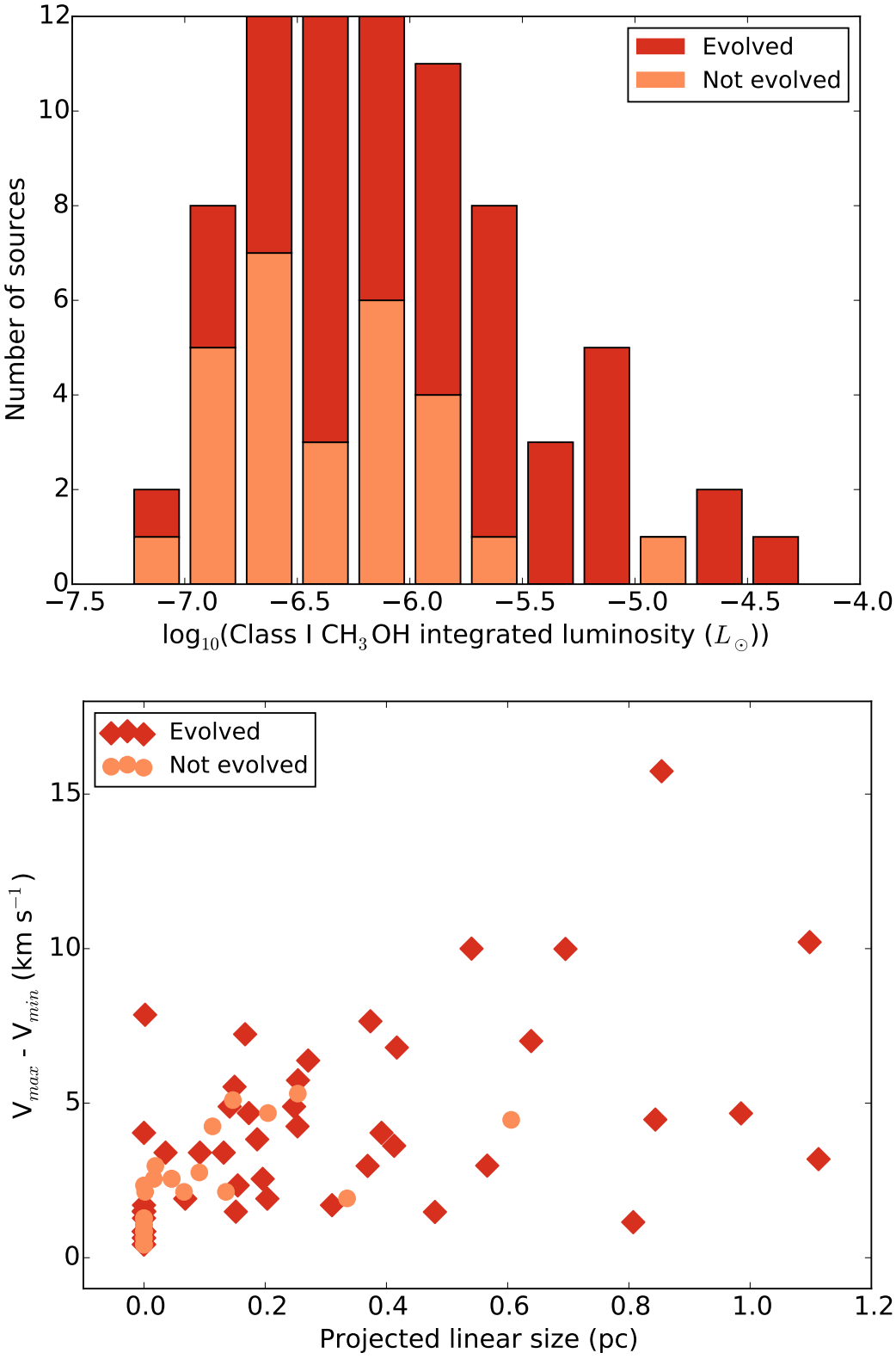

Figure 4.4: Luminosities, projected linear sizes and velocity spreads of class I CH_3OH maser regions. The distribution of luminosities approximates a Gaussian, with a peak around $10^{-6.25}\,L_\odot$. The majority of maser regions have small project linear sizes and velocity spreads. Regions that are not evolved tend to have lower luminosities and smaller projected linear sizes and velocity spreads.

Voronkov et al. (2014) also indicate the presence or absence of an OH maser in their sample, and find that class I CH_3OH masers without an associated OH maser are confined to small projected linear sizes (<0.4 pc) and velocity spreads (<10 km s^{-1}). Thus, despite being biased toward class II CH_3OH masers, the class I CH_3OH masers observed by Voronkov et al. (2014) have larger projected linear sizes and velocity spreads only when associated with OH masers; this corroborates the trend seen in Fig. 4.4.

The spatial distributions of class I CH_3OH masers have been discussed in literature, but typically use a common reference point, such as a H II region or class II CH_3OH maser, to determine the extent of maser emission. The distribution shown in Fig. 4.4 is without a reference point, instead using the maximum distance between any two spots in a maser region. To compare the results of the masers found in this chapter with other investigations using a reference point, the projected linear offsets between class I CH_3OH masers and other masers associated with star formation is presented in §4.4.3.1.

Six maser regions can be seen with a linear size greater than 0.8 pc; these regions are G330.876−0.362, G331.279−0.189, G331.492−0.082, G331.503−0.109, G331.530−0.099 and G333.558−0.293. Upon inspection of the distribution of these masers and the location of infrared emission within these regions, it is likely that not all the class I CH_3OH masers are related to a single high-mass object; see Appendix B.3. G330.876−0.362 has only two spots, very distant from each other; one is closely associated with class II CH_3OH, H_2O and OH masers, the other with an infrared dark cloud (IRDC). G331.279−0.189 has a single maser spot very distant from the rest of the relatively clustered spots, but this spot may not be powered by the same obvious infrared source. G331.492−0.082 has two groups of spots; both are very compact, but widely separated from each other and have different infrared colours. G333.558−0.293 has the largest projected linear distance between two individual spots; however, the infrared emission toward it reveals what appears to be a different IRDC associated with each, implying different powering sources. The case for G331.503−0.109 and G331.530−0.099 is unclear; they are well separated, however, there is a strong H_2O and OH maser source located at G331.512−0.100 that lies between the two class I CH_3OH masers in question, and so may be the powering source. Further observations are needed to resolve the true nature of these masers.

While it is difficult to disentangle the origin of each maser spot, it seems that the large offsets between spots are rare, and those maser regions showing large offset may be due to multiple independent maser sites within. This in turn strengthens the argument that class I CH_3OH maser regions tend to have small projected linear sizes and velocity spreads. While these masers are collisionally-excited, they are perhaps tracing weak shocks rather than powerful ones. We expect stronger shocks to at least have broad velocity coverage. An indication of regions where more powerful shocks are present may be gleaned by the presence of thermal SiO, or even more evolved maser species such as class II CH_3OH or OH.

4.4.3 Comparing class I CH_3OH masers with other masers and thermal lines

Paper I investigated associations of class I CH_3OH masers with class II CH_3OH, H_2O and OH masers. As Paper I used class I CH_3OH maser positions from auto-correlated data, the

positional uncertainty is much higher than these data. Maser associations within 60 arcsec between each of the four species can be seen as a Venn diagram in Fig. 3.20 of Paper I. The same analysis was carried out with these data, but with a maximum association range of 45 arcsec, to better associate masers from the same source; the resulting populations within each intersection of the same Venn diagram changes only very slightly (1 or 2 differences in some intersections). Consequently, MALT-45 observations accurately reveal the maser associations toward class I CH_3OH masers. However, high-resolution data are required to accurately compare the projected linear distances between masers and accurately associate masers with other objects, such as IRDCs and dust continuum sources.

4.4.3.1 Separation from other maser species in star-forming regions

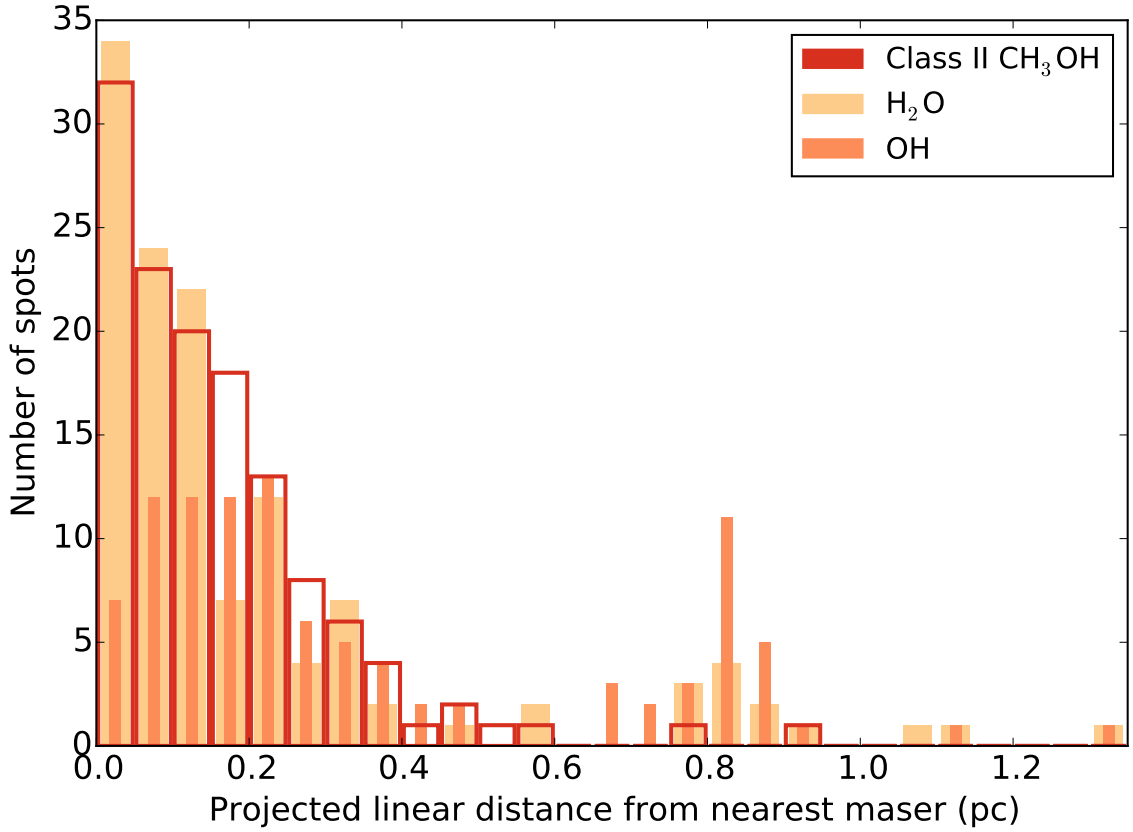

Figure 4.5: Histogram of the projected linear distance between every class I CH_3OH maser spot position and class II CH_3OH, OH and H_2O masers. This histogram uses the projected distance between masers only when their angular offset is less than 60 arcsec. The majority of projected linear distances to masers are located within 0.5 pc, and a second population appears around 0.8 pc.

Projected linear distances between every class I CH_3OH maser spot and class II CH_3OH, OH and H_2O masers are calculated and presented in Fig. 4.5. The other star formation maser positions were gathered from Caswell et al. (2011); Sevenster et al. (1997); Caswell (1998); Breen et al. (2010a); Walsh et al. (2014). Masers were only considered up to 60 arcsec away. If more than one of the same type of maser are within 60 arcsec of a class I CH_3OH maser spot, only the closest was used comparison.

Most projected linear distances are less than 0.5 pc. Kurtz et al. (2004) find that the distance between class I CH_3OH masers and H II regions tend to be within 0.5 pc, agreeing with our results. Voronkov et al. (2014) were able to model an exponential decay to the number of class I CH_3OH masers with distance from class II CH_3OH masers; with their larger sample size, they see many masers at projected linear distances beyond 0.5 pc. However, the vast majority are within 0.5 pc, also agreeing with our results. Given that our maser spots are derived from an unbiased sample, it seems that typical regions of HMSF power class I CH_3OH maser activity within a radius of 0.5 pc.

There is a small, isolated population of projected linear distances around 0.8 pc, particularly with OH masers. The class I CH_3OH maser regions comprising projected linear distances between 0.65 and 0.95 pc to OH masers are: G330.876−0.362, G331.279−0.189, G331.503−0.109, G333.121−0.433, G333.126−0.439, G333.595−0.211 and G333.900−0.099. Of these regions, G330.876−0.362 and G331.279−0.189 have been discussed in §4.4.2 as examples of maser regions without a single, common high-mass object. Thus, Fig. 4.5 may be providing misleading information for projected linear distances at ∼0.8 pc; the class I CH_3OH maser regions in question may not be associated with the OH maser. The remaining regions are discussed in the following text. Figures contained within Appendix B.3 aid to clarify the spatial association of the masers in question.

G331.503−0.109 includes four class I CH_3OH maser spots, with one very distant from the others. The three spots are clustered at a projected linear distance of ∼0.85 pc to the OH maser, while the fourth spot is at a distance of 1.4 pc (the largest of all offsets within 60 arcsec). Infrared GLIMPSE images hint that all masers appear to be associated with the same cloud, although this requires further investigation to determine the truth. If the class I CH_3OH masers are related to the location featuring both OH and H_2O masers, the powering source influences gas at large offsets. This may also explain the class I CH_3OH maser emission seen at G331.530−0.099; the maser spot from this region nearest to the OH maser is at a projected linear distance of 1.1 pc. The other spots are further than 60 arcsec from the OH maser, and have a linear distribution.

G333.121−0.433 and G333.126−0.439 are both at projected linear distances ∼0.8 pc from the same OH maser region located at G333.135−0.432. Each of these class I CH_3OH maser regions appear to be closely associated with their own distinct class II CH_3OH masers. As the OH maser in question is cospatial with another class II CH_3OH maser, and features its own nearby class I CH_3OH masers, it seems likely that this is an independent HMSF region from the other class I CH_3OH maser regions. While it is possible that the source powering the OH maser could also power the class I CH_3OH masers at these large distances, the whole region (located within the G333 giant molecular cloud) is obviously a complex, evolved region of HMSF, making interpretation of cause-and-effect difficult.

The class I CH_3OH masers located at G333.595−0.211 appear near to a very bright H II region. This region features 1612, 1665 and 1667 MHz OH masers, as well as H_2O masers, although all at projected distances ∼0.8 pc from the class I CH_3OH masers. Interestingly, CS (1–0) emission from MALT-45 peaks at the location where class I CH_3OH masers are detected.

Unlike the other maser regions discussed, G333.900−0.099 has few class I CH_3OH maser

spots. Only two spots are detected on either side of a class II CH_3OH maser. The OH maser is at a distance $\sim$0.8 pc from these masers, and appears cospatial with an infrared star in GLIMPSE. Given the small number of spots and the presence of a star at the same location as the OH maser, we do not believe a connection exists between the OH maser and class I CH_3OH masers here.

In general, maser associations are well characterised within distances of 0.5 pc. Genuine associations with distances exceeding 0.5 pc seem to be rare, and perhaps limited to powerful, evolved regions of HMSF.

4.4.3.2 Velocities

The peak velocities of class I CH_3OH masers in auto-correlated data are compared with class II CH_3OH masers, thermal CS, SiO and CH_3OH in Fig. 4.6. We discuss the resulting distributions in the following text.

Voronkov et al. (2014) used a large sample of class I and class II CH_3OH masers to investigate their relative velocities. Analysing the distribution of velocity differences between class I and class II CH_3OH masers, they find a peak velocity difference at $-0.57 \pm 0.07\,\mathrm{km\,s^{-1}}$ with a standard deviation of $3.32 \pm 0.07\,\mathrm{km\,s^{-1}}$ and a slight blueshifted asymmetry. The cause of the blueshift could not be attributed to either the class I or class II CH_3OH masers. The relatively wide spread of class II CH_3OH maser velocities is characterised by the proximity to a YSO; a greater dispersion is expected for molecules found near to the powering source.

The relevant distribution in Fig. 4.6 has the statistics $\mu = -1.17 \pm 0.87\,\mathrm{km\,s^{-1}}$, $\tilde{x} = -1.90\,\mathrm{km\,s^{-1}}$ and $\sigma = 4.75 \pm 0.61\,\mathrm{km\,s^{-1}}$ (μ is the mean, $\tilde{x}$ the median and σ the standard deviation). The parameters of this comparison are consistent with that of Voronkov et al. (2014). The median and mean are blueshifted, but the relatively large standard deviation diminishes their significance; the blueshift assertion requires a larger population to establish its validity. As the sample of Voronkov et al. (2014) is much larger than the one presented here, proving a systematic blueshift would be difficult to achieve.

The differences in peak velocity between class I CH_3OH masers and CS emission are: $\mu = 0.09 \pm 0.18\,\mathrm{km\,s^{-1}}$, $\tilde{x} = 0.04\,\mathrm{km\,s^{-1}}$ and $\sigma = 1.56 \pm 0.17\,\mathrm{km\,s^{-1}}$. Given that CS traces very dense gas ($n_c > 10^5\,\mathrm{cm^{-3}}$), the peak velocity of CS emission is likely closely related to the systemic velocity of a molecular cloud. Therefore, class I CH_3OH masers are also very good probes for these velocities. As we are probing very dense gas in star-forming regions, the CS emission may be optically thick, which may cause the peak velocity of CS emission to not reflect the systemic velocity. To help confirm CS as a reliable tracer of systemic velocities, we analysed the peak velocity of $C^{34}S$ emission. With only one exception, $C^{34}S$ was detected toward each observed class I CH_3OH region; the peak velocity of $C^{34}S$ emission agrees with the peak velocity of CS emission to within $0.5\,\mathrm{km\,s^{-1}}$. This rules out the possibility of optically thick CS emission having non-systemic peak velocities, and therefore peak CS velocities should be considered as more accurate systemic velocity tracers than class II CH_3OH masers.

Paper I presented a histogram of the velocity difference between peak velocities in class I CH_3OH masers and CS (1–0). The resulting mean was $0.0 \pm 0.2\,\mathrm{km\,s^{-1}}$ with a standard deviation of $1.5 \pm 0.1\,\mathrm{km\,s^{-1}}$, corroborating the results presented here.

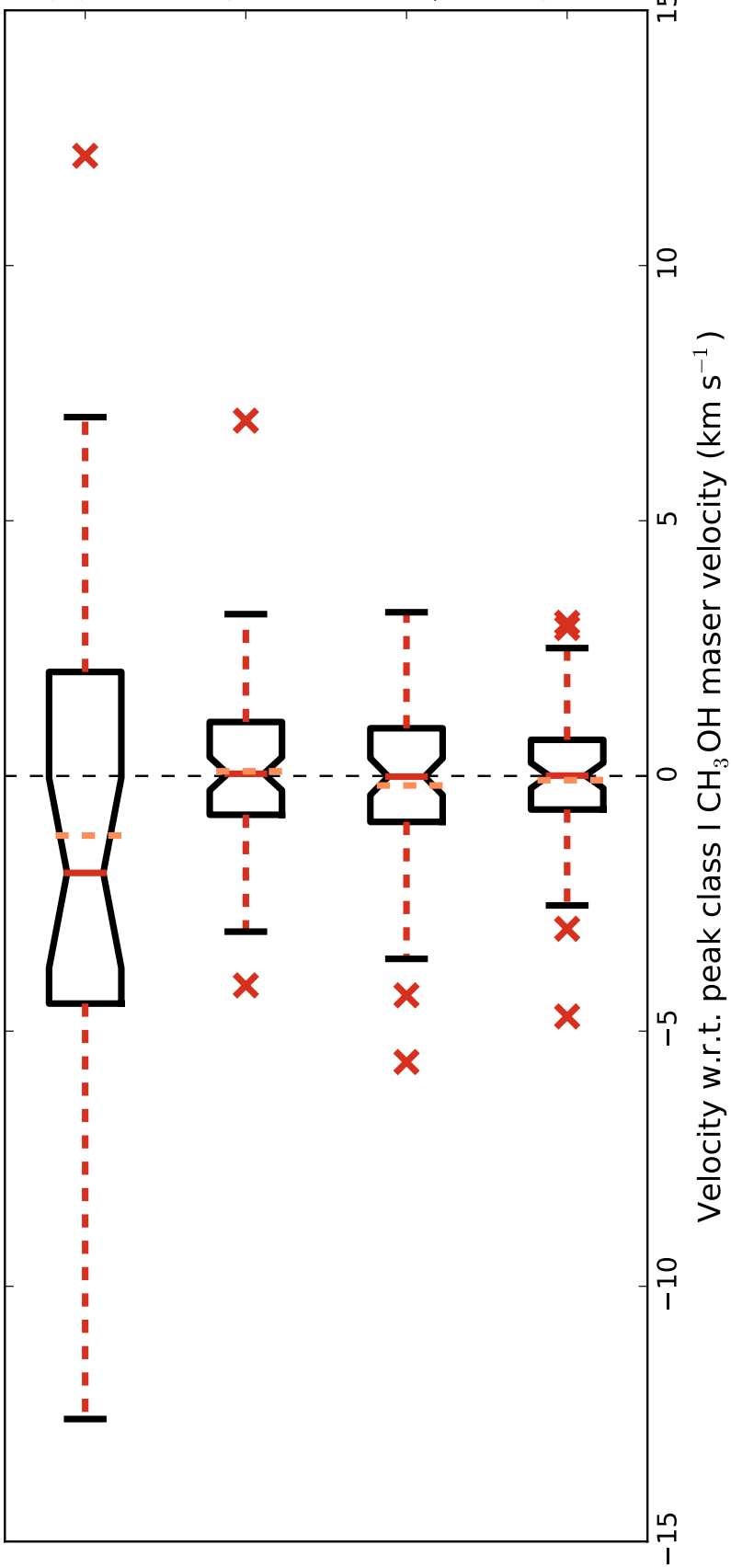

Figure 4.6: Notched box-and-whisker plot of peak velocity differences between class I CH_3OH masers and various species associated with star formation. The red solid vertical line within the boxes indicates the median, the lighter dashed lines the mean. The notched region about the median indicates the 95 per cent confidence interval on the median, and the box covers the interquartile region (IQR; middle 50 per cent of data). Whiskers extend past the IQR by up to 1.5×IQR. Red crosses indicate outlying data. The dashed black line indicates zero peak velocity difference. The class II CH_3OH maser box plot has a wide spread of velocity differences, while each of the other lines does not. CS, SiO and thermal CH_3OH velocities are all closely associated with the maser velocity.

The measured difference between SiO emission and class I CH_3OH maser velocities is similar to the difference between CS emission and class I CH_3OH maser velocities: $\mu = 0.17 \pm 0.20\,\mathrm{km\,s^{-1}}$, $\tilde{x} = 0.01\,\mathrm{km\,s^{-1}}$ and $\sigma = 1.64 \pm 0.14\,\mathrm{km\,s^{-1}}$. The distribution featuring SiO is slightly wider than that featuring CS, but uncertainties are too great to draw any conclusions. Overall, the peak velocities of class I CH_3OH masers and SiO emission closely agree.

The differences in velocity between the thermal 1_0–0_0 A^+ line of CH_3OH and class I CH_3OH masers has an even tighter association than the comparison featuring CS: $\mu = -0.08 \pm 0.15\,\mathrm{km\,s^{-1}}$, $\tilde{x} = 0.01\,\mathrm{km\,s^{-1}}$ and $\sigma = 1.33 \pm 0.11\,\mathrm{km\,s^{-1}}$. As a sufficient abundance of CH_3OH gas is needed for maser emission, it is perhaps not surprising that the thermal velocity is closely matched to the maser velocity. Given the distribution relative to CS, it seems that thermal CH_3OH is also a good tracer of systemic velocities.

The differences in the peak velocity for the thermal CS, SiO and CH_3OH spectral lines all appear similarly, with uncertainties of these peak difference being only a few $\mathrm{km\,s^{-1}}$. The distribution featuring velocity differences using class II CH_3OH masers, however, is broad and has a relatively distinct mean and median blueshift. This hints that the peak velocity of class II CH_3OH masers tend to be blueshifted from the systemic velocity, although the statistics presented above can not conclude this observation. One explanation of the blueshift is that class II CH_3OH masers are being detected in the foreground of star-forming regions rather than in the background; as these 6.7 GHz masers are the lowest frequency of all species considered here, they may be affected by optically thick emission close a high-mass star. This would especially be true for younger sources, which would be more optically thick from their higher densities.

4.4.3.3 Brightness

With a statistically-complete sample of class I CH_3OH masers and enhanced sensitivity to auto-correlated emission, the observations of this work have the opportunity to identify relations, if any, between the brightness of class I CH_3OH masers and other species associated with star formation. In this subsection, we use the auto-correlated integrated flux densities of class I CH_3OH maser emission for comparison. The results of comparing the integrated intensities of thermal CS, SiO and CH_3OH can be seen in Fig. 4.7.

The brightness of CS, SiO and thermal CH_3OH all show a positive correlation with the brightness of class I CH_3OH maser emission, although the degree scatter in each plot is large. The correlation coefficient (r-value) for the CS comparison is 0.41. Curiously, the data in the scatter plot featuring CS seem to be clustered about the median integrated flux density (IFD) of both species; this is more apparent on Fig. 4.7 with the use of a two-dimensional density histogram. Unlike the results seen here, the same comparison in Paper I does not appear to have a concentrated cluster (Fig. 3.12). The median CS integrated intensity is $1.3\,\mathrm{K\,km\,s^{-1}}$, with a median class I CH_3OH maser IFD of $9.9\,\mathrm{Jy\,km\,s^{-1}}$.

SiO (1–0) $v = 0$ is a tracer of strongly-shocked gas, primarily found in outflows. As class I CH_3OH masers are collisionally excited, albeit thought to be powered by weak shocks, a relationship between these species may exist. As discussed earlier, a brightness comparison with SiO was not possible in Paper I, due to their low detection rate and relatively weak

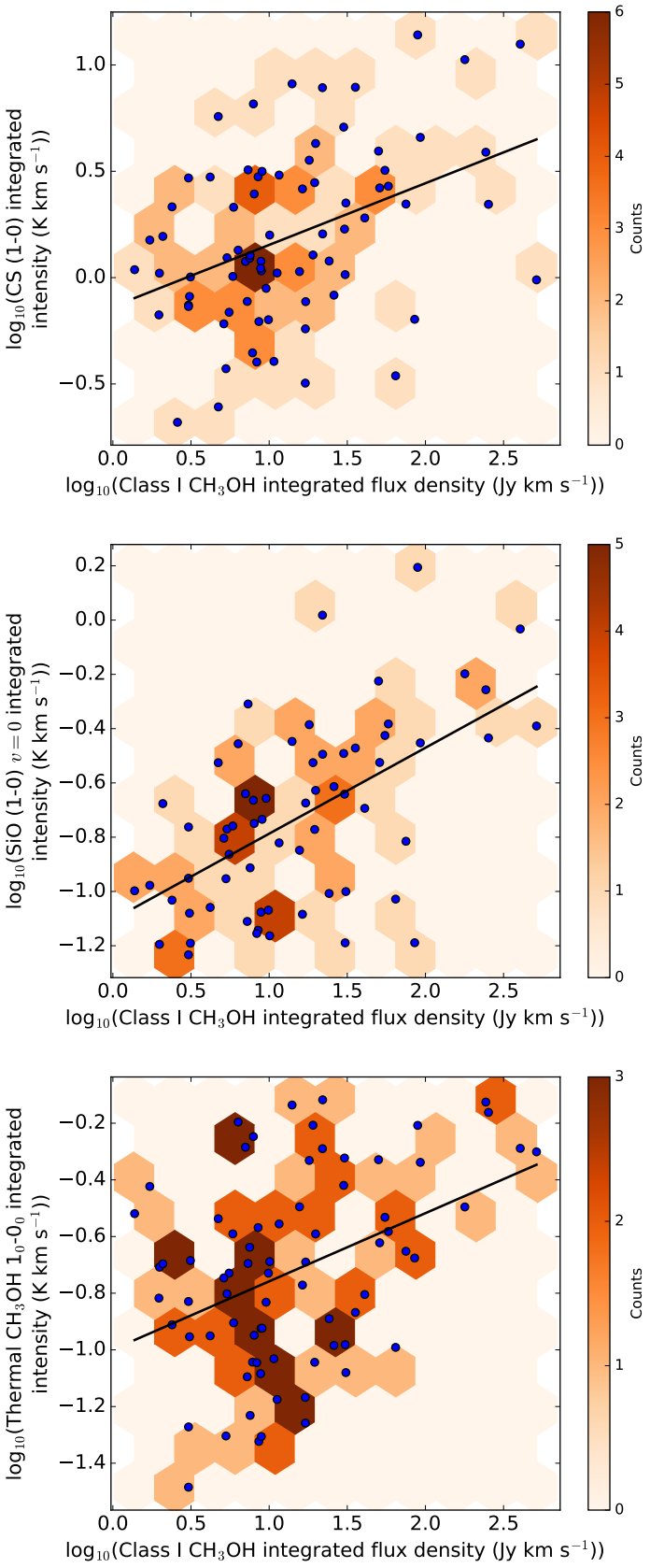

Figure 4.7: Scatter plots of class I CH_3OH maser integrated flux density against CS, SiO and thermal CH_3OH integrated flux densities. Hexagon tile colours represent the density of data, similar to a two-dimensional histogram. All three comparisons show a similar trend, but the degree of scatter is too large to draw any conclusions. Many data points for CS and SiO appear to cluster, indicating some values to be more typical than others.

intensities of SiO (1–0) $v = 0$. Consequently, Paper I speculates on the nature of the class I CH_3OH maser regions, given that the SiO detection rate was quite low (30 per cent). As the majority of regions now have confirmed SiO detections, it seems that a large portion of class I CH_3OH maser regions indeed have shocked gas within them. As bright SiO emission within these maser regions is rare, perhaps their faint intensities indicate weak shocks. The correlation coefficient (r-value) between the integrated intensity of SiO and IFD for class I CH_3OH maser emission is 0.57. SiO has a median integrated intensity of $0.18\,\mathrm{K\,km\,s^{-1}}$, and the median class I CH_3OH maser IFD is $12.8\,\mathrm{Jy\,km\,s^{-1}}$. As with the CS, these median values are close to the most clustered bin in panel 2 of Fig. 4.7.

Similar to SiO, comparisons with thermal CH_3OH was not possible in Paper I. The correlation here is the poorest, with a r-value of 0.40. Unlike the other thermal species, the degree of scatter in these data is so large that no clustering is apparent either. The median thermal CH_3OH integrated intensity is $0.20\,\mathrm{K\,km\,s^{-1}}$, with a median class I CH_3OH maser IFD of $10.1\,\mathrm{Jy\,km\,s^{-1}}$.

The correlation coefficients for each of the comparisons between class I CH_3OH masers and thermal lines is poor. If any significant relationship exists between the brightness of any two of these species, further analysis is required. It is possible that the beaming angle of the masers affects the observed flux-density, preventing a proper brightness comparison.

The luminosity of class I and class II CH_3OH masers was compared, but no correlation was observed, corroborating the results of Paper I. Class II CH_3OH masers are known to be brighter in further evolved regions of HMSF; if there was a relation between class I and class II CH_3OH masers, then the same might be true for class I CH_3OH masers. However, the brightness of class I CH_3OH masers is seemingly independent of the age of the host HMSF region.

4.4.4 Comparing class I CH_3OH masers with 870 μm dust continuum from ATLASGAL

The ATLASGAL survey maps 870 μm dust continuum emission across a large part of the Galactic plane ($330^\circ \leq l \leq 60^\circ$; Contreras et al. 2013; Urquhart et al. 2014b), including the MALT-45 region. This sub-millimetre emission is optically thin, tracing a cold, pre-YSO stage of HMSF, which can be used to infer column densities and clump masses.

The catalogue of Contreras et al. (2013) provides the location and integrated flux densities of 870 μm dust continuum emission point sources. Using these, we can investigate relationships between class I CH_3OH masers and 870 μm emission, such as the brightness of each and the typical clump mass a maser is found in. We associated any class I CH_3OH masers and ATLASGAL clumps within a projected angular offset of 60 arcsec, and list the associations in Table 4.3.

A histogram of projected linear distances between class I CH_3OH maser spots and 870 μm clumps is seen in Fig. 4.8. The vast majority of maser spots are within 0.4 pc of an ATLASGAL source. This is similar to the projected linear distances between class I CH_3OH maser spots and other star formation masers found in Fig. 4.5. Unlike the distances projected linear between masers, there appears to be no trend when highlighting evolved and non-evolved maser regions. Relatively few maser spots are within 0.05 pc of a 870 μm clump, with many

more having projected linear distances within 0.15 pc.

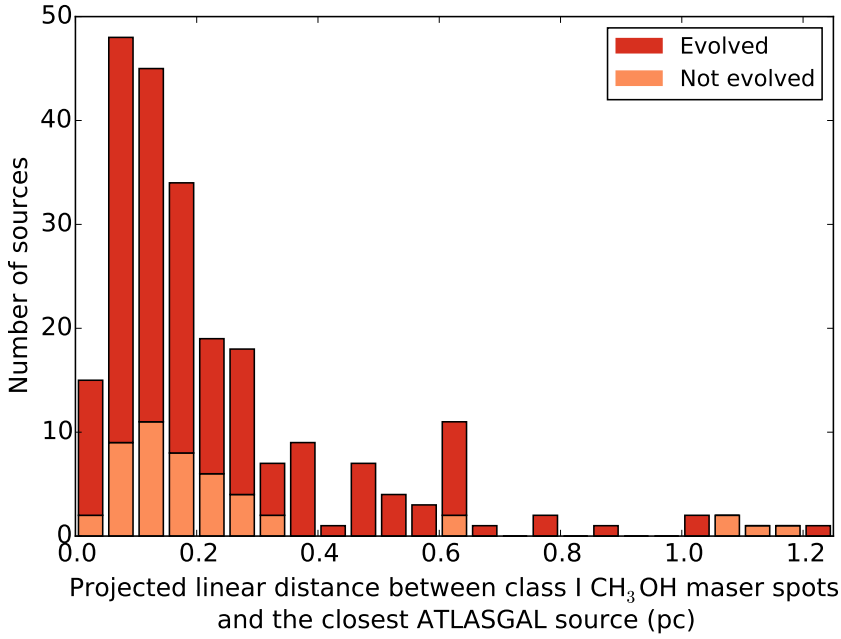

Figure 4.8: A histogram of offsets between ATLASGAL clumps and flux-weighted average positions of class I CH_3OH masers. The majority of associations have projected linear distances less than 0.4 pc, and almost all are less than 0.6 pc. This indicates a strong relation between the region containing the ATLASGAL source and class I CH_3OH maser emission. A small population also exists with projected linear distances larger than 1 pc. Note that for each class I CH_3OH maser, if multiple ATLASGAL sources are present within 60 arcsec, only the closest was used.

Note that Fig. 4.8 includes any ATLASGAL clump within 60 arcsec from a maser spot. Maser regions without ATLASGAL associations are discussed in §4.4.4.1.

Chen et al. (2012) and Urquhart et al. (2013) estimate clump mass with the integrated intensity of millimetre-wavelength continuum emission, assuming the emission is optically thin. In the same manner, we use ATLASGAL data to estimate clump masses via:

$$M_{gas} = \frac{S_\nu D^2 R_d}{\kappa_d B_\nu \left(T_{dust}\right)} \tag{4.1}$$

where M_{gas} is the mass of the gas, S_ν is the integrated flux density of ATLASGAL 870 μm emission, D is kinematic distance to the maser, R_d is the ratio of gas and dust masses, κ_d is the mass-absorption coefficient per unit mass of dust, and $B_\nu\left(T_{dust}\right)$ is the Planck function at temperature T_{dust}. Urquhart et al. (2013) justify the choice of $T_{dust} = 20$ K and $\kappa_d = 1.85\,\mathrm{cm^2\,g^{-1}}$, which we also use here. We also assume $R_d = 100$. The assumption of a single dust temperature is not realistic, but in the absence of temperature measurements toward every individual region, it is a necessary assumption. Pandian et al. (2012) find the kinetic temperature of gas in regions with class II CH_3OH masers, determined by NH_3 observations, have mean and median values of 26 and 23.4 K, respectively. Urquhart et al. (2011) also find mean and median temperatures toward high-mass YSOs to be 22.1 and 21.4 K, respectively. If we instead assume a dust temperature of 25 K, masses will decrease to 73 per cent of those determined with 20 K. Using a temperature of 15 K increases masses by

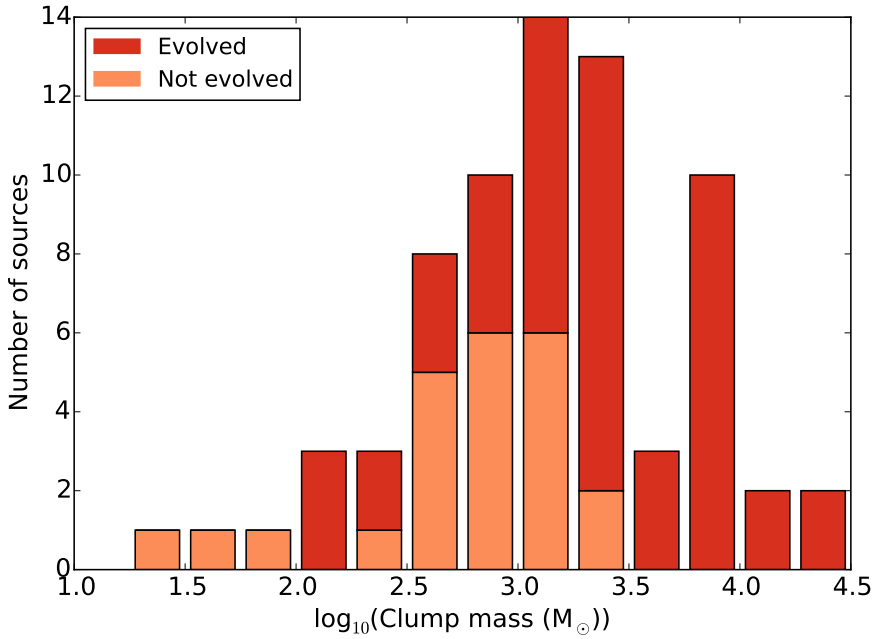

Figure 4.9: A stacked histogram of clump masses associated with class I CH_3OH masers, determined by using 870 μm ATLASGAL dust continuum emission. The distribution peaks between 10^3 and $10^{3.5}$ $M_\odot$, but has a wide spread of low- and high-mass clump associations. The highest mass values are restricted to evolved masers regions, while the lower masses tend to have non-evolved maser regions.

56 per cent relative to the 20 K masses. These uncertainties are comparable to those given by the kinematic distances, so we use a T_{dust} of 20 K. The histogram of determined masses can be seen in Fig. 4.9.

Class I CH_3OH masers appear to be associated with a wide range of clump masses ($10^{1.25} < \frac{M}{M_\odot} < 10^{4.5}$). This is not unexpected; we knew of associations with low-mass star formation as well as non-star-forming phenomena. Unfortunately, this analysis fails to help isolate or predict where class I CH_3OH maser emission can occur. Non-evolved class I CH_3OH maser regions have masses up to $10^{3.5}$ $M_\odot$, but tend to have lower mass values, and evolved maser regions dominate masses larger than $10^{3.25}$ $M_\odot$.

Fig. 4.10 shows the comparison between the IFD of ATLASGAL clumps and the IFD class I CH_3OH masers, but no significant correlation was found. Chen et al. (2012) performed a similar comparison, using 95 GHz class I CH_3OH masers towards Bolocam Galactic Plane Survey (BGPS) 1.1 mm thermal dust emission (Fig. 6 of their paper). They find a strong correlation between the maser luminosity and clump mass, with a p-value of 8.1×10^{-13} and r-value 0.84. Our line of best fit has the coefficients $r = 0.43$, $p = 1.6\times10^{-4}$, and is shown on Fig. 4.10. The Chen et al. (2012) sample may have a significant correlation due to the selection bias of targeting BGPS sources.

Fig. 4.10 shows a comparison between the IFD of ATLASGAL sources and class I CH_3OH masers, but any correlation is unlikely. Further analyses were conducted with projected linear distances and integrated intensities, but no correlation is found in any comparison. While class I CH_3OH masers are often found towards ATLASGAL clumps, their properties are seemingly independent of the sub-millimetre dust emission. Again, this may be related to the nature of

maser amplification, i.e. the beaming angle being different in each region. Unlike the maser emission, the integrated intensity of CS (1–0) demonstrates a close relation with the IFD of 870 μm dust emission; Fig. 4.11 shows this comparison and finds a correlation coefficient $r = 0.84$. As the correlation between the brightness of CS and class I CH_3OH maser emission is also weak, the brightness of class I CH_3OH masers seems difficult to predict with respect to other star formation tracers.

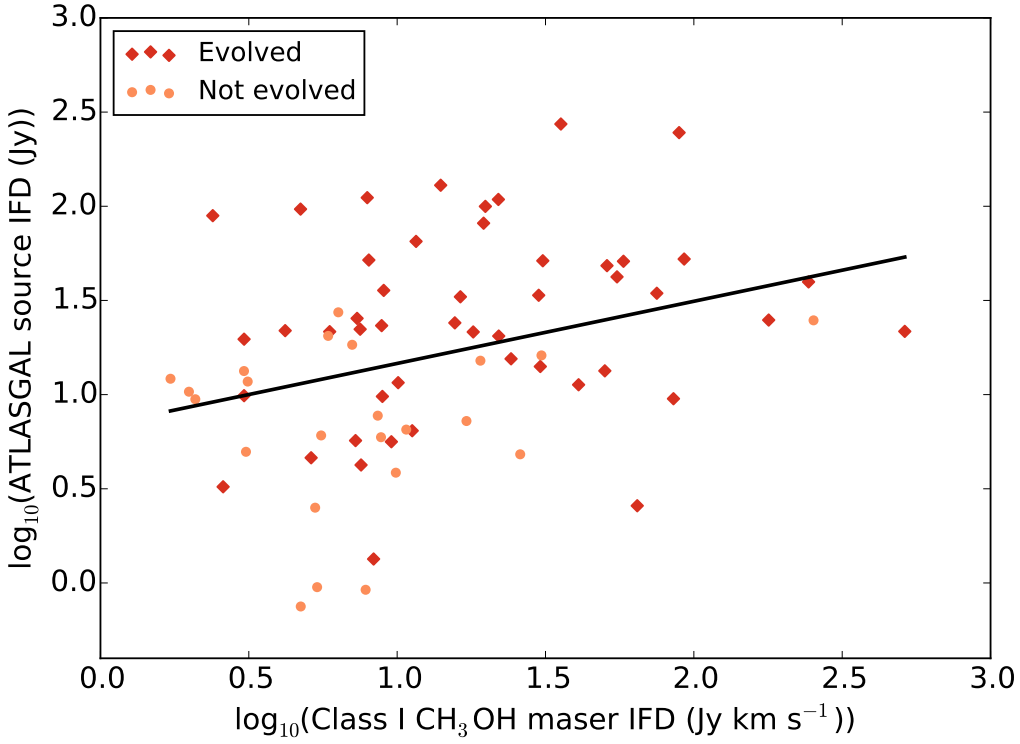

Figure 4.10: Scatter plot of integrated flux densities from ATLASGAL and class I CH_3OH maser regions. The correlation is very poor with a r-value of 0.33.

4.4.4.1 Class I CH_3OH masers without associated ATLASGAL emission

Of all the ATLASGAL clumps provided by the catalogue of Contreras et al. (2013), only four class I CH_3OH maser regions are without an associated ATLASGAL clump: G331.371−0.145, G331.442−0.158, G333.772−0.010 and G333.818−0.303. Using the data provided by the ATLASGAL team, we are able to investigate the 870 μm emission in each of these regions. Within ∼12 arcsec, G331.371−0.145, G331.442−0.158 and G333.818−0.303 each have peak ATLASGAL flux densities of 0.41, 0.63 and 0.23 Jy beam^{-1}, respectively. The ATLASGAL sensitivity over the MALT-45 area is approximately 60 mJy beam^{-1}. Point sources were classified by the source extraction algorithm SExtractor. Despite the pixel values of 870 μm dust emission toward these three maser regions being at least 3σ, SExtractor has most likely not been satisfied with a spatial morphology criterion. However, we do consider the 870 μm emission at these locations to be genuine. For these three regions, we determine the IFD of 870 μm emission to be 0.57, 0.28 and 0.24 Jy, respectively. Using Equation 4.1, these values correspond to clump masses of 85, 40 and 15 $M_\odot$, respectively. These masses are

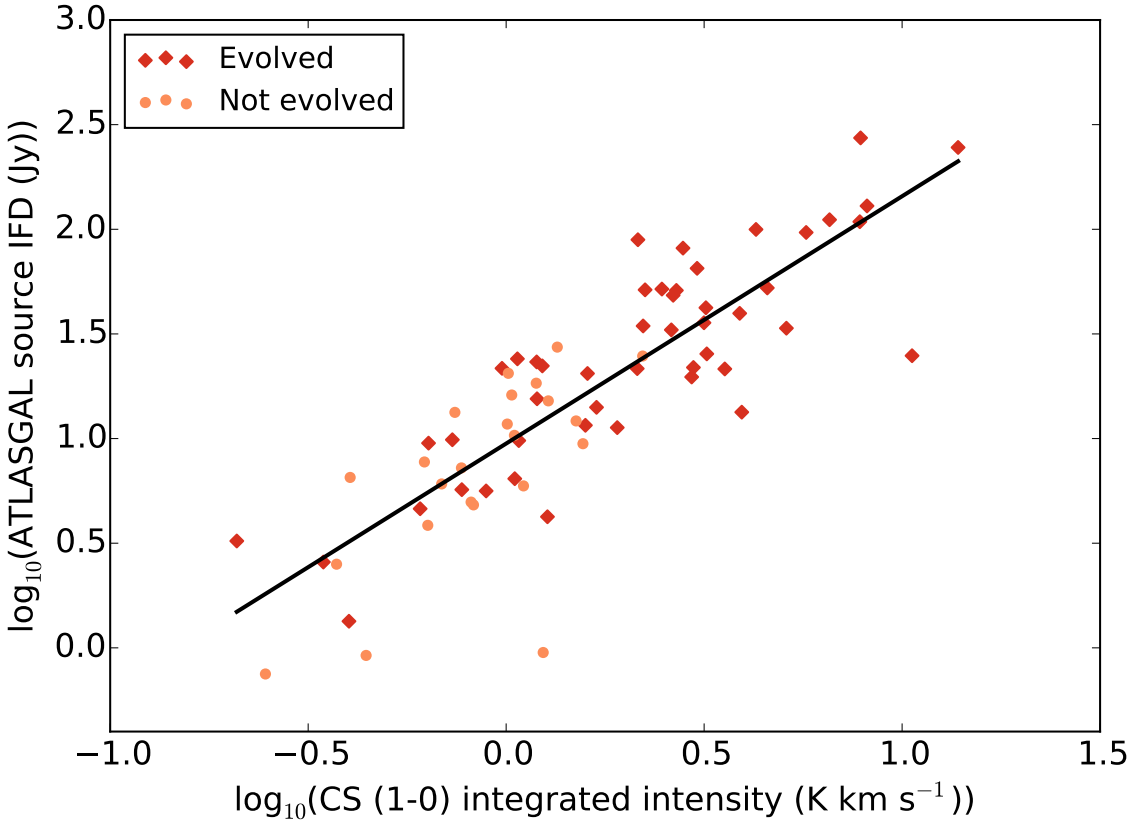

Figure 4.11: Scatter plot of integrated flux densities from ATLASGAL and CS emission from class I CH_3OH maser regions. A strong correlation is apparent with a r-value of 0.84. As the integrated intensity of the dust emission is directly proportional to clump mass, CS appears to be a good indicator of mass.

relatively low compared to those discussed in §4.4.4, but even lower masses were determined from integrated flux densities in the ATLASGAL catalogue.

The class I CH_3OH maser region G333.772−0.010 has a single pixel of 870 μm dust continuum emission with a peak flux density of 0.25 Jy beam^{-1} at a projected linear distance of ∼27 arcsec. However, unlike the other discussed regions of 870 μm emission, nearby pixels are relatively dim (<0.14 Jy beam^{-1}, ∼2σ), indicating this pixel is likely a random noise spike. Compared to other ATLASGAL sources at a similar distance (∼5.2 kpc), we might expect to see a similar distribution of 870 μm emission, but this is not the case. The class I CH_3OH maser emission is closely associated with compact infrared emission. Interestingly, the maser emission is strong (peak of 17.7 Jy, IFD of 11.7 Jy km s^{-1}). The lack of dust emission toward this maser region does not necessarily indicate non-star-forming mechanisms, as class II CH_3OH masers have also been detected without 870 μm emission (Urquhart et al. 2015).

4.4.5 Comparing class I CH_3OH maser emission in cross- and auto-correlation

Minier et al. (2002) and Bartkiewicz et al. (2014) discuss class II CH_3OH maser emission detected in very-long-baseline interferometry and single-dish/auto-correlation. These comparisons between cross- and auto-correlation data reveals a significant amount of flux being

resolved out; Bartkiewicz et al. (2014) report between 24 and 86 per cent. Naturally, an interferometer will resolve out any extended emission without adequate *uv*-coverage. The authors elaborate that the 'missing flux' is not dependant on distance, and that lower-resolution cross-correlation data have similar compact structures. This suggests that missing emission is quite diffuse, and is seemingly independent of the properties of compact maser emission. Minier et al. (2002) also attribute missing flux as being due to diffuse emission.

While these investigations were exclusively focused on class II CH_3OH masers, the observations detailed in this chapter are able to undertake a similar investigation for class I CH_3OH masers. It is worth noting that the observations of Minier et al. (2002) and Bartkiewicz et al. (2014) have a spatial resolution approximately two orders of magnitude smaller than ours, which may result in differences. Auto-correlation spectra for the CH_3OH masers were extracted using the method discussed in §4.2.1.2. Cross-correlation spectra were then plotted with their corresponding auto-correlation spectrum; three example regions are shown in Fig. 4.12. As stated earlier, the maximum detectable scale for these follow-up observations is approximately 4.6 arcsec.

The relative strength of compact maser emission to diffuse emission of a class I CH_3OH maser region was assessed by computing the ratio of cross-correlation IFD to auto-correlation IFD, i.e., if the cross-correlation IFD closely matches the auto-correlation IFD, the emission is compact. Fig. 4.12 shows a large variation in missing flux-density is across several regions. Fig. 4.13 attempts to quantify the ratio of cross-correlated IFD to auto-correlated IFD with a histogram, but no trends are apparent for evolved, non-evolved or total populations. The ratio of cross-correlated IFD to auto-correlated IFD was also compared against the flux-density of the masers, but no trend was observed. Class I CH_3OH emission can be strongly confined to compact structures (cross-correlated emission $\approx$ auto-correlated emission), extended (auto-correlated emission $\gg$ cross-correlated emission), or a combination of the two. This explains why three target regions were not detected in the cross-correlation dataset (G331.44−0.14, G331.72−0.20 and G333.24+0.02); their 44 GHz emission is likely too extended and lacks any bright, compact maser components.

To test if compact or diffuse regions can be separated, populations were investigated with and without various maser associations. These associations included class II CH_3OH, H_2O and OH masers, but no dependence was found for the proportion compact to diffuse maser emission with and without these associations. This proportion of compact to diffuse emission was also compared with thermal line integrated intensities in CS (1–0), SiO (1–0) $v = 0$ and CH_3OH 1_0–0_0; see Fig. 4.14. A similar trend can be seen in each comparison, however, the degree of scatter is too large to observe any correlation.

Any indication of class I CH_3OH emission being dominated by compact components or otherwise remains a mystery. Another star formation tracer may reveal a correlation with the property of maser strength discussed here. Further observations of class I CH_3OH maser regions with better sensitivity and *uv*-coverage will also help to identify weaker, more diffuse cross-correlation emission, in order to better understand the relationship between the diffuse and compact components of the CH_3OH maser emission.

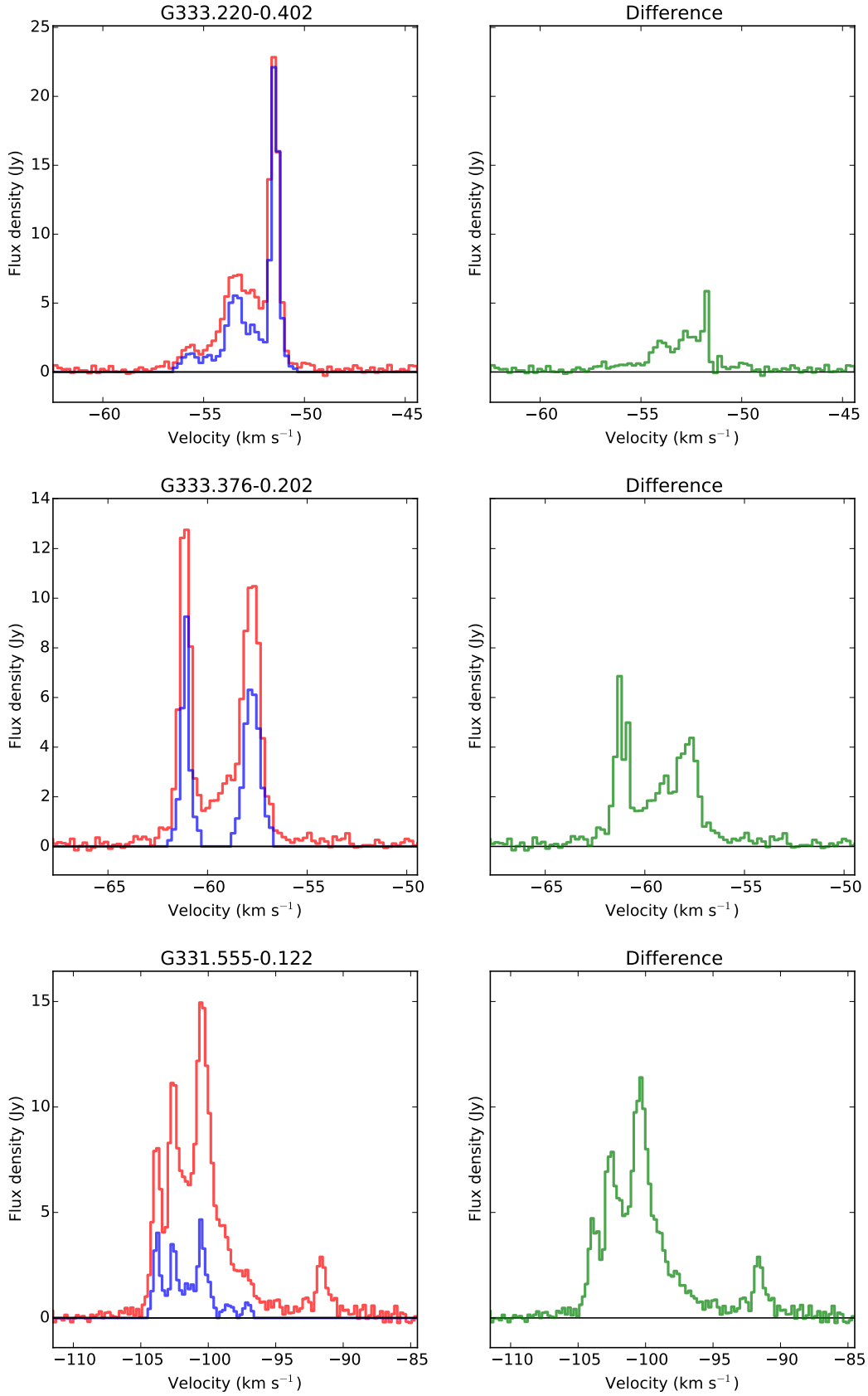

Figure 4.12: Cross- and auto-correlation spectra of three class I CH_3OH maser regions, with strong, moderate and weak maser strengths. Auto-correlation spectra are plotted red, cross-correlation spectra blue and the difference green. These comparisons allow maser strength determination for each region.

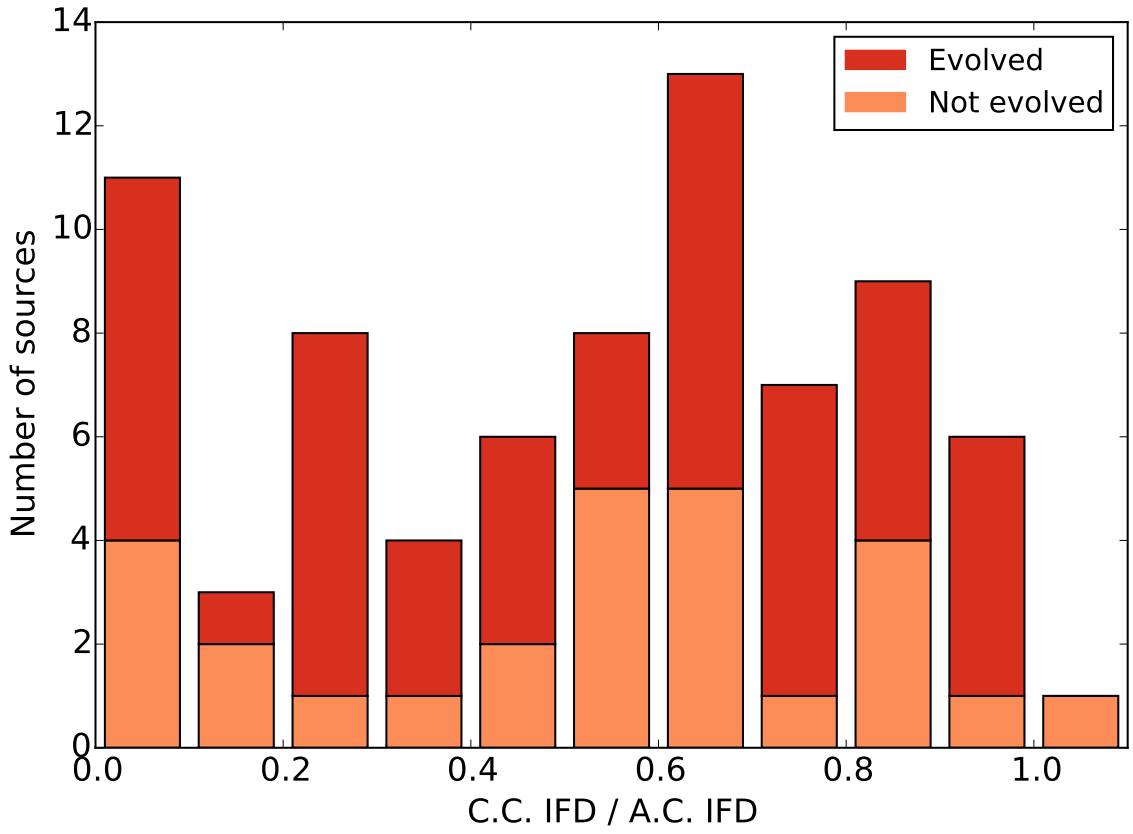

Figure 4.13: Histogram of the ratio of IFD in cross-correlation (C.C.) and auto-correlation (A.C.), for each class I CH_3OH maser region. No trend is apparent in the overall population, nor in evolved and non-evolved categories. The single datum with a ratio greater than one is due to an over-contribution of cross-correlation emission, due to spectral blending in nearby maser spots.

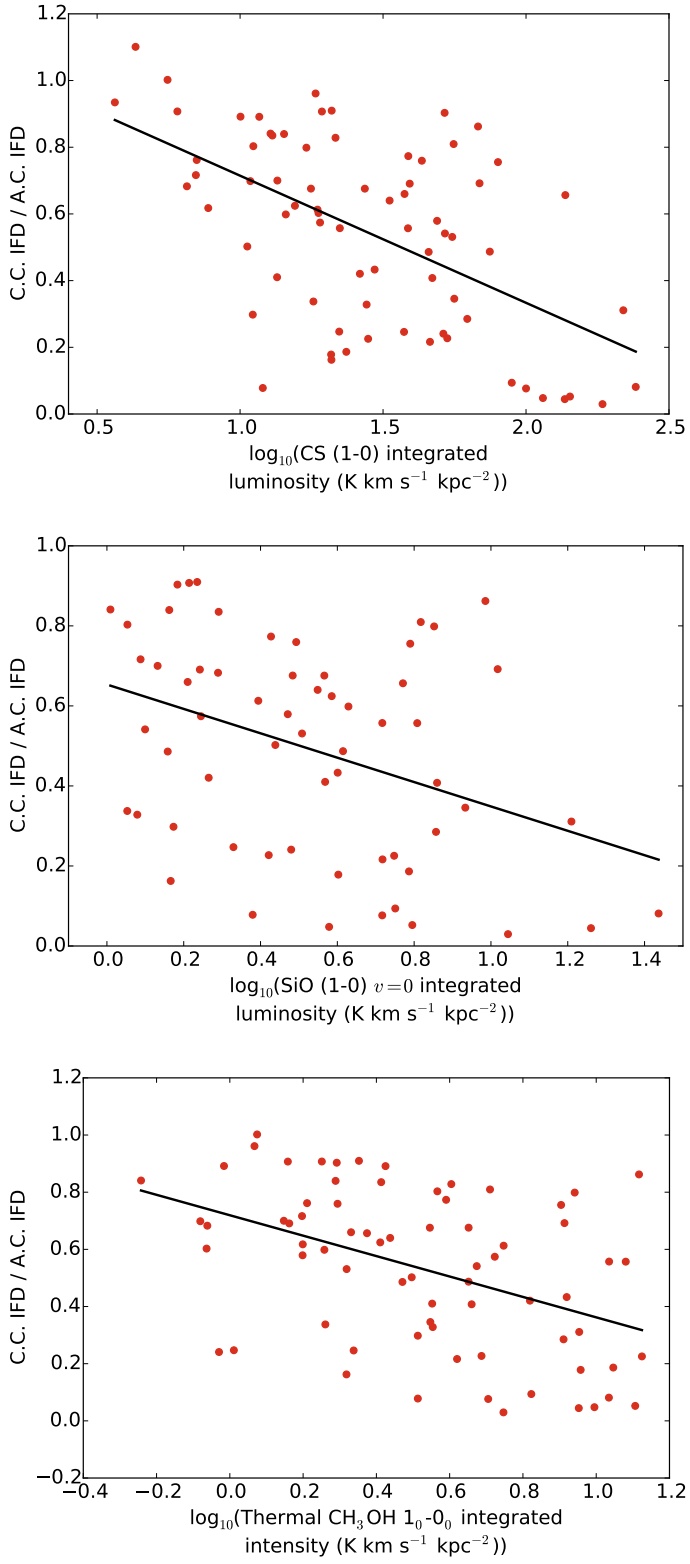

Figure 4.14: Scatter plots of the ratio of cross-correlation IFD to auto-correlation IFD (maser strength) against the thermal integrated intensity of CS, SiO and CH_3OH. The solid line represents the least squares fit. A similar, weak trend appears for all lines, but the large scatter hampers correlation (r-values of -0.55, -0.38 and -0.45, respectively). The single datum with a maser strength above 1 has an over-contribution of cross-correlation emission, due to spectral blending in nearby maser spots.

4.5 Summary and conclusions

We have extracted high-resolution positions, flux-densities and velocities for class I methanol masers detected in the MALT-45 survey, and presented various properties for each observed region. The unbiased population from MALT-45 provides the first opportunity to assess class I methanol masers free from other selection biases, such as class II methanol masers or extended green objects. In addition, the thermal lines mapped by MALT-45 were observed with better sensitivity toward each maser region, providing more detail about the regions containing the class I methanol masers. The discussion presented in this chapter includes:

(i) Class I methanol maser regions with less spots of emission are less likely to be associated with a class II methanol or hydroxyl maser;

(ii) Class I methanol masers without an associated class II methanol or hydroxyl maser have lower luminosities.

(iii) The spatial extent and velocity range of class I methanol masers is typically small ($<$0.5 pc and $<$5 km s^{-1}, respectively), particularly for those without an associated class II methanol or hydroxyl maser;

(iv) Class I methanol masers are generally located within 0.5 pc of a class II methanol or hydroxyl maser, but can be up to 0.8 pc away;

(v) Class I methanol masers are reliable tracers of systemic velocities;

(vi) The brightness of class I methanol masers correlate poorly with that of the thermal CS (1–0), SiO (1–0) $v = 0$ and CH_3OH 1_0–0_0 lines;

(vii) Class I methanol masers have high association rates with 870 μm dust continuum point sources catalogued by ATLASGAL, with typical offsets not exceeding 0.4 pc;

(viii) Class I methanol masers are found towards a large range of clump masses ($10^{1.25}$ to $10^{4.5}$ $M_\odot$), but peak between $10^{3.0}$ and $10^{3.5}$ $M_\odot$. Additionally, masers associated with clump masses between $10^{3.25}$ and $10^{4.5}$ $M_\odot$ are almost all evolved;

(ix) The amount of diffuse emission in the 44 GHz class I methanol transition is poorly understood, but appears to increase as the brightness of thermal lines increase.

Chapter 5

Additional analyses with CS (1–0) and NH_3 (1,1)

This chapter provides additional investigations with CS (1–0) mapped by MALT-45. Temperatures calculated using HOPS NH_3 (1,1) and (2,2) data are compared with the distribution of CS emission. Does the amount of CS emission relate to kinetic temperatures across a range of molecular clumps? The projected distances from peaks of CS emission to class I CH_3OH masers and ATLASGAL sources are also detailed. Can we learn something about the spatial distribution of CS, relative to these other types of emission?

5.1 Analysis of temperature across the MALT-45 survey region

Fig. 4.11 of Chapter 4 reveals a good correlation between CS (1–0) intensity and clump mass. Furthermore, differences in the CS (1–0) and NH_3 (1,1) distributions were discussed in Chapter 3. Another useful physical parameter in studying the star-forming process is the kinetic temperature of the gas within dense molecular gas. Using HOPS NH_3 (1,1) and (2,2) data, the temperatures across the MALT-45 survey region can be calculated and compared with the CS data.

5.1.1 Methodology

Temperatures were derived using a similar procedure to that of Lu et al. (2014). The pipeline steps include:

(i) HOPS NH_3 (1,1) and (2,2) cubes were smoothed with a 60 arcsec FWHM kernel;

(ii) The optical depth of the NH_3 (1,1) line was derived using:

$$\frac{T_B(1,1,m)}{T_B(1,1,s)} = \frac{1-\exp\left(-\tau(1,1,m)\right)}{1-\exp\left(-a\tau(1,1,m)\right)} \tag{5.1}$$

where T_B is the brightness temperature, (J,K,m) designates the main line, (J,K,s) designates the inner satellite line, a is the relative intensity between the main and inner satellite lines under optically thin conditions and τ is the optical depth. Note that this is the same as Equation 1.3, and assumes equal beam-filling factors and excitation temperatures for

hyperfine lines, local thermodynamic equilibrium and that the cosmic microwave background temperature of 2.7 K can be ignored. The a value is taken from Purcell (2006) ($^{0.139}/_{0.502} \approx 0.277$);

(iii) The optical depth of the NH_3 (2,2) line was derived using the NH_3 (1,1) optical depth:

$$\frac{T_B(1,1,m)}{T_B(2,2,m)} = \frac{1-\exp\left(-\tau(1,1,m)\right)}{1-\exp\left(-\tau(2,2,m)\right)} \tag{5.2}$$

This equation assumes the excitation temperature for both transitions is the same;

(iv) The rotational temperature is derived using:

$$T_R = \frac{-41.5\,K}{\ln\left(0.282\frac{\tau(2,2,m)}{\tau(1,1,m)}\right)} \tag{5.3}$$

(v) Kinetic temperature is derived from the rotational temperature via:

$$T_R = \frac{T_K}{1+\frac{T_K}{41.5}\ln\left(1+0.6\exp\left(\frac{-15.7}{T_K}\right)\right)} \tag{5.4}$$

Equations 5.1, 5.2, 5.3 and 5.4 were taken from Lu et al. (2014). NH_3 (1,1) and (2,2) cubes provided by HOPS are gridded with 15 arcsec pixels in both Galactic longitude and latitude, and temperatures were calculated on a pixel-by-pixel basis. Unfortunately, a number of issues were encountered when building this pipeline. Primarily, the sensitivity of HOPS NH_3 (1,1) and (2,2) is poor, resulting in reliable temperatures being derived for only a few clumps. The restrictions put into place were:

(i) The HOPS team provides integrated intensity (moment 0) maps of NH_3 data. These maps are blanked where no emission is detected, and are smoothed over regions of emission. Calculations of optical depth (and consequently temperature) are not performed on pixels that have been blanked on the moment 0 map;

(ii) Using the spatially smoothed maps described above, the spectral data of NH_3 (1,1) and (2,2) was smoothed with a Hanning window of width 5. This results in a velocity resolution of $\sim 0.38\,\mathrm{km\,s^{-1}}$. Gaussian fits were then attempted for the main and inner satellite components, in order to derive values necessary for Equation 5.1. As the sensitivity is poor, detection of satellite lines is unreliable, and thus cannot properly derive values for τ. This problem was resolved by comparing the Gaussians fitted to the main line of NH_3 (1,1) emission and their corresponding moment 0 values: any pixels with a moment 0 value less than $1\,\mathrm{K\,km\,s^{-1}}$ were considered optically thin (assigned $\tau = 0.001$), otherwise, the integrated intensity of the Gaussian was subtracted from the moment 0 value. $1\,\mathrm{K\,km\,s^{-1}}$ acts as a suitable cutoff for bright NH_3 (1,1), as satellite lines are often not detected at this level. If the integrated intensity of the Gaussian is larger than the moment 0 value, it was assumed that there were no detected satellite lines, as the Gaussian characterised all the emission present, and thus the pixel is optically thin. If the moment 0 value exceeds the integrated intensity of the Gaussian, the difference between the two was characterised based on the relative intensities of satellite lines to the main line. Furthermore, the presence of satellite lines was modulated by the moment 0 value. The determination of the integrated intensity of the inner satellite line is expressed algebraically as:

$$I(1,1,s) = \frac{\text{remainder}}{2}\left(1 - \frac{b}{a+b}\left(1 - \exp\left(\frac{-\text{mom0}}{5}\right)\right)\right) \tag{5.5}$$

where $I(1,1,s)$ is the integrated intensity of the inner satellite line, 'remainder' is the emission left after performing the subtraction described above, a is the relative intensity between the main and inner satellite lines ($^{0.139}/_{0.502} \approx 0.277$), b is the relative intensity between the main and outer satellite lines ($^{0.111}/_{0.502} \approx 0.221$) and 'mom0' is the moment 0 value. The division by two is necessary to calculate the integrated intensity of only one of the inner satellite lines. The moment 0 value is divided by 5 such that only pixels with significant integrated intensities contribute with $^{b}/_{a+b}$. The $^{b}/_{a+b}$ factor isolates the inner satellite from the outer. Once the integrated intensity of the inner satellite line is obtained, Equation 5.1 was used to solve for τ. Note that Equation 5.1 uses brightness temperatures instead of integrated intensities; by also using the integrated intensity of the main line, i.e. $I(1,1,m)$, we assume that the ratio of $^{I(1,1,m)}/_{I(1,1,s)}$ approximates $^{T_B(1,1,m)}/_{T_B(1,1,s)}$;

(iii) Gaussian widths were restricted to be no wider than widest line of NH_3 (1,1) found in the data. Given the general form of a Gaussian:

$$f(x) = a\exp\left(\frac{-(x-b)^2}{2c^2}\right) \tag{5.6}$$

the standard deviation c was restricted to be no greater than 2.3, which is equivalent to a FWHM of $5.4\,\mathrm{km\,s^{-1}}$. This permits the widest main lines of NH_3 (1,1) to be fitted accurately, without automated fitting routines contaminating the main line with satellite lines;

(iv) If $^{I(1,1,s)}/_{I(1,1,m)} > 0.8$, $^{I(1,1,s)}/_{I(1,1,m)}$ was set to 0.8. The calculated $I(1,1,s)$ can sometimes be much larger than $I(1,1,m)$, due to the moment 0 value provided being much larger than the intensity of the Gaussian fitted to the main line of NH_3 (1,1). This cap effectively sets the corresponding pixel to be optically thick. Consequently, this restricts the minimum possible kinetic temperature to be around 10 K. This condition was satisfied primarily in the centres of cold clumps, such as those seen over the G333 giant molecular cloud;

(v) If the peak spectral value of a pixel was less than 0.4 K for NH_3 (2,2) ($\sim 2\sigma$), it was rejected as insignificant. Without this requirement, noise peaks were often fitted as they were brighter than real emission;

(vi) If a negative τ was produced, it was due to insufficient satellite line contribution, and the pixel was considered optically thin;

(vii) Finally, if $\tau_{(1,1)} < 0.5$, instead of using Equation 5.3 the rotational temperature was calculated directly with:

$$T_R = \frac{-41.5\,K}{\ln\left(0.282\frac{T_B(2,2,m)}{T_B(1,1,m)}\right)} \tag{5.7}$$

We estimate the error of determined kinetic temperatures to be approximately 20 per cent. Another possible source of error in this method is if there is more than one velocity component along the line of sight, because this may affect the moment 0 value reported by the HOPS team and the resulting optical depth for that pixel would be over estimated. However, after visually inspecting the data, there are no cases where there are two velocity components along the same line of sight in the HOPS data within the MALT-45 region.

This pipeline was developed in the PYTHON programming language, using the ASTROPY library for FITS file reading and saving, and the SCIPY library for Gaussian fitting and equation solving. The resulting kinetic temperature map (T_K) is shown in Fig. 5.1.

There are a few gas clumps with temperatures less than 15 K. Typically, these regions are surrounded by gas with temperatures up to 30 K. There are three distinct clumps containing only high-temperature gas (pixels of at least 30 K); two of these (G330.95−0.19 and G333.60−0.20) are particularly active regions, and were discussed in Chapter 3.

5.1.2 Relation with CS (1–0) emission

In an attempt to investigate if there is a relationship between temperature and CS (1–0) emission, kinetic temperatures, peak CS intensities, kinematic distances and the presence of star formation masers have been compiled in Table 5.1. Typically, the available temperature information coincides with a peak of CS emission. Hence, the temperature recorded is the average value around the peak of CS emission. One exception is G333.33−0.36, which does not have a distinct peak of CS emission, but has many class I CH_3OH masers, and a different temperature to nearby CS peaks. Detailed descriptions of each region are given in §5.1.3.

Many of the clumps with available temperature information are also detailed by Lowe et al. (2014). Using the 70 m Tidbinbilla radio telescope, Lowe et al. (2014) conducted observations of NH_3 (1,1) and (2,2) over the G333 giant molecular cloud, and used these data to calculate kinetic temperatures. There are differences between their derived temperatures and those calculated by this work. With only two outliers, these differences are well characterised by the following relation:

$$T_L = 1.98T_H - 9.39 \tag{5.8}$$

where T_L is the kinetic temperature derived by Lowe et al. (2014) and T_H is the temperature derived from HOPS data (this work). Including the two outliers, the correlation coefficient (r-value) is 0.87, which indicates a predictable systematic differences between these datasets. These differences can be explained by the difference in size between the two telescopes used. Tidbinbilla is much larger than Mopra (70 m compared to 22 m), resulting in a significantly smaller primary beam for the observations of NH_3 (1,1) and (2,2) ($\sim$119 arcsec compared to $\sim$37 arcsec). Consequently, the cores of NH_3 used are less affected by spatial smearing, resulting in a more representative spectrum of emission within gas clumps. As the temperatures of Lowe et al. (2014) are consistently hotter than those derived by this work, it is likely that the smaller primary beam of Tidbinbilla probes gas that is closer to the star formation centres, and is therefore hotter. The temperatures derived from this work are more sensitive to the gas further away from the star formation centres (i.e. cooler), and are thus reflective of the larger scale gas clumps.

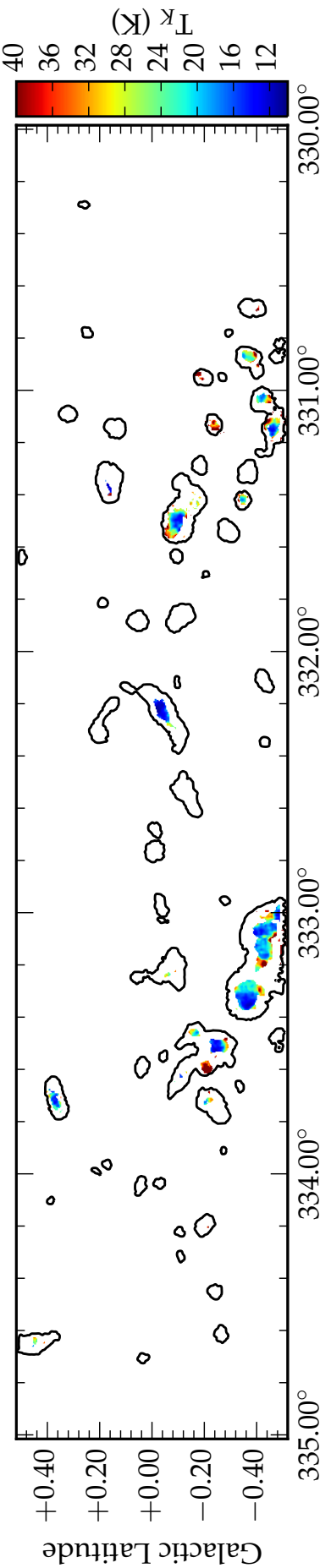

Figure 5.1: Gas temperatures calculated via NH_3 (1,1) and (2,2). Contours indicate regions with detected NH_3 (1,1). Temperature information exists in few regions across the map, primarily limited by NH_3 (2,2) detections. Many regions have temperatures less than 20 K, surrounded by warmer gas. Only three regions have consistently high temperatures (>30 K; G330.95−0.19, G331.14−0.24 and G333.60−0.20).

The two exceptions to the relation given in Equation 5.8 are G333.01−0.48 and G333.72−0.21. Only a few pixels of NH_3 (1,1) and (2,2) emission are available in G333.01−0.48, which makes determining a temperature difficult. However, the additional sensitivity provided by the observations of Lowe et al. (2014) are able to provide a temperature. G333.72−0.21 also has little NH_3 (1,1) and (2,2) data, although the determined kinetic temperature from these data closely agrees with that of Lowe et al. (2014). HOPS sensitivity is likely exacerbating the issue here, but there is not enough information to conclude this point.

A scatter plot of temperature against CS intensity can be seen in Fig. 5.2. There is a weak correlation after removing two outliers (r^2-value of 0.46); this hints that observations of CS may be used to help indicate the temperature of gas. However, this result should be taken with caution, as it suffers from low-number statistics. Additionally, the temperature is derived from the optical depth of NH_3, which may also correlate with the amount of CS present. The presence of other star-forming tracers was noted for each region, but no trends associated with their presence or absence is apparent.

CS (1–0) is a good tracer of all dense gas in a clump, not just that near to a YSO or in an outflow. Higher transitions of CS are more likely to be powered close to a YSO, and therefore better at identifying high-mass, hot regions. If the luminosity of CS does correlate with temperature, then higher CS transitions, when compared with CS (1–0), should also help to identify cold regions of gas, given that it is less likely to appear there.

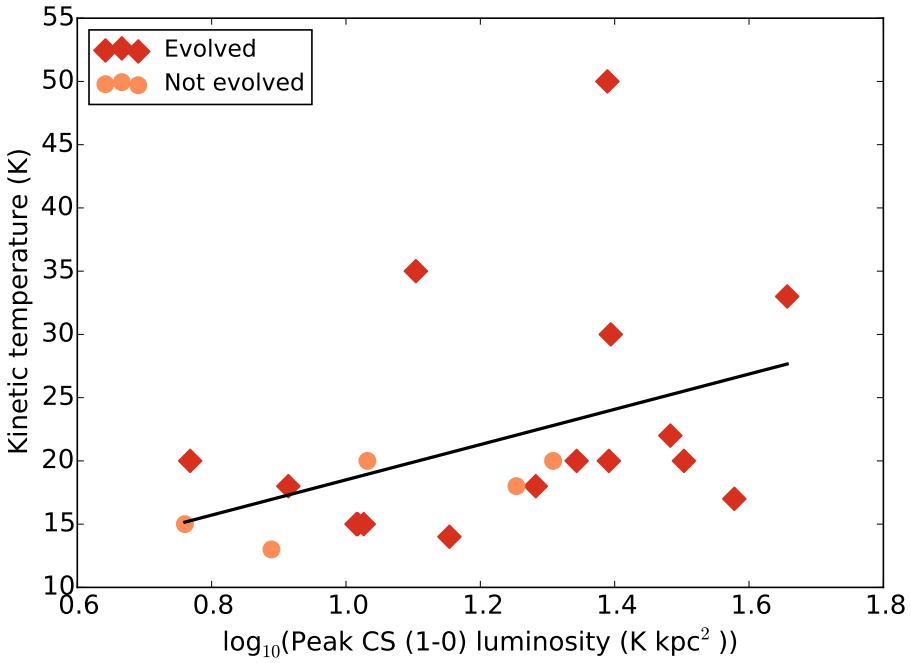

Figure 5.2: Scatter plot of temperature vs. peak CS (1–0) luminosity in clumps with temperature information. The line of best fit for all data has an r^2-value of 0.17. When removing the two outlying data points (temperature >35 K), the r^2 increases to 0.36. The outliers are G333.00−0.44 and G333.60−0.20. Clumps are classified as evolved if the CS peak has an associated class II CH_3OH maser, OH maser or H53α radio recombination line; not enough data is present to identify trends with or without evolved species.

Table 5.1: Regions with temperature information. Each region is focused around a peak of CS emission (except for G333.33−0.36); temperature values here reflect an average around this peak of emission. Column 1 lists the coordinates of the CS peak in Galactic coordinates. Column 2 lists the calculated kinetic temperature derived from NH_3 (1,1) and (2,2) data. Column 3 lists the main-beam temperature of the CS peak. Column 4 lists the assumed distance, which is taken from the kinematic distances in Chapter 4. If a region was without a kinematic distance, a value was taken from another nearby gas clump with a similar peak CS velocity. Columns 5 through 9 list the presence of various star formation tracers. These are indicated if known ('Y') or not ('N'). If the presence is uncertain, it is designated with a question mark ('?'); these only apply to the H53α radio recombination lines. Column 10 lists the kinetic temperature from Lowe et al. (2014), where available. The single dashed value corresponding to G333.60−0.20 represents the inability of Lowe et al. (2014) to supply a kinetic temperature for this region.

Region of interest	Kinetic temp. (K)	Peak CS (1–0) (K)	Assumed distance (kpc)	Presence of:					Kinetic temp. from Lowe et al. (2014) (K)
				Class I CH_3OH maser?	Class II CH_3OH maser?	OH maser?	H_2O maser?	H53α RRL?	
G330.88−0.37	22	1.9	4.0	Y	Y	Y	Y	Y	
G330.95−0.18	33	1.5	5.5	Y	Y	Y	Y	Y	
G331.03−0.43	18	0.97	4.3	N	N	N	N	?	
G331.13−0.24	30	0.85	5.4	Y	Y	Y	Y	N	
G331.13−0.48	20	1.10	4.3	Y	N	N	N	?	
G331.42−0.35	20	0.61	4.2	N	N	N	N	?	
G331.52−0.10	17	1.4	5.2	Y	N	Y	Y	Y	
G332.24−0.04	13	0.67	3.4	Y	N	N	N	N	
G333.00−0.44	35	0.88	3.8	Y	N	N	Y	Y	63.6
G333.01−0.48	15	0.82	3.6	Y	N	N	N	Y	35.6
G333.07−0.40	15	0.8	3.6	Y	Y	N	Y	Y	19.8
G333.07−0.44	18	1.4	3.7	Y	Y	N	Y	Y	25.7
G333.13−0.43	20	2.6	3.5	Y	Y	Y	Y	Y	31.9
G333.28−0.38	20	1.9	3.6	Y	N	N	N	Y	29.2
G333.30−0.35	20	1.8	3.5	Y	N	N	N	Y	25.5
G333.33−0.36	14	1.1	3.6	Y	N	N	N	Y	
G333.46−0.16	20	0.61	3.1	Y	Y	Y	Y	Y	24.4
G333.52−0.27	15	0.85	3.5	Y	N	N	N	Y	20.3
G333.60−0.20	50	2.0	3.5	Y	N	Y	Y	Y	-
G333.72−0.21	18	0.67	3.5	Y	N	N	N	Y	17.8
G333.72+0.37	15	0.47	3.5	N	N	N	N	?	

5.1.3 Individual source descriptions

The following text briefly discusses CS (1–0) emission with select regions, given the availability of temperature information. Fig. 5.3 shows the temperature of each of these regions along with CS contours. The peak velocity of CS emission is used to infer the distance of objects; if velocities are similar between nearby clumps, they are assumed to be at similar distances. Unless otherwise stated, when referring to all types of star formation masers, the presence of class I CH_3OH, class II CH_3OH, H_2O and OH masers is indicated.

5.1.3.1 Regions near G331.03−0.32

The three southern-most clumps seen in Fig. 5.3 all have similar temperatures (∼20 to 25 K), but have some other differences. The G330.87−0.37 clump has a very high peak of CS (∼1.5 K), as well as all types of star formation masers, but has similar temperatures to the other two clumps, despite their lack of other star formation masers. Both other clumps have an approximate peak of 1 K in CS, but G331.13−0.48 has two class I CH_3OH masers while G331.03−0.43 has none. Given the strong presence of NH_3 (required to calculate temperature) and CS (well correlated with mass), perhaps these clumps are young star-forming regions that may eventually appear similar to G330.87−0.37.

Both of the northern-most clumps (G330.95−0.19 and G331.13−0.24) have high temperatures (at least 30 K), are associated with all types of star formation masers and are approximately at the same distance. However, they exhibit very different strengths in CS; 1.5 K for G330.95−0.19 and 0.8 K for G331.13−0.24.

5.1.3.2 Regions near G331.48−0.23

The large region centred on G331.52−0.09 is a giant H II region with many class I CH_3OH masers, but one distinct CS peak. This peak has a low temperature (∼16 K) but is slightly offset from the coldest gas to the west (∼14 K).

G331.42−0.35 appears similar to G331.03−0.43 and G331.13−0.48; the temperature is approximately 20 K with a CS peak of 0.6 K, but no star formation masers are present. Like the others, the presence of CS and NH_3 hints that this clump is in the early stages of star formation.

5.1.3.3 G332.24−0.04

The arc structure traced by CS here closely follows infrared absorption, highlighting dense IRDCs. The temperature data is roughly cospatial with the class I CH_3OH masers detected; in Chapter 4 I show that when class I CH_3OH masers appear in large numbers and spatial extent, the associated star-forming region is more evolved in an evolutionary timeline. This source is the exception, classified as 'young' due to its lack of class II CH_3OH or OH masers, as well as H51α or H53α emission. This classification is reinforced by the low temperature found here (∼13 K). The peak of CS (0.7 K) is slightly offset from the maser emission (∼36 arcsec).

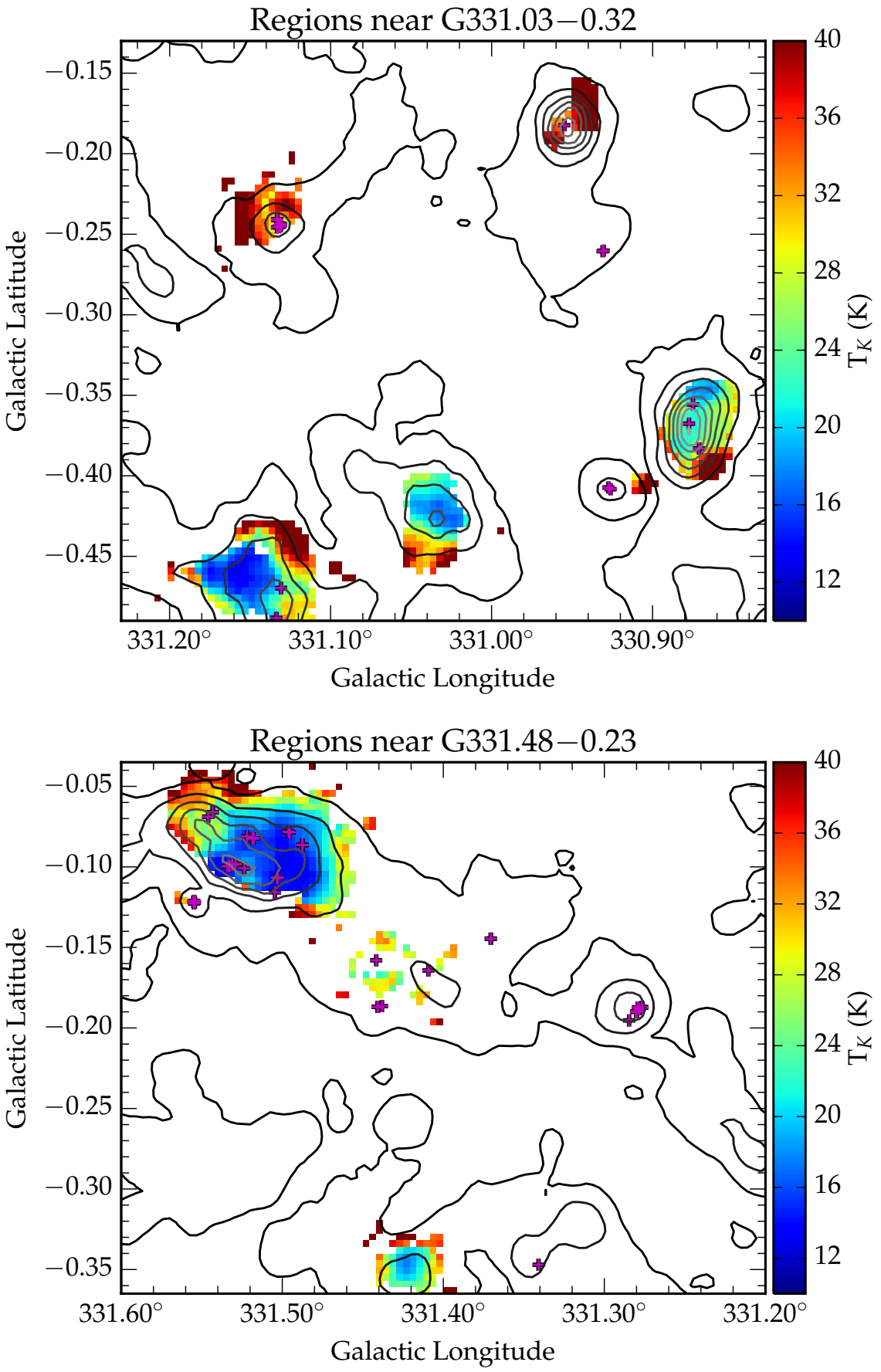

Figure 5.3: Specific regions with kinetic temperature information. Contours are CS (1–0) emission from MALT-45, and magenta plus symbols designate high-resolution class I CH_3OH maser positions. Contour levels are 0.15, 0.40, ..., 2.9 K.

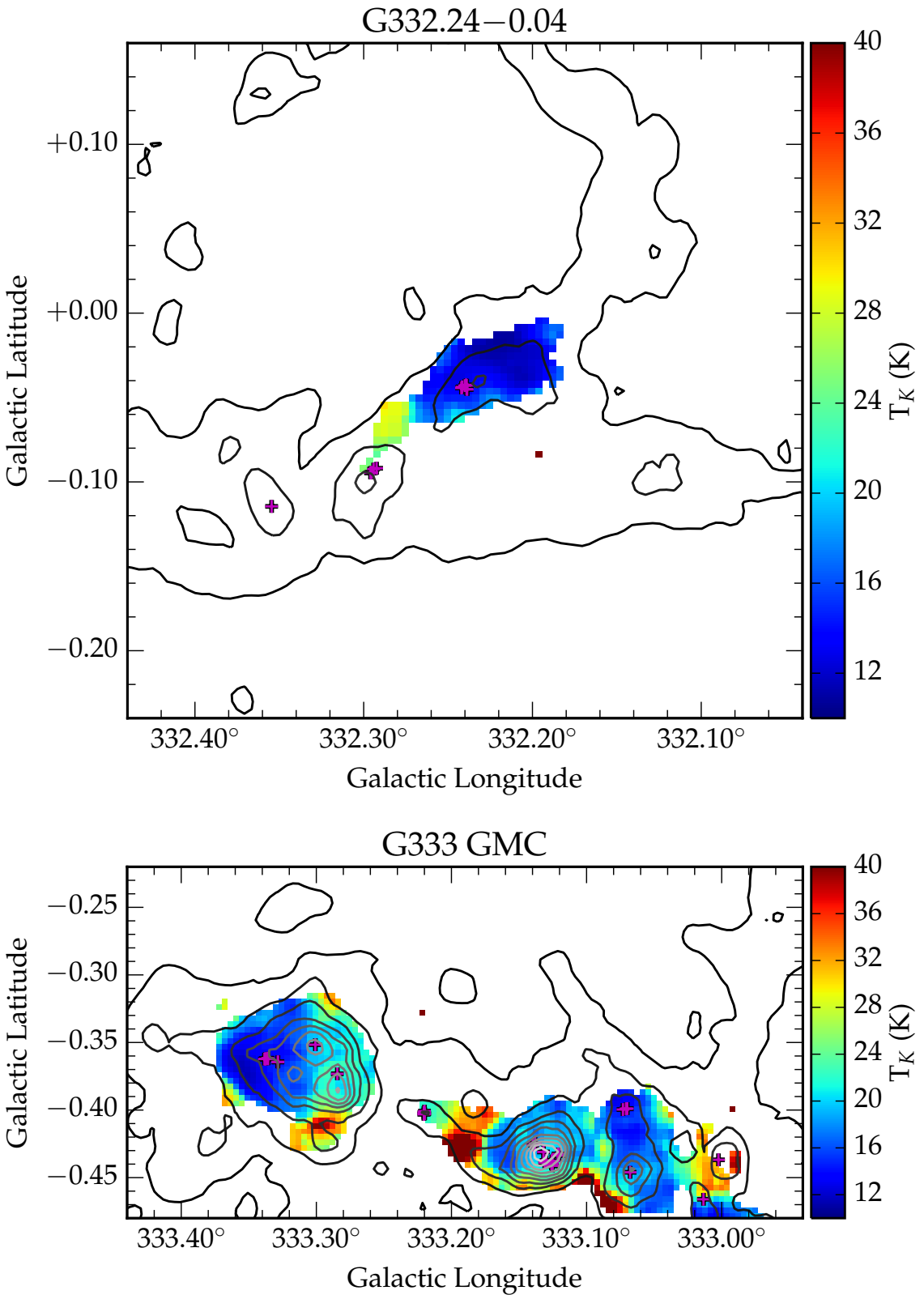

Figure 5.3: *continued*

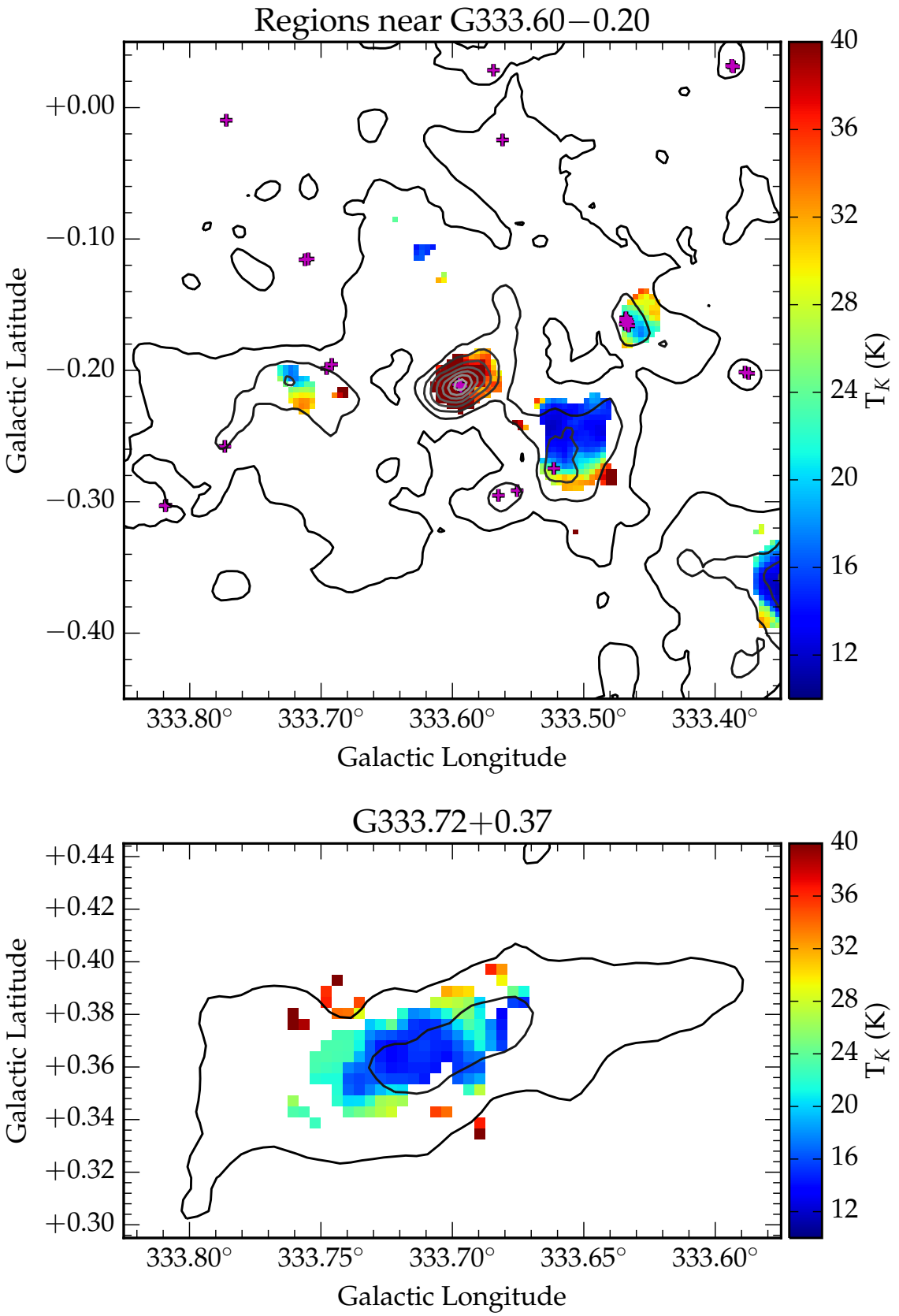

Figure 5.3: *continued*

5.1.3.4 G333

The CS peak at G333.01−0.48 has a temperature ∼15 K. This may be contaminated by hot gas originating to the north, with a temperature around 30 K. Another nearby CS peak at G333.00−0.44 has an even higher temperature (between 35 and 40 K), and is seemingly active; G333.00−0.44 and the region between G333.00−0.44 and G333.01−0.48 both have a H_2O maser detection, highlighting outflow activity. This is also presumably the cause of these higher temperatures. If the hotter gas is not associated with G333.01−0.48, then G333.01−0.48 may be another example of a cold, dense core with some class I CH_3OH maser activity. The RMS survey classifies both of these clumps as diffuse H II regions (Urquhart et al. 2014a).

The CS structure of the peak at G333.07−0.44 is interesting. This peak has a temperature of 18 K and CS brightness 1.4 K. There is a class II CH_3OH maser cospatial with the CS peak, while approximately 50 arcsec to the north-west of the peak lies a H_2O maser detection. Far to the north at G333.07−0.40, the temperature drops to 13 K and there are multiple class I CH_3OH masers. There appears to be an infrared source cospatial with these masers, such that this region is probably distinct from G333.07−0.44, but the significantly offset H_2O maser may indicate the presence of a powerful outflow that influences the CS presence in G333.07−0.40. Both maser sources have RRL detections in Chapter 4; the emission may originate from both regions, or one is contaminating the other. Given the low temperature and weak star formation maser association of G333.07−0.40, the latter seems more likely.

G333.13−0.43 is the brightest CS peak in the entire MALT-45 survey (2.6 K), and has a kinetic temperature of ∼20 K. This region features many star formation maser species, with four class II CH_3OH maser detections from the MMB. Only the most north-eastern class I CH_3OH masers are without an RRL detection. Perhaps there is such a large mass of molecular gas that despite the evolved nature of this source, the temperature still appears low as it better reflects the bulk of the gas present.

Another CS peak at G333.22−0.40 has temperature information. The temperature of this small region is between 20 and 25 K, but this may be contaminated by the high-temperate gas between G333.22−0.40 and G333.13−0.43. Like G333.07−0.40, Chapter 4 lists the presence of RRL emission, although given the temperature and lack of star formation masers, the RRL emission may be originating elsewhere.

The G333.33−0.36 clump appears to have three distinct regions, highlighted by the presence class I CH_3OH masers. G333.28−0.38 and G333.30−0.35 have CS peaks of 1.9 and 1.8 K, respectively, but both have temperatures ∼20 K. Another CS peak at G333.31−0.38 has a strength of 1.5 K, but is not as closely associated with class I CH_3OH masers. This temperature is a little lower at ∼16 K. The remaining class I CH_3OH masers appear toward the coldest part of the clump (∼13 K). As RRL emission was detected toward each of these masers in Chapter 4, this clump appears to feature a giant H II region; indeed, Urquhart et al. (2014a) classify both G333.28−0.38 and G333.31−0.38 as H II regions.

5.1.3.5 Regions near G333.60−0.20

G333.60−0.20 is noted for being the brightest H II region in the MALT-45 survey. It has been discussed in Chapter 3 as being quite an evolved stage of HMSF, and is thought to contain roughly 10 O-type stars Fujiyoshi et al. (2006). The weak NH_3 emission gives questionable temperature information; the temperature varies from 30 to 55 K across the clump. The strong CS peak (2.0 K) coincides with class I CH_3OH maser positions, which is offset from H_2O and OH masers (∼36 arcsec). Lowe et al. (2014) do not supply a temperature for this clump, due to the weak NH_3 emission; the fact that we were able to calculate a temperature with the HOPS NH_3 data suggests that the NH_3 emission is dominant outside the clump. This in turn helps to explain variable temperature seen over the clump.

G333.46−0.16 features all star formation masers with a temperature of 20 K. However, unlike other regions which also feature multiple masers, this one has a relatively low peak CS (0.61 K), despite having the smallest distance of those analysed (3.1 kpc).

Temperature information is available throughout a large fraction of the G333.52−0.27 clump, indicating the widespread presence of NH_3 (1,1) and (2,2). Across the CS peak shown, the temperature gradient increases to the south, and the CS peak ends near the detection of a class I CH_3OH maser. Using 1.2 mm dust emission, Lowe et al. (2014) detail three dust clumps over the single clump discussed here (G333.521−0.239, G333.524−0.272 and G333.539−0.245). In their interpretation, the authors note that each of the three clumps is associated with 160 μm emission from *Herschel* Hi-GAL data.

G333.72−0.21 has a small CS peak, unusually offset from masers. Two class I CH_3OH masers have a large offset from the CS peak, and a class II CH_3OH maser is approximately the same distance away from the CS peak to the south-east. Lowe et al. (2014) note a compact 160 μm object toward the peak of their 1.2 μm dust emission, and speculate that this clump is likely to be in the earliest stages of star formation.

5.1.3.6 G333.72+0.37

The CS emission contours trace an IRDC, with temperature information lying within. The lowest temperature pixel (13.4 K) lies to the east of the cloud, and is cospatial with an infrared feature within the boundary of the IRDC, but the average temperature value was taken to be 15 K. There are no maser detections associated with this IRDC, despite this spatial overlap. This IRDC may be pre-star-forming, and thus a good example to study the initial conditions of star formation.

5.1.3.7 Summary

Fig. 5.2 shows a slight correlation between CS (1–0) luminosity and temperature, although this relation suffers from small number statistics. Qualitative investigations of these regions shows that both cold and hot regions of gas can have very different CS brightnesses; without high-resolution observations, it is difficult to disentangle the bulk of the gas from cores containing YSOs. For example, the CS brightnesses of 'hot' clumps are 0.8, 1.5 and 2.0 K. These are not unusual values when compared to the 'cold' clumps (G333.13−0.43 is brightest at 2.6 K with a temperature of 20 K).

The discussion above is primarily limited by the quality of NH_3 (1,1) and (2,2) data used to determine the temperatures. Higher resolution and higher sensitivity observations of NH_3 (1,1), (2,2) and CS (1–0), as well as higher energy transitions of CS, would be effective at highlighting the gas temperature distribution across clumps. This is relatively easy to do, as all of these spectral lines are bright and the ATCA is capable of producing high-quality data in a short amount of time. All of the regions discussed have a CS (1–0) peak of at least 0.6 K. A preliminary target list could include CS (1–0) peaks from MALT-45 with a brightness of at least 0.3 K ($\sim 10\sigma$). Chapter 3 mentions a few class I CH_3OH maser regions with dim CS association (<0.11 K); these, and other class I CH_3OH maser regions, would also make for interesting targets for follow-up observations of thermal gas with the ATCA.

5.2 Spatial offsets between peaks of CS (1–0) emission and class I CH_3OH masers

At a few points in this thesis, CS (1–0) emission has been compared with class I CH_3OH masers. Chapter 4 shows that their intensities appear to be un-correlated, although their velocities match very closely; see Fig. 4.6. As seen in §5.1, peaks of CS emission also tend to feature class I masers. Chapter 4 also discusses the offsets between class I CH_3OH maser positions and other maser species, finding that offsets tend to be within <0.5 pc. An investigation into the spatial offsets between CS (1–0) and class I CH_3OH masers is detailed below.

5.2.1 Methodology

Similar to §5.1.1, results were calculated using PYTHON with ASTROPY for FITS file reading. The peak intensity map (moment -2) of CS (1–0) emission was taken from the MALT-45 survey detailed in Chapter 3, and high-resolution class I CH_3OH positions were taken from Chapter 4. To smooth the data, CS channels were binned into groups of 10. All CS pixels within 4 pixels ($\sim$60 arcsec) were identified from each class I CH_3OH spot. Rather than simply accepting the brightest CS pixel within 4 pixels as the associated peak of CS emission, CS intensities were modulated with spatial offset according to the following formula:

$$T_m = T_d \cos\left(\frac{\text{offset}}{\frac{3}{2}\pi}\right) \tag{5.9}$$

where T_m is the modulated main-beam temperature, T_d is main-beam temperature of the CS pixel, and 'offset' is the spatial offset in pixels. The $\cos(\text{offset}/\frac{3}{2}\pi)$ factor tapers the CS values at large distances from the class I CH_3OH maser spots, such that local peaks are preferred. At a distance of 4 pixels, a CS brightness is tapered by a factor of $\sim$0.66. Finally, spatial offsets are converted to projected linear offsets using the kinematic distances prescribed to each maser in Chapter 4.

In an effort to obtain more precise CS peak positions, rather than just using pixel values, two-dimensional Gaussian fits were attempted with both PYTHON libraries and the MIRIAD software suite. However, these proved unreliable even in simple cases, and so pixel positions

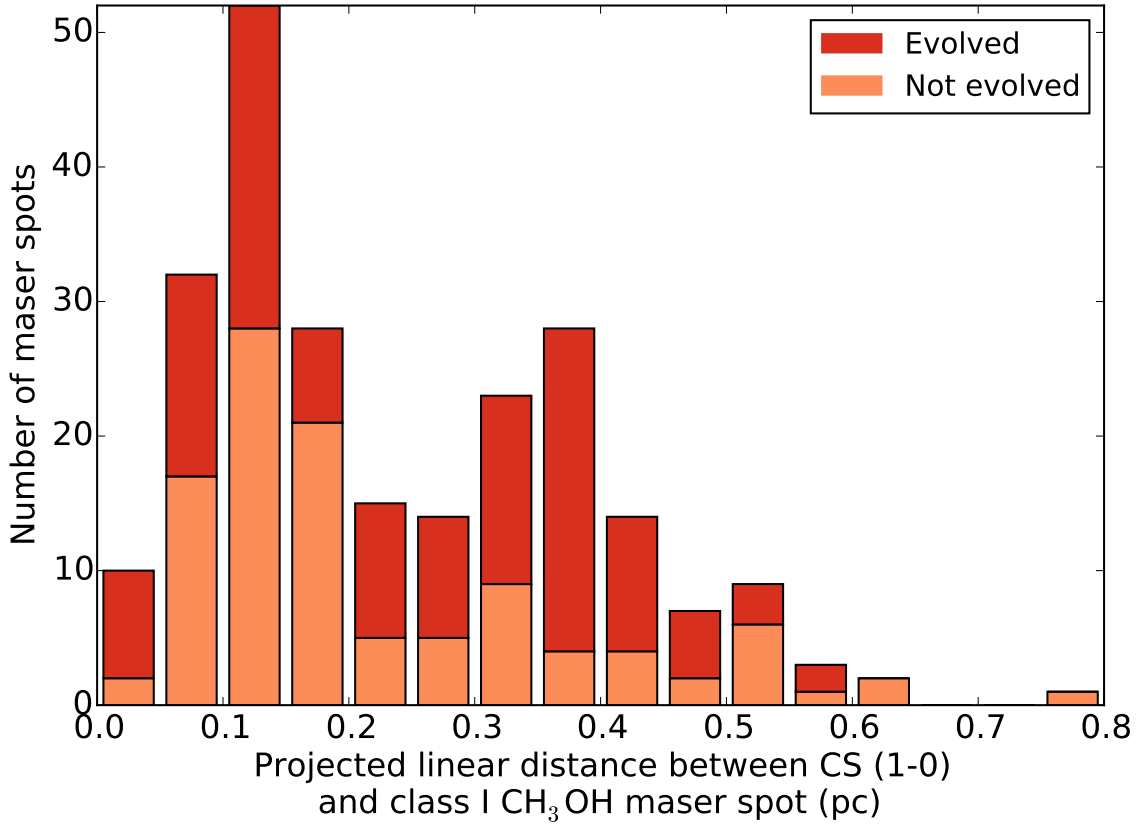

Figure 5.4: Projected distances between CS (1–0) and class I CH_3OH masers. Most maser spots are separated by less than 0.5 pc from a peak CS emission. Two peaks in this distribution are apparent, centred on approximately 0.10 and 0.33 pc. The presence of a class II CH_3OH maser, OH maser or the H53α radio recombination line classifies a maser spot as evolved. No trend with or without evolved star formation tracers is apparent.

were used instead. This results in the uncertainty of each CS peak position being approximately 15 arcsec.

5.2.2 Results and discussion

Fig. 5.4 shows the resulting histogram of projected linear distances between class I CH_3OH masers and the associated CS peak. As with the projected linear distances between class I CH_3OH masers and other masers associated with star formation, almost all class I CH_3OH maser spots appear within 0.5 pc of a CS peak. This result further highlights the close association between CS and class I CH_3OH masers. The lack of sources in the smallest bin may be erroneous, given the crude spatial resolution of the CS data. With high-resolution data, more associations within 0.05 pc may be observed.

There are two population peaks in Fig. 5.4; Gaussians fitted to the histogram have approximate centres of 0.10 and 0.33 pc. It is difficult to tell if these distinct offsets are real or otherwise; again, the relatively poor spatial resolution of the CS data hinders detailed interpretation of this histogram. The evolved criterion of Chapter 4 is also used in this plot, although no trend is apparent for evolved or non-evolved populations. The linear distance was also compared with the integrated intensity of both CS and class I CH_3OH masers, but

no correlation was found.

Without high-resolution CS data, robust interpretation is difficult. However, the observation of this 0.5 pc boundary is similar to that discussed in Chapter 4 and affirms that class I CH_3OH masers typically have a maximum separation from other star formation species.

5.3 CS (1–0) and ATLASGAL 870 μm dust emission

Within the region mapped by the MALT-45 survey, 664 ATLASGAL point sources have been identified by Urquhart et al. (2014b). Using the same method to determine offsets as described in §5.2, the vast majority of ATLASGAL sources are near to a CS (1–0) peak with a brightness of at least 0.1 K (624/664, 94 per cent). The distribution of these sources with CS (1–0) emission can be seen in Fig. 5.5.

Fig. 5.6 shows the projected linear distances between ATLASGAL sources and peaks of CS emission. Few associations are within 2.5 arcsec, but this is probably due to the relatively poor spatial resolution of the CS. Otherwise, a steady decrease in the association between peaks of CS emission and ATLASGAL point sources is observed with increasing offset. Assuming near kinematic distances for each of the ATLASGAL point sources is likely to be erroneous, as some portion of this large sample will be at a the far distance. However, the majority are expected to be at the near distance. At this longitude range, a typical distance of 4 kpc with an angular offset of 25 arcsec corresponds to a linear distance of 0.48 pc. Therefore, most ATLASGAL sources and CS peaks are expected to be within 0.5 pc of each other, similar to masers associated with star formation.

Fig. 5.7 compares the brightness of ATLASGAL point sources to the associated peaks of CS emission. The trend is similar to Fig. 4.11 of Chapter 4, but the correlation is not as good. Fig. 4.11 uses an integrated intensity of CS, whereas Fig. 5.7 uses only peak intensity; in this case, the difference in correlation is insignificant. It is possible that the comparison shown in Chapter 4 does not have a large enough sample of CS data to reproduce the relatively poor correlation observed here. On the other hand, perhaps CS correlates more closely with 870 μm dust emission when associated with class I CH_3OH masers.

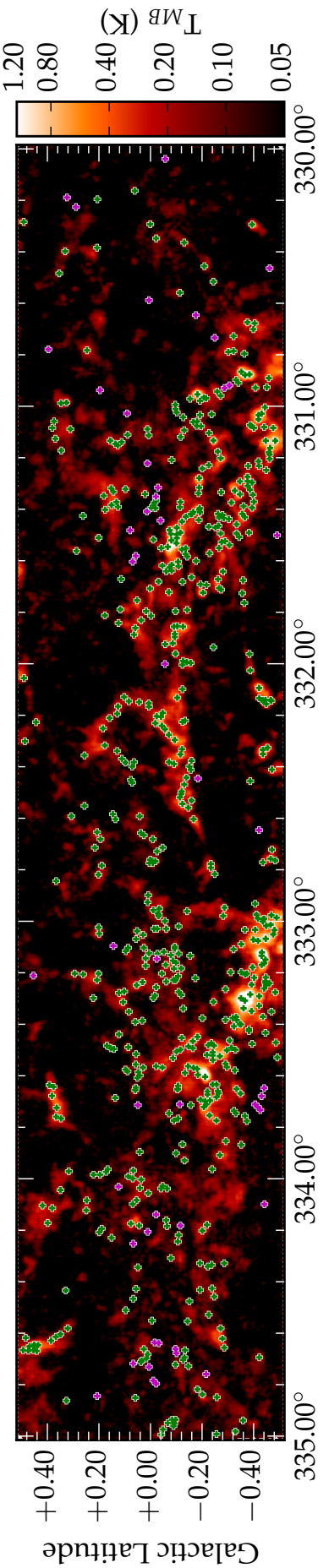

Figure 5.5: Peak-intensity MALT-45 CS (1–0) emission with ATLASGAL point sources. Plus symbols represent ATLASGAL point sources; green symbols are associated with a CS peak of at least 0.1 K, whereas magenta symbols have peaks of CS less than 0.1 K. A main-beam temperature of 0.1 K represents a 3σ peak of emission.

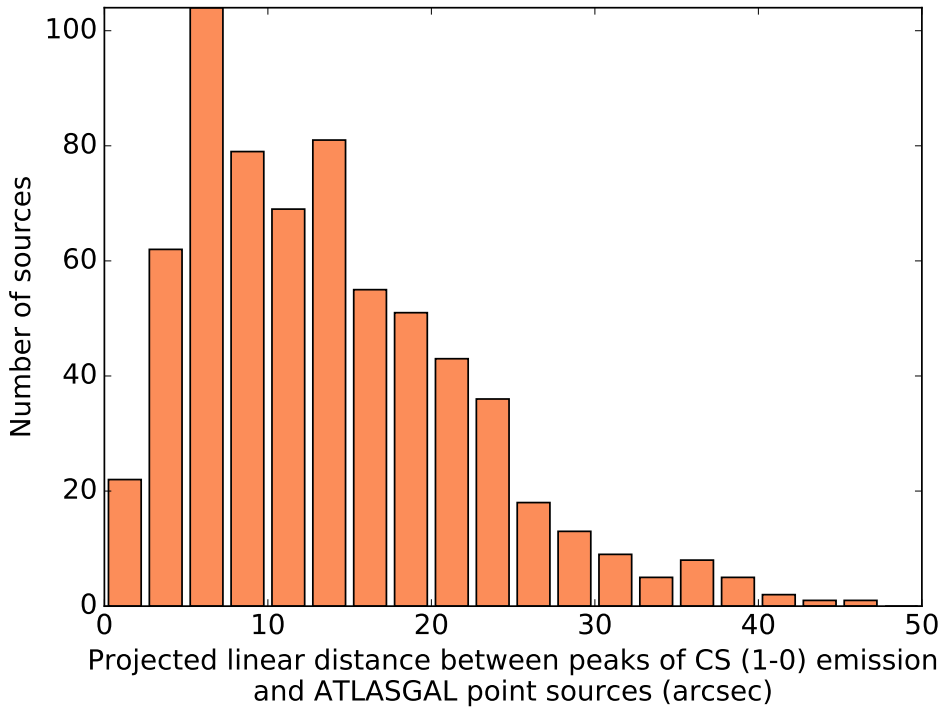

Figure 5.6: Projected linear distances between ATLASGAL sources and associated peaks of CS emission. A peak-intensity map of CS was used to locate peaks of CS emission. Few ATLASGAL sources are within 2.5 arcsec to a peak of CS emission, likely due to the poor spatial resolution of the CS data. Most projected offsets are approximately 8 arcsec, and the association steadily decreases with offset. The majority of the sample is within 25 arcsec.

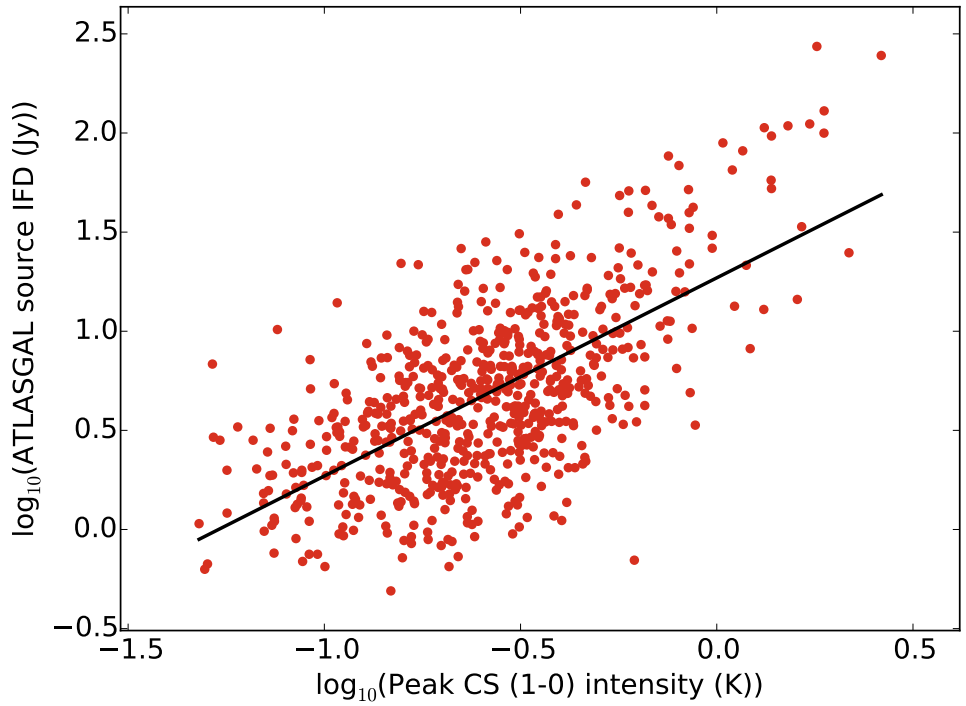

Figure 5.7: Scatter plot of ATLASGAL point source intensities with associated CS peak intensities. The positive trend in this comparison is obvious, but correlation is hampered by the scatter. The line of best fit is shown in black, and has r-value is 0.65.

Chapter 6

Summary and conclusion

This thesis has investigated the 7 mm environment of HMSF through the MALT-45 survey, primarily by searching for CS (1–0) emission and class I CH_3OH masers. The following text briefly discusses the major results of the previous chapters, as well as future projects which may build upon these results.

The MALT-45 pilot survey (Chapter 2) demonstrated the feasibility of auto-correlation with an interferometer, to achieve a sensitivity that would otherwise be too time consuming. By doing so, this work paved the way for a 5 square-degree survey with MALT-45. This technique is not limited to the 7 mm waveband, and could easily be used for other surveys.

The MALT-45 survey (Chapter 3) observed the $330^\circ \leq l \leq 335^\circ$, $b = \pm 0.5^\circ$ region of the Galactic Plane, using a technique refined from the pilot observations. This technique was successful in detecting many new class I CH_3OH masers and SiO masers, as well as detecting extended CS (1–0) emission over the entire region.

The number of known class I CH_3OH masers in the MALT-45 region was increased from 19 to 77, and all SiO masers were new detections. With an unbiased sample of class I CH_3OH masers, as well as CS information toward each maser, class I CH_3OH masers were found to have small velocity offsets from systemic velocities. Additionally, class I masers were found with and without any other star formation maser counterpart, indicating their association with a wide range of HMSF evolutionary stages. For class I masers associated with other star formation masers, no correlation in intensity or luminosity was observed between maser species.

Using maps of NH_3 (1,1) emission from HOPS, a comparison with CS (1–0) emission from MALT-45 revealed dense clumps of hot (>30 K) and cold (∼20 K) gas. The cold regions typically feature self-absorption of CS emission and a relatively high amount of NH_3 emission, while the hotter regions contain trace amounts of NH_3 emission. It seems that NH_3 is destroyed in these hotter regions as they are more evolved regions of star formation, while the CS abundance is enhanced. Comparisons between the emission of CS and $C^{34}S$ also reveal a close infrared alignment for regions containing an over-abundance of $C^{34}S$.

All SiO masers detected by MALT-45 appear to be associated with infrared evolved stars. The brightness of these SiO masers usually decreases with vibrational mode ($v = 1, 2, 3$), but 11 regions have stronger $v = 2$ line emission than $v = 1$. Another 2 regions contain only $v = 2$ maser lines. Additionally, 3 rare $v = 3$ maser lines were detected.

High-resolution, follow-up observations of the class I CH_3OH masers detected by MALT-45 further detail the properties of these masers (Chapter 4). These masers are typically near to other maser species associated with star formation (<0.5 pc), but are occasionally at large angular extents, especially when associated with class II CH_3OH or OH masers, indicating the more evolved nature of the source.

Almost all class I masers are associated with an 870 μm dust emission point source from the ATLASGAL survey. However, no relation between the flux densities of maser emission and dust continuum was established. ATLASGAL data were used to calculate clump masses, and these correlated well with the CS (1–0) emission in the class I CH_3OH maser regions. Additionally, the majority of projected linear distances between class I CH_3OH masers and ATLASGAL sources was less than 0.5 pc.

The cross- and auto-correlated emission for class I CH_3OH masers was compared. In some cases, cross-correlation identified most of the emission contained in auto-correlated data, but most masers had some degree of emission being resolved out. The histogram of ratios between cross- and auto-correlated has an irregular distribution, but most maser regions have approximately 50 per cent of emission being resolved out. The maximum detectable scale of the relevant observations was approximately 4.6 arcsec, which is unlikely to resolve out any compact maser components. No relation of cross- to auto-correlation with some other factor could be established.

In an effort to identify the evolutionary state of class I maser regions, the presence of class II CH_3OH masers, OH masers and the H53α radio recombination line were used. Regions without these evolved tracers were found to have lower luminosities than those with an evolved tracer. Almost all non-evolved regions appear toward an IRDC. In addition, class I CH_3OH maser regions without an associated OH maser tend to have only a few maser spots.

A temperature map of the MALT-45 region was calculated using HOPS NH_3 (1,1) and (2,2) data; a slight correlation between peak CS (1–0) luminosity and the temperature was found, although this suffers from low-number statistics. The temperature of the molecular gas appears to be independent of the presence or absence of class I CH_3OH masers.

Spatial peaks of CS (1–0) emission appear to be closely related to both class I CH_3OH masers and ATLASGAL point sources. Peak velocities of CS are also closely related to class I CH_3OH masers, although their luminosities do not appear to be correlated. On the other hand, ATLASGAL luminosities are well correlated with CS (1–0).

6.1 Future work

Within the $330^\circ \leq l \leq 335^\circ$, $b = \pm 0.5^\circ$ survey area, the amount of information gleaned from MALT-45 observations is vast. With additional observations, MALT-45 can reveal more Galactic structure and dense clumps of gas through CS emission, simultaneously identifying new class I CH_3OH and SiO masers. Finding more class I CH_3OH masers would be particularly interesting, as they may designate un-studied, young regions of HMSF. High-resolution observations of new class I masers adds data to the statistically-complete population, aiding our understanding of these masers.

6.1.1 Short-term projects

Chapter 5 was able to use noisy NH_3 (1,1) and (2,2) to analyse temperatures across the MALT-45 region; ATCA observations of these lines towards other CS (1–0) peaks and class I CH_3OH masers would provide a large dataset for temperature comparisons. Are CS peaks usually cold? Do peaks of NH_3 (1,1) and (2,2) coincide better with masers than that of CS? Are the temperatures of regions featuring class I CH_3OH masers dictated by evolutionary stage? Such observations could help to answer these questions relatively quickly. Additionally, sensitive observations for NH_3 (1,1) and (2,2) could easily include the other HOPS spectral lines. HOPS is quite shallow with its sensitivity limit to H_2O masers (98 per cent complete at 8.4 Jy); with sensitive observations, perhaps the weaker H_2O masers will have better associations with class I CH_3OH masers in non-evolved regions of HMSF.

Continuum at 7 mm is notably absent from the work presented in this thesis. It may yet be possible to extract data from the MALT-45 survey, although this is potentially a significant investment in time. These data potentially hold great value; the 7 mm waveband represents an important component of the spectral energy distribution for star formation regions, as this is where the dominant emission mechanism changes from cool dust to ionised gas. Therefore, not only does MALT-45 continuum data potentially reveal new regions of star formation, it could also help to identify the evolutionary stage by determining the frequency at which the spectrum transitions from being dominated by ionised emission to cool dust. In addition, comparison with other dust continuum surveys, such as ATLASGAL and BGPS, may reveal interesting properties, as these surveys will give a detailed account of the dust continuum whereas MALT-45 continuum will give information on the ionised gas component, as well as the dust, giving us a reliable comparison between these two components.

Bibliography

Aguirre, J. E., Ginsburg, A. G., Dunham, M. K., et al. 2011, ApJS, 192, 4

Assaf, K. A., Diamond, P. J., Richards, A. M. S., & Gray, M. D. 2011, MNRAS, 415, 1083

Bains, I., Wong, T., Cunningham, M., et al. 2006, MNRAS, 367, 1609

Bania, T. M., Anderson, L. D., Balser, D. S., & Rood, R. T. 2010, ApJ, 718, L106

Barnes, P. J., Muller, E., Indermuehle, B., et al. 2015, ArXiv e-prints, arXiv:1507.05095

Barrett, A. H., Schwartz, P. R., & Waters, J. W. 1971, ApJ, 168, L101

Bartkiewicz, A., Szymczak, M., & van Langevelde, H. J. 2005, A&A, 442, L61

—. 2014, A&A, 564, A110

Bartkiewicz, A., Szymczak, M., van Langevelde, H. J., Richards, A. M. S., & Pihlström, Y. M. 2009, A&A, 502, 155

Batrla, W., Matthews, H. E., Menten, K. M., & Walmsley, C. M. 1987, Nature, 326, 49

Battersby, C., Bally, J., Ginsburg, A., et al. 2011, A&A, 535, A128

Bayet, E., Yates, J., & Viti, S. 2011, ApJ, 728, 114

Benjamin, R. A., Churchwell, E., Babler, B. L., et al. 2003, PASP, 115, 953

Bergin, E. A., Ciardi, D. R., Lada, C. J., Alves, J., & Lada, E. A. 2001, ApJ, 557, 209

Beuther, H., Churchwell, E. B., McKee, C. F., & Tan, J. C. 2007, Protostars and Planets V, 165

Beuther, H., Schilke, P., Gueth, F., et al. 2002a, A&A, 387, 931

Beuther, H., Schilke, P., Sridharan, T. K., et al. 2002b, A&A, 383, 892

Bolatto, A. D., Wolfire, M., & Leroy, A. K. 2013, ARA&A, 51, 207

Bonnell, I. A. 2008, in Astronomical Society of the Pacific Conference Series, Vol. 390, Pathways Through an Eclectic Universe, ed. J. H. Knapen, T. J. Mahoney, & A. Vazdekis, 26

Bonnell, I. A., Bate, M. R., & Zinnecker, H. 1998, MNRAS, 298, 93

Braiding, C., Burton, M. G., Blackwell, R., et al. 2015, PASA, 32, 20

Breen, S. L., Caswell, J. L., Ellingsen, S. P., & Phillips, C. J. 2010a, MNRAS, 406, 1487

Breen, S. L., Ellingsen, S. P., Caswell, J. L., et al. 2011, ApJ, 733, 80

Breen, S. L., Ellingsen, S. P., Caswell, J. L., & Lewis, B. E. 2010b, MNRAS, 401, 2219

Breen, S. L., Ellingsen, S. P., Contreras, Y., et al. 2013, MNRAS, 435, 524

Brogan, C. L., Goss, W. M., Hunter, T. R., et al. 2013, ApJ, 771, 91

Bronfman, L., Nyman, L.-A., & May, J. 1996, A&AS, 115, 81

Burton, M. G., Braiding, C., Glueck, C., et al. 2013, PASA, 30, 44

Carey, S. J., Clark, F. O., Egan, M. P., et al. 1998, ApJ, 508, 721

Carruthers, G. R. 1970, ApJ, 161, L81

Caselli, P., & Myers, P. C. 1995, ApJ, 446, 665

Caswell, J. L. 1997, MNRAS, 289, 203

—. 1998, MNRAS, 297, 215

Caswell, J. L., Fuller, G. A., Green, J. A., et al. 2011, MNRAS, 417, 1964

Cesaroni, R., Beltrán, M. T., Zhang, Q., Beuther, H., & Fallscheer, C. 2011, A&A, 533, A73

Chen, X., Ellingsen, S. P., Baan, W. A., et al. 2015, ApJ, 800, L2

Chen, X., Ellingsen, S. P., Shen, Z.-Q., Titmarsh, A., & Gan, C.-G. 2011, ApJS, 196, 9

Chen, X., Ellingsen, S. P., He, J.-H., et al. 2012, ApJS, 200, 5

Cheung, A. C., Rank, D. M., Townes, C. H., Thornton, D. D., & Welch, W. J. 1968, Physical Review Letters, 21, 1701

Chin, Y.-N., Henkel, C., Whiteoak, J. B., Langer, N., & Churchwell, E. B. 1996, A&A, 305, 960

Cho, S.-H., Kim, H.-G., Park, Y.-S., Choi, C.-H., & Ukita, N. 2005, ApJ, 622, 390

Churchwell, E. 2002, ARA&A, 40, 27

Claussen, M. J., Goss, W. M., Frail, D. A., & Seta, M. 1999, AJ, 117, 1387

Contreras, Y., Schuller, F., Urquhart, J. S., et al. 2013, A&A, 549, A45

Cooper, H. D. B., Lumsden, S. L., Oudmaijer, R. D., et al. 2013, MNRAS, 430, 1125

Cragg, D. M., Johns, K. P., Godfrey, P. D., & Brown, R. D. 1992, MNRAS, 259, 203

Csengeri, T., Urquhart, J. S., Schuller, F., et al. 2014, A&A, 565, A75

Cyganowski, C. J., Brogan, C. L., Hunter, T. R., & Churchwell, E. 2009, ApJ, 702, 1615

Cyganowski, C. J., Whitney, B. A., Holden, E., et al. 2008, AJ, 136, 2391

Dame, T. M., Hartmann, D., & Thaddeus, P. 2001, ApJ, 547, 792

Dame, T. M., & Thaddeus, P. 2008, ApJ, 683, L143

Dame, T. M., Ungerechts, H., Cohen, R. S., et al. 1987, ApJ, 322, 706

Dawson, J. R., Walsh, A. J., Jones, P. A., et al. 2014, MNRAS, 439, 1596

De Buizer, J. M. 2003, MNRAS, 341, 277

De Buizer, J. M., Bartkiewicz, A., & Szymczak, M. 2012, ApJ, 754, 149

De Buizer, J. M., Redman, R. O., Longmore, S. N., Caswell, J., & Feldman, P. A. 2009, A&A, 493, 127

De Buizer, J. M., & Vacca, W. D. 2010, AJ, 140, 196

de Villiers, H. M., Chrysostomou, A., Thompson, M. A., et al. 2015, MNRAS, 449, 119

di Francesco, J., Evans, II, N. J., Caselli, P., et al. 2007, Protostars and Planets V, 17

Draine, B. T. 2003, ARA&A, 41, 241

Egan, M. P., Shipman, R. F., Price, S. D., et al. 1998, ApJ, 494, L199

Eldridge, J. J., & Relaño, M. 2011, MNRAS, 411, 235

Elitzur, M. 1992, ARA&A, 30, 75

Ellingsen, S. P. 2005, MNRAS, 359, 1498

—. 2006, ApJ, 638, 241

Ellingsen, S. P., Breen, S. L., Sobolev, A. M., et al. 2011, ApJ, 742, 109

Ellingsen, S. P., Breen, S. L., Voronkov, M. A., & Dawson, J. R. 2013, MNRAS, 429, 3501

Ellingsen, S. P., Chen, X., Qiao, H.-H., et al. 2014, ApJ, 790, L28

Ellingsen, S. P., von Bibra, M. L., McCulloch, P. M., et al. 1996, MNRAS, 280, 378

Evans, II, N. J. 1999, ARA&A, 37, 311

Felli, M., Palagi, F., & Tofani, G. 1992, A&A, 255, 293

Foster, J. B., Jackson, J. M., Barnes, P. J., et al. 2011, ApJS, 197, 25

Fujiyoshi, T., Smith, C. H., Caswell, J. L., et al. 2006, MNRAS, 368, 1843

Fuller, G. A., & Myers, P. C. 1993, ApJ, 418, 273

Gan, C.-G., Chen, X., Shen, Z.-Q., Xu, Y., & Ju, B.-G. 2013, ApJ, 763, 2

Garay, G., Mardones, D., Bronfman, L., et al. 2010, ApJ, 710, 567

Garay, G., Mardones, D., Rodríguez, L. F., Caselli, P., & Bourke, T. L. 2002, ApJ, 567, 980

Garay, G., Mardones, D., Bronfman, L., et al. 2007, A&A, 463, 217

Gibb, A. G., Hoare, M. G., Little, L. T., & Wright, M. C. H. 2003, MNRAS, 339, 1011

Goddi, C., Greenhill, L. J., Chandler, C. J., et al. 2009, ApJ, 698, 1165

Goddi, C., & Moscadelli, L. 2006, A&A, 447, 577

Goddi, C., Moscadelli, L., Alef, W., et al. 2005, A&A, 432, 161

Gómez, Y. 2007, in IAU Symposium, Vol. 242, IAU Symposium, ed. J. M. Chapman & W. A. Baan, 292–298

Gonidakis, I., Chapman, J. M., Deacon, R. M., & Green, A. J. 2014, MNRAS, 443, 3819

Gonidakis, I., Diamond, P. J., & Kemball, A. J. 2013, MNRAS, 433, 3133

Gray, M. D., Wittkowski, M., Scholz, M., et al. 2009, MNRAS, 394, 51

Green, A. J., Frail, D. A., Goss, W. M., & Otrupcek, R. 1997, AJ, 114, 2058

Green, J. A., & McClure-Griffiths, N. M. 2011, MNRAS, 417, 2500

Green, J. A., Caswell, J. L., Fuller, G. A., et al. 2009, MNRAS, 392, 783

—. 2012, MNRAS, 420, 3108

Guibert, J., Rieu, N. Q., & Elitzur, M. 1978, A&A, 66, 395

Habart, E., Walmsley, M., Verstraete, L., et al. 2005, Space Sci. Rev., 119, 71

Hirota, T., Kim, M. K., & Honma, M. 2012, ApJ, 757, L1

Hirota, T., Kim, M. K., Kurono, Y., & Honma, M. 2014, ApJ, 782, L28

Ho, P. T. P., & Townes, C. H. 1983, ARA&A, 21, 239

Hoare, M. G., Kurtz, S. E., Lizano, S., Keto, E., & Hofner, P. 2007, Protostars and Planets V, 181

Hoare, M. G., Purcell, C. R., Churchwell, E. B., et al. 2012, PASP, 124, 939

Ilee, J. D., Wheelwright, H. E., Oudmaijer, R. D., et al. 2013, MNRAS, 429, 2960

Jackson, J. M., Finn, S. C., Chambers, E. T., Rathborne, J. M., & Simon, R. 2010, ApJ, 719, L185

Jackson, J. M., Rathborne, J. M., Shah, R. Y., et al. 2006, ApJS, 163, 145

Jeans, J. H. 1902, Royal Society of London Philosophical Transactions Series A, 199, 1

Jordan, C. H., Walsh, A. J., Lowe, V., et al. 2013, MNRAS, 429, 469

—. 2015, MNRAS, 448, 2344

Kahn, F. D. 1974, A&A, 37, 149

Kalenskii, S. V., Johansson, L. E. B., Bergman, P., et al. 2010, MNRAS, 405, 613

Kalenskii, S. V., & Sobolev, A. M. 1994, Astronomy Letters, 20, 91

Kauffmann, J., & Pillai, T. 2010, ApJ, 723, L7

Kauffmann, J., Pillai, T., Shetty, R., Myers, P. C., & Goodman, A. A. 2010, ApJ, 716, 433

Kaufmann, P., Gammon, R. H., Ibanez, A. L., et al. 1976, Nature, 260, 306

Kim, K.-T., & Koo, B.-C. 2001, ApJ, 549, 979

Kim, M. K., Hirota, T., Honma, M., et al. 2008, PASJ, 60, 991

Kurtz, S., Hofner, P., & Álvarez, C. V. 2004, ApJS, 155, 149

Lada, C. J., & Lada, E. A. 2003, ARA&A, 41, 57

Lee, K., Looney, L. W., Schnee, S., & Li, Z.-Y. 2013, ApJ, 772, 100

Leurini, S., Codella, C., López-Sepulcre, A., et al. 2014, A&A, 570, A49

Lilley, A. E., & Palmer, P. 1968, ApJS, 16, 143

Lizano, S. 2008, in Astronomical Society of the Pacific Conference Series, Vol. 387, Massive Star Formation: Observations Confront Theory, ed. H. Beuther, H. Linz, & T. Henning, 232

Lo, N., Redman, M. P., Jones, P. A., et al. 2011, MNRAS, 415, 525

Lo, N., Cunningham, M. R., Jones, P. A., et al. 2009, MNRAS, 395, 1021

Lockman, F. J. 1979, ApJ, 232, 761

Longmore, S. N., Rathborne, J., Bastian, N., et al. 2012, ApJ, 746, 117

Lopez, R., Morata, O., Sepulveda, I., et al. 1994, Ap&SS, 216, 151

López-Sepulcre, A., Codella, C., Cesaroni, R., Marcelino, N., & Walmsley, C. M. 2009, A&A, 499, 811

Lowe, V., Cunningham, M. R., Urquhart, J. S., et al. 2014, MNRAS, 441, 256

Lu, X., Zhang, Q., Liu, H. B., Wang, J., & Gu, Q. 2014, ApJ, 790, 84

Lumsden, S. L., Hoare, M. G., Urquhart, J. S., et al. 2013, ApJS, 208, 11

Martin-Pintado, J., Bachiller, R., & Fuente, A. 1992, A&A, 254, 315

McClure-Griffiths, N. M., Dickey, J. M., Gaensler, B. M., et al. 2005, ApJS, 158, 178

McEwen, B. C., Pihlström, Y. M., & Sjouwerman, L. O. 2014, ApJ, 793, 133

McKee, C. F., & Tan, J. C. 2003, ApJ, 585, 850

Meidt, S. E., Schinnerer, E., Knapen, J. H., et al. 2012, ApJ, 744, 17

Menten, K. M. 1991, ApJ, 380, L75

Minier, V., Booth, R. S., & Conway, J. E. 2002, A&A, 383, 614

Minier, V., Ellingsen, S. P., Norris, R. P., & Booth, R. S. 2003, A&A, 403, 1095

Moeckel, N., & Clarke, C. J. 2011, MNRAS, 410, 2799

Molinari, S., Swinyard, B., Bally, J., et al. 2010, A&A, 518, L100

Moscadelli, L., Cesaroni, R., & Rioja, M. J. 2005, A&A, 438, 889

Moscadelli, L., & Goddi, C. 2014, A&A, 566, A150

Moscadelli, L., Testi, L., Furuya, R. S., et al. 2006, A&A, 446, 985

Müller, H. S. P., Schlöder, F., Stutzki, J., & Winnewisser, G. 2005, Journal of Molecular Structure, 742, 215

Müller, H. S. P., Spezzano, S., Bizzocchi, L., et al. 2013, Journal of Physical Chemistry A, 117, 13843

Navarete, F., Damineli, A., Barbosa, C. L., & Blum, R. D. 2015, MNRAS, 450, 4364

Nguyen-Lu'o'ng, Q., Motte, F., Carlhoff, P., et al. 2013, ApJ, 775, 88

Niederhofer, F., Humphreys, E. M. L., & Goddi, C. 2012, A&A, 548, A69

Norris, R. P., Caswell, J. L., Gardner, F. F., & Wellington, K. J. 1987, ApJ, 321, L159

Olguin, F. A., Hoare, M. G., Wheelwright, H. E., et al. 2015, MNRAS, 449, 2784

Ott, J., Weiß, A., Staveley-Smith, L., Henkel, C., & Meier, D. S. 2014, ApJ, 785, 55

Pandian, J. D., Wyrowski, F., & Menten, K. M. 2012, ApJ, 753, 50

Peretto, N., & Fuller, G. A. 2009, A&A, 505, 405

Peretto, N., Fuller, G. A., Duarte-Cabral, A., et al. 2013, A&A, 555, A112

Pihlström, Y. M., Sjouwerman, L. O., Frail, D. A., et al. 2014, AJ, 147, 73

Pillai, T., Kauffmann, J., Tan, J. C., et al. 2015, ApJ, 799, 74

Pillai, T., Kauffmann, J., Wyrowski, F., et al. 2011, A&A, 530, A118

Pratap, P., Dickens, J. E., Snell, R. L., et al. 1997, ApJ, 486, 862

Purcell, C. R. 2006, PhD thesis, The University of New South Wales, Australia

Purcell, C. R., & Hoare, M. G. 2010, Highlights of Astronomy, 15, 781

Purcell, C. R., Balasubramanyam, R., Burton, M. G., et al. 2006, MNRAS, 367, 553

Purcell, C. R., Minier, V., Longmore, S. N., et al. 2009, A&A, 504, 139

Purcell, C. R., Longmore, S. N., Walsh, A. J., et al. 2012, MNRAS, 426, 1972

Purcell, C. R., Hoare, M. G., Cotton, W. D., et al. 2013, ApJS, 205, 1

Qiao, H.-H., Walsh, A. J., Gómez, J. F., et al. 2016, ApJ, 817, 37

Rathborne, J. M., Jackson, J. M., & Simon, R. 2006, ApJ, 641, 389

Rathborne, J. M., Longmore, S. N., Jackson, J. M., et al. 2015, ApJ, 802, 125

Reid, M. J., Menten, K. M., Zheng, X. W., et al. 2009, ApJ, 700, 137

Robitaille, T. P., Meade, M. R., Babler, B. L., et al. 2008, AJ, 136, 2413

Rodgers, A. W., Campbell, C. T., & Whiteoak, J. B. 1960, MNRAS, 121, 103

Schilke, P., Walmsley, C. M., Pineau des Forets, G., & Flower, D. R. 1997, A&A, 321, 293

Schuller, F., Menten, K. M., Contreras, Y., et al. 2009, A&A, 504, 415

Sevenster, M. N., Chapman, J. M., Habing, H. J., Killeen, N. E. B., & Lindqvist, M. 1997, A&AS, 124, 509

Shu, F. H. 1977, ApJ, 214, 488

Simon, R., Jackson, J. M., Rathborne, J. M., & Chambers, E. T. 2006, ApJ, 639, 227

Sjouwerman, L. O., Pihlström, Y. M., & Fish, V. L. 2010, ApJ, 710, L111

Slysh, V. I., Kalenskii, S. V., Valtts, I. E., & Otrupcek, R. 1994, MNRAS, 268, 464

Smith, R. J., Glover, S. C. O., & Klessen, R. S. 2014, MNRAS, 445, 2900

Stahler, S. W., & Palla, F. 2005, The Formation of Stars

Tafalla, M., Myers, P. C., Caselli, P., & Walmsley, C. M. 2004, A&A, 416, 191

Tafalla, M., Myers, P. C., Caselli, P., Walmsley, C. M., & Comito, C. 2002, ApJ, 569, 815

Taylor, S. D., Morata, O., & Williams, D. A. 1998, A&A, 336, 309

Tielens, A. G. G. M. 2008, ARA&A, 46, 289

Titmarsh, A. M., Ellingsen, S. P., Breen, S. L., Caswell, J. L., & Voronkov, M. A. 2013, ApJ, 775, L12

—. 2014, MNRAS, 443, 2923

Townes, C. H., & Schawlow, A. L. 1955, Microwave Spectroscopy

Urquhart, J. S., Figura, C. C., Moore, T. J. T., et al. 2014a, MNRAS, 437, 1791

Urquhart, J. S., Hoare, M. G., Lumsden, S. L., et al. 2009, A&A, 507, 795

Urquhart, J. S., Hoare, M. G., Purcell, C. R., et al. 2010, PASA, 27, 321

Urquhart, J. S., Morgan, L. K., Figura, C. C., et al. 2011, MNRAS, 418, 1689

Urquhart, J. S., Moore, T. J. T., Schuller, F., et al. 2013, MNRAS, 431, 1752

Urquhart, J. S., Csengeri, T., Wyrowski, F., et al. 2014b, A&A, 568, A41

Urquhart, J. S., Moore, T. J. T., Menten, K. M., et al. 2015, MNRAS, 446, 3461

Val'tts, I. E., Ellingsen, S. P., Slysh, V. I., et al. 2000, MNRAS, 317, 315

van Dishoeck, E. F., & Blake, G. A. 1998, ARA&A, 36, 317

Voronkov, M. A., Caswell, J. L., Britton, T. R., et al. 2010a, MNRAS, 408, 133

Voronkov, M. A., Caswell, J. L., Ellingsen, S. P., et al. 2012, in IAU Symposium, Vol. 287, IAU Symposium, ed. R. S. Booth, W. H. T. Vlemmings, & E. M. L. Humphreys, 433–440

Voronkov, M. A., Caswell, J. L., Ellingsen, S. P., Green, J. A., & Breen, S. L. 2014, MNRAS, 439, 2584

Voronkov, M. A., Caswell, J. L., Ellingsen, S. P., & Sobolev, A. M. 2010b, MNRAS, 405, 2471

Walsh, A. J., Burton, M. G., Hyland, A. R., & Robinson, G. 1998, MNRAS, 301, 640

Walsh, A. J., Lo, N., Burton, M. G., et al. 2008, PASA, 25, 105

Walsh, A. J., Purcell, C. R., Longmore, S. N., et al. 2014, MNRAS, 442, 2240

Walsh, A. J., Breen, S. L., Britton, T., et al. 2011, MNRAS, 416, 1764

Wang, J., Zhang, J., Gao, Y., et al. 2014, Nature Communications, 5, 5449

Wang, K., Testi, L., Ginsburg, A., et al. 2015, MNRAS, 450, 4043

Ward-Thompson, D., & Whitworth, A. P. 2011, An Introduction to Star Formation

Weaver, H., Williams, D. R. W., Dieter, N. H., & Lum, W. T. 1965, Nature, 208, 29

Weinreb, S., Barrett, A. H., Meeks, M. L., & Henry, J. C. 1963, Nature, 200, 829

Whelan, E. T., Ray, T. P., Comeron, F., Bacciotti, F., & Kavanagh, P. J. 2012, ApJ, 761, 120

Wilson, T. L., Walmsley, C. M., Jewell, P. R., & Snyder, L. E. 1984, A&A, 134, L7

Wilson, W. E., Ferris, R. H., Axtens, P., et al. 2011, MNRAS, 416, 832

Wong, T., Ladd, E. F., Brisbin, D., et al. 2008, MNRAS, 386, 1069

Wood, D. O. S., & Churchwell, E. 1989, ApJ, 340, 265

Wu, J., Evans, II, N. J., Shirley, Y. L., & Knez, C. 2010, ApJS, 188, 313

Yen, H.-W., Takakuwa, S., Ohashi, N., et al. 2014, ApJ, 793, 1

Yu, N., & Wang, J.-J. 2014, MNRAS, 440, 1213

Yusef-Zadeh, F., Cotton, W., Viti, S., Wardle, M., & Royster, M. 2013, ApJ, 764, L19

Zapata, L. A., Menten, K., Reid, M., & Beuther, H. 2009, ApJ, 691, 332

Zinnecker, H., & Yorke, H. W. 2007, ARA&A, 45, 481

Appendices

Appendix A

Supplementary material from the MALT-45 survey

This appendix contains reference material for the publication outlined in Chapter 3. For each of the spectral lines discussed, a noise map can be seen §A.1. Detected class I CH_3OH maser spectra are contained in §A.2. Auto-correlated images not contained in the main body of the publication are shown in §A.3. Finally, SiO $v = 1, 2, 3$ maser spectra are contained in §A.4. Each of the maps show the region $330° \leq l \leq 335°$, $b = \pm 0.5°$.

A.1 RMS noise maps

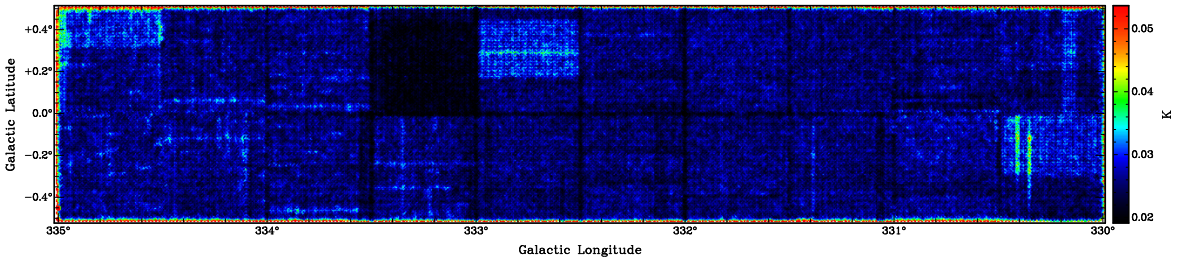

Figure A.1: RMS noise map for the SiO (1–0) $v = 0$ zoom window. The colour scale ranges from 0.02 to 0.05 K.

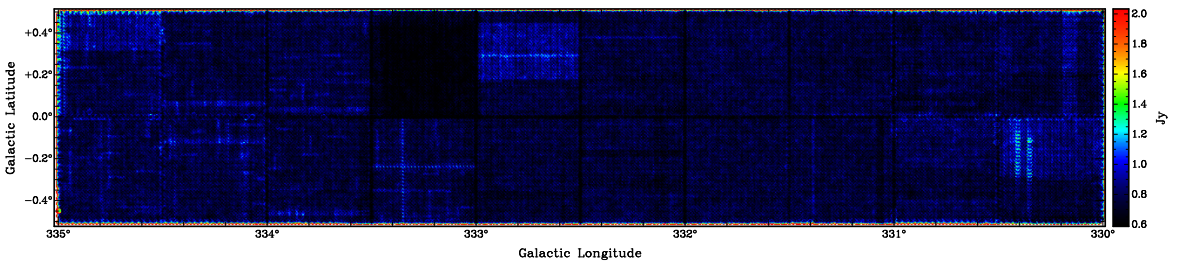

Figure A.2: RMS noise map for the SiO (1–0) $v = 1$ zoom window. The colour scale ranges from 0.6 to 2.0 Jy.

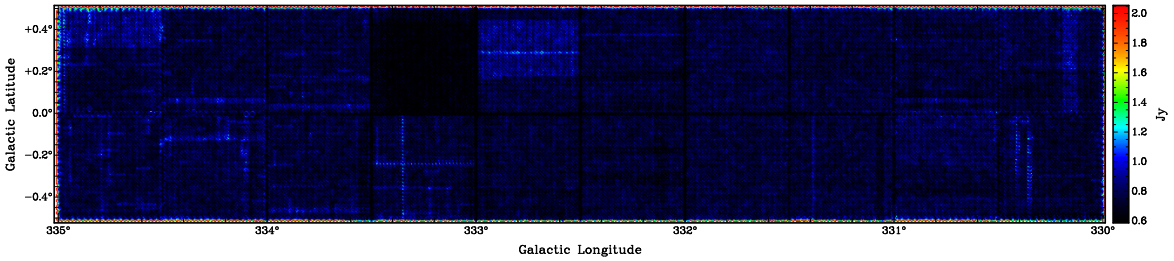

Figure A.3: RMS noise map for the SiO (1–0) $v = 2$ zoom window. The colour scale ranges from 0.6 to 2.0 Jy.

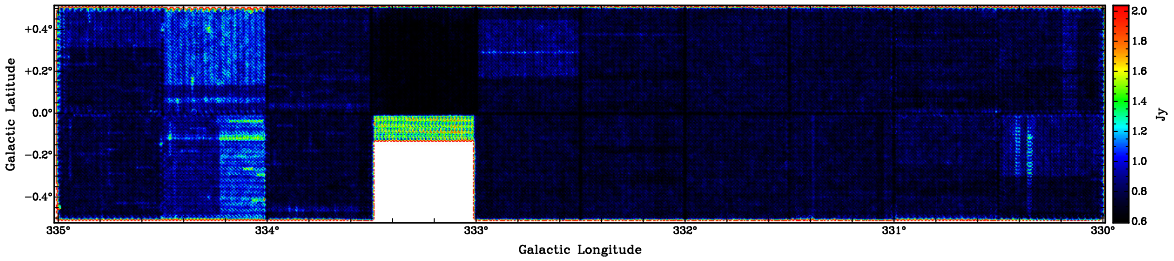

Figure A.4: RMS noise map for the SiO (1–0) $v = 3$ zoom window. The colour scale ranges from 0.6 to 2.0 Jy.

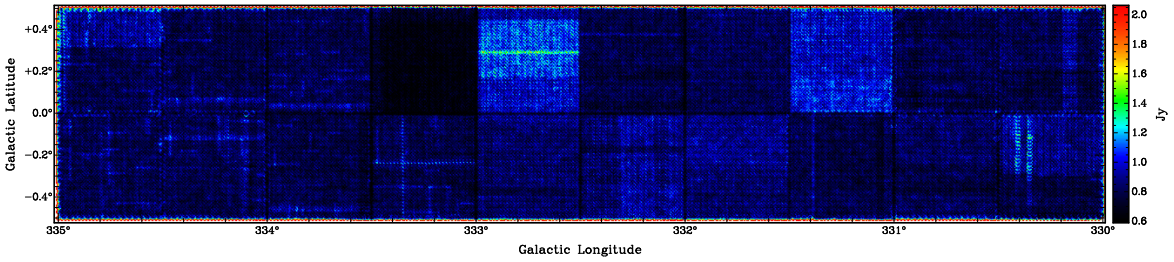

Figure A.5: RMS noise map for the class I CH_3OH zoom window. The colour scale ranges from 0.6 to 2.0 Jy.

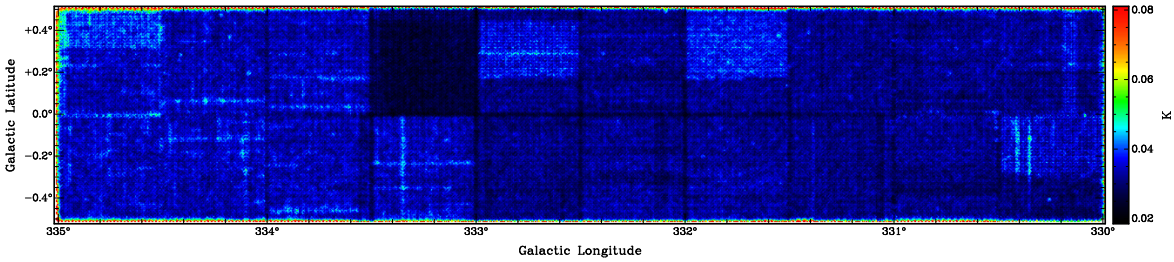

Figure A.6: RMS noise map for the CS (1–0) zoom window. The colour scale ranges from 0.02 to 0.08 K.

A.2 Class I CH_3OH maser spectra

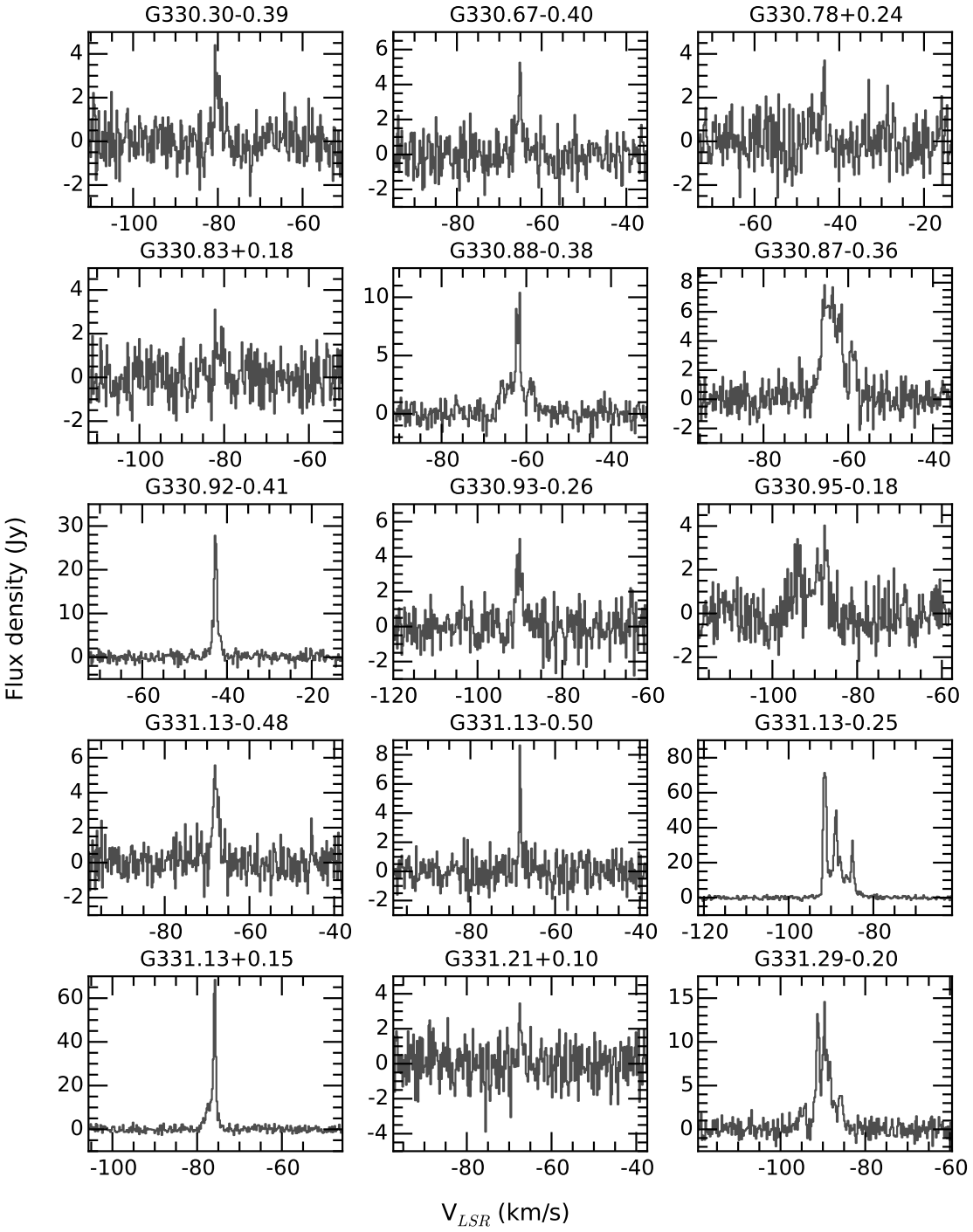

Figure A.7: Spectra of each detected class I CH_3OH maser.

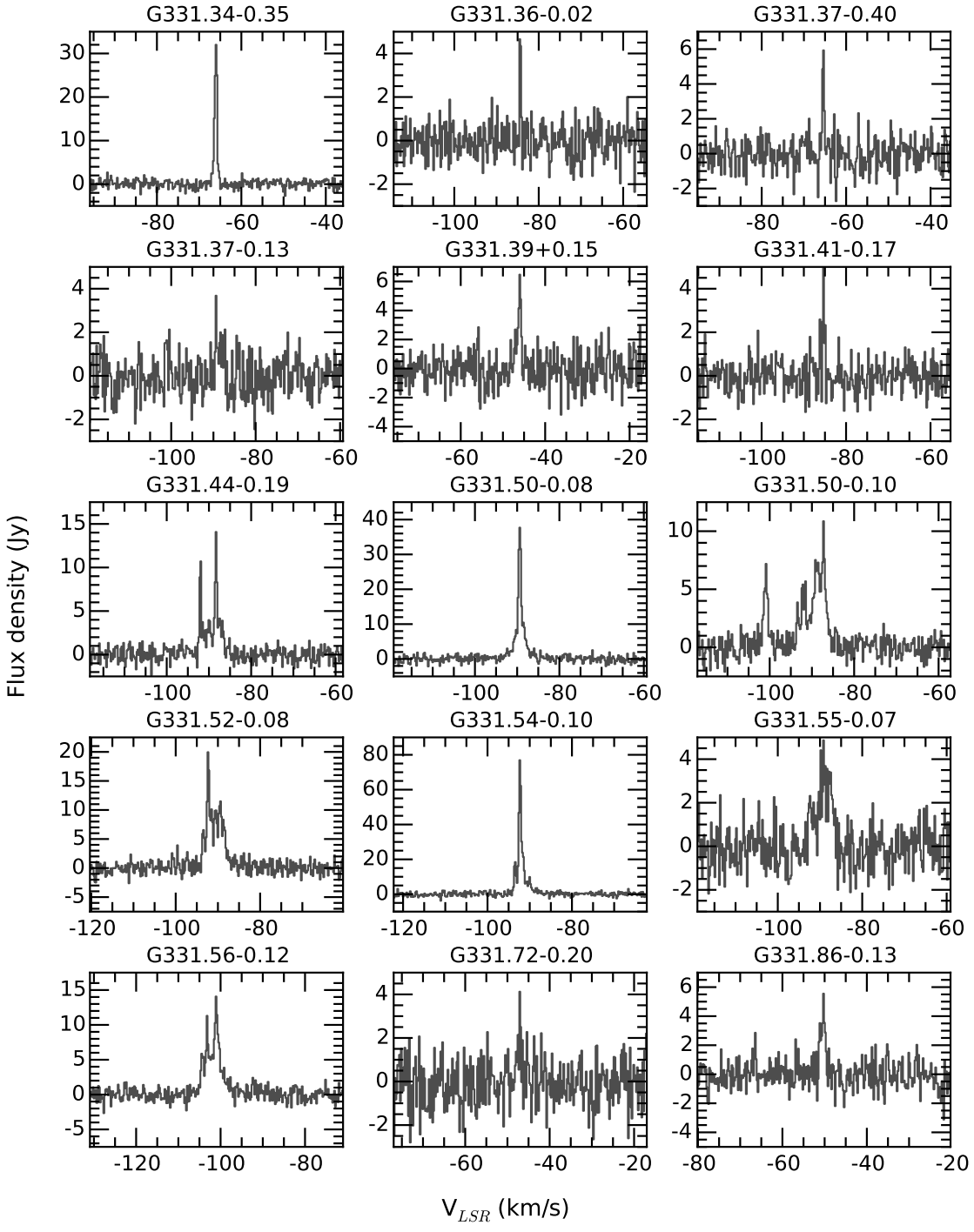

Figure A.7: *continued*

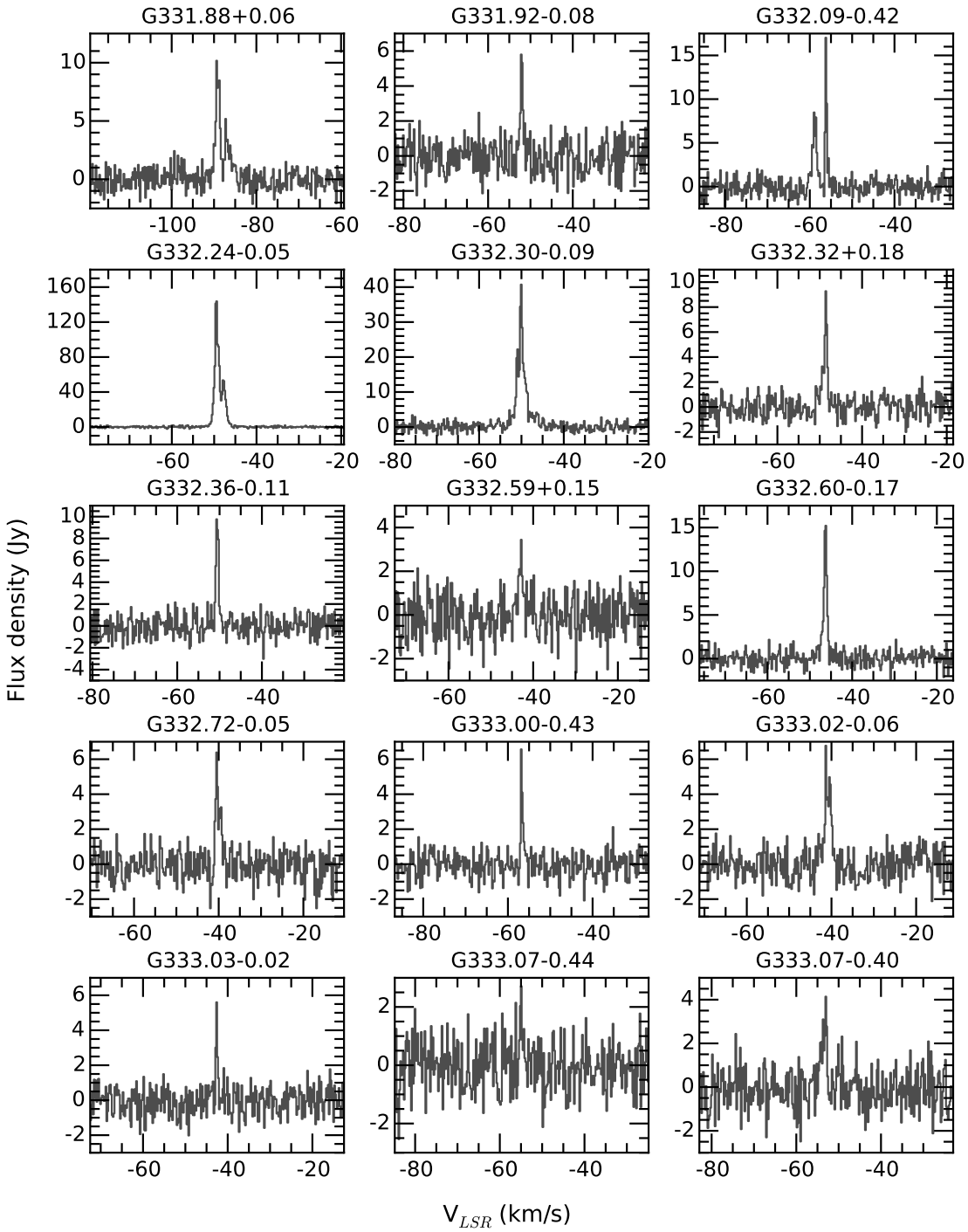

Figure A.7: *continued*

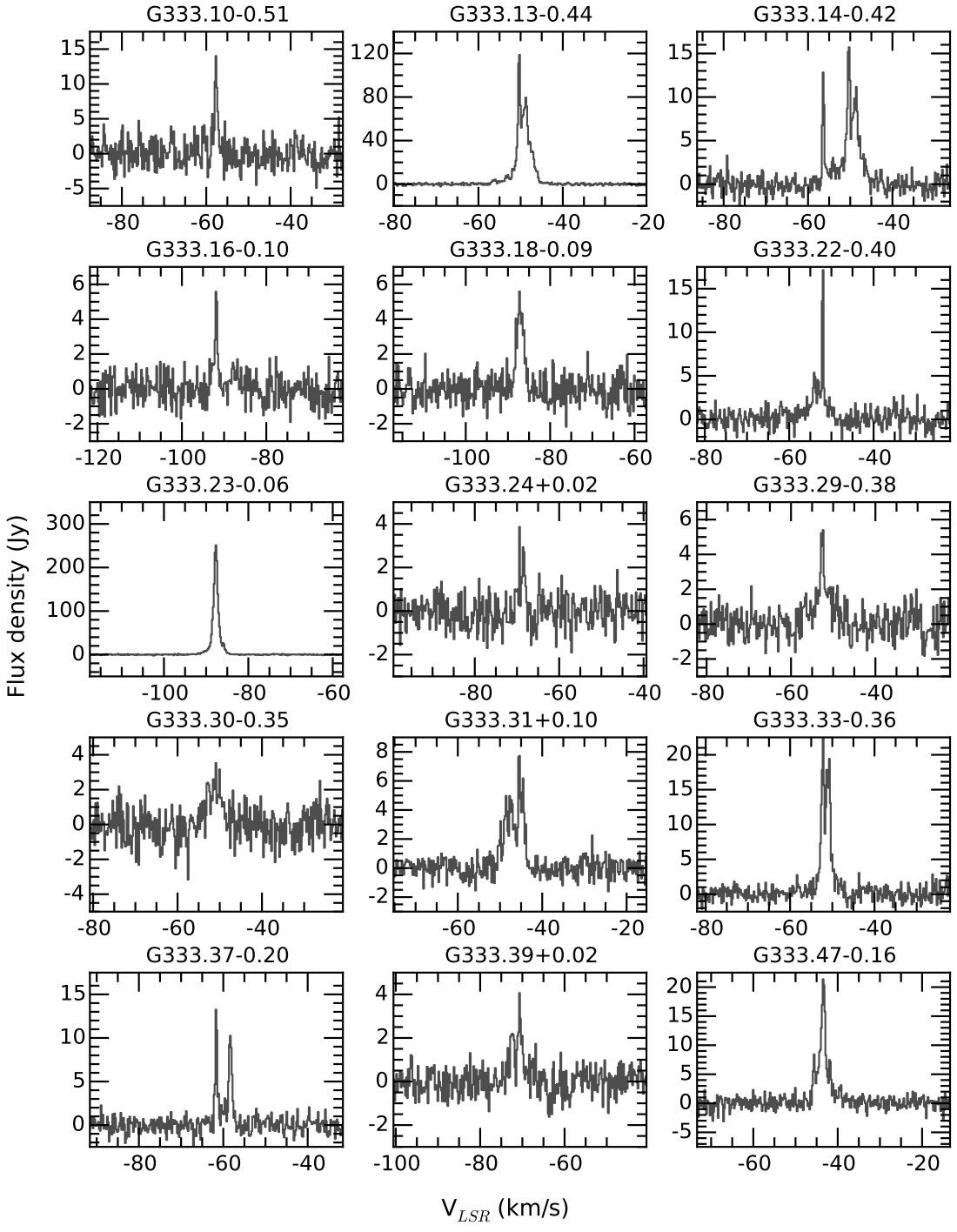

Figure A.7: *continued*

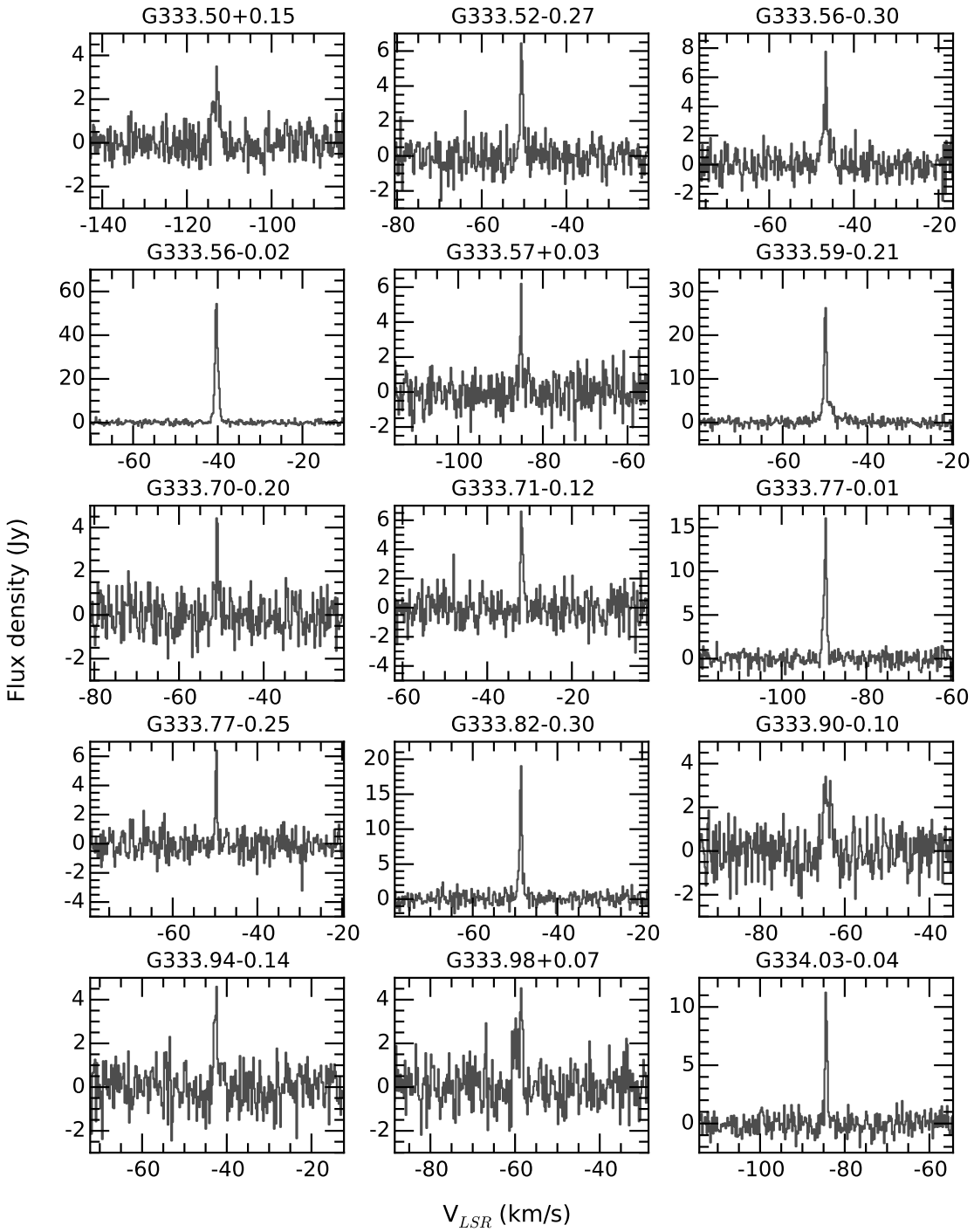

Figure A.7: *continued*

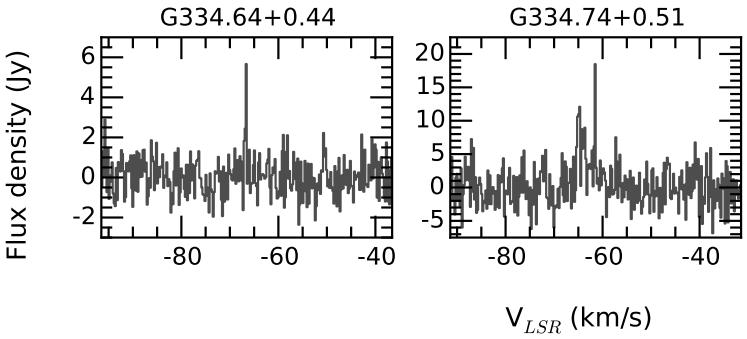

Figure A.7: *continued*

A.3 Auto-correlated maps

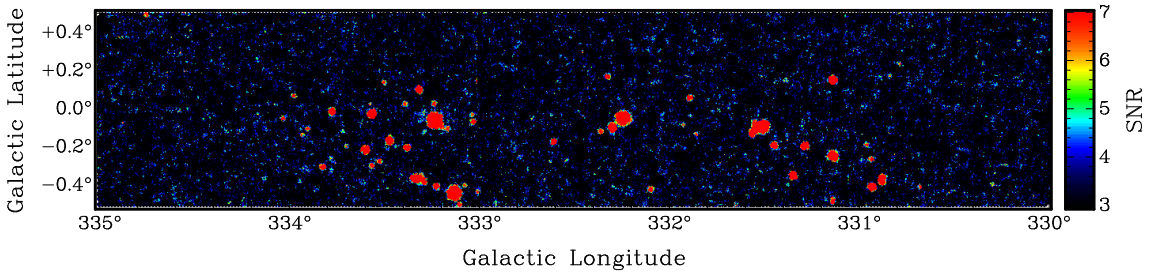

Figure A.8: Auto-correlated class I CH_3OH maser emission, in a peak signal-to-noise map. 77 masers are found within these data. The colour scale ranges with ratios from 2 to 7.

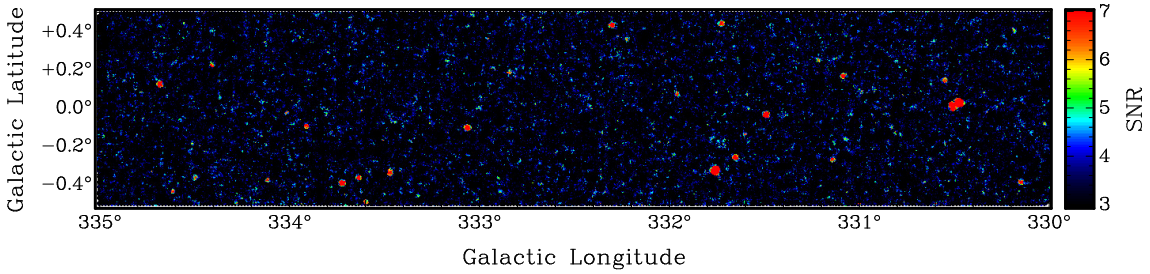

Figure A.9: Auto-correlated SiO (1–0) $v = 1$ maser emission, in a peak signal-to-noise map. 45 masers are found within these data. The colour scale ranges with ratios from 2 to 7.

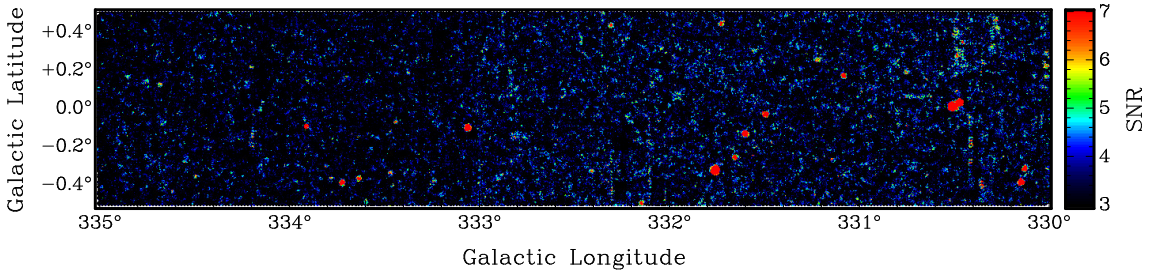

Figure A.10: Auto-correlated SiO (1–0) $v = 2$ maser emission, in a peak signal-to-noise map. 37 masers are found within these data. The colour scale ranges with ratios from 2 to 7.

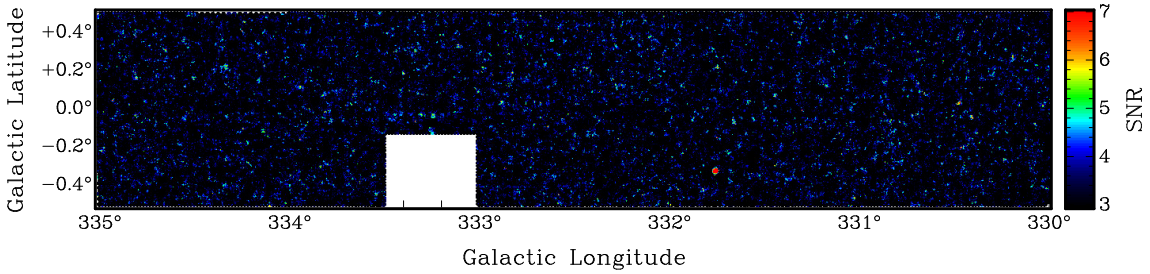

Figure A.11: Auto-correlated SiO (1–0) $v = 3$ maser emission, in a peak signal-to-noise map. The gap in the G333.0−0.5 tile is due to a correlator fault for that day of observing. 3 masers are found within these data. The colour scale ranges with ratios from 2 to 7.

A.4 SiO maser spectra

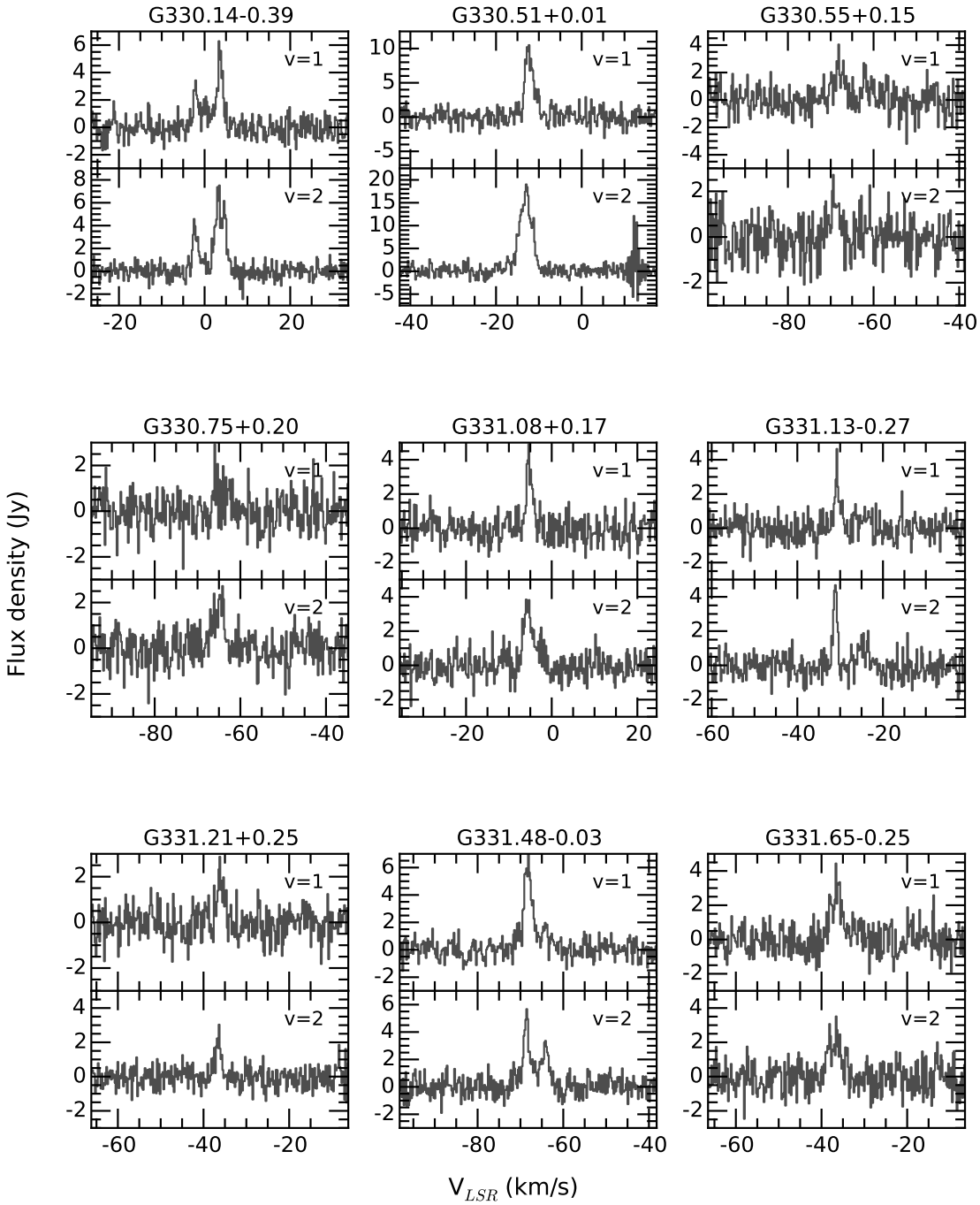

Figure A.12: Spectra of regions containing SiO $v = 1$ and $v = 2$ maser detections. G330.51+0.01 contains a correlator defect within the $v = 2$ spectrum at around $v = 10\,\mathrm{km\,s^{-1}}$.

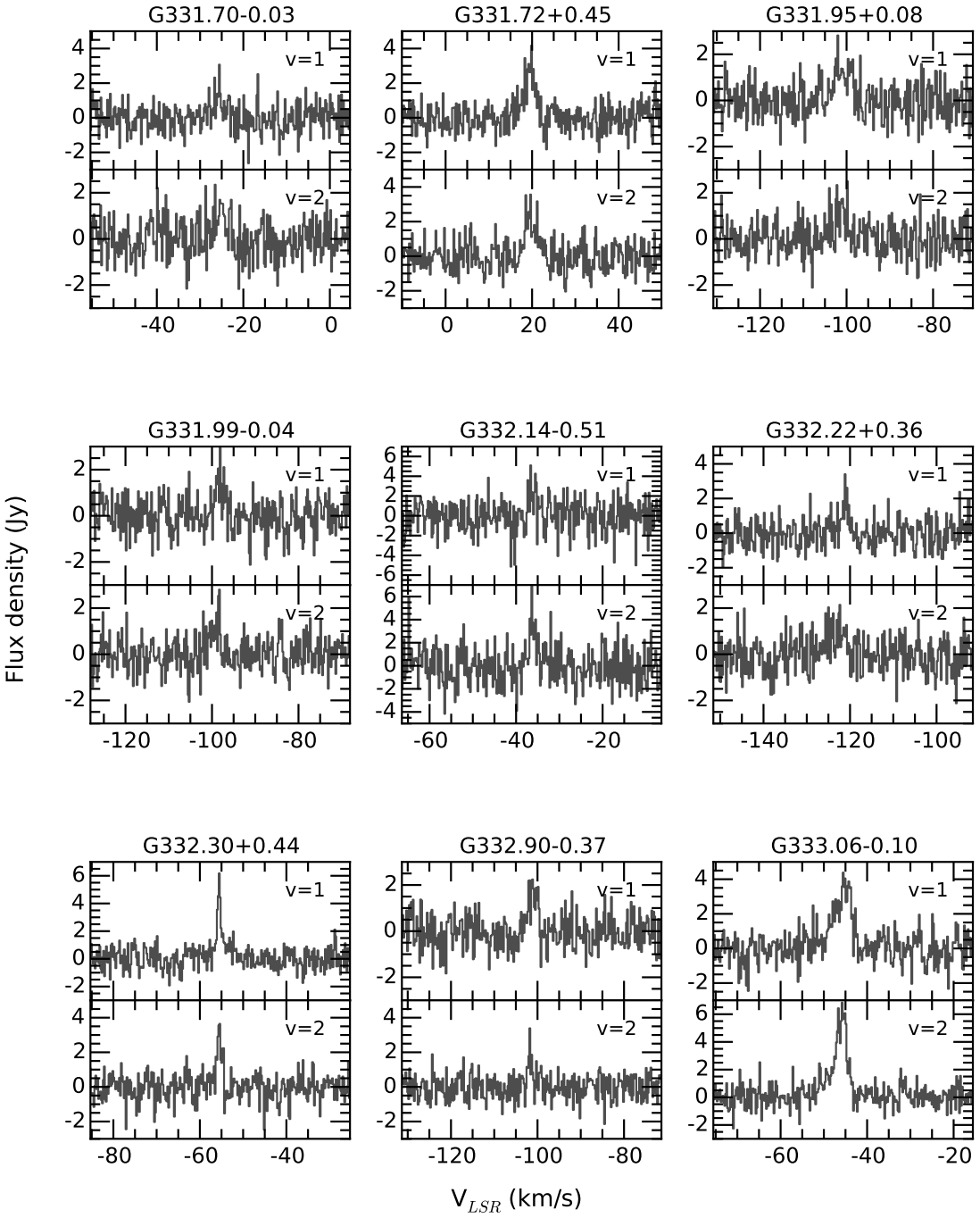

Figure A.12: *continued*

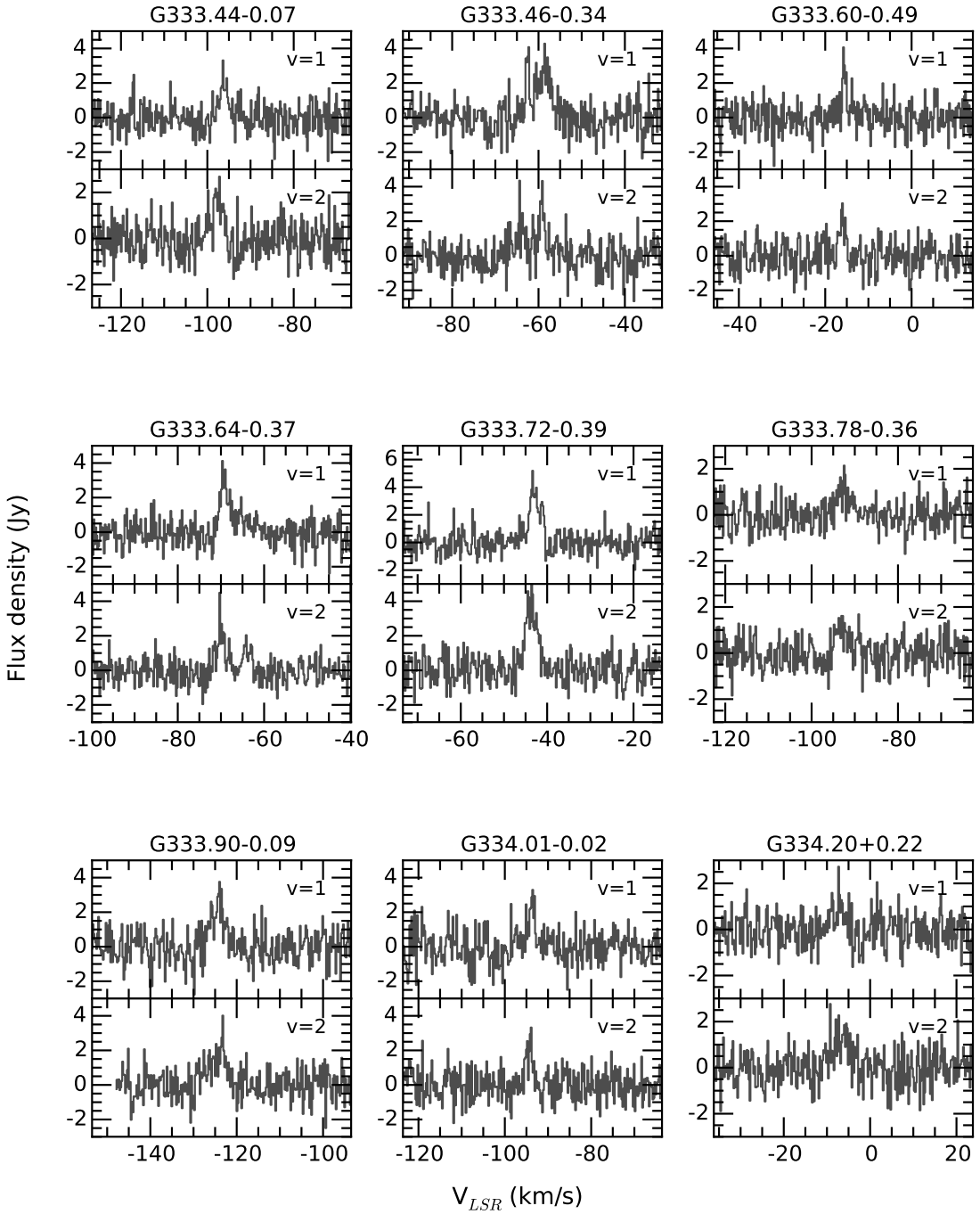

Figure A.12: *continued*

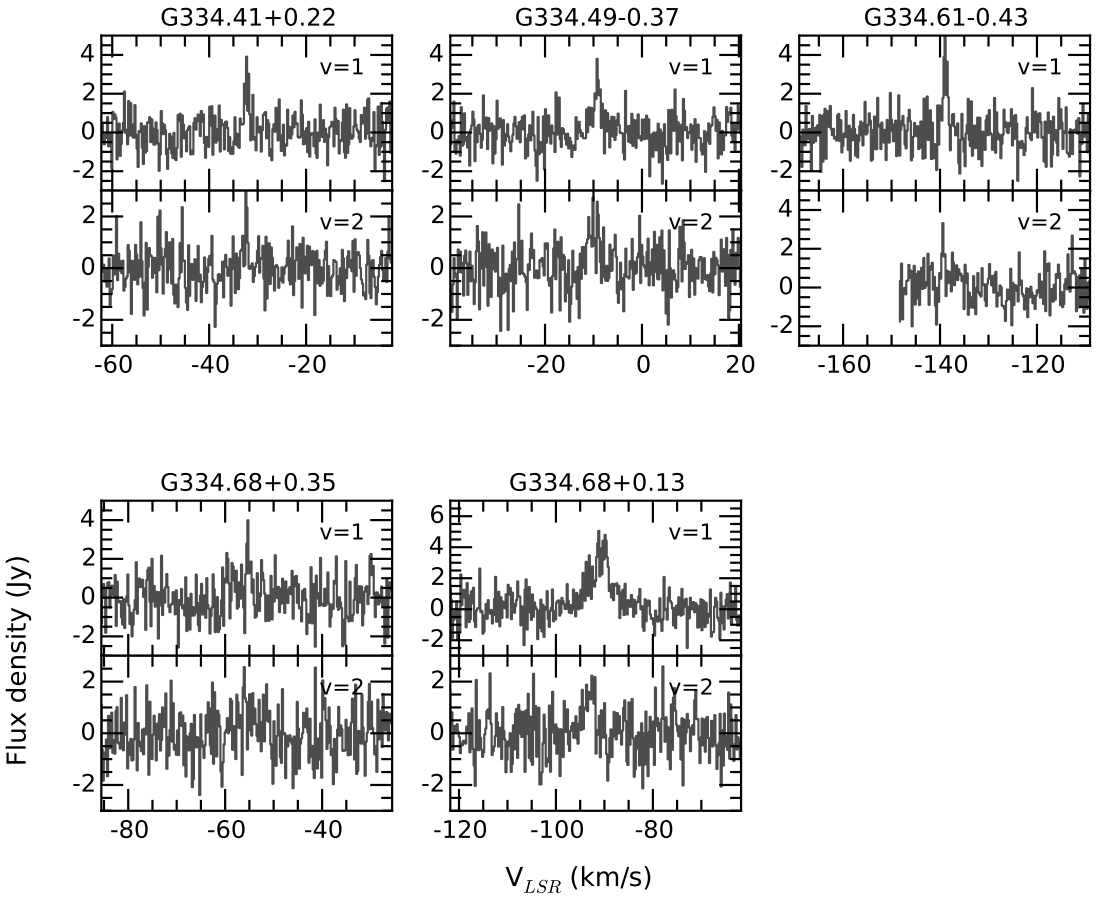

Figure A.12: *continued*

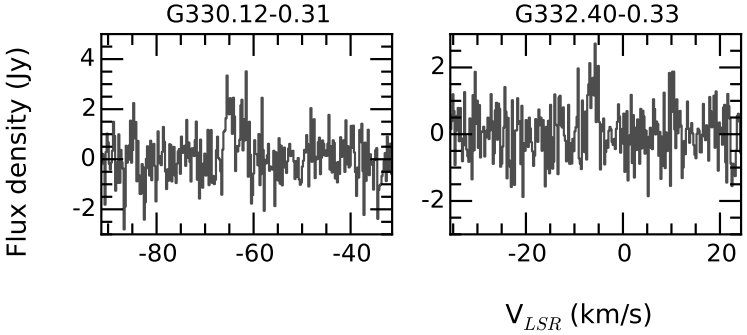

Figure A.13: Spectra of regions containing only SiO $v = 2$ maser detections.

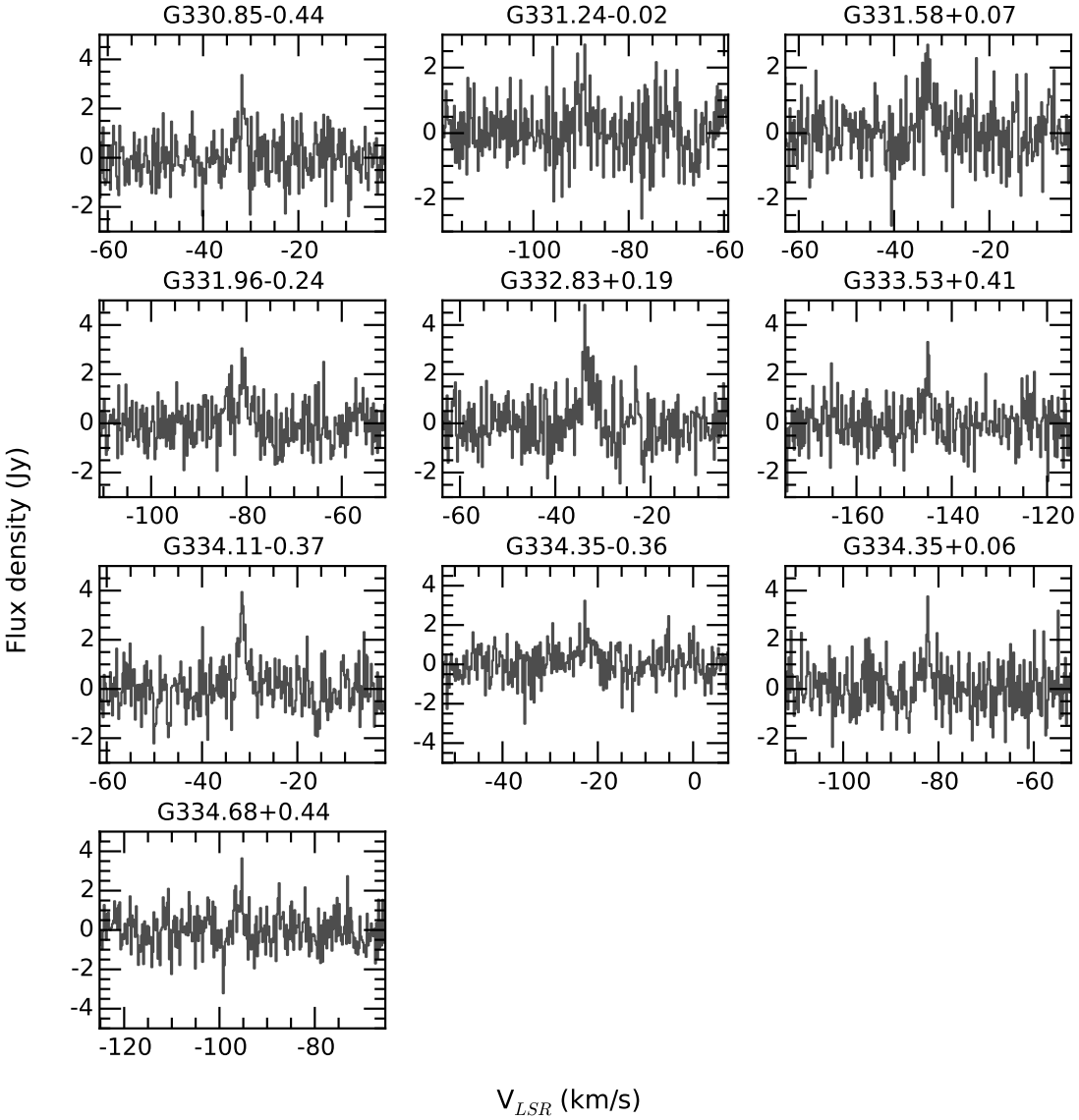

Figure A.14: Spectra of regions containing only SiO $v = 1$ maser detections.

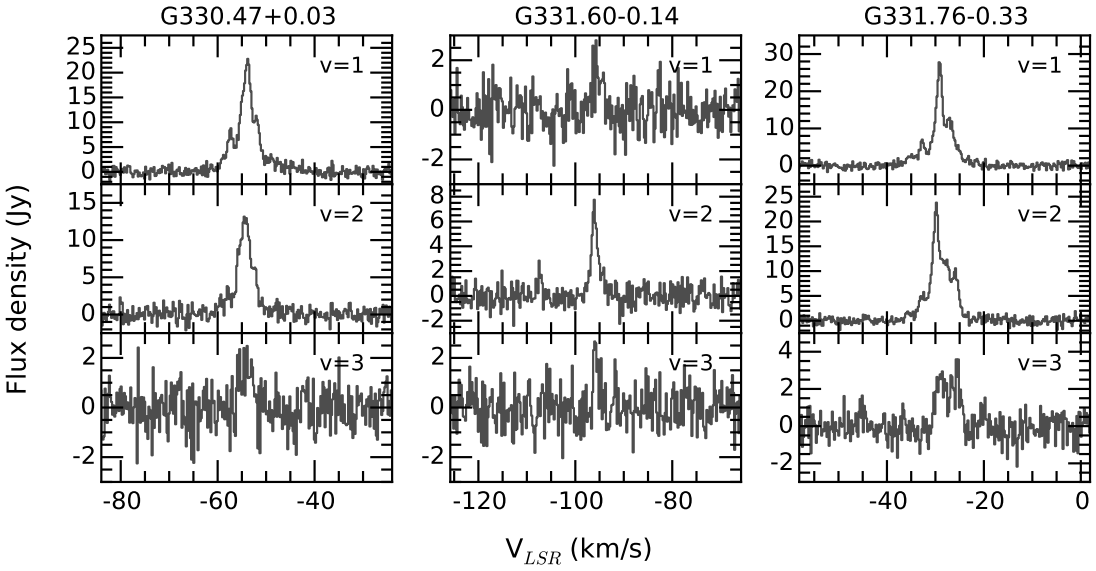

Figure A.15: Spectra of regions containing SiO $v = 1$, $v = 2$ and $v = 3$ masers.

Appendix B

Supplementary material from the MALT-45 class I CH_3OH maser follow-up survey

This appendix contains reference material for the publication outlined in Chapter 4. Each class I CH_3OH maser spot is characterised by Gaussian fits in §B.1. For each class I CH_3OH maser region, CS, SiO and thermal CH_3OH emission are characterised by Gaussian fits in §B.2. GLIMPSE three-colour images in 3.6, 4.5 and 8.0 μm emission with class I CH_3OH, class II CH_3OH, H_2O and OH masers can be seen in §B.3.

B.1 Gaussian fits to cross-correlated class I CH_3OH maser emission

Table B.1: Gaussian fits for the class I CH_3OH maser spots. Column 1 lists the maser spot name, along with a letter designating the spot. Spots labelled with an asterisk (∗) have been manually fitted; see §4.2.1.1. Columns 2 and 3 list the fitted position for the Gaussian. Columns 4 through 6 list the fitted Gaussian parameters. Note that the uncertainty for each parameter is quoted in parentheses, in units of the least significant figure. Column 7 lists the integrated flux density of the Gaussian. Rows without spot names correspond to a second Gaussian fitted to the spot directly above.

Spot name	α_{2000} (h:m:s)		δ_{2000} (°:′:″)		Peak flux density (Jy)		Peak velocity ($km\,s^{-1}$)		FWHM ($km\,s^{-1}$)		Integrated flux density ($Jy\,km\,s^{-1}$)
G330.2940−0.3921A	16:07:37.51	(5)	−52:30:56.1	(2)	1.00	(4)	−80.13	(2)	0.90	(4)	0.679
G330.2945−0.3943A	16:07:38.24	(4)	−52:31:00.5	(1)	0.52	(3)	−77.55	(2)	0.93	(5)	0.363
G330.6780−0.4023A	16:09:31.70	(5)	−52:15:50.7	(1)	1.73	(6)	−64.78	(1)	0.78	(3)	1.015
G330.7790+0.2488A	16:07:09.75	(3)	−51:42:53.76	(5)	0.72	(2)	−43.227	(6)	0.57	(1)	0.308
G330.8749−0.3557A	16:10:15.99	(6)	−52:05:46.6	(1)	14.3	(1)	−61.284	(2)	0.476	(5)	5.120
G330.8774−0.3676A	16:10:19.8	(1)	−52:06:12.1	(2)	2.4	(1)	−58.06	(2)	0.84	(5)	1.519
G330.8711−0.3830A	16:10:22.13	(8)	−52:07:08.23	(9)	0.85	(6)	−58.10	(4)	1.08	(8)	0.690
G330.8711−0.3830B	16:10:22.1	(1)	−52:07:08.3	(1)	0.77	(5)	−62.86	(3)	0.89	(7)	0.513
					0.51	(4)	−64.50	(8)	2.2	(2)	0.340
G330.9261−0.4083A	16:10:44.6	(2)	−52:06:00.37	(4)	11.8	(4)	−42.36	(1)	0.66	(2)	5.877
					1.2	(2)	−41.37	(5)	0.7	(1)	0.598
G330.9274−0.4072A	16:10:44.723	(9)	−52:05:54.29	(9)	1.9	(1)	−41.41	(2)	0.52	(4)	0.744
G330.9304−0.2602A	16:10:06.61	(4)	−51:59:18.5	(1)	3.9	(1)	−90.00	(1)	0.91	(3)	2.675
G330.9311−0.2605A	16:10:06.87	(6)	−51:59:17.78	(5)	3.94	(8)	−89.014	(5)	0.50	(1)	1.480
G330.9548−0.1823A	16:09:52.99	(5)	−51:54:52.8	(2)	1.55	(6)	−93.66	(1)	0.57	(3)	0.670
G331.1308−0.4696A	16:11:59.38	(9)	−52:00:19.5	(2)	0.78	(5)	−68.94	(2)	0.59	(5)	0.346
G331.1308−0.4698A	16:11:59.4	(1)	−52:00:20.24	(5)	2.6	(1)	−67.45	(3)	1.47	(8)	2.876
G331.1336−0.4882A	16:12:05.14	(2)	−52:01:01.37	(5)	3.13	(6)	−67.911	(4)	0.459	(9)	1.082
G331.1308−0.2441A	16:10:59.53	(2)	−51:50:25.79	(4)	13.0	(6)	−87.50	(3)	1.45	(7)	14.148
G331.1308−0.2441B	16:10:59.54	(6)	−51:50:25.72	(5)	21	(4)	−90.1	(1)	1.6	(3)	24.901
G331.1308−0.2441C	16:10:59.54	(6)	−51:50:25.68	(9)	93	(3)	−91.11	(1)	0.93	(3)	65.276
G331.1333−0.2458A	16:11:00.7	(5)	−51:50:23.97	(6)	45	(1)	−88.531	(8)	0.70	(2)	23.769
G331.1333−0.2410A	16:10:59.41	(2)	−51:50:11.8	(1)	23.1	(2)	−84.630	(2)	0.610	(5)	10.604
G331.1333−0.2410B	16:10:59.45	(2)	−51:50:11.64	(2)	2.9	(1)	−86.19	(1)	0.53	(3)	1.151
G331.1322−0.2454A	16:11:00.25	(6)	−51:50:25.71	(1)	6.5	(2)	−84.34	(1)	0.81	(3)	3.986
G331.1322−0.2454B	16:11:00.29	(4)	−51:50:26.0	(1)	6.3	(2)	−87.667	(8)	0.47	(2)	2.244
G331.1332−0.2407A	16:10:59.30	(4)	−51:50:10.90	(3)	2.11	(6)	−85.718	(8)	0.59	(2)	0.931
G331.1313−0.2434A	16:10:59.499	(9)	−51:50:22.76	(5)	4.19	(7)	−86.097	(3)	0.412	(7)	1.300
G331.1315−0.2441A	16:10:59.73	(8)	−51:50:24.2	(1)	0.90	(5)	−82.85	(2)	0.57	(4)	0.386
G331.1313−0.2451A	16:10:59.9	(2)	−51:50:27.2	(2)	0.89	(7)	−82.53	(4)	0.91	(8)	0.610
G331.1329+0.1560A	16:09:15.03	(5)	−51:32:42.42	(7)	1.03	(9)	−78.36	(3)	0.66	(7)	0.509
G331.1339+0.1569A	16:09:15.07	(6)	−51:32:37.79	(4)	1.42	(3)	−78.336	(8)	0.72	(2)	0.768
G331.1348+0.1562A	16:09:15.50	(2)	−51:32:37.3	(1)	10.0	(3)	−77.19	(1)	0.77	(3)	5.760
G331.1332+0.1565A	16:09:15.00	(7)	−51:32:40.5	(1)	76	(1)	−75.532	(5)	0.56	(1)	32.195
					4.0	(6)	−76.48	(6)	0.8	(1)	1.694

Table B.1: *continued*

Spot name	α_{2000} (h:m:s)		δ_{2000} (°:′:″)		Peak flux density (Jy)		Peak velocity ($km\,s^{-1}$)		FWHM ($km\,s^{-1}$)		Integrated flux density ($Jy\,km\,s^{-1}$)
G331.1335+0.1562A	16:09:15.16	(2)	−51:32:40.63	(9)	10.4	(2)	−76.139	(5)	0.60	(1)	4.664
G331.1331+0.1568A	16:09:14.884	(9)	−51:32:40.070	(7)	4.8	(1)	−74.512	(8)	0.52	(2)	1.889
G331.2846−0.1953A	16:11:30.32	(4)	−51:41:59.9	(1)	1.08	(4)	−94.03	(3)	1.44	(6)	1.168
G331.2800−0.1899A	16:11:27.57	(5)	−51:41:56.89	(5)	8.4	(6)	−89.31	(3)	0.77	(6)	4.883
G331.2800−0.1899B	16:11:28	(0)	−51:41:57.02	(1)	6.3	(9)	−89.94	(6)	0.9	(2)	4.333
G331.2800−0.1899C	16:11:27.58	(7)	−51:41:57.03	(2)	12.2	(3)	−90.77	(1)	0.81	(3)	7.417
G331.2800−0.1899D	16:11:27.55	(6)	−51:41:57.07	(1)	6	(5)	−91.31	(5)	0.2	(2)	1.021
					1.0	(1)	−92.17	(8)	1.2	(2)	0.170
G331.2802−0.1898A*	16:11:27.6	(2)	−51:41:56.4	(2)	5.4	(6)	−89.92	(5)	0.8	(1)	3.427
G331.2803−0.1899A	16:11:27.66	(4)	−51:41:56.26	(7)	5.0	(4)	−88.49	(3)	0.88	(7)	3.306
G331.2768−0.1870A	16:11:25.91	(5)	−51:41:57.21	(5)	3.0	(3)	−86.83	(4)	0.8	(1)	1.861
G331.2793−0.1873A	16:11:26.69	(2)	−51:41:51.98	(7)	2.7	(1)	−85.764	(9)	0.44	(2)	0.890
G331.2764−0.1874A	16:11:25.91	(3)	−51:41:59.38	(4)	3.78	(7)	−85.259	(6)	0.67	(1)	1.896
G331.2783−0.1884A	16:11:26.71	(3)	−51:41:57.3	(1)	1.34	(4)	−87.816	(6)	0.38	(1)	0.382
G331.2765−0.1871A	16:11:25.85	(2)	−51:41:58.05	(3)	2.0	(1)	−87.76	(1)	0.50	(3)	0.752
G331.3409−0.3470A	16:12:26.40	(4)	−51:46:20.50	(2)	30.7	(9)	−65.69	(1)	0.67	(2)	15.454
G331.3703−0.3990A	16:12:48.54	(5)	−51:47:24.39	(5)	5.15	(9)	−65.132	(4)	0.471	(9)	1.826
G331.3705−0.1446A	16:11:41.22	(4)	−51:36:15.37	(7)	0.90	(5)	−87.95	(3)	1.09	(7)	0.740
G331.3705−0.1446B	16:11:41.23	(5)	−51:36:15.3	(1)	0.90	(7)	−89.07	(3)	0.76	(7)	0.517
G331.3798+0.1490A	16:10:26.81	(2)	−51:22:58.5	(1)	1.47	(7)	−45.72	(2)	0.74	(4)	0.816
G331.4093−0.1643A	16:11:57.37	(4)	−51:35:32.033	(9)	1.27	(2)	−85.050	(5)	0.54	(1)	0.518
G331.4407−0.1869A	16:12:12.2	(1)	−51:35:14.1	(2)	3.3	(3)	−91.66	(2)	0.49	(4)	1.228
					0.56	(4)	−90.06	(6)	1.5	(1)	0.208
G331.4408−0.1869A	16:12:12.25	(7)	−51:35:13.88	(6)	1.10	(6)	−87.94	(2)	0.65	(4)	0.536
G331.4381−0.1864A	16:12:11.3	(1)	−51:35:19.3	(1)	1.57	(3)	−87.756	(6)	0.56	(1)	0.660
					0.70	(9)	−86.88	(5)	0.8	(1)	0.294
G331.4417−0.1580A	16:12:04.85	(5)	−51:33:55.74	(3)	0.73	(3)	−85.98	(2)	1.05	(5)	0.574
G331.4876−0.0863A	16:11:58.9	(1)	−51:28:54.33	(6)	0.73	(7)	−90.19	(4)	0.9	(1)	0.483
G331.4954−0.0786A	16:11:59.05	(2)	−51:28:14.81	(6)	31.7	(4)	−89.001	(4)	0.673	(9)	16.069
G331.4962−0.0780A	16:11:59.12	(4)	−51:28:11.66	(2)	1.7	(1)	−88.45	(3)	0.84	(7)	1.073
G331.4874−0.0865A	16:11:58.87	(3)	−51:28:55.23	(3)	1.41	(4)	−87.906	(7)	0.54	(2)	0.575
G331.5046−0.1158A	16:12:11.44	(3)	−51:29:30.20	(3)	2.43	(4)	−100.45	(1)	1.19	(2)	2.171
G331.5033−0.1066A	16:12:08.64	(8)	−51:29:09.1	(1)	0.70	(4)	−88.39	(2)	0.73	(5)	0.386
G331.5028−0.1068A	16:12:08.55	(2)	−51:29:10.76	(4)	1.39	(7)	−86.90	(1)	0.49	(3)	0.508
G331.5032−0.1067A	16:12:08.65	(9)	−51:29:09.71	(6)	0.87	(8)	−86.18	(4)	1.0	(1)	0.625
G331.5219−0.0811A	16:12:07.16	(6)	−51:27:16.2	(2)	0.65	(4)	−90.84	(1)	0.49	(4)	0.237
G331.5179−0.0823A	16:12:06.36	(3)	−51:27:29.28	(3)	3.7	(2)	−88.04	(3)	0.97	(6)	2.708
					2.5	(3)	−89.36	(4)	0.8	(1)	1.830
G331.5179−0.0823B	16:12:06.34	(6)	−51:27:29.42	(5)	7.2	(3)	−90.08	(1)	0.60	(3)	3.267
G331.5185−0.0823A	16:12:06.52	(7)	−51:27:27.81	(5)	0.53	(2)	−87.063	(8)	0.50	(2)	0.199
G331.5290−0.0982A	16:12:13.665	(9)	−51:27:43.92	(2)	18.7	(6)	−93.017	(7)	0.50	(2)	7.093

Table B.1: *continued*

Spot name	α_{2000} (h:m:s)		δ_{2000} (°:′:″)		Peak flux density (Jy)		Peak velocity ($km\,s^{-1}$)		FWHM ($km\,s^{-1}$)		Integrated flux density ($Jy\,km\,s^{-1}$)
G331.5327−0.0993A	16:12:15.00	(9)	−51:27:37.6	(2)	79	(2)	−91.827	(9)	0.58	(2)	34.306
					10	(1)	−91.06	(3)	0.45	(6)	4.343
G331.5237−0.1009A	16:12:12.87	(2)	−51:28:04.02	(1)	4.53	(9)	−91.082	(4)	0.422	(9)	1.437
G331.5312−0.0987A	16:12:14.40	(2)	−51:27:39.71	(6)	1.21	(3)	−90.662	(5)	0.42	(1)	0.380
G331.5341−0.0997A	16:12:15.50	(5)	−51:27:35.31	(6)	3.82	(6)	−89.621	(6)	0.75	(1)	2.160
G331.5432−0.0660A	16:12:09.17	(2)	−51:25:44.2	(1)	1.6	(1)	−88.77	(3)	0.74	(8)	0.893
G331.5432−0.0660B	16:12:09.18	(2)	−51:25:44.24	(7)	0.80	(8)	−89.54	(4)	0.9	(1)	0.519
G331.5461−0.0688A	16:12:10.73	(6)	−51:25:44.6	(2)	0.62	(3)	−87.74	(1)	0.59	(3)	0.274
					0.44	(5)	−87.02	(3)	0.52	(7)	0.194
G331.5548−0.1227A	16:12:27.4	(1)	−51:27:44.49	(1)	3.2	(1)	−104.01	(1)	0.59	(3)	1.418
G331.5544−0.1221A	16:12:27.1	(1)	−51:27:44.1	(1)	3.8	(3)	−100.68	(3)	0.95	(8)	2.714
G331.5544−0.1221B	16:12:27.10	(3)	−51:27:44.13	(6)	1.2	(1)	−102.05	(5)	1.0	(1)	0.912
G331.5544−0.1221C	16:12:27.09	(2)	−51:27:44.1	(1)	0.68	(7)	−103.75	(6)	1.2	(1)	0.595
G331.5547−0.1211A	16:12:26.90	(2)	−51:27:40.69	(4)	4.01	(9)	−102.801	(4)	0.40	(1)	1.215
G331.5552−0.1215A	16:12:27.16	(3)	−51:27:40.6	(2)	0.74	(2)	−97.311	(8)	0.62	(2)	0.348
G331.5552−0.1215B	16:12:27.15	(7)	−51:27:40.7	(1)	0.64	(3)	−98.72	(2)	0.87	(5)	0.419
G331.8527−0.1295A	16:13:52.5	(1)	−51:15:46.63	(6)	1.15	(8)	−49.77	(4)	1.05	(9)	0.913
G331.8855+0.0619A	16:13:11.24	(2)	−51:06:04.75	(3)	0.99	(2)	−89.865	(5)	0.58	(1)	0.433
G331.8855+0.0627A	16:13:11.05	(6)	−51:06:02.6	(2)	4.3	(3)	−88.88	(3)	0.86	(6)	2.774
G331.8854+0.0625A*	16:13:11.1	(2)	−51:06:03.5	(2)	3.7	(2)	−88.81	(2)	0.76	(5)	2.112
G331.8847+0.0617A	16:13:11.08	(9)	−51:06:07.4	(2)	2.06	(4)	−88.375	(4)	0.436	(9)	0.675
G331.8854+0.0630A	16:13:10.96	(2)	−51:06:02.21	(2)	0.82	(2)	−87.135	(5)	0.405	(9)	0.250
G331.8892+0.0641A	16:13:11.70	(2)	−51:05:49.90	(8)	0.85	(3)	−86.785	(8)	0.46	(2)	0.294
					0.56	(3)	−86.12	(2)	0.58	(4)	0.194
G331.8864+0.0618A	16:13:11.522	(9)	−51:06:02.7	(1)	0.73	(3)	−86.378	(9)	0.42	(2)	0.230
G331.8898+0.0658A	16:13:11.44	(3)	−51:05:43.9	(1)	0.80	(3)	−85.978	(8)	0.48	(2)	0.286
G331.8880+0.0658A	16:13:10.94	(3)	−51:05:48.5	(1)	1.51	(1)	−86.863	(1)	0.330	(2)	0.375
G331.9209−0.0829A	16:13:59.17	(7)	−51:10:56.00	(6)	4.7	(2)	−51.63	(1)	0.44	(3)	1.549
					0.7	(2)	−52.18	(4)	0.4	(1)	0.231
G332.0933−0.4213A	16:16:16.59	(7)	−51:18:27.90	(8)	3.6	(2)	−58.82	(1)	0.53	(3)	1.442
					1.7	(2)	−58.16	(3)	0.67	(8)	0.681
G332.0911−0.4194A	16:16:15.44	(5)	−51:18:28.51	(8)	8.1	(2)	−55.849	(6)	0.45	(1)	2.742
G332.0908−0.4184A	16:16:15.12	(3)	−51:18:26.51	(5)	0.68	(3)	−58.05	(1)	0.53	(3)	0.270
G332.2420−0.0443A	16:15:17.74	(6)	−50:55:58.09	(9)	2.4	(2)	−47.32	(3)	0.89	(6)	1.599
G332.2420−0.0443B	16:15:17.78	(8)	−50:55:58.0	(1)	121	(3)	−49.178	(7)	0.63	(2)	57.263
					15	(4)	−49.91	(5)	0.36	(9)	7.099
G332.2417−0.0437A	16:15:17.53	(2)	−50:55:57.30	(4)	14.4	(3)	−48.527	(4)	0.509	(9)	5.513
G332.2393−0.0425A	16:15:16.55	(2)	−50:55:60.0	(1)	6.8	(5)	−48.51	(3)	0.61	(6)	3.146
G332.2401−0.0429A	16:15:16.88	(2)	−50:55:59.27	(2)	6.1	(4)	−47.93	(1)	0.40	(3)	1.838
G332.2390−0.0451A	16:15:17.2	(2)	−50:56:07.5	(4)	34	(1)	−47.31	(1)	0.86	(3)	21.996
G332.2387−0.0452A*	16:15:17.1	(2)	−50:56:08.7	(2)	6.5	(8)	−46.78	(3)	0.50	(7)	2.442

Table B.1: *continued*

Spot name	α_{2000} (h:m:s)		δ_{2000} (°:′:″)		Peak flux density (Jy)		Peak velocity ($km\,s^{-1}$)		FWHM ($km\,s^{-1}$)		Integrated flux density ($Jy\,km\,s^{-1}$)
G332.2390−0.0428A	16:15:16.55	(6)	−50:56:01.78	(7)	1.10	(4)	−46.247	(9)	0.44	(2)	0.367
G332.2959−0.0945A	16:15:45.8	(2)	−50:55:54.5	(3)	20.2	(8)	−49.70	(2)	0.91	(4)	13.820
G332.2959−0.0945B	16:15:45.80	(5)	−50:55:54.47	(6)	21.4	(6)	−50.627	(9)	0.59	(2)	9.558
					14.9	(2)	−49.98	(1)	0.13	(2)	6.655
G332.2956−0.0945A*	16:15:45.7	(2)	−50:55:55.0	(2)	15.5	(5)	−49.83	(1)	0.60	(2)	6.951
G332.2953−0.0944A	16:15:45.61	(8)	−50:55:55.62	(5)	9.0	(2)	−48.355	(7)	0.58	(2)	3.924
G332.2941−0.0924A	16:15:44.771	(9)	−50:55:53.23	(5)	4.5	(2)	−48.915	(7)	0.35	(2)	1.180
G332.2924−0.0919A	16:15:44.15	(2)	−50:55:56.39	(6)	2.69	(7)	−46.107	(9)	0.74	(2)	1.492
G332.3191+0.1763A	16:14:41.1	(2)	−50:43:12.02	(8)	2.9	(2)	−48.15	(2)	0.82	(5)	1.799
G332.3174+0.1817A	16:14:39.18	(5)	−50:43:02.11	(2)	0.55	(3)	−49.28	(1)	0.54	(3)	0.222
G332.3546−0.1145A	16:16:07.18	(3)	−50:54:19.9	(4)	6.1	(1)	−50.221	(8)	0.81	(2)	3.698
G332.5832+0.1469A	16:16:00.97	(5)	−50:33:30.96	(9)	3.01	(5)	−42.631	(6)	0.76	(1)	1.718
G332.6036−0.1679A	16:17:29.34	(5)	−50:46:15.0	(1)	1.6	(1)	−46.15	(3)	0.63	(7)	0.763
G332.6042−0.1668A	16:17:29.21	(4)	−50:46:10.9	(1)	10.5	(3)	−45.836	(9)	0.72	(2)	5.714
G332.7163−0.0480A	16:17:28.34	(6)	−50:36:22.70	(4)	2.8	(1)	−40.02	(2)	1.11	(5)	2.347
G332.7167−0.0488A	16:17:28.65	(5)	−50:36:23.9	(1)	1.10	(5)	−39.71	(1)	0.58	(3)	0.480
					0.82	(5)	−38.66	(2)	0.77	(5)	0.358
G333.0024−0.4368A	16:20:28.68	(3)	−50:41:00.91	(5)	5.7	(2)	−56.387	(8)	0.48	(2)	2.041
					1.4	(1)	−55.77	(3)	0.57	(7)	0.501
G333.0289−0.0623A	16:18:56.54	(6)	−50:23:53.6	(1)	0.755	(5)	−42.125	(2)	0.513	(5)	0.292
					0.768	(3)	−43	(8)	0.14	(2)	0.297
G333.0290−0.0629A	16:18:56.73	(1)	−50:23:55.17	(4)	6.7	(2)	−40.03	(1)	0.75	(3)	3.800
G333.0290−0.0629B	16:18:56.70	(4)	−50:23:55.09	(3)	7.4	(4)	−40.88	(2)	0.63	(4)	3.502
G333.0294−0.0243A	16:18:46.64	(2)	−50:22:14.57	(4)	5.60	(7)	−42.224	(3)	0.419	(5)	1.767
G333.0135−0.4660A	16:20:39.46	(2)	−50:41:47.45	(3)	1.21	(5)	−52.65	(1)	0.58	(3)	0.528
G333.0678−0.4460A	16:20:48.72	(5)	−50:38:38.7	(2)	0.49	(2)	−54.19	(2)	0.71	(4)	0.262
G333.0731−0.3996A	16:20:37.76	(3)	−50:36:26.66	(8)	2.13	(2)	−52.639	(3)	0.676	(7)	1.084
G333.0699−0.3989A	16:20:36.7	(2)	−50:36:32.92	(7)	0.68	(1)	−53.451	(7)	0.63	(2)	0.321
G333.0708−0.3990A	16:20:37.0	(1)	−50:36:30.80	(9)	0.68	(3)	−53.75	(2)	0.81	(4)	0.415
G333.1040−0.5027A	16:21:13.55	(1)	−50:39:31.22	(5)	5.4	(2)	−57.356	(9)	0.51	(2)	2.077
G333.1037−0.5036A	16:21:13.7	(1)	−50:39:34.49	(6)	1.66	(7)	−58.22	(1)	0.54	(3)	0.677
G333.1045−0.5025A	16:21:13.65	(2)	−50:39:29.68	(3)	0.89	(4)	−56.89	(1)	0.55	(3)	0.371
G333.1003−0.4985A	16:21:11.43	(5)	−50:39:30.1	(2)	0.56	(6)	−55.15	(2)	0.45	(5)	0.192
G333.1210−0.4325A	16:20:59.39	(3)	−50:35:48.95	(6)	4.4	(1)	−50.780	(7)	0.45	(2)	1.505
G333.1205−0.4337A	16:20:59.6	(2)	−50:35:53.4	(4)	1.30	(6)	−53.17	(1)	0.56	(3)	0.551
G333.1206−0.4330A	16:20:59.42	(5)	−50:35:51.3	(1)	2.23	(6)	−52.661	(6)	0.45	(1)	0.759
					1.01	(7)	−51.86	(2)	0.70	(6)	0.344
G333.1214−0.4334A	16:20:59.75	(2)	−50:35:50.46	(4)	0.8	(2)	−53.51	(3)	0.3	(1)	0.181
					0.62	(1)	−53.908	(4)	0.372	(9)	0.141
G333.1254−0.4412A	16:21:02.90	(8)	−50:36:00.1	(1)	3.5	(3)	−47.16	(4)	1.06	(9)	2.804
G333.1254−0.4412B	16:21:02.87	(3)	−50:36:00.1	(1)	55	(1)	−49.983	(5)	0.52	(1)	21.447
					13	(2)	−49.12	(8)	1.4	(2)	5.069

Table B.1: *continued*

Spot name	α_{2000} (h:m:s)		δ_{2000} (°:′:″)		Peak flux density (Jy)		Peak velocity ($km\,s^{-1}$)		FWHM ($km\,s^{-1}$)		Integrated flux density ($Jy\,km\,s^{-1}$)
G333.1254−0.4412C	16:21:02.88	(3)	−50:36:00.0	(2)	6.5	(4)	−48.12	(2)	0.48	(4)	2.339
					3.1	(9)	−47.61	(6)	0.4	(1)	1.115
G333.1300−0.4373A	16:21:03.06	(1)	−50:35:38.51	(2)	4.35	(2)	−51.528	(1)	0.358	(2)	1.172
G333.1310−0.4389A	16:21:03.75	(1)	−50:35:40.05	(7)	16.7	(2)	−50.238	(5)	0.69	(1)	8.702
					10	(1)	−49.704	(4)	0.26	(3)	5.211
G333.1256−0.4398A	16:21:02.58	(7)	−50:35:56.2	(2)	11.8	(5)	−49.09	(1)	0.56	(3)	4.978
G333.1257−0.4378A	16:21:02.0	(1)	−50:35:50.7	(1)	12	(1)	−48.633	(6)	0.30	(3)	2.680
					3.6	(3)	−49.04	(3)	0.53	(6)	0.804
G333.1256−0.4378A	16:21:02.03	(4)	−50:35:50.78	(6)	10	(1)	−48.69	(2)	0.47	(5)	3.545
G333.1255−0.4379A	16:21:02.03	(6)	−50:35:51.6	(1)	16.7	(8)	−48.05	(1)	0.52	(3)	6.571
G333.1260−0.4398A	16:21:02.7	(3)	−50:35:55.12	(9)	11.6	(7)	−47.40	(2)	0.56	(4)	4.893
G333.1254−0.4387A	16:21:02.20	(3)	−50:35:53.79	(8)	15.3	(3)	−46.730	(6)	0.67	(1)	7.756
					5.8	(4)	−45.81	(3)	0.96	(8)	2.940
G333.1381−0.4247A	16:21:01.89	(3)	−50:34:45.58	(8)	10.8	(2)	−56.070	(3)	0.464	(7)	3.771
G333.1319−0.4310A	16:21:01.92	(1)	−50:35:17.60	(5)	2.33	(9)	−55.586	(8)	0.40	(2)	0.702
G333.1398−0.4260A	16:21:02.69	(6)	−50:34:44.92	(4)	1.28	(5)	−53.770	(9)	0.54	(2)	0.522
G333.1629−0.1010A	16:19:42.69	(5)	−50:19:54.74	(7)	5.63	(6)	−91.480	(4)	0.730	(9)	3.093
G333.1631−0.1011A	16:19:42.75	(7)	−50:19:54.56	(4)	1.4	(2)	−90.83	(4)	0.7	(1)	0.690
G333.1610−0.1009A	16:19:42.15	(2)	−50:19:59.57	(5)	1.12	(3)	−92.337	(5)	0.45	(1)	0.379
					0.62	(6)	−92.83	(3)	0.54	(6)	0.210
G333.1850−0.0929A	16:19:46.47	(2)	−50:18:38.1	(2)	0.97	(4)	−86.18	(1)	0.73	(3)	0.536
G333.1839−0.0904A	16:19:45.53	(3)	−50:18:34.63	(4)	2.0	(1)	−86.69	(2)	0.90	(5)	1.361
G333.1828−0.0880A	16:19:44.59	(6)	−50:18:31.04	(2)	1.41	(7)	−86.83	(1)	0.33	(2)	0.355
G333.2302−0.0583A	16:19:49.41	(7)	−50:15:15.4	(1)	280	(3)	−87.298	(6)	1.07	(1)	224.818
					7	(2)	−89.2	(3)	1.6	(6)	5.620
G333.2344−0.0628A	16:19:51.71	(2)	−50:15:16.24	(4)	1.51	(3)	−91.542	(7)	0.65	(2)	0.733
G333.2323−0.0568A	16:19:49.59	(1)	−50:15:06.13	(3)	2.4	(1)	−90.44	(1)	0.70	(3)	1.259
G333.2305−0.0582A*	16:19:49.5	(2)	−50:15:14.2	(2)	35	(4)	−87.87	(3)	0.59	(7)	15.509
					8	(3)	−88.3	(2)	1.4	(5)	3.545
G333.2325−0.0628A	16:19:51.22	(2)	−50:15:21.18	(2)	3.76	(3)	−89.012	(2)	0.429	(5)	1.213
G333.2332−0.0627A	16:19:51.37	(8)	−50:15:19.10	(4)	6.3	(6)	−88.10	(2)	0.44	(5)	2.077
G333.2332−0.0627B	16:19:51.38	(7)	−50:15:19.0	(1)	2.1	(5)	−88.5	(1)	0.8	(2)	1.329
G333.2307−0.0585A	16:19:49.6	(2)	−50:15:14.54	(9)	5.3	(8)	−86.56	(4)	0.6	(1)	2.583
G333.2307−0.0585B	16:19:49.61	(7)	−50:15:14.4	(1)	10.2	(7)	−88.16	(2)	0.47	(4)	3.634
G333.2345−0.0640A	16:19:52.10	(1)	−50:15:19.02	(9)	8.0	(3)	−86.098	(9)	0.44	(2)	2.666
G333.2336−0.0632A	16:19:51.61	(7)	−50:15:19.14	(6)	2.9	(3)	−85.42	(5)	1.0	(1)	2.107
G333.2337−0.0625A	16:19:51.45	(5)	−50:15:17.1	(1)	12.1	(2)	−85.556	(4)	0.377	(7)	3.431
					5.2	(7)	−84.99	(4)	0.7	(1)	1.475
G333.2343−0.0610A	16:19:51.24	(8)	−50:15:11.92	(8)	8.62	(9)	−85.492	(3)	0.506	(7)	3.285
G333.2198−0.4027A	16:21:17.90	(2)	−50:30:22.21	(8)	21.5	(2)	−51.675	(2)	0.422	(5)	6.821
					1.58	(7)	−51.86	(4)	1.54	(8)	0.501

Table B.1: *continued*

Spot name	α_{2000} (h:m:s)		δ_{2000} (°:′:″)		Peak flux density (Jy)		Peak velocity ($km\,s^{-1}$)		FWHM ($km\,s^{-1}$)		Integrated flux density ($Jy\,km\,s^{-1}$)
G333.2204−0.4030A	16:21:18.13	(8)	−50:30:21.58	(9)	0.92	(5)	−54.65	(2)	0.82	(5)	0.566
G333.2204−0.4030B	16:21:18.14	(5)	−50:30:21.57	(4)	1.32	(7)	−55.82	(3)	1.15	(7)	1.146
G333.2200−0.4008A	16:21:17.43	(4)	−50:30:16.9	(2)	2.9	(2)	−53.74	(3)	0.90	(7)	1.964
G333.2203−0.4018A	16:21:17.8	(2)	−50:30:18.6	(3)	1.8	(1)	−53.61	(2)	0.75	(4)	1.018
G333.2203−0.4019A	16:21:17.8	(1)	−50:30:19.0	(2)	2.5	(2)	−52.72	(2)	0.56	(4)	1.050
					1.6	(2)	−53.43	(4)	0.8	(1)	0.672
G333.2845−0.3732A	16:21:27.31	(4)	−50:26:22.48	(8)	0.78	(5)	−52.09	(3)	0.90	(6)	0.530
G333.3008−0.3516A	16:21:25.92	(8)	−50:24:46.3	(1)	0.53	(3)	−49.45	(2)	0.70	(4)	0.279
G333.3117+0.1033A	16:19:28.67	(5)	−50:04:54.82	(2)	3.34	(6)	−45.161	(4)	0.480	(9)	1.208
G333.3137+0.1071A	16:19:28.21	(4)	−50:04:39.96	(6)	1.72	(6)	−48.22	(1)	0.69	(3)	0.887
G333.3123+0.1063A	16:19:28.05	(2)	−50:04:45.64	(5)	1.51	(4)	−47.186	(7)	0.58	(2)	0.658
G333.3146+0.1054A	16:19:28.90	(1)	−50:04:42.00	(2)	2.5	(2)	−44.43	(5)	1.0	(1)	1.941
G333.3358−0.3620A	16:21:38.02	(8)	−50:23:43.51	(6)	19.6	(4)	−51.927	(8)	0.81	(2)	11.951
G333.3358−0.3620B	16:21:38.05	(7)	−50:23:43.35	(5)	12.5	(2)	−52.43	(8)	0.2	(2)	1.883
					3	(3)	−52.87	(5)	0.2	(2)	0.452
G333.3376−0.3621A	16:21:38.54	(4)	−50:23:39.2	(1)	2.0	(9)	−49.96	(4)	0.2	(1)	0.369
					1.0	(3)	−49.52	(1)	0.25	(7)	0.184
G333.3376−0.3621B	16:21:38.5	(1)	−50:23:39.3	(1)	6.6	(3)	−50.29	(1)	0.41	(2)	2.047
G333.3376−0.3621C	16:21:38.5	(1)	−50:23:39.3	(2)	0.81	(5)	−54.10	(2)	0.60	(4)	0.365
G333.3284−0.3643A	16:21:36.67	(5)	−50:24:08.16	(2)	4.9	(1)	−50.867	(9)	0.68	(2)	2.519
G333.3285−0.3645A	16:21:36.73	(2)	−50:24:08.35	(5)	3.2	(3)	−50.22	(3)	0.63	(8)	1.509
G333.3359−0.3616A	16:21:37.95	(7)	−50:23:42.20	(7)	4.2	(1)	−51.098	(7)	0.41	(1)	1.303
					1.92	(8)	−50.54	(2)	1.01	(5)	0.596
G333.3384−0.3623A	16:21:38.79	(3)	−50:23:37.62	(2)	0.56	(3)	−47.60	(2)	0.82	(5)	0.347
G333.3874+0.0322A	16:20:07.52	(3)	−50:04:45.95	(4)	3.1	(1)	−70.22	(2)	0.96	(4)	2.231
G333.3860+0.0311A	16:20:07.42	(5)	−50:04:52.28	(5)	0.97	(9)	−72.57	(3)	0.65	(7)	0.473
G333.3862+0.0311A	16:20:07.48	(6)	−50:04:51.84	(4)	1.65	(5)	−72.03	(1)	0.83	(3)	1.027
G333.3872+0.0316A	16:20:07.62	(3)	−50:04:48.0	(2)	1.44	(6)	−68.44	(1)	0.49	(2)	0.528
G333.3745−0.2023A	16:21:05.93	(4)	−50:15:17.91	(7)	9.1	(4)	−61.31	(1)	0.44	(2)	3.000
G333.3773−0.2013A	16:21:06.42	(7)	−50:15:08.52	(7)	6.5	(1)	−57.979	(7)	0.93	(2)	4.574
G333.4679−0.1601A	16:21:19.62	(2)	−50:09:33.1	(2)	17.3	(1)	−43.007	(2)	0.558	(5)	7.267
G333.4679−0.1601B	16:21:19.61	(2)	−50:09:32.95	(2)	0.6	(1)	−43.94	(9)	0.9	(2)	0.405
G333.4669−0.1621A	16:21:19.88	(4)	−50:09:40.75	(6)	6.1	(1)	−45.275	(5)	0.55	(1)	2.508
					0.8	(1)	−45.2	(1)	1.4	(3)	0.329
G333.4658−0.1660A	16:21:20.62	(3)	−50:09:53.44	(7)	2.1	(1)	−44.10	(1)	0.52	(3)	0.815
G333.4658−0.1660B	16:21:20.62	(1)	−50:09:53.47	(3)	0.6	(1)	−44.79	(8)	0.8	(2)	0.364
G333.4664−0.1633A	16:21:20.05	(4)	−50:09:45.2	(1)	5.5	(2)	−43.467	(7)	0.41	(2)	1.716
G333.4681−0.1613A	16:21:19.97	(9)	−50:09:35.64	(7)	1.1	(1)	−42.11	(2)	0.53	(5)	0.435
G333.4681−0.1616A	16:21:20.1	(2)	−50:09:36.55	(4)	3.69	(8)	−41.518	(6)	0.55	(1)	1.530
G333.4684−0.1649A	16:21:21.00	(6)	−50:09:44.19	(3)	1.31	(6)	−38.91	(1)	0.51	(3)	0.502
G333.4973+0.1431A	16:20:07.59	(4)	−49:55:23.7	(1)	2.7	(2)	−112.39	(3)	0.75	(7)	1.531
					0.71	(7)	−113.60	(4)	0.85	(9)	0.403

Table B.1: *continued*

Spot name	α_{2000} (h:m:s)		δ_{2000} (°:′:″)		Peak flux density (Jy)		Peak velocity ($km\,s^{-1}$)		FWHM ($km\,s^{-1}$)		Integrated flux density ($Jy\,km\,s^{-1}$)
G333.4967+0.1424A	16:20:07.61	(3)	−49:55:26.86	(8)	0.70	(5)	−113.53	(2)	0.64	(5)	0.339
G333.4967+0.1421A	16:20:07.69	(3)	−49:55:28.0	(1)	0.75	(3)	−113.060	(8)	0.49	(2)	0.277
G333.5228−0.2747A	16:22:04.49	(1)	−50:12:05.3	(1)	7.2	(2)	−50.220	(9)	0.78	(2)	4.211
G333.5507−0.2915A	16:22:16.36	(6)	−50:11:36.91	(4)	1.96	(6)	−46.232	(7)	0.44	(2)	0.653
G333.5650−0.2952A	16:22:21.11	(4)	−50:11:09.8	(1)	1.16	(9)	−46.65	(3)	0.72	(6)	0.631
G333.5618−0.0246A	16:21:08.74	(4)	−49:59:48.85	(8)	60	(1)	−39.98	(1)	0.85	(2)	38.498
G333.5687+0.0284A	16:20:56.61	(3)	−49:57:15.91	(7)	7.1	(1)	−84.796	(4)	0.504	(9)	2.693
G333.5934−0.2122A	16:22:06.63	(4)	−50:06:26.6	(1)	27.7	(3)	−49.561	(3)	0.617	(7)	12.863
G333.5950−0.2108A	16:22:06.70	(2)	−50:06:19.2	(1)	1.2	(1)	−48.75	(5)	1.1	(1)	1.021
G333.5950−0.2108B	16:22:06.7	(1)	−50:06:18.8	(2)	2.3	(1)	−50.25	(3)	0.79	(6)	1.374
G333.5950−0.2108C	16:22:06.7	(2)	−50:06:18.77	(6)	0.8	(1)	−51.34	(5)	0.7	(1)	0.407
G333.5941−0.2116A	16:22:06.66	(3)	−50:06:23.07	(8)	1.26	(6)	−48.60	(2)	0.81	(4)	0.768
G333.6919−0.1955A	16:22:28.19	(2)	−50:01:32.9	(1)	3.29	(9)	−50.610	(5)	0.358	(9)	0.886
					0.46	(9)	−50.7	(1)	1.1	(2)	0.124
G333.6958−0.1986A	16:22:30.06	(5)	−50:01:30.8	(1)	0.94	(3)	−51.43	(1)	0.76	(3)	0.535
G333.7123−0.1158A	16:22:12.50	(4)	−49:57:18.37	(5)	6.2	(1)	−31.495	(6)	0.73	(1)	3.407
G333.7098−0.1152A	16:22:11.69	(2)	−49:57:23.17	(8)	0.45	(5)	−28.12	(4)	0.70	(9)	0.236
G333.7733−0.2578A	16:23:06.16	(4)	−50:00:43.31	(2)	2.55	(5)	−49.405	(5)	0.51	(1)	0.985
G333.7722−0.0096A	16:22:00.29	(3)	−49:50:15.79	(5)	17.7	(8)	−89.33	(2)	0.88	(4)	11.671
G333.8181−0.3026A	16:23:29.83	(2)	−50:00:42.0	(1)	20.4	(8)	−48.31	(1)	0.58	(3)	8.895
G333.8187−0.3031A	16:23:30.11	(4)	−50:00:41.93	(3)	2.3	(2)	−47.70	(3)	0.70	(7)	1.219
G333.8993−0.0977A	16:22:56.86	(8)	−49:48:35.3	(1)	1.5	(2)	−63.65	(4)	0.8	(1)	0.885
					1.5	(1)	−62.83	(3)	0.65	(7)	0.885
G333.9007−0.0993A	16:22:57.65	(8)	−49:48:35.9	(2)	1.36	(8)	−64.36	(2)	0.84	(5)	0.861
G333.9307−0.1342A	16:23:14.73	(2)	−49:48:47.5	(1)	3.8	(2)	−42.10	(2)	0.69	(4)	1.960
G333.9305−0.1343A	16:23:14.71	(2)	−49:48:48.46	(4)	3.0	(2)	−42.55	(2)	0.60	(5)	1.356
G333.9303−0.1316A	16:23:13.95	(2)	−49:48:41.8	(1)	0.89	(6)	−41.67	(2)	0.52	(4)	0.345
G333.9744+0.0737A	16:22:31.40	(3)	−49:38:08.44	(4)	6.7	(2)	−58.30	(1)	0.72	(3)	3.610
G333.9746+0.0736A	16:22:31.49	(2)	−49:38:08.19	(2)	3.2	(3)	−59.67	(4)	0.93	(9)	2.246
G334.0266−0.0465A	16:23:16.67	(1)	−49:41:00.19	(2)	10.4	(1)	−84.040	(4)	0.721	(9)	5.641
G334.7452+0.5068A	16:23:57.70	(1)	−48:46:59.92	(4)	3.52	(7)	−64.554	(5)	0.51	(1)	1.360
G334.7459+0.5063A	16:23:57.99	(2)	−48:46:59.41	(8)	1.60	(5)	−63.49	(1)	0.70	(3)	0.845
G334.7469+0.5058A	16:23:58.40	(7)	−48:46:58.0	(1)	2.3	(2)	−61.15	(2)	0.46	(4)	0.803
					0.45	(5)	−60.22	(4)	0.8	(1)	0.157

B.2 Gaussian fits to auto-correlated thermal line emission

Table B.2: Gaussian fits for the thermal lines detected towards class I CH_3OH maser regions. Column 1 lists the maser region. Columns 2 to 5 contain information for CS, columns 6 to 9 for SiO, columns 10 to 13 for thermal CH_3OH. The columns for each type of emission list the fitted Gaussian parameters, as well as the integrated intensity bounded by these Gaussians. Note that the uncertainty for each parameter is quoted in parentheses, in units of the least significant figure. Rows without region names correspond to a second Gaussian fitted to the region directly above. If no Gaussian information is listed for an emission type, it was not detected.

Region name	CS (1–0) parameters							SiO (1–0) $v = 0$ parameters								CH_3OH 1_0-0_0 parameters							
	Peak intensity (K)		Peak velocity ($km\,s^{-1}$)		FWHM ($km\,s^{-1}$)		Integrated intensity ($K\,km\,s^{-1}$)	Peak intensity (K)		Peak velocity ($km\,s^{-1}$)		FWHM ($km\,s^{-1}$)		Integrated intensity ($K\,km\,s^{-1}$)		Peak intensity (K)		Peak velocity ($km\,s^{-1}$)		FWHM ($km\,s^{-1}$)		Integrated intensity ($K\,km\,s^{-1}$)
G330.294−0.393	0.507	(3)	−80.68	(1)	5.62	(4)	2.143									0.02	(2)	−80.7	(3)	9.7	(7)	0.147
G330.678−0.402	0.298	(4)	−63.87	(3)	5.32	(7)	1.194	0.013	(1)	−64.0	(2)	8.6	(4)	0.084		0.05	(3)	−63.53	(6)	3.4	(2)	0.127
G330.779+0.249	0.336	(5)	−43.51	(1)	2.72	(3)	0.687	0.027	(1)	−43.81	(9)	6.7	(2)	0.137		0.10	(4)	−43.48	(3)	2.55	(7)	0.192
G330.876−0.362	1.24	(1)	−62.79	(2)	4.58	(4)	4.279	0.044	(1)	−63.35	(6)	7.1	(1)	0.236		0.09	(4)	−62.91	(5)	4.0	(1)	0.272
G330.871−0.383	1.39	(1)	−62.94	(2)	4.88	(4)	5.102	0.060	(1)	−63.63	(5)	7.1	(1)	0.322		0.10	(4)	−63.25	(5)	4.9	(1)	0.370
G330.927−0.408	0.47	(2)	−41.38	(4)	2.9	(1)	1.040	0.016	(1)	−42.5	(1)	5.4	(3)	0.065		0.05	(4)	−41.49	(7)	2.8	(2)	0.106
G330.931−0.260	0.158	(4)	−90.18	(6)	5.2	(1)	0.622									0.02	(4)	−89.1	(2)	3.2	(4)	0.048
G330.955−0.182	1.483	(8)	−91.16	(1)	7.01	(4)	7.820	0.174	(1)	−90.01	(3)	7.96	(7)	1.043		0.12	(5)	−90.59	(6)	5.5	(1)	0.496
G331.131−0.470	0.870	(7)	−67.50	(1)	4.55	(3)	2.979	0.023	(1)	−67.2	(1)	4.2	(2)	0.072		0.09	(3)	−67.78	(4)	4.2	(1)	0.286
G331.134−0.488	0.526	(6)	−66.23	(2)	5.43	(5)	2.152	0.016	(1)	−66.5	(2)	7.7	(4)	0.093		0.03	(2)	−66.1	(1)	5.4	(2)	0.123
G331.132−0.244	0.897	(5)	−86.94	(1)	5.76	(3)	3.889	0.087	(1)	−86.74	(5)	8.5	(1)	0.554		0.19	(4)	−86.33	(3)	5.35	(8)	0.765
G331.134+0.156	0.277	(6)	−76.96	(3)	3.05	(6)	0.637	0.017	(1)	−76.2	(1)	5.1	(3)	0.065		0.06	(3)	−76.52	(5)	4.4	(1)	0.198
G331.279−0.189	0.808	(5)	−88.29	(1)	5.25	(3)	3.195	0.046	(1)	−87.2	(1)	10.9	(3)	0.376		0.11	(3)	−88.06	(3)	3.61	(7)	0.299
G331.341−0.347	0.519	(8)	−65.90	(2)	3.06	(5)	1.197	0.019	(1)	−66.5	(1)	6.9	(3)	0.098		0.04	(2)	−66.46	(6)	4.2	(1)	0.126
G331.370−0.399	0.255	(6)	−64.80	(3)	3.62	(8)	0.695	0.009	(1)	−66.3	(4)	12.3	(8)	0.083		0.02	(2)	−66.5	(2)	8.2	(5)	0.124
	0.051	(5)	−69.9	(1)	3.1	(3)	0.121															
G331.371−0.145	0.167	(3)	−87.06	(4)	4.16	(9)	0.523									0.03	(3)	−87.7	(1)	6.1	(3)	0.138
	0.052	(3)	−91.0	(1)	3.7	(3)	0.145															
G331.380+0.149	0.344	(8)	−45.05	(5)	4.8	(1)	1.255	0.069	(1)	−44.63	(6)	6.7	(1)	0.350		0.20	(6)	−45.03	(3)	4.32	(7)	0.650
	0.07	(1)	−50.3	(1)	1.9	(3)	0.098															
G331.409−0.164	0.348	(4)	−86.36	(4)	5.73	(8)	1.502	0.028	(1)	−85.05	(9)	5.0	(2)	0.105		0.11	(3)	−85.99	(4)	4.48	(8)	0.371
G331.44−0.14	0.169	(5)	−86.6	(1)	8.2	(3)	1.049	0.017	(1)	−85.6	(1)	5.0	(3)	0.064		0.05	(3)	−85.89	(8)	5.7	(2)	0.213
G331.440−0.187	0.240	(7)	−88.0	(1)	8.9	(3)	1.605	0.060	(1)	−87.97	(6)	7.1	(1)	0.320		0.18	(4)	−88.36	(3)	5.51	(7)	0.746
G331.442−0.158	0.203	(3)	−87.10	(6)	7.1	(1)	1.090	0.021	(1)	−87.0	(1)	6.4	(3)	0.101		0.09	(4)	−86.75	(5)	4.5	(1)	0.306
G331.492−0.082	0.586	(7)	−88.83	(2)	4.33	(6)	1.908	0.035	(1)	−88.8	(1)	7.7	(2)	0.202		0.06	(5)	−88.72	(7)	3.3	(2)	0.149
G331.503−0.109	0.63	(2)	−88.14	(7)	5.3	(2)	2.511	0.037	(1)	−88.0	(1)	7.4	(3)	0.206		0.08	(7)	−87.9	(1)	4.0	(2)	0.240
	0.269	(6)	−101.38	(6)	5.2	(1)	1.055	0.032	(1)	−100.8	(2)	8.5	(4)	0.206		0.08	(4)	−101.30	(6)	4.0	(1)	0.238
G331.519−0.082	0.785	(4)	−89.35	(1)	4.73	(3)	2.797	0.027	(1)	−89.3	(2)	8.3	(4)	0.169		0.04	(5)	−89.3	(1)	3.3	(3)	0.100
G331.530−0.099	1.196	(6)	−88.58	(1)	5.07	(3)	4.566	0.063	(1)	−88.63	(6)	7.4	(1)	0.353		0.14	(5)	−89.16	(4)	4.21	(9)	0.443
G331.544−0.067	0.842	(9)	−88.27	(2)	4.79	(6)	3.036	0.038	(1)	−88.50	(7)	5.3	(2)	0.151		0.10	(5)	−88.66	(5)	3.8	(1)	0.287
G331.555−0.122	0.558	(7)	−100.37	(3)	4.51	(6)	1.894	0.024	(1)	−98.2	(2)	16.5	(6)	0.299		0.09	(5)	−100.56	(5)	3.6	(1)	0.247
	0.113	(5)	−88.8	(2)	8.8	(4)	0.747															
G331.72−0.20	0.464	(6)	−47.44	(2)	2.88	(4)	1.007	0.020	(1)	−46.5	(1)	4.3	(2)	0.064		0.05	(4)	−46.7	(1)	6.0	(3)	0.225
G331.853−0.129	0.452	(4)	−50.57	(2)	3.50	(4)	1.191	0.056	(1)	−50.69	(5)	5.4	(1)	0.229		0.13	(6)	−50.84	(7)	5.4	(2)	0.531
G331.887+0.063	0.343	(3)	−87.57	(2)	4.95	(5)	1.278	0.081	(1)	−87.39	(3)	4.89	(7)	0.298		0.20	(4)	−87.44	(2)	4.06	(5)	0.611
G331.921−0.083	0.297	(8)	−51.59	(4)	3.3	(1)	0.742	0.015	(1)	−50.9	(2)	9.9	(5)	0.112		0.06	(5)	−51.56	(8)	3.6	(2)	0.162
G332.092−0.420	0.776	(6)	−56.73	(2)	4.47	(4)	2.613	0.018	(1)	−57.0	(2)	6.1	(4)	0.082		0.06	(4)	−56.97	(7)	4.1	(2)	0.185
G332.240−0.044	0.462	(5)	−47.97	(2)	3.93	(4)	1.365	0.053	(1)	−48.67	(8)	9.2	(2)	0.368		0.19	(6)	−48.18	(4)	4.8	(1)	0.693
	0.080	(3)	−48.6	(2)	14.1	(5)	0.847															
G332.295−0.094	0.564	(7)	−48.86	(2)	3.68	(5)	1.561	0.022	(1)	−50.3	(1)	9.2	(3)	0.153		0.06	(3)	−49.38	(8)	5.3	(2)	0.239
	0.095	(4)	−49.3	(2)	9.2	(5)	0.656															
G332.318+0.179	0.197	(5)	−48.30	(3)	2.50	(7)	0.370	0.022	(1)	−47.9	(1)	5.2	(3)	0.085		0.06	(4)	−48.23	(6)	4.1	(1)	0.183
	0.059	(3)	−48.2	(2)	5.9	(4)	0.264															
G332.355−0.114	0.523	(5)	−49.97	(1)	2.73	(3)	1.076									0.03	(3)	−50.20	(5)	2.1	(2)	0.048
G332.583+0.147	0.124	(9)	−45.03	(8)	2.2	(2)	0.209															
G332.604−0.167	0.40	(1)	−46.66	(5)	3.5	(1)	1.068	0.025	(1)	−46.5	(1)	7.5	(3)	0.142		0.07	(4)	−46.51	(9)	6.1	(2)	0.320

Table B.2: *continued*

Region name	CS (1–0) parameters						SiO (1–0) $v = 0$ parameters						CH_3OH 1_0-0_0 parameters					
	Peak intensity (K)		Peak velocity ($km\,s^{-1}$)		FWHM ($km\,s^{-1}$)	Integrated intensity ($K\,km\,s^{-1}$)	Peak intensity (K)		Peak velocity ($km\,s^{-1}$)		FWHM ($km\,s^{-1}$)	Integrated intensity ($K\,km\,s^{-1}$)	Peak intensity (K)		Peak velocity ($km\,s^{-1}$)		FWHM ($km\,s^{-1}$)	Integrated intensity ($K\,km\,s^{-1}$)
G332.716−0.048	0.140	(5)	−39.54	(7)	4.2 (2)	0.443							0.03	(4)	−39.8	(1)	3.5 (3)	0.080
G333.002−0.437	0.860	(6)	−55.62	(1)	3.31 (3)	2.140	0.019	(1)	−54.5	(1)	6.1 (3)	0.087	0.02	(3)	−54.6	(2)	6.5 (5)	0.097
	0.358	(7)	−51.63	(3)	3.08 (7)	0.831												
G333.029−0.063	0.49	(1)	−41.24	(3)	2.87 (7)	1.058							0.03	(4)	−41.3	(1)	3.4 (4)	0.077
G333.029−0.024	0.45	(1)	−41.73	(3)	2.16 (7)	0.731	0.016	(1)	−41.3	(2)	4.9 (4)	0.058	0.02	(7)	−41.77	(9)	2.1 (2)	0.031
G333.014−0.466	0.818	(8)	−54.33	(2)	4.40 (5)	2.707	0.027	(1)	−53.8	(1)	8.5 (3)	0.173	0.01	(6)	−54.9	(4)	5.9 (9)	0.045
	0.10	(1)	−60.6	(2)	3.2 (4)	0.239												
G333.068−0.446	1.43	(1)	−53.48	(2)	4.68 (4)	5.039	0.064	(1)	−53.27	(6)	6.2 (1)	0.298	0.10	(8)	−53.73	(5)	4.1 (1)	0.306
	0.190	(9)	−59.9	(1)	4.7 (3)	0.671												
G333.071−0.399	0.842	(7)	−53.59	(2)	5.07 (5)	3.212	0.047	(2)	−52.5	(1)	6.0 (2)	0.213	0.06	(7)	−53.68	(8)	4.6 (2)	0.209
							0.020	(1)	−58.4	(4)	18 (1)	0.278						
G333.103−0.502	1.156	(9)	−55.87	(1)	3.63 (3)	3.159	0.027	(1)	−55.4	(1)	9.1 (4)	0.184	0.04	(7)	−56.37	(8)	3.5 (2)	0.106
G333.121−0.433	2.24	(1)	−51.50	(2)	5.65 (4)	9.533	0.096	(2)	−51.54	(7)	8.8 (2)	0.634	0.07	(8)	−51.23	(8)	5.7 (2)	0.302
	0.207	(8)	−60.8	(1)	6.8 (3)	1.063												
G333.126−0.439	2.54	(2)	−50.98	(2)	5.74 (5)	10.976	0.139	(2)	−50.99	(6)	8.9 (1)	0.927	0.1	(1)	−50.49	(7)	6.0 (2)	0.455
	0.30	(1)	−59.5	(1)	6.7 (3)	1.521												
G333.137−0.427	2.84	(1)	−52.32	(1)	6.48 (4)	13.843	0.171	(2)	−52.80	(5)	6.8 (1)	0.876	0.13	(9)	−52.82	(6)	6.4 (1)	0.625
							0.077	(2)	−44.9	(1)	11.9 (3)	0.688						
G333.162−0.101	0.35	(1)	−92.06	(4)	2.47 (9)	0.651							0.02	(4)	−88.8	(4)	16 (1)	0.242
	0.151	(8)	−87.0	(1)	5.1 (3)	0.580												
G333.184−0.090	0.522	(9)	−86.14	(3)	3.09 (6)	1.216	0.018	(1)	−86.4	(2)	5.1 (4)	0.069	0.08	(8)	−86.23	(5)	3.6 (1)	0.216
	0.134	(9)	−90.4	(1)	3.7 (3)	0.370												
G333.233−0.061	0.157	(6)	−88.7	(2)	8.3 (4)	0.976	0.091	(2)	−87.85	(5)	5.9 (1)	0.407	0.15	(7)	−87.93	(3)	4.52 (6)	0.510
G333.220−0.402	0.842	(9)	−52.00	(2)	3.19 (4)	2.024	0.027	(1)	−52.3	(1)	4.9 (3)	0.100	0.04	(8)	−52.24	(7)	2.7 (2)	0.081
	0.101	(9)	−47.1	(1)	2.9 (3)	0.220												
G333.24+0.02	0.348	(8)	−69.87	(5)	4.7 (1)	1.240	0.019	(1)	−68.4	(2)	11.9 (5)	0.170	0.03	(5)	−69.1	(1)	6.8 (3)	0.153
G333.284−0.373	1.983	(7)	−51.947	(9)	5.46 (2)	8.154	0.098	(2)	−51.52	(4)	4.84 (9)	0.357	0.2	(1)	−51.90	(3)	4.44 (7)	0.668
G333.301−0.352	1.623	(8)	−50.27	(1)	4.80 (3)	5.868	0.066	(1)	−50.42	(4)	4.4 (1)	0.217	0.18	(9)	−50.48	(3)	4.06 (6)	0.551
	0.191	(8)	−58.7	(1)	4.8 (2)	0.690												
G333.313+0.106	0.468	(8)	−46.41	(4)	4.80 (9)	1.691	0.039	(1)	−46.8	(1)	7.8 (3)	0.228	0.11	(9)	−46.25	(6)	5.5 (1)	0.459
G333.335−0.363	1.112	(8)	−50.70	(2)	4.70 (4)	3.936	0.067	(2)	−49.93	(9)	6.0 (2)	0.302	0.16	(8)	−50.29	(2)	3.80 (5)	0.457
							0.019	(1)	−59.3	(6)	21 (1)	0.293						
G333.387+0.031	0.324	(9)	−69.87	(5)	3.6 (1)	0.890	0.025	(1)	−69.3	(2)	11.7 (5)	0.220	0.05	(8)	−69.88	(7)	3.6 (2)	0.136
G333.376−0.202	0.357	(8)	−59.94	(4)	3.08 (8)	0.827	0.021	(1)	−55.5	(3)	15.4 (7)	0.244	0.03	(6)	−59.0	(1)	4.9 (3)	0.111
G333.467−0.163	0.35	(1)	−43.81	(4)	3.0 (1)	0.802	0.041	(1)	−44.1	(1)	9.6 (3)	0.298	0.07	(7)	−43.49	(6)	4.6 (1)	0.244
	0.284	(6)	−44.52	(9)	8.8 (2)	1.890	0.011	(1)	−58.2	(6)	14 (1)	0.117						
G333.497+0.143	0.18	(4)	−113.3	(3)	2.8 (6)	0.379	0.013	(1)	−114.6	(3)	11.4 (8)	0.111	0.03	(6)	−113.28	(7)	2.4 (2)	0.053
G333.523−0.275	0.936	(8)	−49.68	(1)	3.51 (3)	2.474	0.037	(1)	−49.3	(1)	6.4 (2)	0.178	0.05	(8)	−49.64	(6)	2.9 (1)	0.110
G333.558−0.293	0.589	(9)	−45.83	(2)	2.87 (5)	1.272	0.013	(1)	−47.8	(3)	12.5 (8)	0.122	0.03	(7)	−45.95	(7)	2.4 (2)	0.055
G333.562−0.025	0.145	(9)	−46.7	(1)	3.2 (2)	0.345	0.016	(1)	−38.9	(2)	7.8 (5)	0.094	0.03	(7)	−39.5	(1)	4.2 (3)	0.096
G333.569+0.028	0.256	(9)	−84.67	(9)	5.3 (2)	1.013	0.031	(1)	−84.4	(1)	7.5 (3)	0.174	0.08	(6)	−84.64	(4)	4.2 (1)	0.254
G333.595−0.211	1.96	(1)	−47.56	(1)	5.33 (3)	7.858	0.069	(1)	−47.93	(6)	6.5 (1)	0.338	0.0	(1)	−47.9	(1)	3.8 (2)	0.000
G333.694−0.197	0.289	(9)	−50.53	(4)	2.8 (1)	0.606	0.026	(1)	−49.9	(2)	8.0 (4)	0.157	0.08	(7)	−50.47	(3)	2.98 (8)	0.180
G333.711−0.115	0.071	(7)	−29.0	(2)	4.6 (5)	0.247												
G333.773−0.258	0.377	(6)	−47.69	(4)	5.5 (1)	1.563	0.048	(1)	−48.64	(8)	5.8 (2)	0.211	0.06	(6)	−48.66	(7)	4.9 (2)	0.220
G333.772−0.010	0.121	(8)	−86.0	(1)	3.5 (3)	0.319							0.01	(5)	−86.8	(4)	7.5 (9)	0.057
G333.818−0.303	0.141	(6)	−46.6	(1)	5.4 (3)	0.574							0.01	(3)	−46.6	(4)	9 (1)	0.069
G333.900−0.098	0.134	(7)	−65.1	(1)	4.0 (2)	0.401	0.014	(1)	−65.1	(2)	6.6 (5)	0.070	0.03	(6)	−64.9	(1)	4.6 (3)	0.104
G333.930−0.133	0.198	(7)	−40.01	(9)	5.2 (2)	0.773	0.020	(1)	−39.4	(1)	5.2 (3)	0.078	0.02	(6)	−39.9	(2)	5.1 (4)	0.077
G333.974+0.074	0.22	(1)	−59.93	(7)	2.4 (2)	0.406							0.01	(5)	−58.0	(5)	10 (1)	0.072
G334.027−0.047	0.366	(8)	−84.93	(4)	3.67 (9)	1.011							0.03	(5)	−84.72	(7)	3.3 (2)	0.075
	0.06	(1)	−89.0	(2)	2.0 (4)	0.089												
G334.746+0.506	0.255	(7)	−62.45	(6)	4.0 (1)	0.771	0.023	(1)	−62.0	(2)	12.2 (5)	0.212	0.06	(7)	−62.36	(6)	4.4 (2)	0.201

B.3 GLIMPSE images

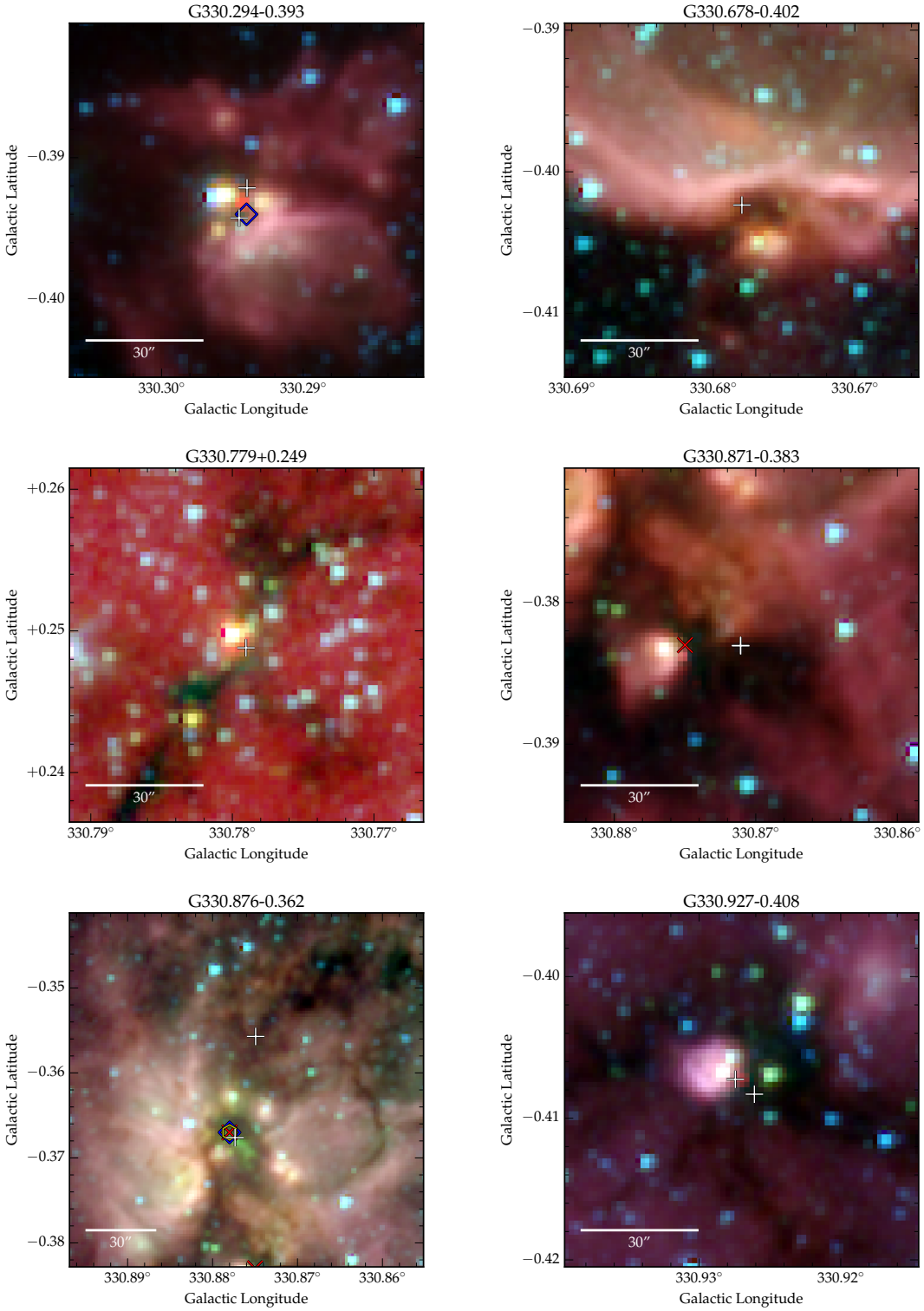

Figure B.1: *Spitzer* GLIMPSE three-colour images (RGB = 3.6, 4.5 and 8.0 μm) overlaid with the positions of class I CH_3OH masers (white plus symbols). The size of these symbols reflects the maximum positional uncertainty for maser spot. The published positions of class II CH_3OH, H_2O and OH masers are overlaid (red crosses, blue diamonds and yellow hexagon symbols, respectively; Caswell et al. 2011; Breen et al. 2010a; Walsh et al. 2011, 2014; Sevenster et al. 1997; Caswell 1998).

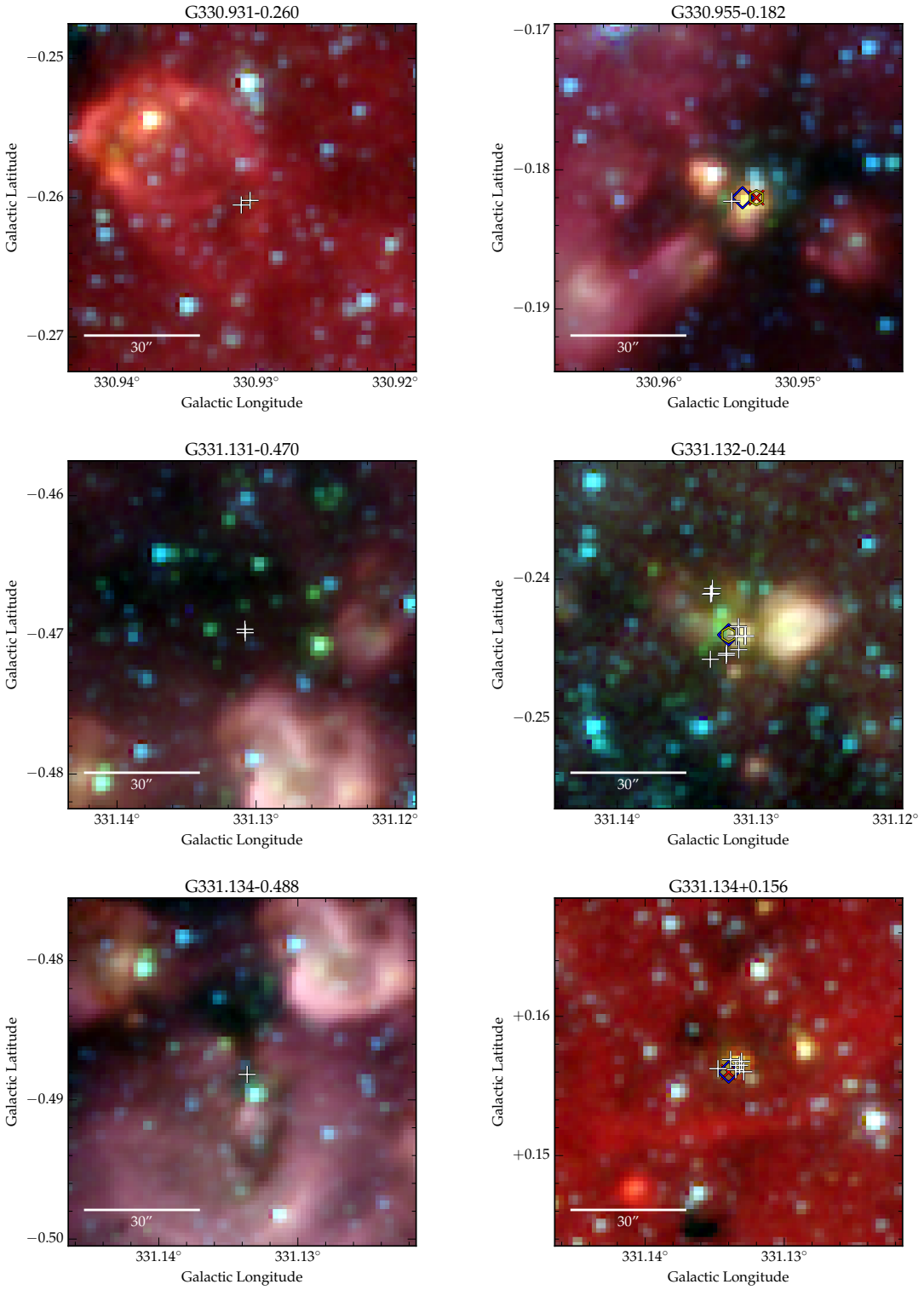

Figure B.1: *continued*

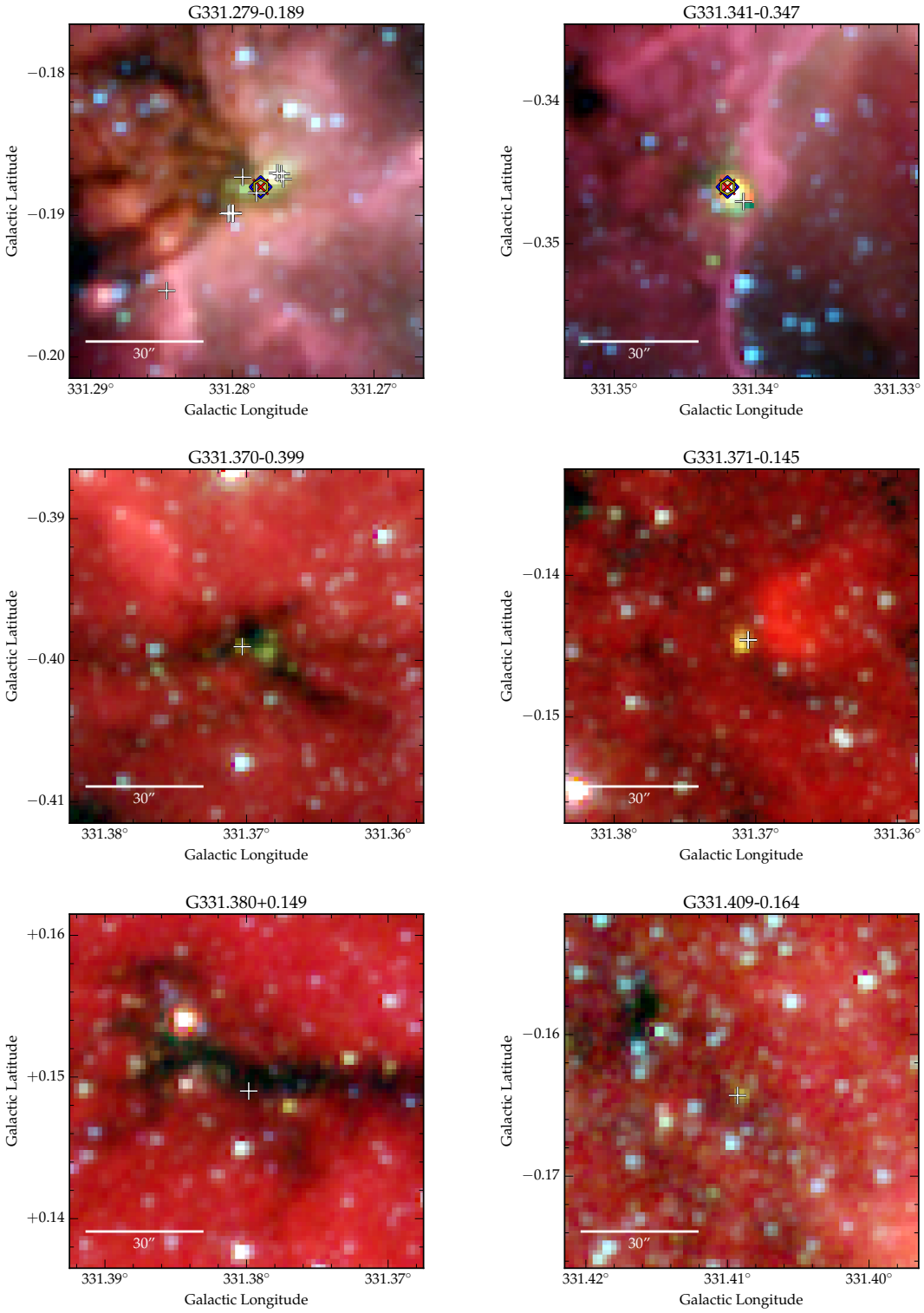

Figure B.1: *continued*

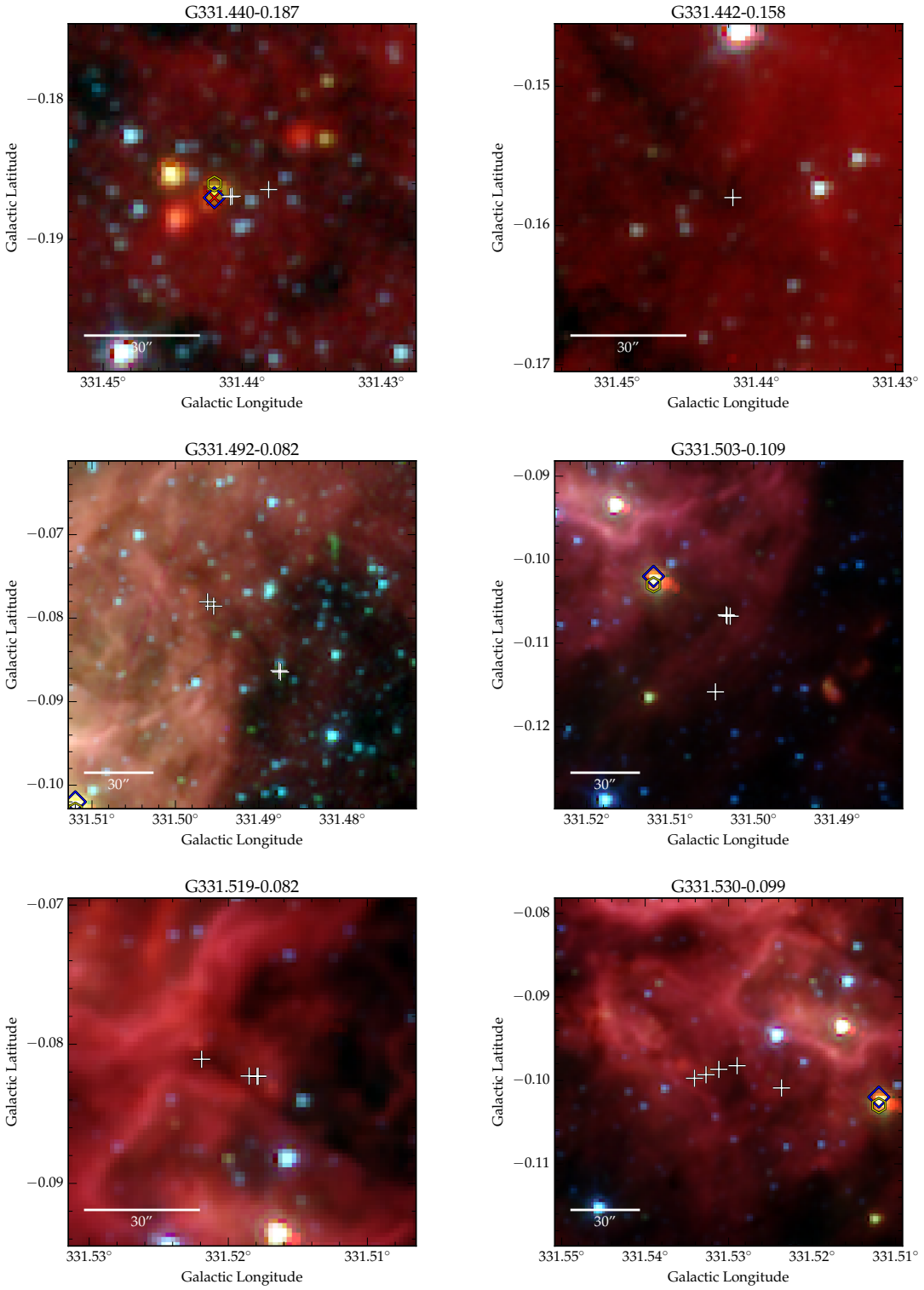

Figure B.1: *continued*

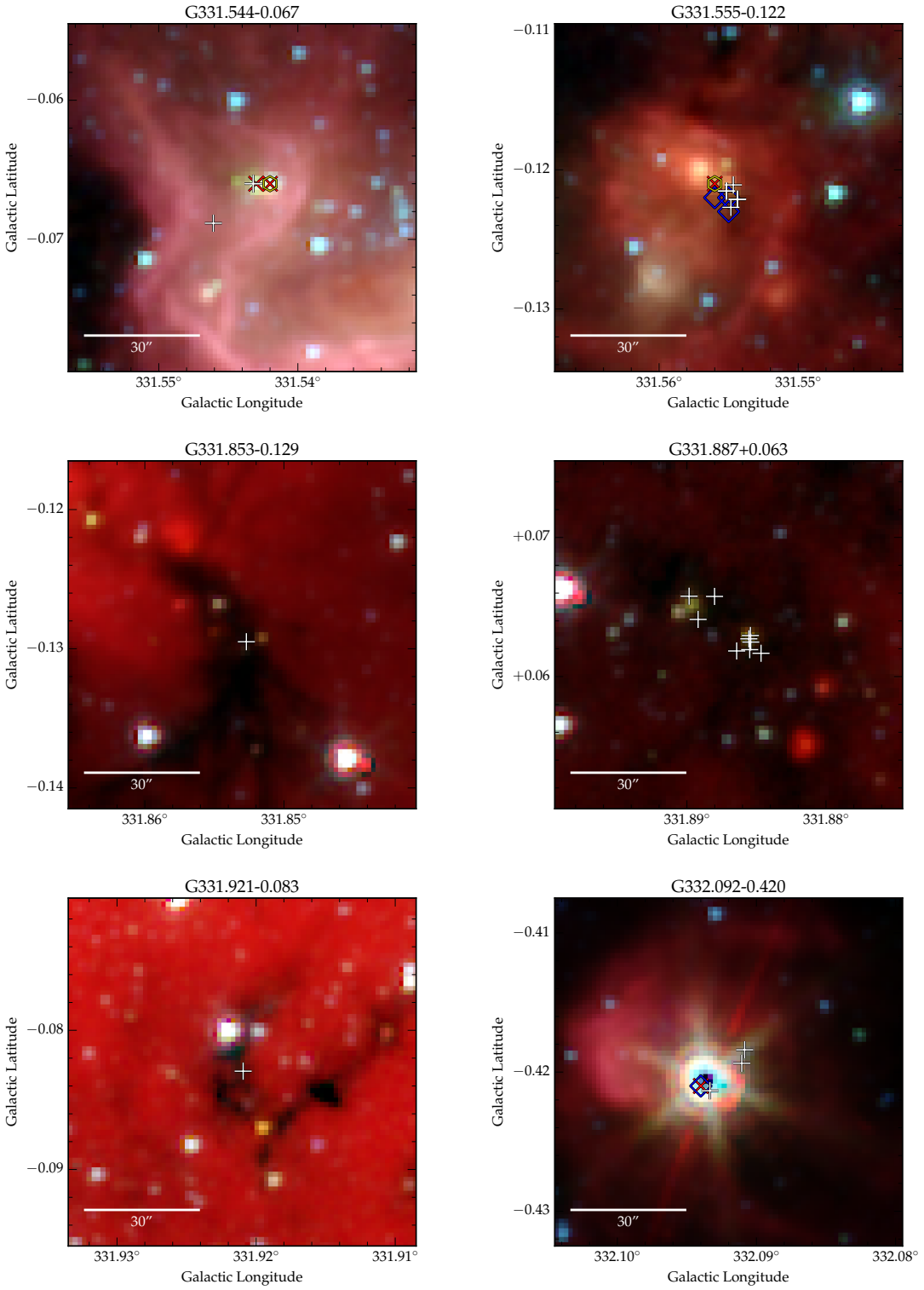

Figure B.1: *continued*

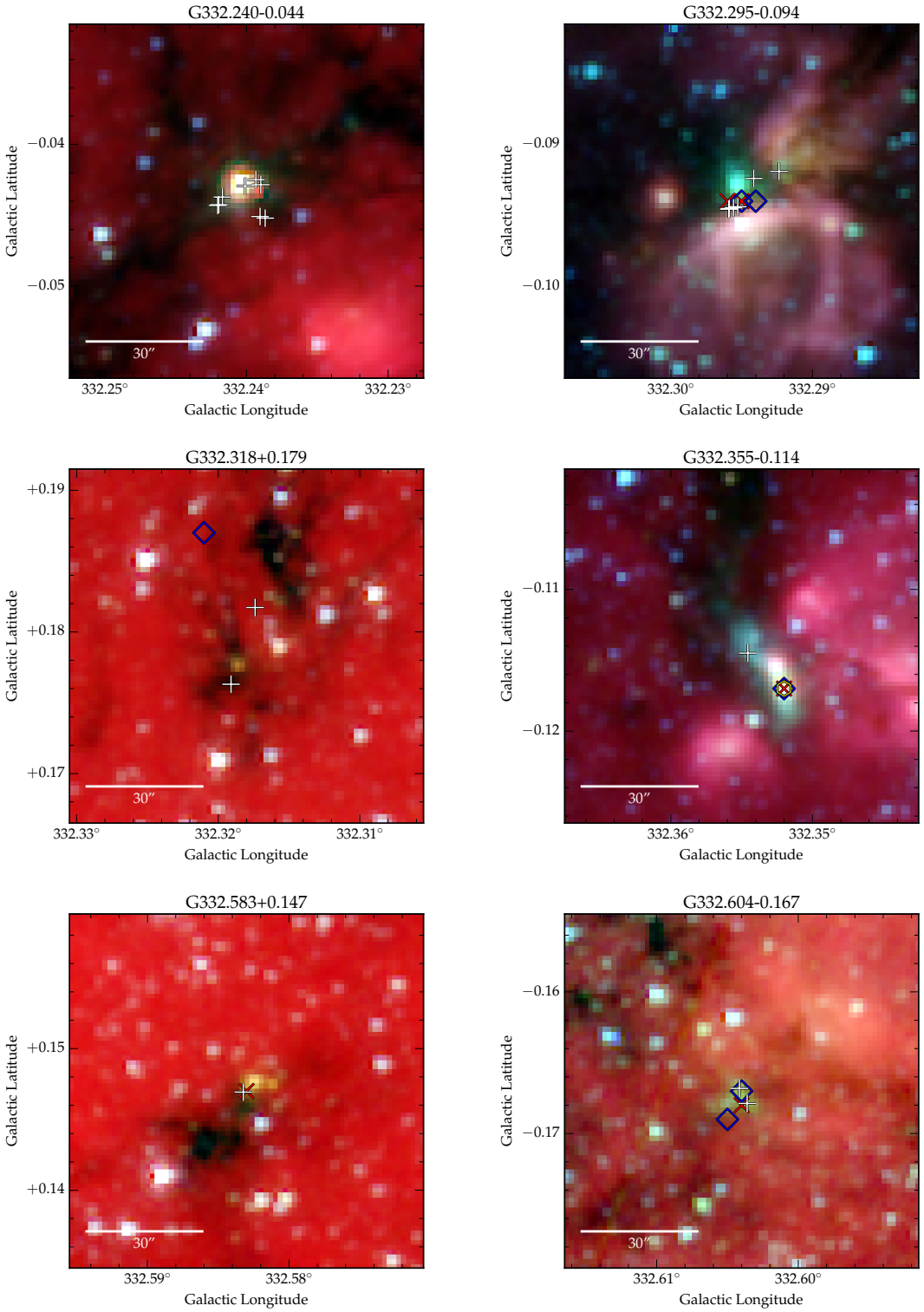

Figure B.1: *continued*

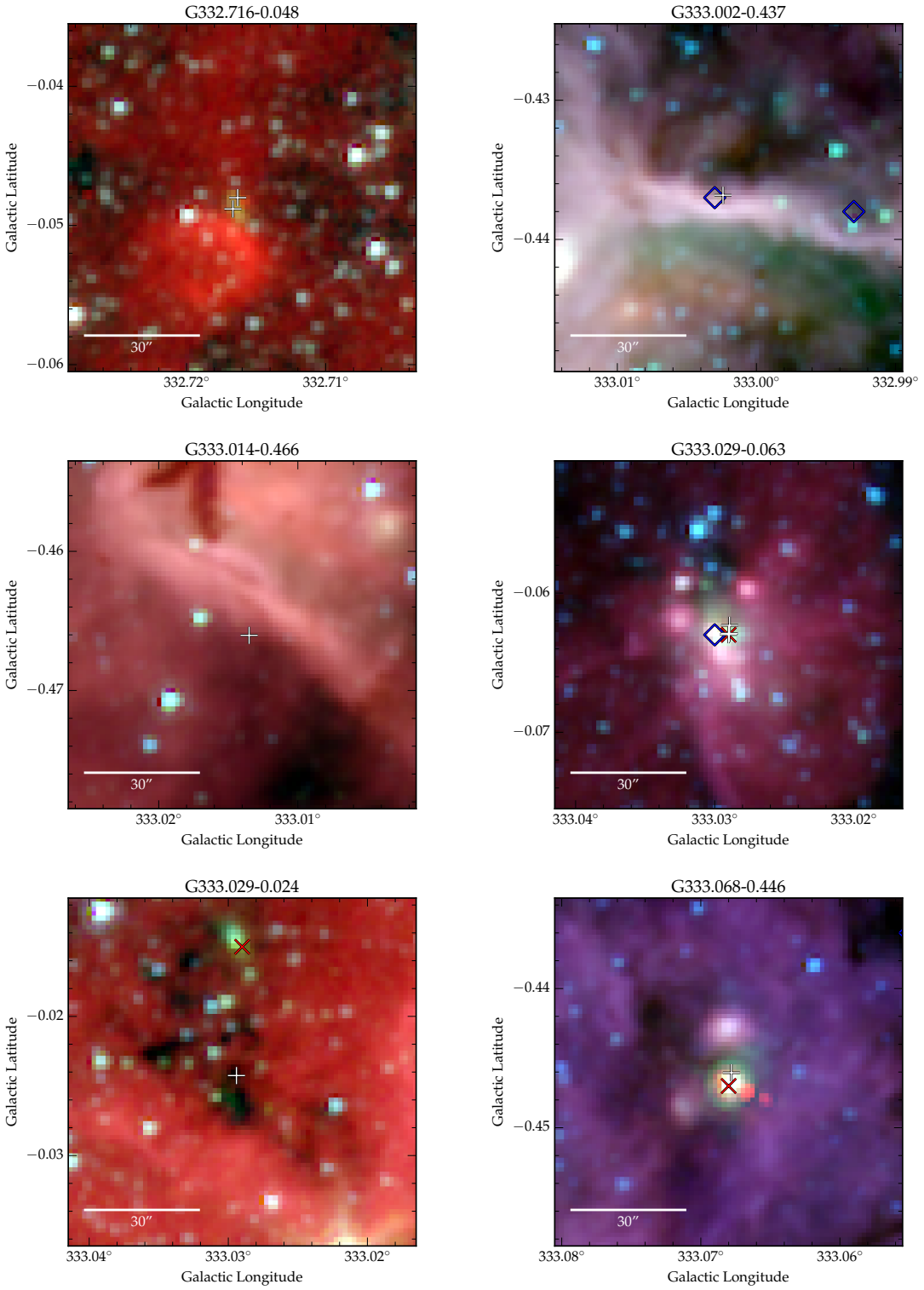

Figure B.1: *continued*

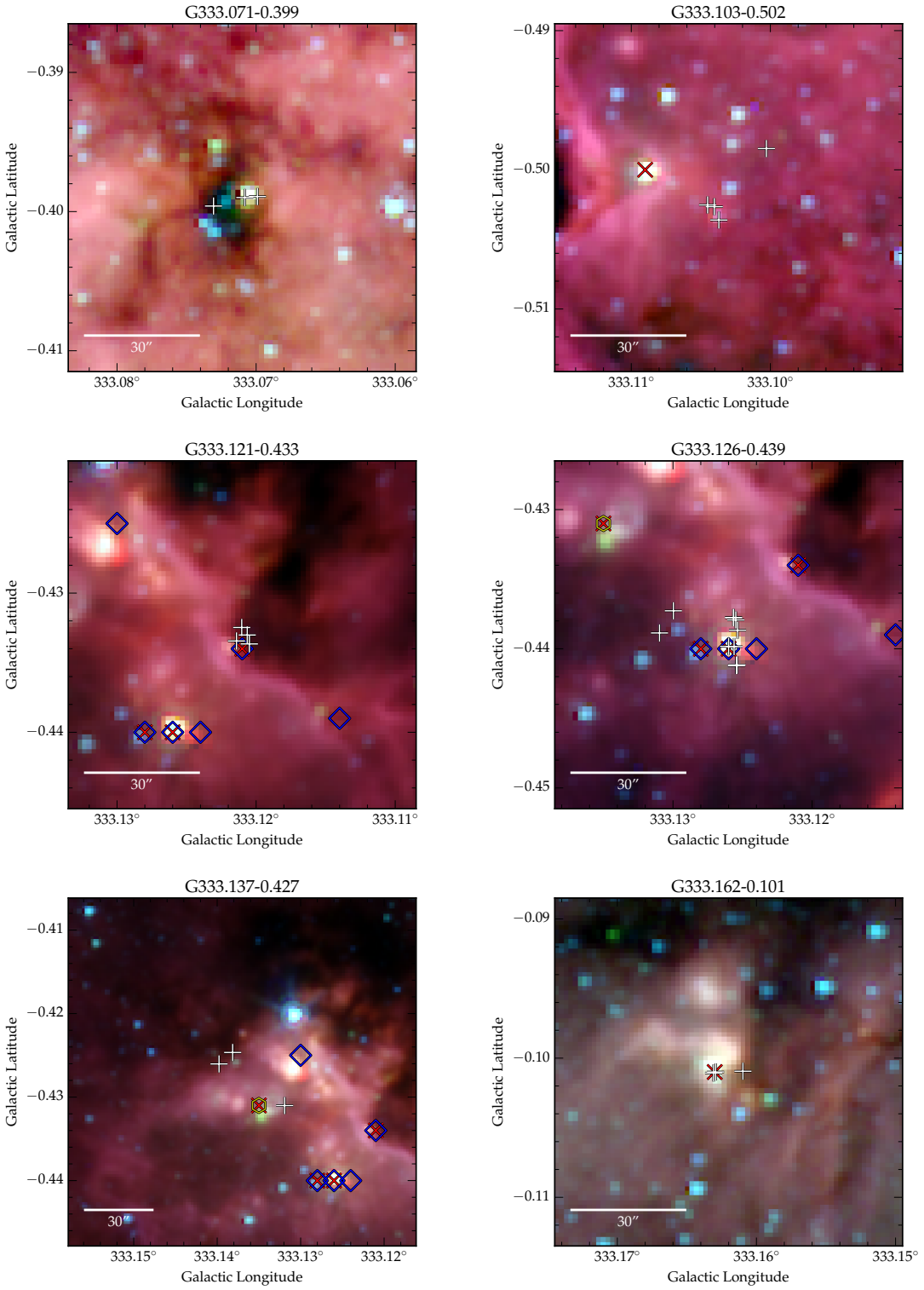

Figure B.1: *continued*

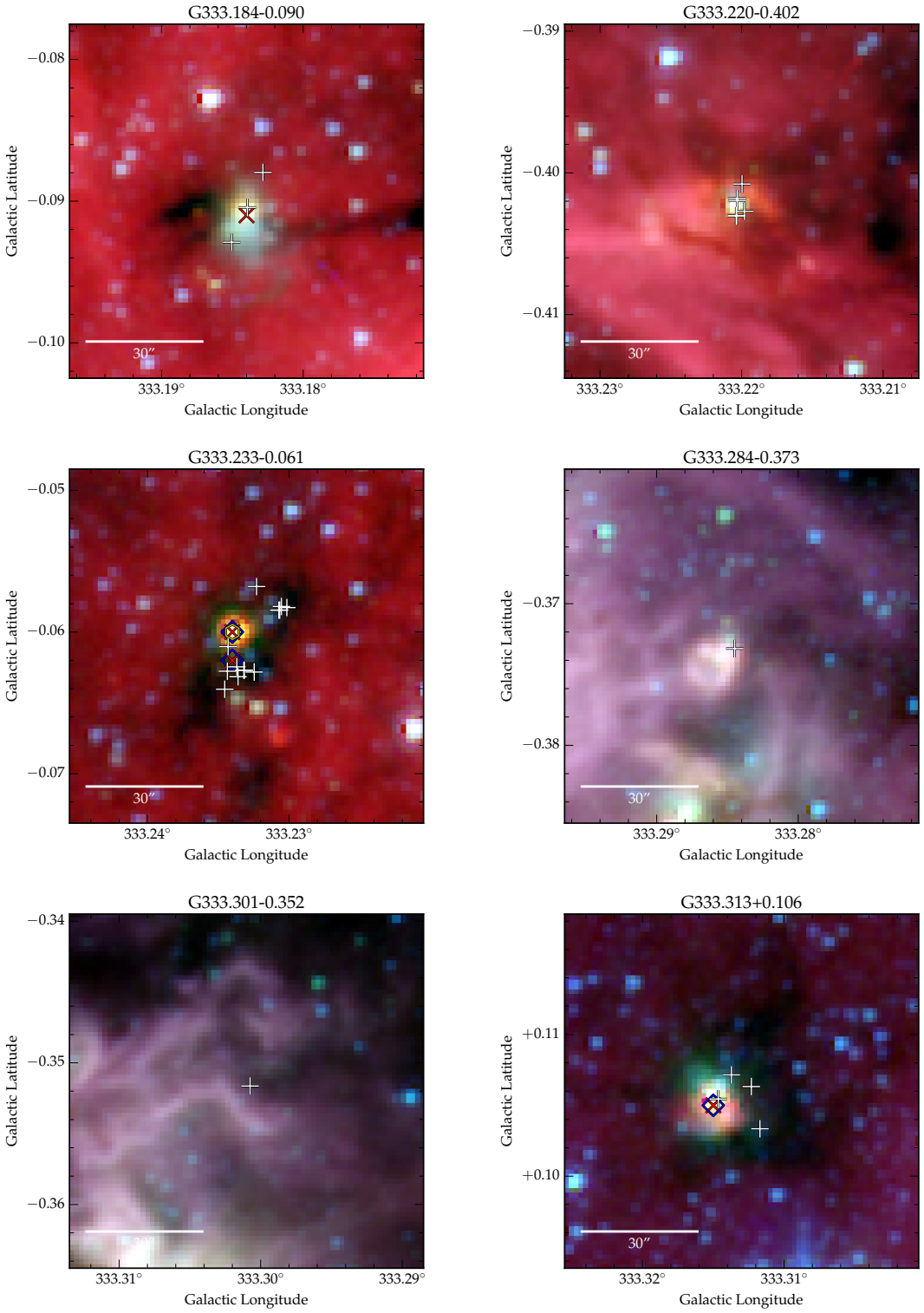

Figure B.1: *continued*

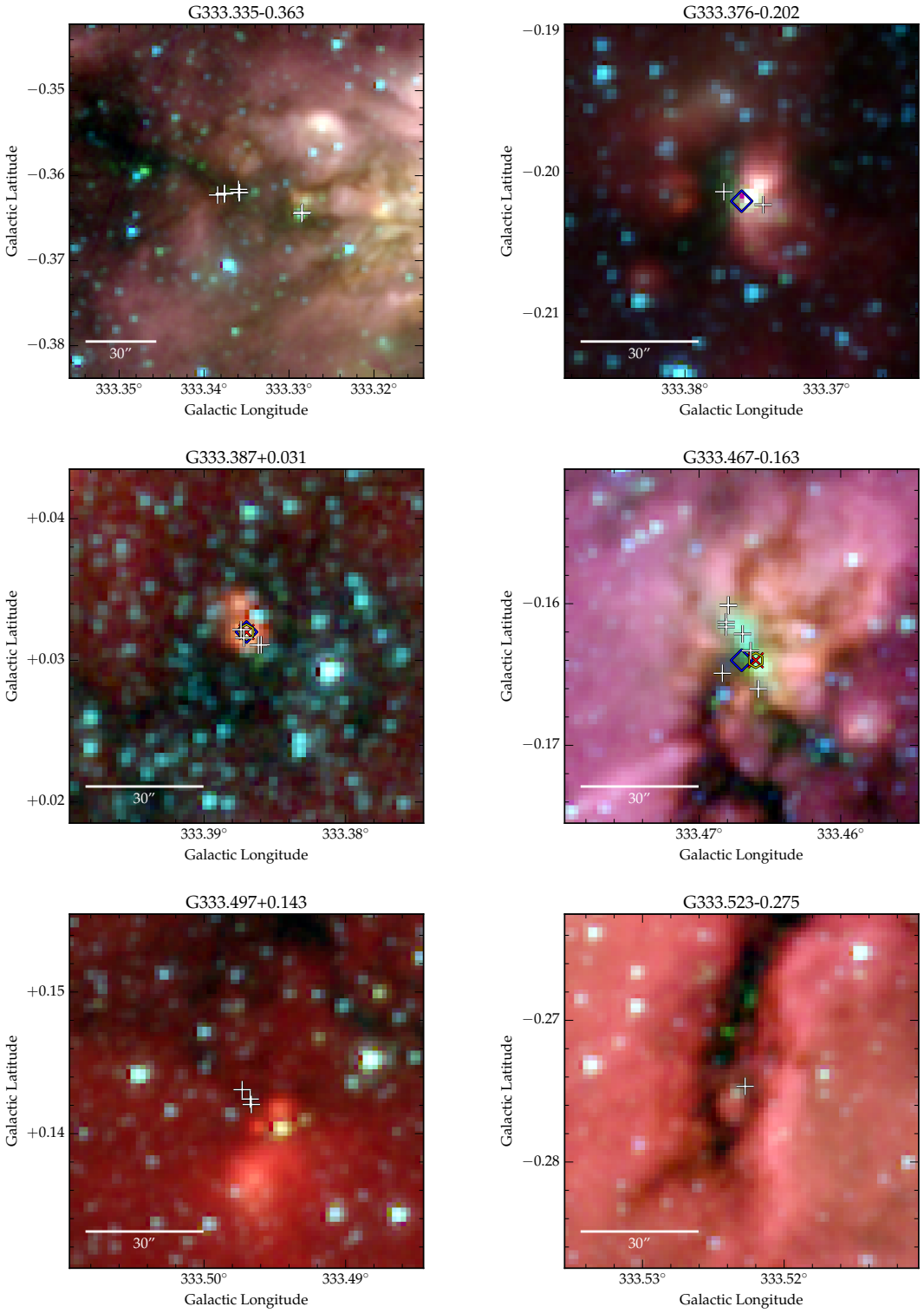

Figure B.1: *continued*

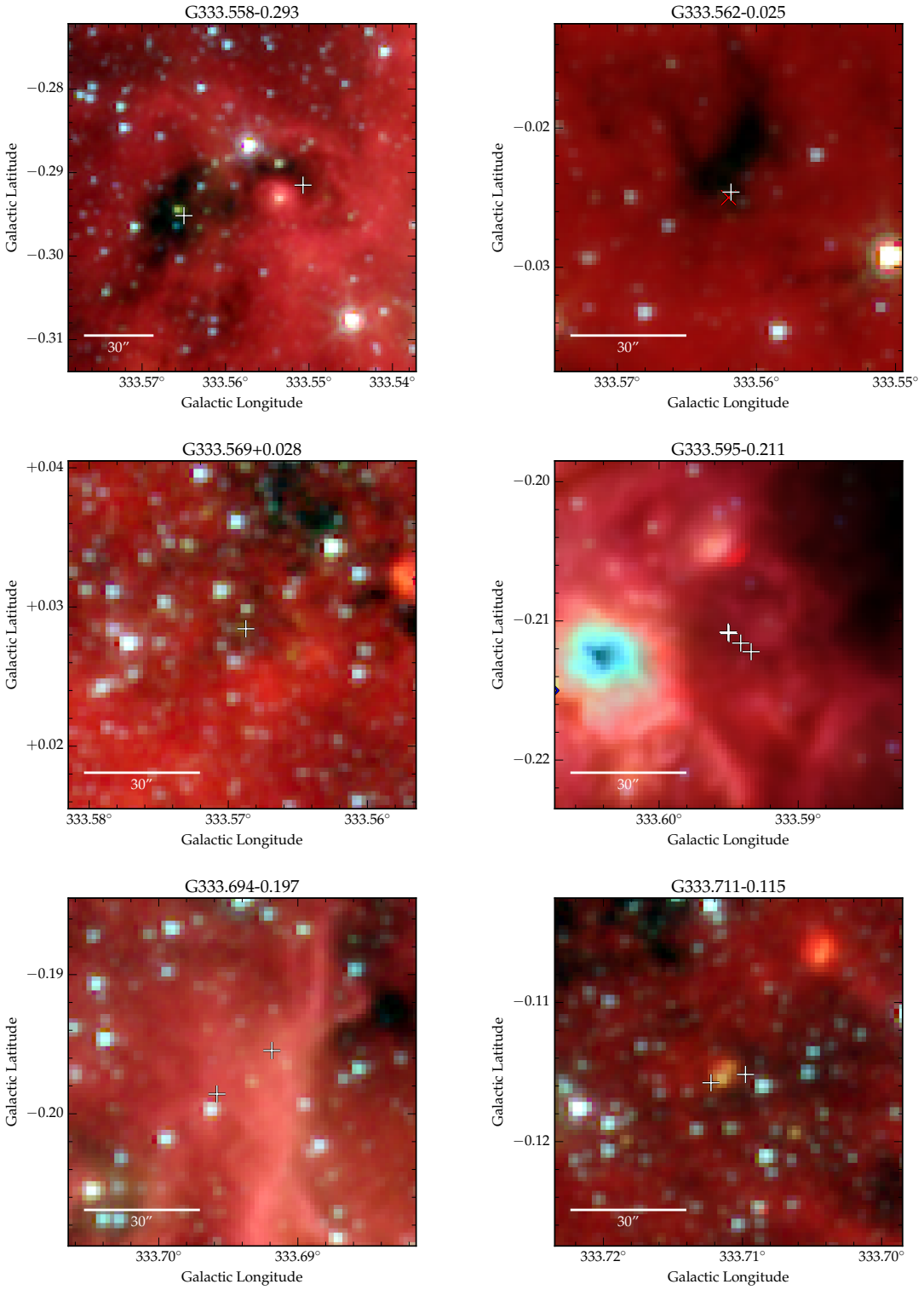

Figure B.1: *continued*

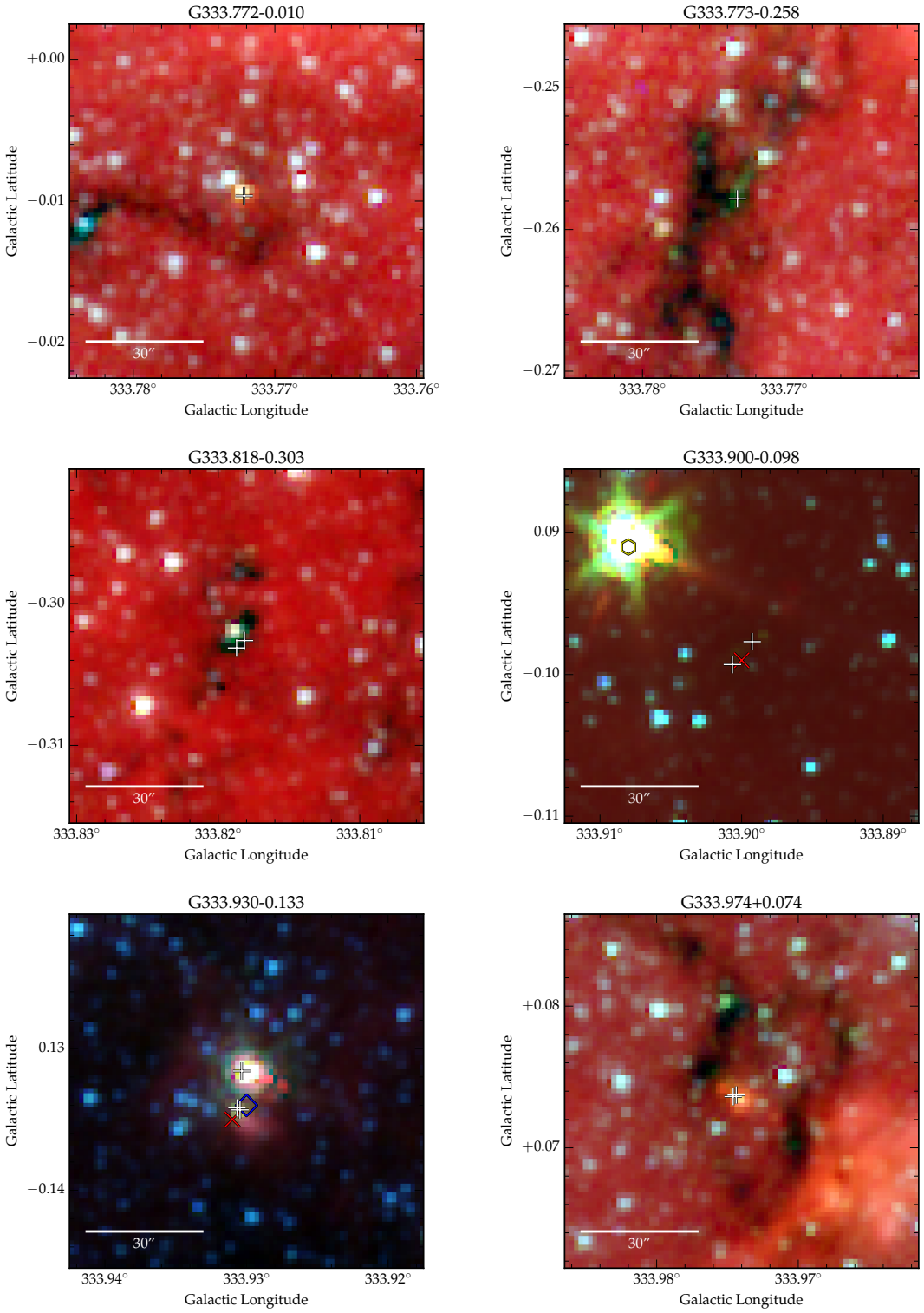

Figure B.1: *continued*

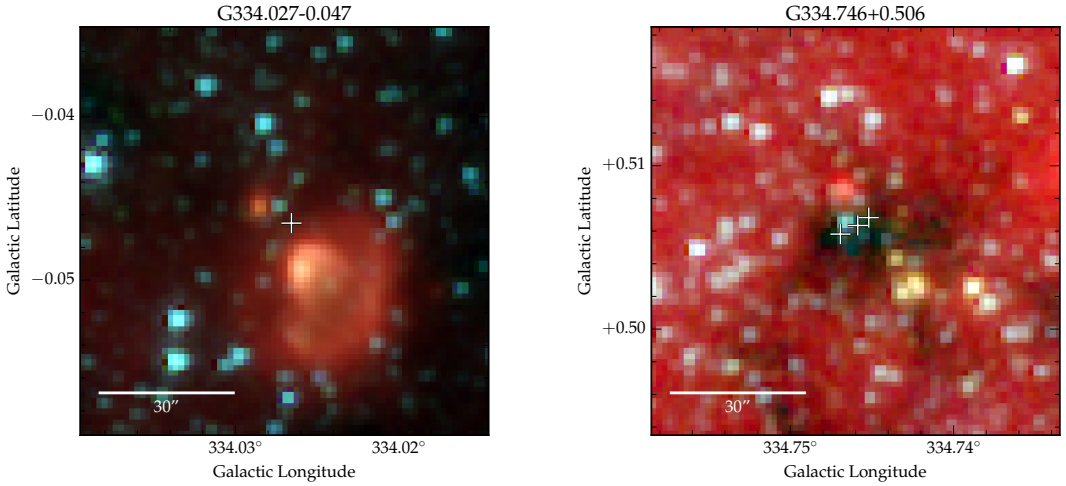

Figure B.1: *continued*